

3. Renton (1991)³ provided a closed form solution for shear area of rectangular sections. For a rectangular section of depth $2a$ and breadth $2b$.

$$\kappa = \frac{6}{5} + \left(\frac{\nu}{1+\nu}\right)^2 \sum_{m=0}^{\infty} \sum_{n=1}^{\infty} \frac{144(b/a)^4}{\pi^6(2m+1)^2 n^2 [(2m+1)^2(b/2a)^2 + n^2]} \quad (307.4)$$

For square cross section, $b = a$, therefore,

$$\kappa = \frac{6}{5} + \left(\frac{\nu}{1+\nu}\right)^2 \sum_{m=0}^{\infty} \sum_{n=1}^{\infty} \frac{144}{\pi^6(2m+1)^2 n^2 [(2m+1)^2(1/2)^2 + n^2]} \quad (307.5)$$

To simplify the equation above, according to the Renton (1991), the intermediate values are given by

$$\kappa = \frac{6}{5} + C_1 \left(\frac{\nu}{1+\nu}\right)^2 \left(\frac{b}{a}\right)^4 \quad (307.6)$$

where C_1 is the parameter determined by the ratio of a and b . When $b = a$, the equation becomes

$$\kappa = \frac{6}{5} + 0.1392 \left(\frac{\nu}{1+\nu}\right)^2 \quad (307.7)$$

307.2.2 Verification of 8 node brick cantilever beam (static)

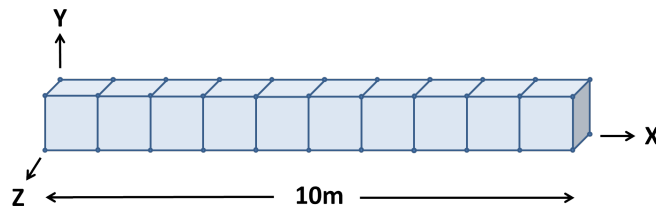
Problem description: Length=10m, Force=4N, E=100000Pa, $I = \frac{1}{12}$

Theoretical displacement:

$$d = \frac{PL^3}{3EI} = \frac{4 \times 1000}{3 \times 100000 \times \frac{1}{12}} = 0.16m \quad (307.8)$$

Numerical simulation results:

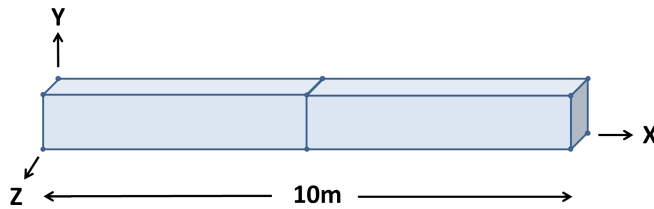
1m element size (10 elements):



$$\text{error} = \frac{0.16 - 0.1072}{0.16} = 33\% \quad (307.9)$$

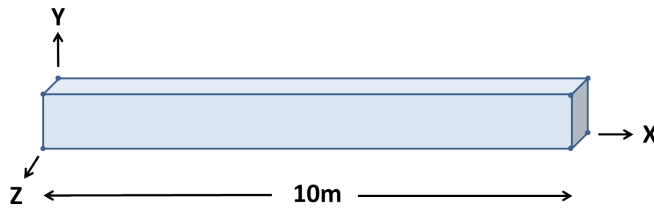
5m element size (2 elements):

³Renton, J. D. "Generalized beam theory applied to shear stiffness." International Journal of Solids and Structures 27.15 (1991): 1955-1967.



$$\text{error} = \frac{0.16 - 0.011911}{0.16} = 92.5\% \quad (307.10)$$

10m element size (1 element):



$$\text{error} = \frac{0.16 - 0.00315}{0.16} = 98\% \quad (307.11)$$

1m element size with 10% nodal offset (10 elements):

$$\text{error} = \frac{0.16 - 0.1057}{0.16} = 34\% \quad (307.12)$$

1m element size with 20% nodal offset (10 elements):

$$\text{error} = \frac{0.16 - 0.1016}{0.16} = 36\% \quad (307.13)$$

307.2.3 Verification of 27 node brick cantilever beam (static)

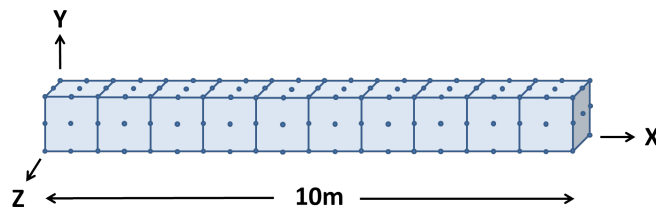
Problem description: Length=10m, Force=9N, E=100000Pa, $I = \frac{1}{12}$

Theoretical displacement:

$$d = \frac{PL^3}{3EI} = \frac{9 \times 1000}{3 \times 100000 \times \frac{1}{12}} = 0.36m \quad (307.14)$$

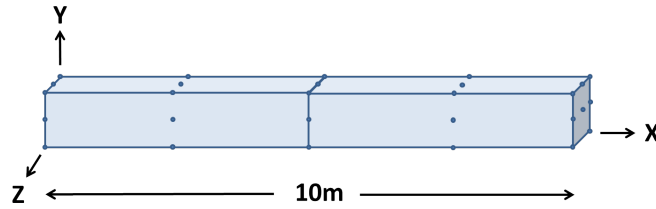
Numerical simulation results:

1m element size (10 elements):



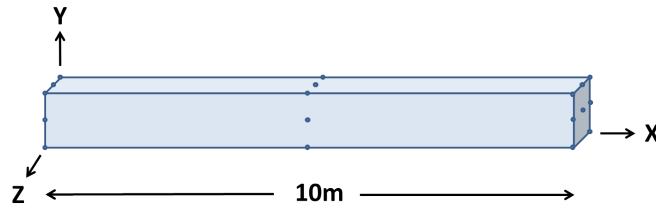
$$\text{error} = \frac{0.361721 - 0.36}{0.36} = 0.47\% \quad (307.15)$$

5m element size (2 elements):



$$\text{error} = \frac{0.36 - 0.345719}{0.36} = 3.96\% \quad (307.16)$$

10m element size (1 element):



$$\text{error} = \frac{0.36 - 0.279989}{0.36} = 22\% \quad (307.17)$$

1m element size with 10% nodal offset (10 elements):

$$\text{error} = \frac{0.361225 - 0.36}{0.36} = 0.35\% \quad (307.18)$$

1m element size with 20% nodal offset (10 elements):

$$\text{error} = \frac{0.36 - 0.359741}{0.36} = 0.07\% \quad (307.19)$$

1m element size with 30% nodal offset (10 elements):

$$\text{error} = \frac{0.36 - 0.357004}{0.36} = 0.83\% \quad (307.20)$$

1m element size with 40% nodal offset (10 elements):

$$\text{error} = \frac{0.36 - 0.352604}{0.36} = 2\% \quad (307.21)$$

307.2.4 Verification of 8NodeBrick cantilever beams

Problem description: Length=6m, Width=1m, Height=1m, Force=100N, E=1E8Pa, $\nu = 0.0$. Use the shear deformation coefficient $\kappa = 1.2$. The force direction was shown in Figure (307.2).

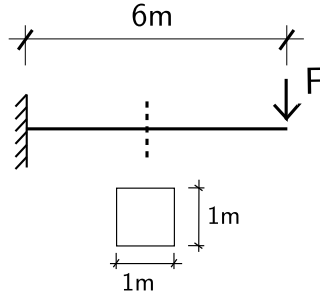


Figure 307.2: Problem description for cantilever beams.

Theoretical displacement (bending and shear deformation):

$$\begin{aligned}
 d &= \frac{FL^3}{3EI} + \frac{FL}{GA_v} \\
 &= \frac{FL^3}{3E \frac{bh^3}{12}} + \frac{FL}{\frac{E}{2(1+\nu)} \frac{bh}{\kappa}} \\
 &= \frac{100N \times 6^3 m^3}{3 \times 10^8 N/m^2 \times \frac{1}{12} m^4} + \frac{100N \times 6m}{\frac{10}{2} \times 10^7 N/m^2 \times 1m^2 \times \frac{5}{6}} \\
 &= 8.64 \times 10^{-4} m + 0.144 \times 10^{-4} m \\
 &= 8.784 \times 10^{-4} m
 \end{aligned} \tag{307.22}$$

Numerical model:

The 8NodeBrick elements are shown in Figure (307.6).

An example Real-ESSI script is shown below.

All the Real-ESSI results are listed in Table (307.1). The theoretical solution is 8.784E-04 m.

Table 307.1: Results for 8NodeBrick cantilever beams of different element numbers.

Element number	1	2	6
8NodeBrick	4.61E-05 m	1.59E-04 m	5.84E-04 m
Error	94.75%	81.87%	33.52%

The errors are plotted in Figure (307.7).

The Real-ESSI model fei/DSL files for the table above are [HERE](#).

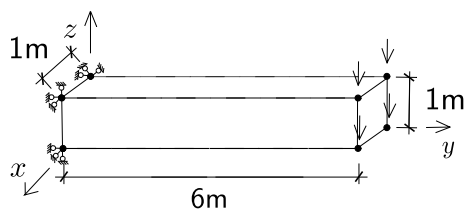


Figure 307.3: One 8NodeBrick element.

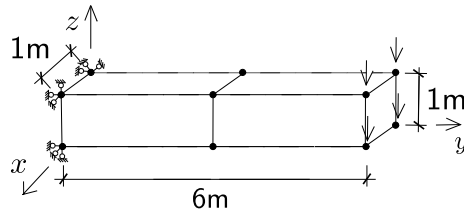


Figure 307.4: Two 8NodeBrick elements.

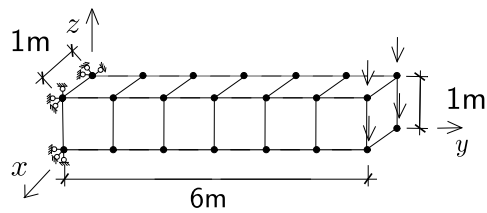


Figure 307.5: Six 8NodeBrick elements.

Figure 307.6: 8NodeBrick elements for cantilever beams.

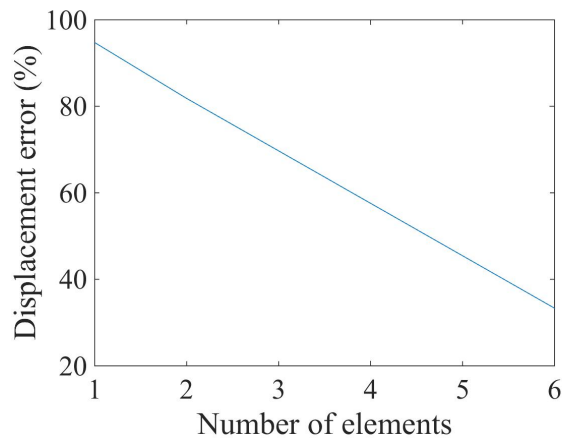


Figure 307.7: 8NodeBrick cantilever beam for different element number Displacement error versus Number of elements

307.2.5 Verification of 8NodeBrick cantilever beam for different Poisson's ratio

Problem description: Length=6m, Width=1m, Height=1m, Force=100N, E=1E8Pa, $\nu = 0.0 - 0.49$. The force direction was shown in Figure (307.8).

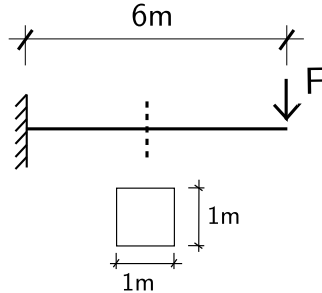


Figure 307.8: Problem description for cantilever beams of different Poisson's ratios.

The theoretical solution for $\nu = 0.0$ was calculated below, while the solution for other Poisson's ratio are calculated by the similar process.

Theoretical displacement (bending and shear deformation):

$$\begin{aligned}
 d &= \frac{FL^3}{3EI} + \frac{FL}{GA_v} \\
 &= \frac{FL^3}{3E \frac{bh^3}{12}} + \frac{FL}{\frac{E}{2(1+\nu)} \frac{bh}{\kappa}} \\
 &= \frac{100N \times 6^3 m^3}{3 \times 10^8 N/m^2 \times \frac{1}{12} m^4} + \frac{100N \times 6m}{\frac{10}{2} \times 10^7 N/m^2 \times 1m^2 \times \frac{5}{6}} \\
 &= 8.64 \times 10^{-4} m + 0.144 \times 10^{-4} m \\
 &= 8.784 \times 10^{-4} m
 \end{aligned} \tag{307.23}$$

The rotation angle at the end:

$$\theta = \frac{FL^2}{2EI} = \frac{100N \times 6^2 m^2}{2 \times 10^8 N/m^2 \times \frac{1}{12} m^4} = 2.16 \times 10^{-4} rad = 0.0124^\circ \tag{307.24}$$

The 8NodeBrick elements for cantilever beams of different Poisson's ratios are shown in Figure (307.9):

All the displacement results are listed in Table (307.2) - (307.4).

Using the same geometry, the element was meshed using much smaller element (0.5m).

Finally, in the same geometry, the element side length was cut into 0.25m.

The errors are plotted in Figure (307.10).

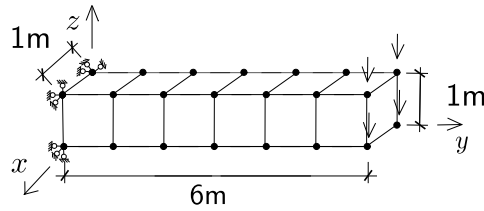


Figure 307.9: 8NodeBrick elements for cantilever beams of different Poisson's ratios.

Table 307.2: Displacement results for 8NodeBrick cantilever beams with element side length 1 m.

Poisson's ratio	8NodeBrick displacement	Theory displacement (bending)	Theory displacement (shear)	Theory displacement(all)	Error
0.00	5.840E-04 m	8.640E-04 m	1.440E-05 m	8.784E-04 m	33.52%
0.05	5.924E-04 m	8.640E-04 m	1.512E-05 m	8.791E-04 m	32.62%
0.10	5.969E-04 m	8.640E-04 m	1.586E-05 m	8.799E-04 m	32.16%
0.15	5.971E-04 m	8.640E-04 m	1.659E-05 m	8.806E-04 m	32.20%
0.20	5.922E-04 m	8.640E-04 m	1.734E-05 m	8.813E-04 m	32.81%
0.25	5.814E-04 m	8.640E-04 m	1.808E-05 m	8.821E-04 m	34.09%
0.30	5.634E-04 m	8.640E-04 m	1.884E-05 m	8.828E-04 m	36.19%
0.35	5.364E-04 m	8.640E-04 m	1.959E-05 m	8.836E-04 m	39.29%
0.40	4.970E-04 m	8.640E-04 m	2.035E-05 m	8.844E-04 m	43.80%
0.45	4.353E-04 m	8.640E-04 m	2.111E-05 m	8.851E-04 m	50.82%
0.49	3.142E-04 m	8.640E-04 m	2.173E-05 m	8.857E-04 m	64.52%

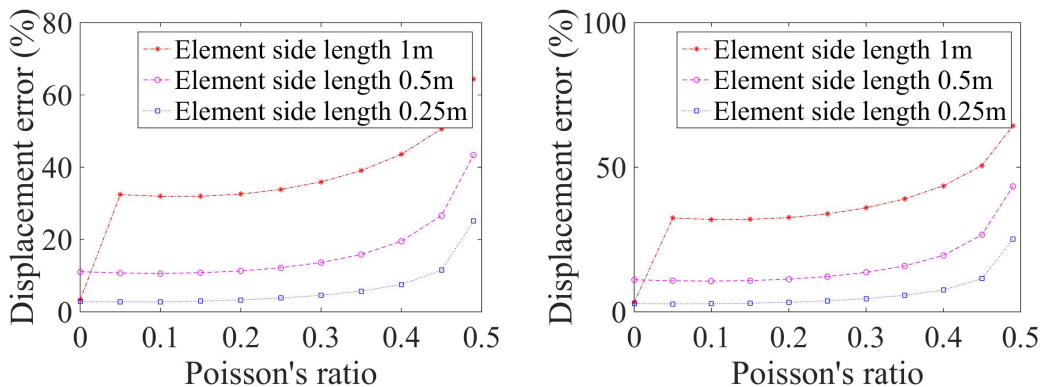


Figure 307.10: 8NodeBrick cantilever beam for different Poisson's ratio. Displacement error versus Poisson's ratio. Left: Error scale 0% - 80%, Right: Error scale 0% - 100%.

Table 307.3: Displacement results for 8NodeBrick cantilever beams with element side length 0.5 m.

Poisson's ratio	8NodeBrick displacement	Theory displacement (bending)	Theory displacement (shear)	Theory displacement(all)	Error
0.00	7.787E-04 m	8.640E-04 m	1.440E-05 m	8.784E-04 m	11.35%
0.05	7.824E-04 m	8.640E-04 m	1.512E-05 m	8.791E-04 m	11.00%
0.10	7.839E-04 m	8.640E-04 m	1.586E-05 m	8.799E-04 m	10.91%
0.15	7.829E-04 m	8.640E-04 m	1.659E-05 m	8.806E-04 m	11.09%
0.20	7.790E-04 m	8.640E-04 m	1.734E-05 m	8.813E-04 m	11.61%
0.25	7.717E-04 m	8.640E-04 m	1.808E-05 m	8.821E-04 m	12.51%
0.30	7.597E-04 m	8.640E-04 m	1.884E-05 m	8.828E-04 m	13.95%
0.35	7.406E-04 m	8.640E-04 m	1.959E-05 m	8.836E-04 m	16.18%
0.40	7.089E-04 m	8.640E-04 m	2.035E-05 m	8.844E-04 m	19.84%
0.45	6.466E-04 m	8.640E-04 m	2.111E-05 m	8.851E-04 m	26.95%
0.49	4.990E-04 m	8.640E-04 m	2.173E-05 m	8.857E-04 m	43.66%

Table 307.4: Displacement results for 8NodeBrick cantilever beams with element side length 0.25 m.

Poisson's ratio	8NodeBrick displacement	Theory displacement (bending)	Theory displacement (shear)	Theory displacement(all)	Error
0.00	8.511E-04 m	8.640E-04 m	1.440E-05 m	8.784E-04 m	3.11%
0.05	8.525E-04 m	8.640E-04 m	1.512E-05 m	8.791E-04 m	3.03%
0.10	8.527E-04 m	8.640E-04 m	1.586E-05 m	8.799E-04 m	3.09%
0.15	8.518E-04 m	8.640E-04 m	1.659E-05 m	8.806E-04 m	3.27%
0.20	8.494E-04 m	8.640E-04 m	1.734E-05 m	8.813E-04 m	3.62%
0.25	8.455E-04 m	8.640E-04 m	1.808E-05 m	8.821E-04 m	4.15%
0.30	8.393E-04 m	8.640E-04 m	1.884E-05 m	8.828E-04 m	4.93%
0.35	8.299E-04 m	8.640E-04 m	1.959E-05 m	8.836E-04 m	6.08%
0.40	8.141E-04 m	8.640E-04 m	2.035E-05 m	8.844E-04 m	7.94%
0.45	7.801E-04 m	8.640E-04 m	2.111E-05 m	8.851E-04 m	11.86%
0.49	6.603E-04 m	8.640E-04 m	2.173E-05 m	8.857E-04 m	25.45%

The angle results are listed in Table (307.5).

Then, in the same geometry, element side length was cut into 0.5m. The angle results are listed in Table (307.6).

Table 307.5: Rotation angle results for 8NodeBrick cantilever beams with element side length 1 m.

Poisson's ratio	8NodeBrick angle(unit: $^{\circ}$)	Theory angle (unit: $^{\circ}$)	Error
0.00	8.25E-03	1.24E-02	33.46%
0.05	8.36E-03	1.24E-02	32.55%
0.10	8.42E-03	1.24E-02	32.08%
0.15	8.42E-03	1.24E-02	32.10%
0.20	8.35E-03	1.24E-02	32.67%
0.25	8.20E-03	1.24E-02	33.90%
0.30	7.95E-03	1.24E-02	35.89%
0.35	7.59E-03	1.24E-02	38.83%
0.40	7.07E-03	1.24E-02	43.00%
0.45	6.30E-03	1.24E-02	49.21%
0.49	4.93E-03	1.24E-02	60.20%

Table 307.6: Rotation angle results for 8NodeBrick cantilever beams with element side length 0.5 m.

Poisson's ratio	8NodeBrick angle (unit: $^{\circ}$)	Theory angle (unit: $^{\circ}$)	Error
0.00	1.10E-02	1.24E-02	11.28%
0.05	1.10E-02	1.24E-02	10.91%
0.10	1.11E-02	1.24E-02	10.78%
0.15	1.10E-02	1.24E-02	10.90%
0.20	1.10E-02	1.24E-02	11.32%
0.25	1.09E-02	1.24E-02	12.09%
0.30	1.07E-02	1.24E-02	13.33%
0.35	1.05E-02	1.24E-02	15.29%
0.40	1.01E-02	1.24E-02	18.53%
0.45	9.32E-03	1.24E-02	24.87%
0.49	7.52E-03	1.24E-02	39.35%

Finally, in the same geometry, element side length was cut into 0.25m. The angle results are listed in Table (307.7).

Table 307.7: Rotation angle results for 8NodeBrick cantilever beams with with element side length 0.25 m.

Poisson's ratio	8NodeBrick angle (unit:°)	Theory angle (unit:°)	Error
0.00	1.20E-02	1.24E-02	3.06%
0.05	1.20E-02	1.24E-02	2.97%
0.10	1.20E-02	1.24E-02	2.99%
0.15	1.20E-02	1.24E-02	3.12%
0.20	1.20E-02	1.24E-02	3.38%
0.25	1.19E-02	1.24E-02	3.79%
0.30	1.19E-02	1.24E-02	4.40%
0.35	1.17E-02	1.24E-02	5.33%
0.40	1.15E-02	1.24E-02	6.87%
0.45	1.11E-02	1.24E-02	10.22%
0.49	9.64E-03	1.24E-02	22.23%

The errors are plotted in Figure (307.11).

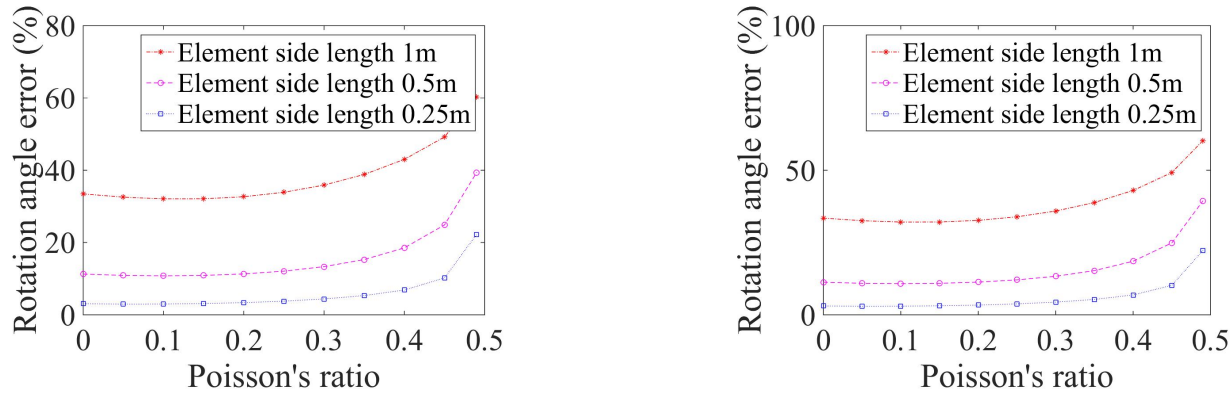


Figure 307.11: 8NodeBrick cantilever beam for different Poisson's ratio Rotation angle error versus Poisson's ratio, Left: Error scale 30% - 70%, Right: Error scale 0% - 100%.

The Real-ESSI model fei/DSL files for the table above are [HERE](#).

307.2.6 Test of irregular shaped 8NodeBrick cantilever beams

Cantilever model was used as an example. Three different shapes are tested.

In the first test, the upper two nodes of each element are moved one half element size along the $y - axis$, while the lower two nodes are kept at the same location. The element shape was shown in Figure (307.12).

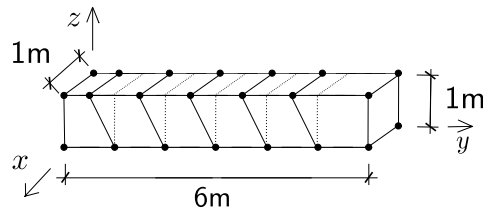


Figure 307.12: 8NodeBrick cantilever beams for irregular Shape 1.

In the second test, the upper two nodes of each element are moved 90% element size along the $y - axis$, while the lower two nodes are moved 90% element size in the other direction along the $y - axis$. The element shape was shown in Figure (307.13).

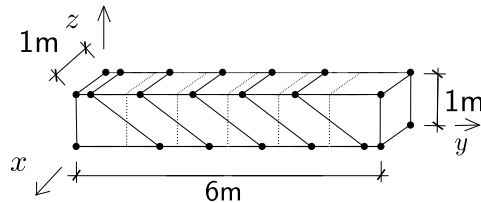


Figure 307.13: 8NodeBrick cantilever beams for irregular Shape 2.

In the third test, the upper two nodes of each element are moved one half element size with different directions along the $y - axis$, while the lower two nodes are kept at the same location. The element shape was shown in Figure (307.14).

The boundary conditions are shown in Figures (307.17), (307.20) and (307.23).

The Real-ESSI results are listed in Table (307.8).

The errors are listed in Table (307.9) and (307.10).

The Real-ESSI model fei/DSL files for the table above are [HERE](#).

Then, the irregular beam was divided into small elements.

Problem description: Length=12m, Width=2m, Height=2m, $q=400\text{N/m}$, $E=1\text{E}8\text{Pa}$, $\nu = 0.0$. Use the shear deformation coefficient $\kappa = 1.2$. The force direction was shown in Figure (307.24).

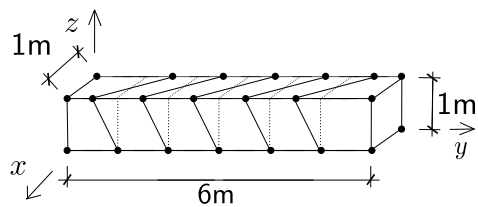


Figure 307.14: 8NodeBrick cantilever beams for irregular Shape 3.

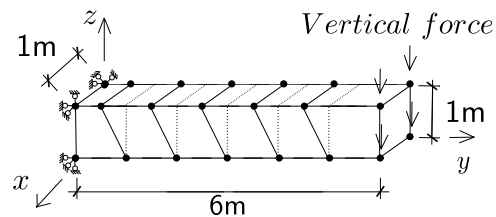


Figure 307.15: Vertical force.

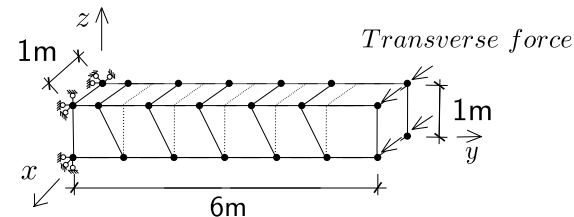


Figure 307.16: Horizontal force.

Figure 307.17: 8NodeBrick cantilever beam boundary conditions for irregular Shape 1.

Table 307.8: Results for 8NodeBrick cantilever beams of irregular shapes.

Element Type	Force direction	Normal shape	Shape 1	Shape 2	Shape 3
8NodeBrick	Vertical (z)	5.840E-04 m	5.751E-04 m	2.959E-04 m	3.883E-04 m
8NodeBrick	Transverse (y)	5.840E-04 m	4.529E-04 m	1.390E-04 m	4.744E-04 m
Theoretical	-	8.784E-04 m	8.784E-04 m	8.784E-04 m	8.784E-04 m

Table 307.9: Errors for irregular shaped 8NodeBrick compared to theoretical solution.

Element Type	Force direction	Normal shape	Shape 1	Shape 2	Shape 3
8NodeBrick	Vertical (z)	33.52%	34.53%	66.31%	55.79%
8NodeBrick	Transverse (y)	33.52%	48.44%	84.18%	45.99%

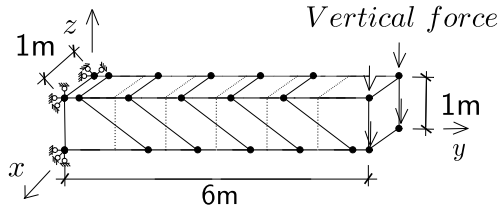


Figure 307.18: Vertical force.

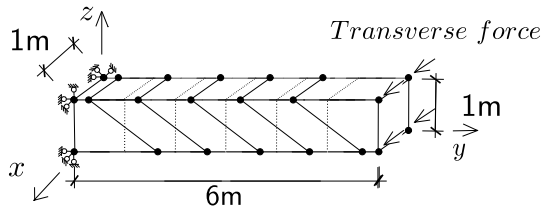


Figure 307.19: Horizontal force.

Figure 307.20: 8NodeBrick cantilever beam boundary conditions for irregular Shape 2.

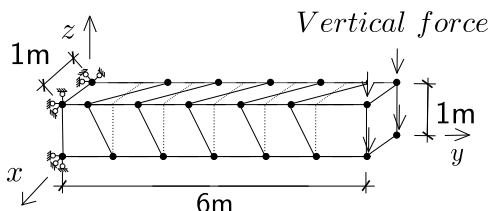


Figure 307.21: Vertical force.

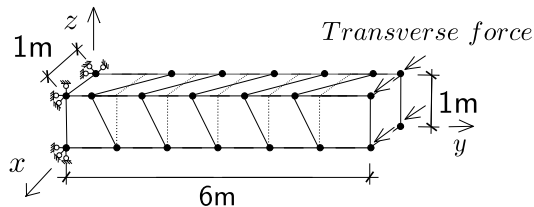


Figure 307.22: Horizontal force.

Figure 307.23: 8NodeBrick cantilever beam boundary conditions for irregular Shape 3.

Theoretical displacement (bending and shear deformation):

$$d = \frac{qL^4}{8EI} + \frac{q\frac{L^2}{2}}{GA_v} \quad (307.25)$$

$$= \frac{qL^4}{8E \frac{bh^3}{12}} + \frac{q\frac{L^2}{2}}{\frac{E}{2(1+\nu)} \frac{bh}{\kappa}} \quad (307.26)$$

$$\begin{aligned} Jeremić et al. & 400N/m \times 12^4 m^4 \\ & 8 \times 10^8 N/m^2 \times \frac{24}{12} m^4 + \frac{400N/m^2 \times 12^2}{2} \\ & = 7.776 \times 10^{-3} m + 1.728 \times 10^{-4} m \end{aligned} \quad (307.27)$$

Table 307.10: Errors for irregular shaped 8NodeBrick compared to normal shape.

Element Type	Force direction	Normal shape	Shape 1	Shape 2	Shape 3
8NodeBrick	Vertical (z)	0.00%	1.52%	49.33%	33.51%
8NodeBrick	Transverse (y)	0.00%	22.45%	76.20%	18.77%

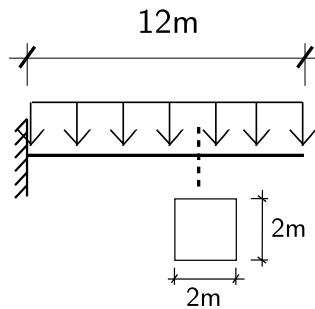


Figure 307.24: Problem description for cantilever beams under uniform load .

The Real-ESSI displacement results are listed in Table (307.11).

Table 307.11: Results for 8NodeBrick cantilever beams of irregular shapes with more elements.

Element Type	Shape	Force direction	Number of division		
			1	2	4
8NodeBrick	shape1	Vertical (z)	5.37E-03 m	7.08E-03 m	7.71E-03 m
8NodeBrick	shape1	Transverse (y)	4.60E-03 m	6.66E-03 m	7.58E-03 m
8NodeBrick	shape2	Vertical (z)	2.74E-03 m	4.75E-03 m	6.43E-03 m
8NodeBrick	shape2	Transverse (y)	1.46E-03 m	2.72E-03 m	4.63E-03 m
8NodeBrick	shape3	Vertical (z)	9.21E-04 m	6.60E-03 m	7.56E-03 m
8NodeBrick	shape3	Transverse (y)	1.09E-03 m	6.09E-03 m	7.37E-03 m
Theoretical solution			7.95E-03 m	7.95E-03 m	7.95E-03 m

The error are listed in Table (307.12).

The errors are shown in Figures (307.25), (307.26) and (307.27).

The Real-ESSI model fei/DSL files for the table above are [HERE](#).

Table 307.12: Errors for 8NodeBrick cantilever beams of irregular shapes with more elements.

Element Type	Shape	Force direction	Number of division		
			1	2	4
8NodeBrick	shape1	Vertical (z)	32.42%	10.95%	3.01%
8NodeBrick	shape1	Transverse (y)	42.16%	16.17%	4.69%
8NodeBrick	shape2	Vertical (z)	65.59%	40.22%	19.05%
8NodeBrick	shape2	Transverse (y)	81.57%	65.76%	41.81%
8NodeBrick	shape3	Vertical (z)	88.42%	16.97%	4.89%
8NodeBrick	shape3	Transverse (y)	86.24%	23.36%	7.28%

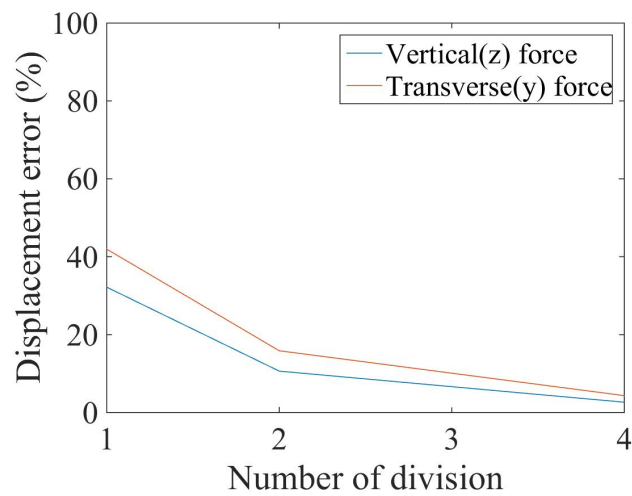


Figure 307.25: 8NodeBrick cantilever beam for irregular Shape 1. Displacement error versus Number of division

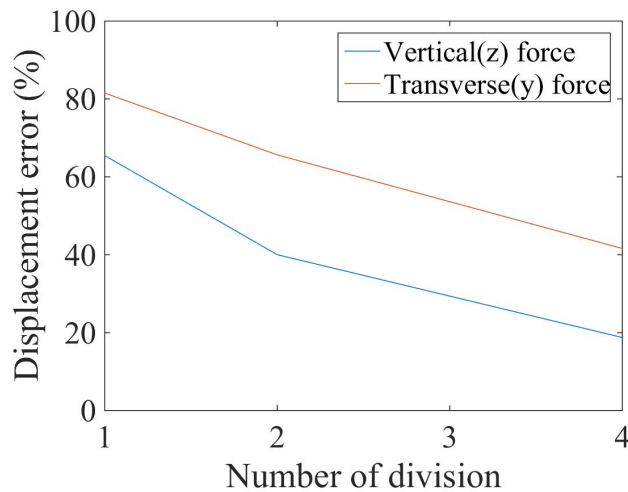


Figure 307.26: 8NodeBrick cantilever beam for irregular Shape 2 · Displacement error versus Number of division

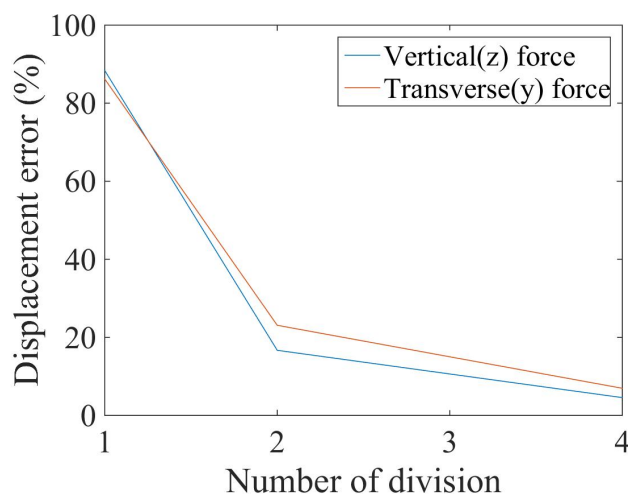


Figure 307.27: 8NodeBrick cantilever beam for irregular Shape 3 · Displacement error versus Number of division

In this section, the beam was cut into smaller elements with element side length 0.5m and 0.25m respectively. And the element side length of the original models is 1.0m. The numerical models are shown in Figures (307.28), (307.29) and (307.30).

Number of division 1:

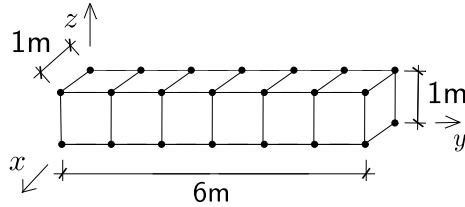


Figure 307.28: 8NodeBrick clamped beams with element side length 1.0m.

Number of division 2:

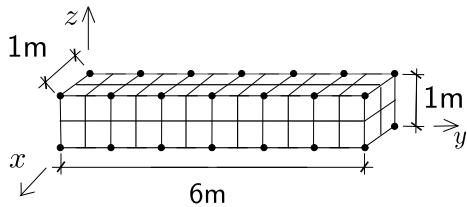


Figure 307.29: 8NodeBrick clamped beams with element side length 0.5m.

Number of division 4:

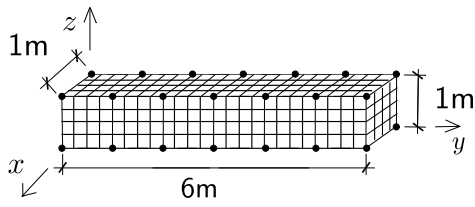


Figure 307.30: 8NodeBrick clamped beams with element side length 0.25m.

The Real-ESSI results are listed in Table (307.13). The theoretical solution is 1.60E-5 m.

The errors are plotted in Figure (307.33).

The Real-ESSI model fei/DSL files for the table above are [HERE](#).

Table 307.13: Results for 8NodeBrick clamped beams with more elements.

Element Type	Element side length		
	1 m	0.5 m	0.25 m
8NodeBrick	1.10E-05 m	1.47E-05 m	1.64E-05 m
Error	33.33%	11.09%	0.73%

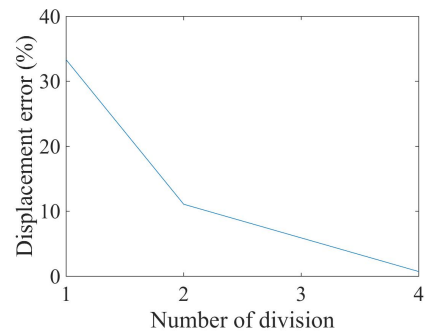


Figure 307.31: Error scale 0% - 40%.

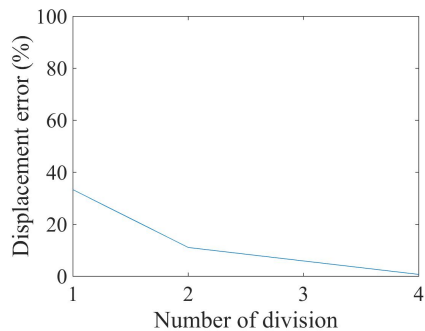


Figure 307.32: Error scale 0% - 100%.

Figure 307.33: 8NodeBrick clamped beam for different element number: Displacement error versus Number of division

307.2.7 Verification of 8NodeBrick stress in cantilever beams

Problem description: Length=6m, Width=1m, Height=1m, Force=100N, E=1E8Pa, $\nu = 0.0$. Use the shear deformation coefficient $\kappa = 1.2$. The force direction was shown in Figure (307.34).

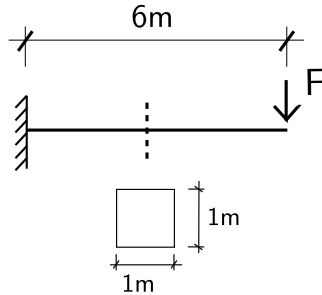


Figure 307.34: Problem description for cantilever beams of stress verification.

The theoretical solution for the stress was calculated below.

The 8NodeBrick elements are shown in Figure (307.35).

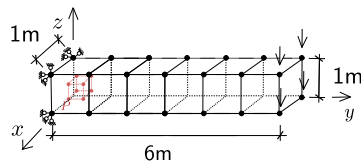


Figure 307.35: 8NodeBrick for cantilever beams of stress verification.

The bending moment at the Gassian Point is

$$M = F(L - P_y) = 100N \times (6 - 0.2113)m = 578.87N \cdot m \quad (307.30)$$

The bending modulus is

$$I = \frac{bh^3}{12} = \frac{1}{12}m^4 \quad (307.31)$$

Therefore, the theoretical stress is

$$\sigma = \frac{M \cdot z}{I} = \frac{578.87N \cdot m \times (0.5 - 0.2113)m}{\frac{1}{12}m^4} = 2005Pa \quad (307.32)$$

To get a better result, the same geometry beam was also cut into small elements. When more elements are used, the theoretical stress was calculated again with the new coordinates. The calculation process is similar to the process above.

The numerical models are shown in Figures(307.36), (307.37) and (307.38).

Number of division 1:

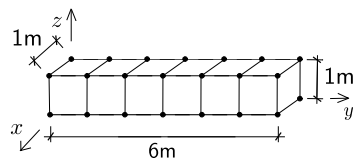


Figure 307.36: 8NodeBrick stress with element side length 1.0m.

Number of division 2:

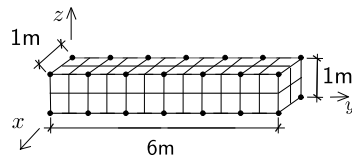


Figure 307.37: 8NodeBrick stress with element side length 0.5m.

Number of division 4:

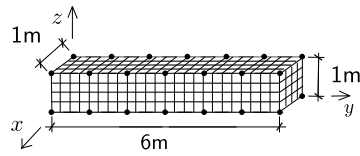


Figure 307.38: 8NodeBrick stress with element side length 0.25m.

All the stress results are listed in Table (307.14).

Table 307.14: Results for 8NodeBrick stress with more elements.

Element Type	Element side length		
	1 m	0.5 m	0.25 m
8NodeBrick	1270.17 Pa	2418.60 Pa	3085.48 Pa
Theoretical	2005.26 Pa	2789.23 Pa	3191.27 Pa
Error	36.66%	13.29%	3.31%

The errors are plotted in Figure (307.41).

The Real-ESSI model fei/DSL files for the table above are [HERE](#).

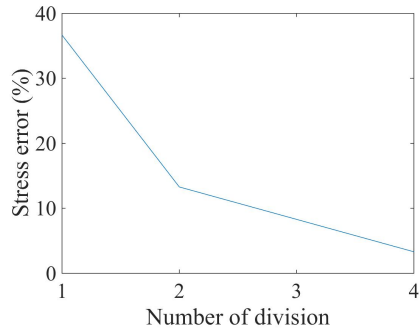


Figure 307.39: Error scale 0% - 40%.

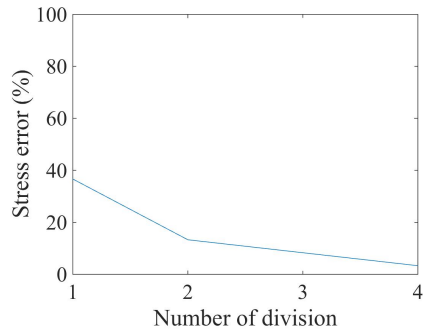


Figure 307.40: Error scale 0% - 100%.

Figure 307.41: 8NodeBrick cantilever beams for stress verification. Stress error versus Number of division

307.2.8 Verification of 8NodeBrick square plate with four edges clamped

Problem description: Length=20m, Width=20m, Height=1m, Force=100N, E=1E8Pa, $\nu = 0.3$.

The four edges are clamped.

The load is the uniform normal pressure on the whole plate.

The plate flexural rigidity is

$$D = \frac{Eh^3}{12(1-\nu^2)} = \frac{10^8 N/m^2 \times 1^3 m^3}{12 \times (1 - 0.3^2)} = 9.1575 \times 10^6 N \cdot m \quad (307.33)$$

The theoretical solution is

$$d = \alpha_c \frac{qa^4}{D} = 0.00406 \times \frac{100N/m^2 \times 20^4 m^4}{9.1575 \times 10^6 N \cdot m} = 2.2015 \times 10^{-3} m \quad (307.34)$$

where α_c is a coefficient, which depends on the ratio of plate length to width. In this problem, the coefficient⁴ α_c is 0.00406.

The 8NodeBrick are shown in Figures (307.42) - (307.47).

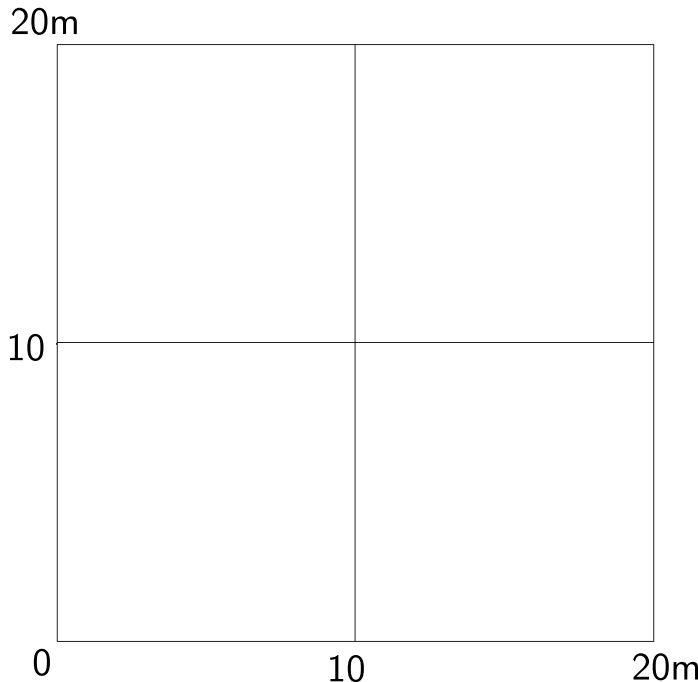


Figure 307.42: 8NodeBrick edge clamped square plate with element side length 10m.

The results are listed in Table (307.15).

The errors are listed in Table (307.2.8).

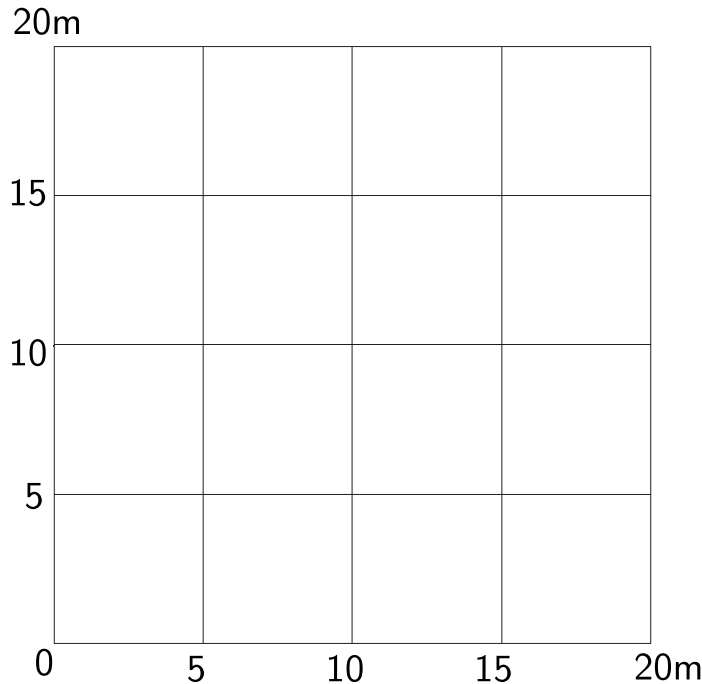


Figure 307.43: 8NodeBrick edge clamped square plate with element side length 5m.

Table 307.15: Results for 8NodeBrick square plate with four edges clamped.

Element type	8NodeBrick	8NodeBrick	8NodeBrick	Theoretical displacement
Number of layers	1layer	2layers	4layers	
Element side length	Height:1.00m	Height:0.50m	Height:0.25m	
10m	9.75E-05 m	9.75E-05 m	9.75E-05 m	2.20E-03 m
5m	3.28E-04 m	3.32E-04 m	3.32E-04 m	2.20E-03 m
2m	1.04E-03 m	1.10E-03 m	1.12E-03 m	2.20E-03 m
1m	1.56E-03 m	1.74E-03 m	1.79E-03 m	2.20E-03 m
0.5m	1.80E-03 m	2.30E-03 m	2.12E-03 m	2.20E-03 m
0.25m	1.87E-03 m	2.14E-03 m	2.23E-03 m	2.20E-03 m

The errors are plotted in Figure (307.48).

The Real-ESSI model fei/DSL files for the table above are [HERE](#).

⁴Stephen Timoshenko, Theory of plates and shells (2nd edition). MrGRAW-Hill Inc, page120, 1959.

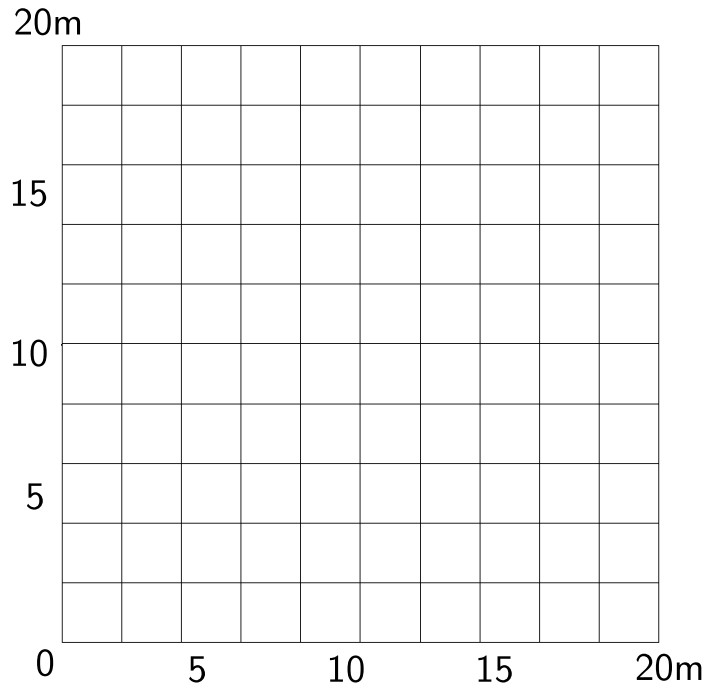


Figure 307.44: 8NodeBrick edge clamped square plate with element side length 2m.

Element type	8NodeBrick	8NodeBrick	8NodeBrick
Number of layers	1layer	2layers	4layers
Element side length	Height:1.00m	Height:0.50m	Height:0.25m
10m	95.57%	95.57%	95.57%
5m	85.09%	84.94%	84.91%
2m	52.98%	50.09%	49.25%
1m	28.93%	21.17%	18.72%
0.5m	18.26%	4.58%	3.56%
0.25m	15.05%	2.70%	1.37%

Table 307.16: Errors for 8NodeBrick square plate with four edges clamped.

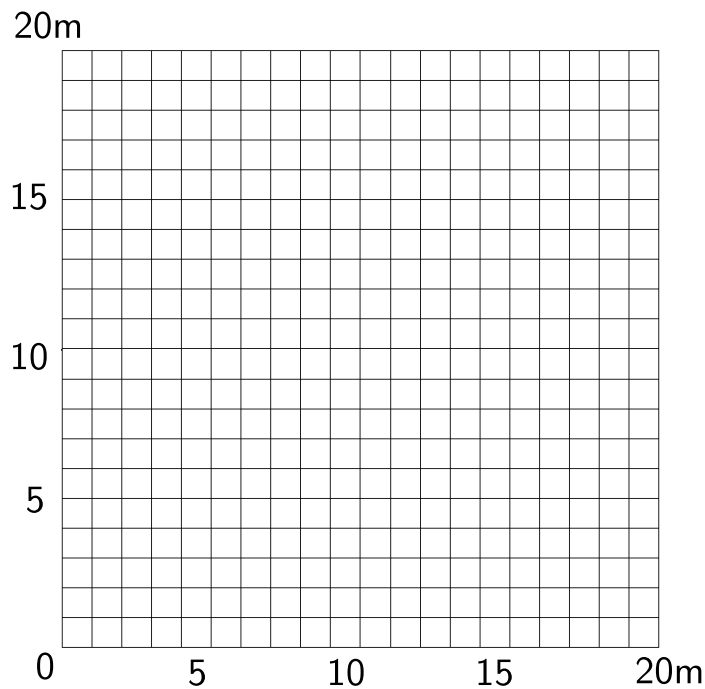


Figure 307.45: 8NodeBrick edge clamped square plate with element side length 1m.

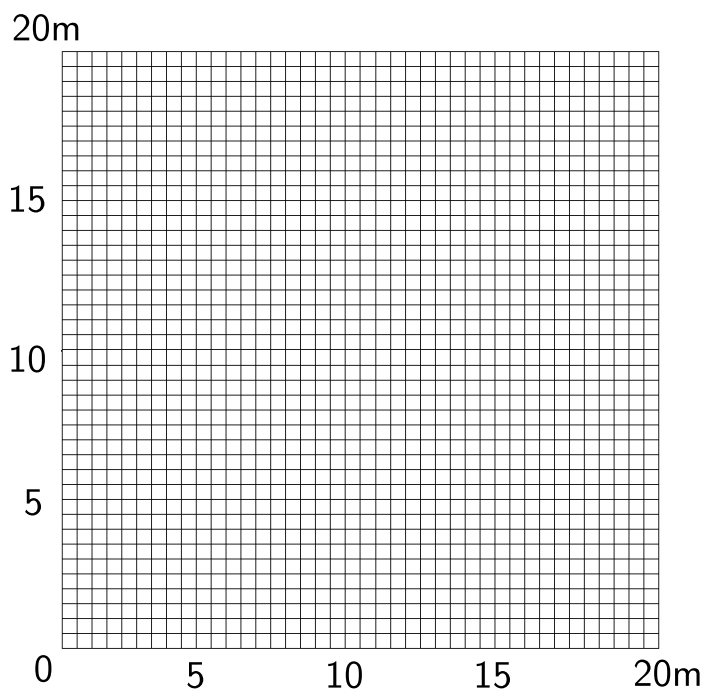


Figure 307.46: 8NodeBrick edge clamped square plate with element side length 0.5m.

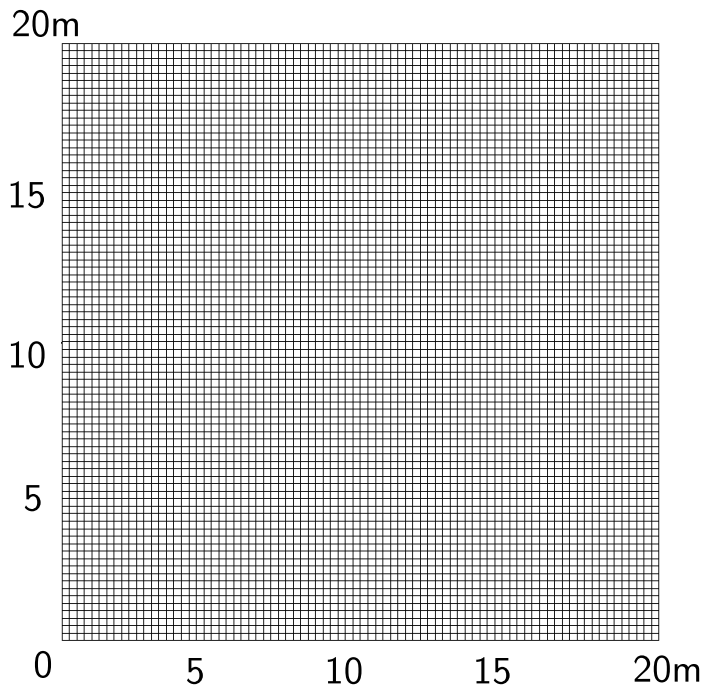


Figure 307.47: 8NodeBrick edge clamped square plate with element side length 0.25m.

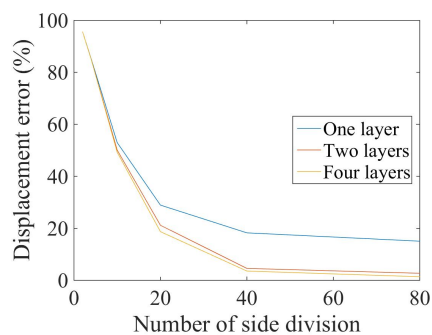


Figure 307.48: 8NodeBrick square plate with edge clamped' Displacement error versus Number of side division

307.2.9 Verification of 8NodeBrick square plate with four edges simply supported

Problem description: Length=20m, Width=20m, Height=1m, Force=100N, E=1E8Pa, $\nu = 0.3$.

The four edges are simply supported.

The load is the uniform normal pressure on the whole plate.

The plate flexural rigidity is

$$D = \frac{Eh^3}{12(1-\nu^2)} = \frac{10^8 N/m^2 \times 1^3 m^3}{12 \times (1 - 0.3^2)} = 9.1575 \times 10^6 N \cdot m \quad (307.35)$$

The theoretical solution is

$$d = \alpha_s \frac{qa^4}{D} = 0.00126 \times \frac{100N/m^2 \times 20^4 m^4}{9.1575 \times 10^6 N \cdot m} = 7.0936 \times 10^{-3} m \quad (307.36)$$

where α_s is a coefficient, which depends on the ratio of plate length to width. In this problem, the coefficient⁵ α_s is 0.00126.

The 8NodeBrick are shown in Figures (307.49) - (307.54).

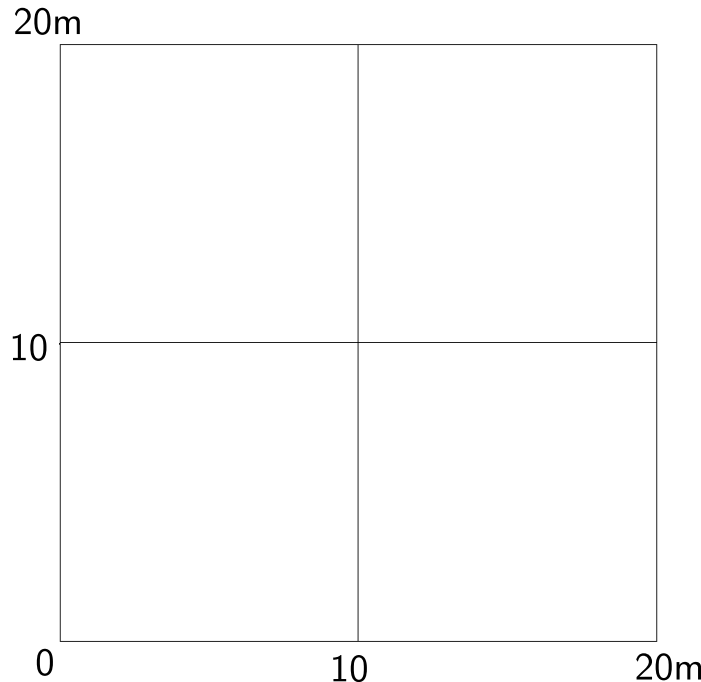


Figure 307.49: 8NodeBrick edge simply supported square plate with element side length 10m.

The results are listed in Table (307.17).

The errors are listed in Table (307.18).

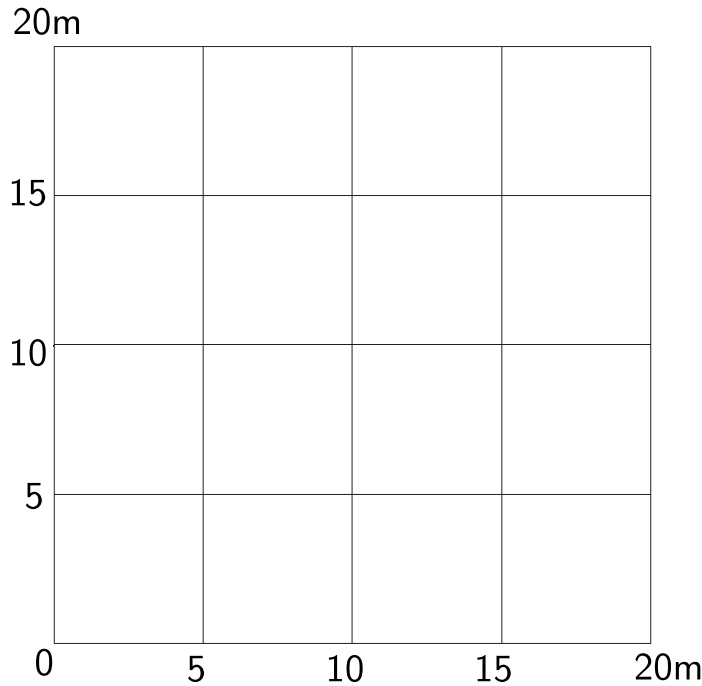


Figure 307.50: 8NodeBrick edge simply supported square plate with element side length 5m.

Table 307.17: Results for 8NodeBrick square plate with four edges simply supported.

Element type	8NodeBrick	8NodeBrick	Theoretical displacement
Number of layers	2layers	4layers	
Element side length	Height:0.50m	Height:0.25m	
10m	3.75E-004 m	3.76E-004 m	7.09E-03 m
5m	1.34E-003 m	1.35E-003 m	7.09E-03 m
2m	4.16E-003 m	4.27E-003 m	7.09E-03 m
1m	5.98E-003 m	6.22E-003 m	7.09E-03 m
0.5m	6.75E-003 m	7.04E-003 m	7.09E-03 m
0.25m	8.07E-003 m	7.30E-003 m	7.09E-03 m

The errors are plotted in Figure (307.55).

The Real-ESSI model fei/DSL files for the table above are [HERE](#).

⁵Stephen Timoshenko, Theory of plates and shells (2nd edition). MrGRAW-Hill Inc, page202, 1959.

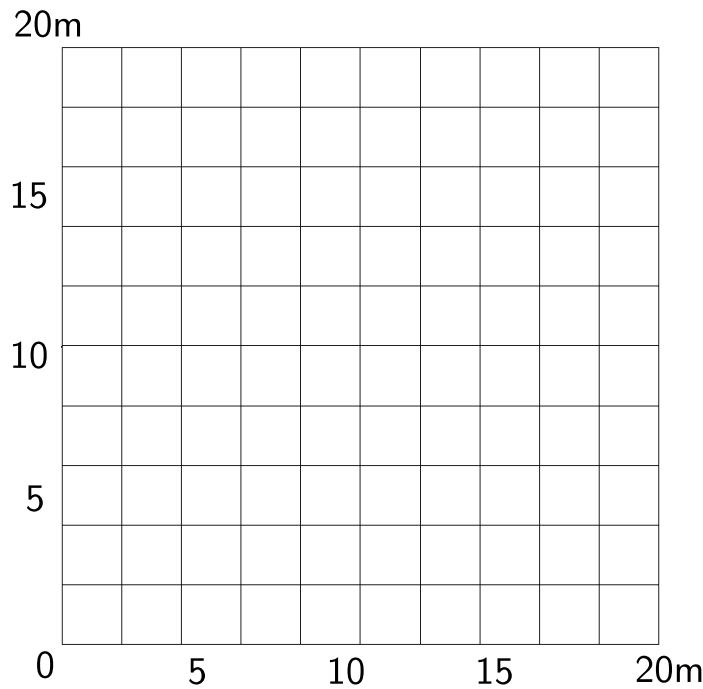


Figure 307.51: 8NodeBrick edge simply supported square plate with element side length 2m.

Table 307.18: Errors for 8NodeBrick square plate with four edges simply supported.

Element type	8NodeBrick	8NodeBrick
Number of layers	2layers	4layers
Element side length	Height:0.50m	Height:0.25m
10m	94.72%	94.71%
5m	81.05%	80.91%
2m	41.31%	39.79%
1m	15.64%	12.38%
0.5m	4.88%	0.70%
0.25m	13.74%	2.86%

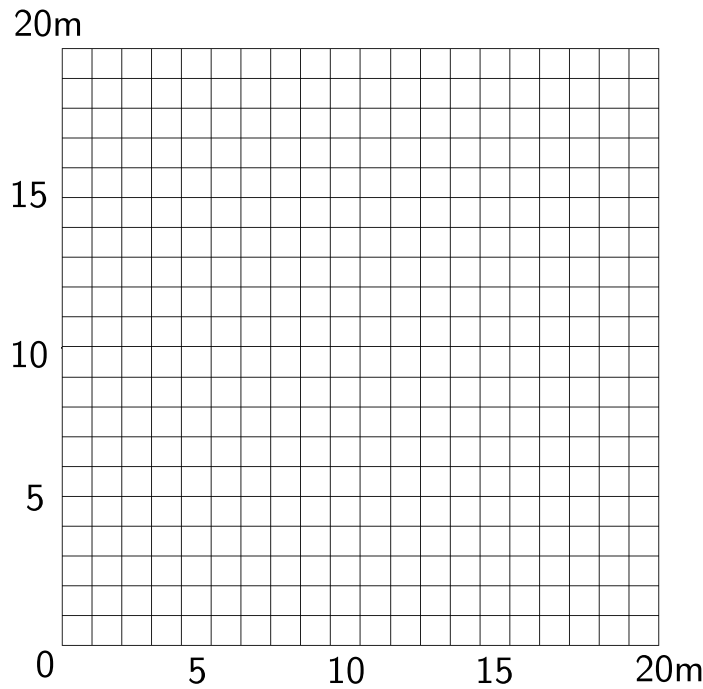


Figure 307.52: 8NodeBrick edge simply supported square plate with element side length 1m.

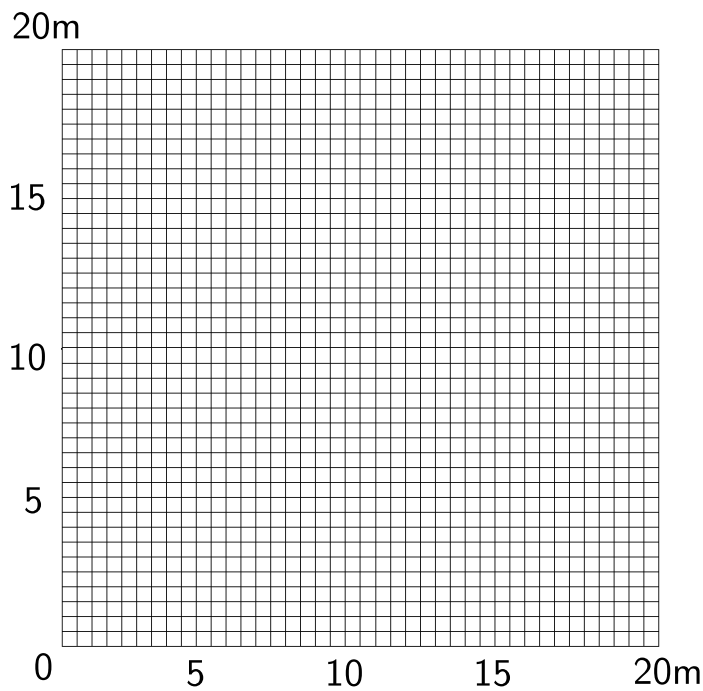


Figure 307.53: 8NodeBrick edge simply supported square plate with element side length 0.5m.

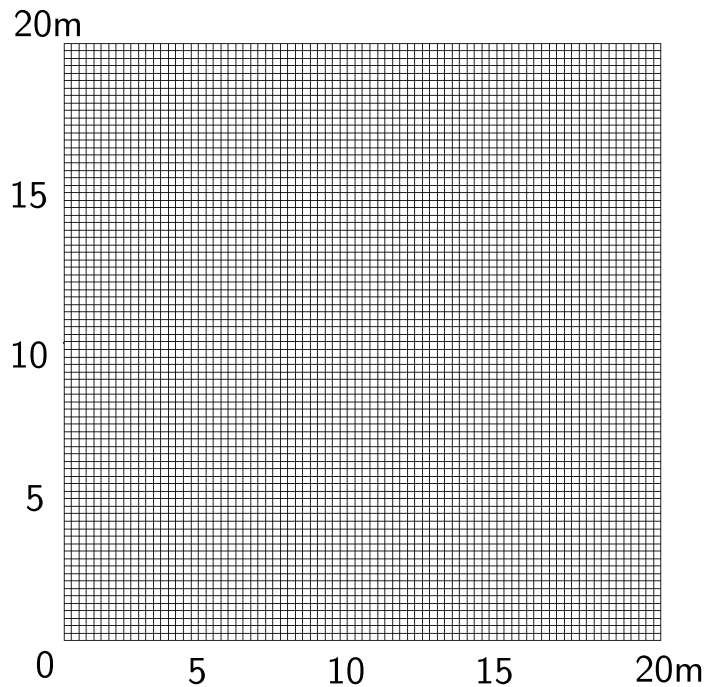


Figure 307.54: 8NodeBrick edge simply supported square plate with element side length 0.25m.

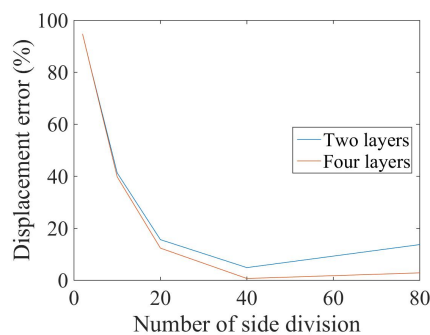


Figure 307.55: 8NodeBrick square plate with four edges simply supported. Displacement error versus Number of side division

307.2.10 Verification of 8NodeBrick circular plate with all edges clamped

Problem description: Diameter=20m, Height=1m, Force=100N, E=1E8Pa, $\nu = 0.3$.

The four edges are clamped.

The load is the uniform normal pressure on the whole plate.

The plate flexural rigidity is

$$D = \frac{Eh^3}{12(1-\nu^2)} = \frac{10^8 N/m^2 \times 1^3 m^3}{12 \times (1 - 0.3^2)} = 9.1575 \times 10^6 N \cdot m \quad (307.37)$$

The theoretical solution⁶ is

$$d = \frac{qa^4}{64D} = \frac{100N/m^2 \times 10^4 m^4}{64 \times 9.1575 \times 10^6 N \cdot m} = 1.7106 \times 10^{-3} m \quad (307.38)$$

The 8NodeBrick are shown in Figures (307.56) - (307.61).

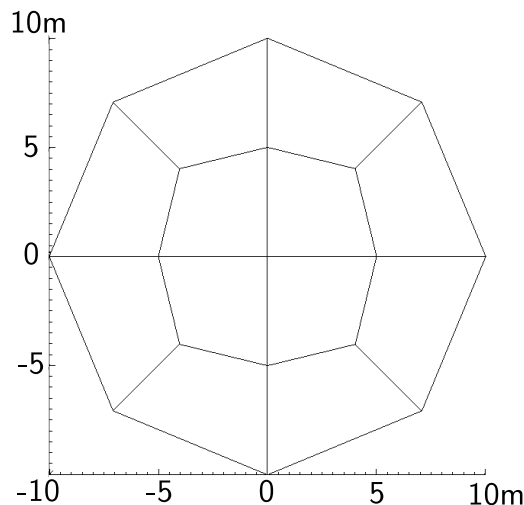


Figure 307.56: 8NodeBrick edge clamped circular plate with element side length 10m.

The results are listed in Table (307.19).

The errors are listed in Table (307.20).

The errors are shown in Figure (307.62).

The Real-ESSI model fei/DSL files for the table above are [HERE](#).

⁶Stephen Timoshenko, Theory of plates and shells (2nd edition). MrGRAW-Hill Inc, page55, 1959.

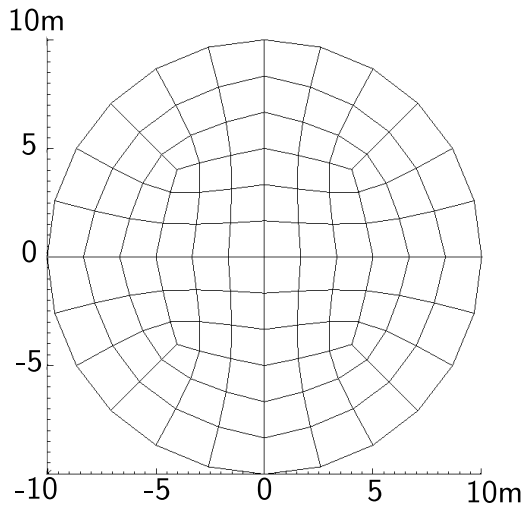


Figure 307.57: 8NodeBrick edge clamped circular plate with element side length 5m.

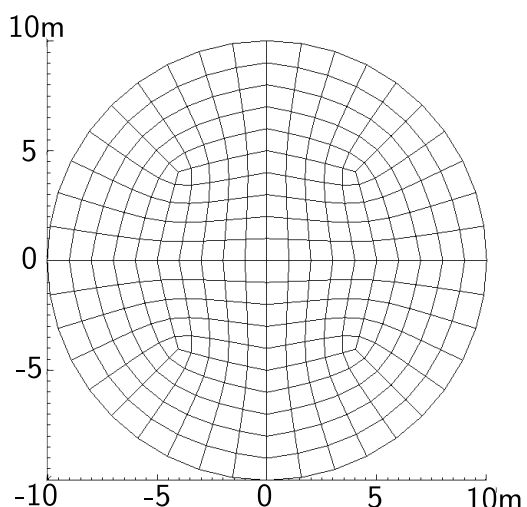


Figure 307.58: 8NodeBrick edge clamped circular plate with element side length 2m.

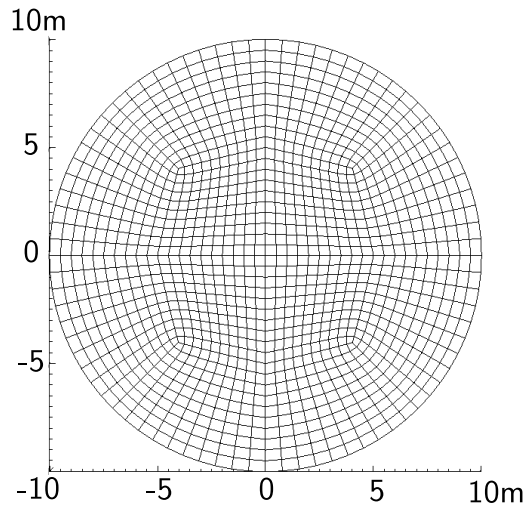


Figure 307.59: 8NodeBrick edge clamped circular plate with element side length 1m.

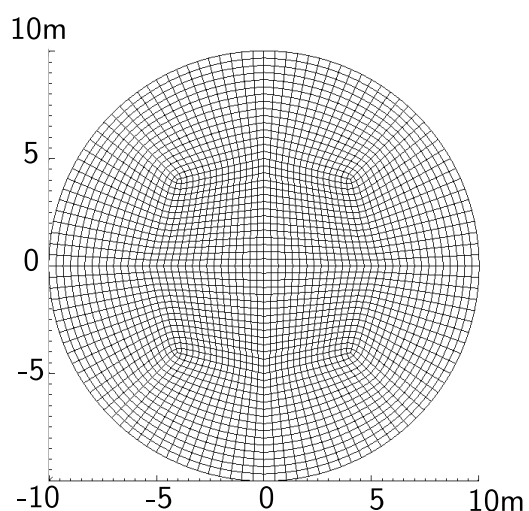


Figure 307.60: 8NodeBrick edge clamped circular plate with element side length 0.5m.

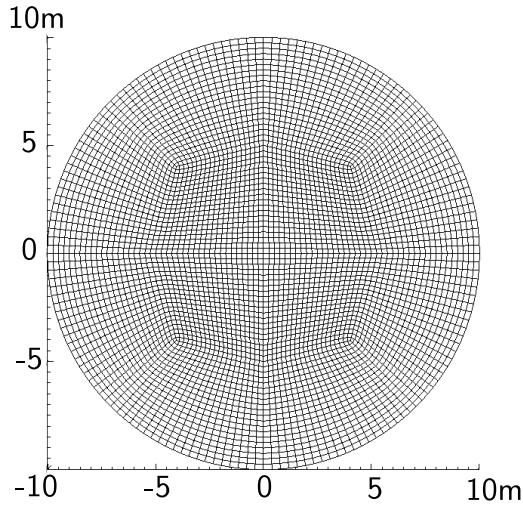


Figure 307.61: 8NodeBrick edge clamped circular plate with element side length 0.25m.

Table 307.19: Results for 8NodeBrick circular plate with four edges clamped.

Element type	8NodeBrick	8NodeBrick	8NodeBrick	Theoretical displacement
Number of layers	1layer	2layers	4layers	
Number of diameter divisions	Height:1.00m	Height:0.50m	Height:0.25m	
4	1.97E-04 m	1.99E-04 m	2.00E-04 m	1.71E-03 m
12	7.95E-04 m	8.47E-04 m	8.62E-04 m	1.71E-03 m
20	1.13E-03 m	1.25E-03 m	1.28E-03 m	1.71E-03 m
40	1.36E-03 m	1.54E-03 m	1.60E-03 m	1.71E-03 m
60	1.41E-03 m	1.62E-03 m	1.68E-03 m	1.71E-03 m
80	1.43E-03 m	1.64E-03 m	1.71E-03 m	1.71E-03 m

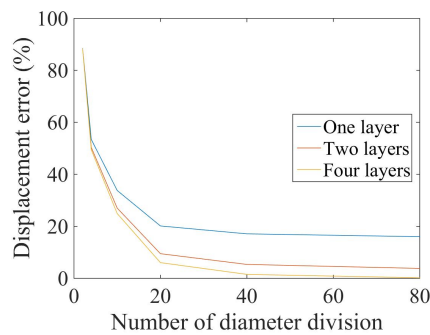


Figure 307.62: 8NodeBrick circular plate with edge clamped' Displacement error versus Number of side division.

Table 307.20: Errors for 8NodeBrick circular plate with four edges clamped.

Element type	8NodeBrick	8NodeBrick	8NodeBrick
Number of layers	1layer	2layers	4layers
Number of diameter divisions	Height:1.00m	Height:0.50m	Height:0.25m
4	88.43%	88.32%	88.30%
12	53.43%	50.35%	49.47%
20	33.79%	27.00%	24.93%
40	20.14%	9.47%	6.03%
60	17.11%	5.34%	1.51%
80	16.01%	3.80%	0.19%

307.2.11 Verification of 8NodeBrick circular plate with all edges simply supported

Problem description: Diameter=20m, Height=1m, Force=100N, E=1E8Pa, $\nu = 0.3$.

The four edges are simply supported.

The load is the uniform normal pressure on the whole plate.

The plate flexural rigidity is

$$D = \frac{Eh^3}{12(1-\nu^2)} = \frac{10^8 N/m^2 \times 1^3 m^3}{12 \times (1 - 0.3^2)} = 9.1575 \times 10^6 N \cdot m \quad (307.39)$$

The theoretical solution⁷ is

$$d = \frac{(5 + \nu)qa^4}{64(1 + \nu)D} = \frac{(5 + 0.3) \times 100N/m^2 \times 10^4 m^4}{64 \times (1 + 0.3) \times 9.1575 \times 10^6 N \cdot m} = 6.956 \times 10^{-3} m \quad (307.40)$$

The 8NodeBrick are shown in Figures (307.63) - (307.68).

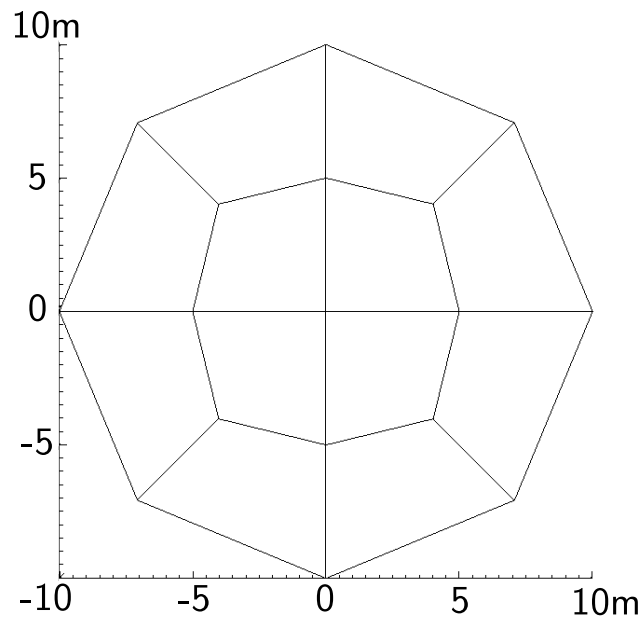


Figure 307.63: 8NodeBrick edge simply supported circular plate with element side length 10m.

The results are listed in Table (307.21).

The errors are listed in Table (307.22).

The errors are plotted in Figure (307.69).

The Real-ESSI model fei/DSL files for the table above are [HERE](#).

⁷Stephen Timoshenko, Theory of plates and shells (2nd edition). MrGRAW-Hill Inc, page55, 1959.

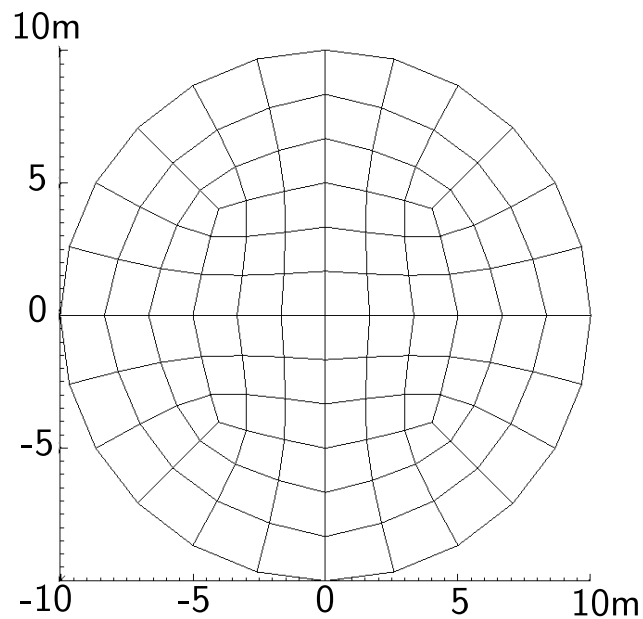


Figure 307.64: 8NodeBrick edge simply supported circular plate with element side length 5m.

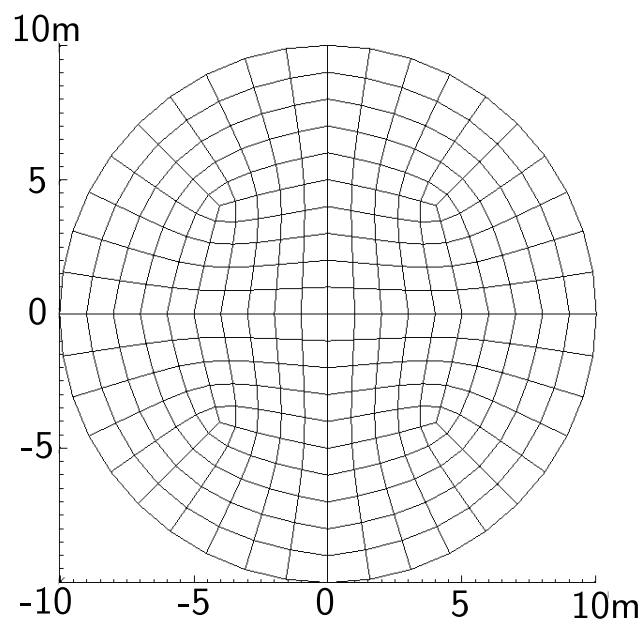


Figure 307.65: 8NodeBrick edge simply supported circular plate with element side length 2m.

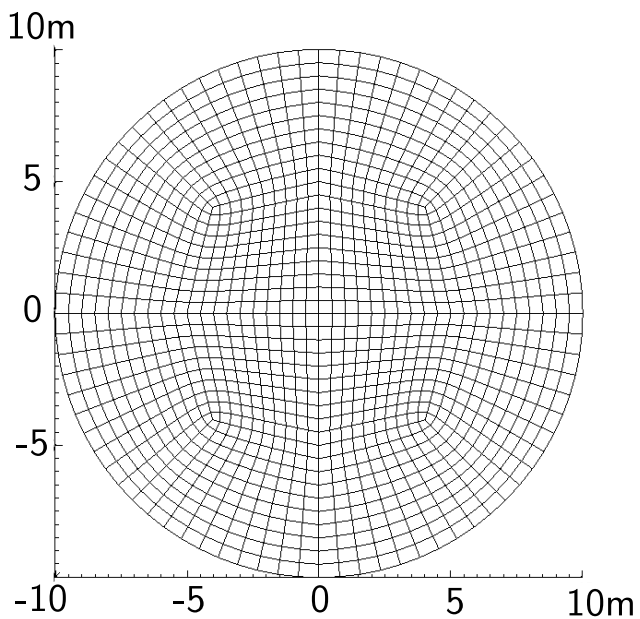


Figure 307.66: 8NodeBrick edge simply supported circular plate with element side length 1m.

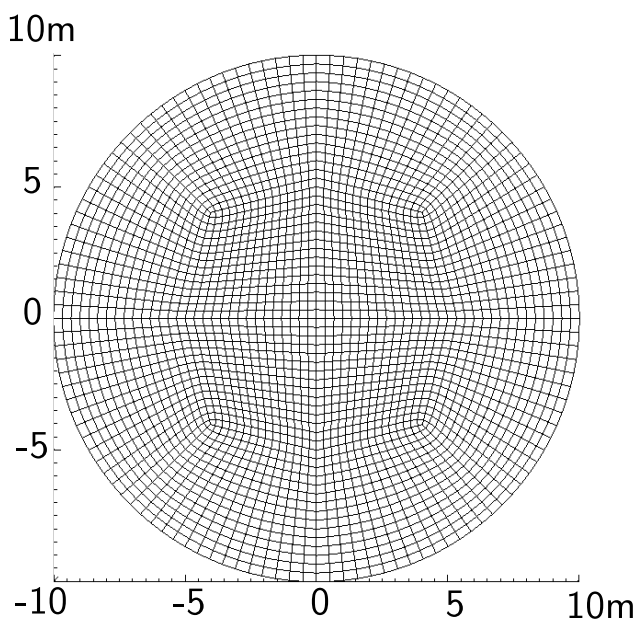


Figure 307.67: 8NodeBrick edge simply supported circular plate with element side length 0.5m.

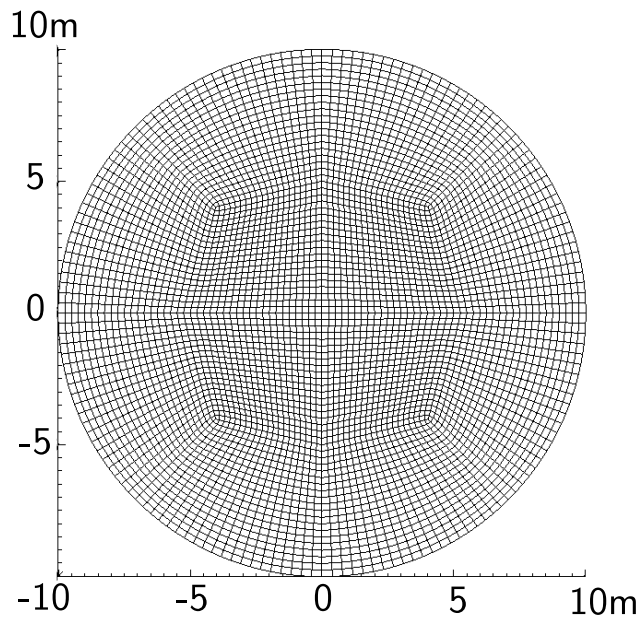


Figure 307.68: 8NodeBrick edge simply supported circular plate with element side length 0.25m.

Table 307.21: Results for 8NodeBrick cicular plate with four edges simply supported.

Element type	8NodeBrick	8NodeBrick	Theoretical displacement
Number of layers	2layers	4layers	
Number of diameter divisions	Height:0.50m	Height:0.25m	
4	6.35E-04 m	6.39E-04 m	6.96E-03 m
12	3.46E-03 m	3.57E-03 m	6.96E-03 m
20	4.96E-03 m	5.18E-03 m	6.96E-03 m
40	6.05E-03 m	6.37E-03 m	6.96E-03 m
60	6.30E-03 m	6.65E-03 m	6.96E-03 m
80	6.39E-03 m	6.76E-03 m	6.96E-03 m

Table 307.22: Errors for 8NodeBrick circular plate with four edges simply supported.

Element type	8NodeBrick	8NodeBrick
Number of layers	2layers	4layers
Number of diameter divisions	Height:0.50m	Height:0.25m
4	90.87%	90.82%
12	50.19%	48.65%
20	28.64%	25.47%
40	13.09%	8.40%
60	9.45%	4.36%
80	8.10%	2.85%

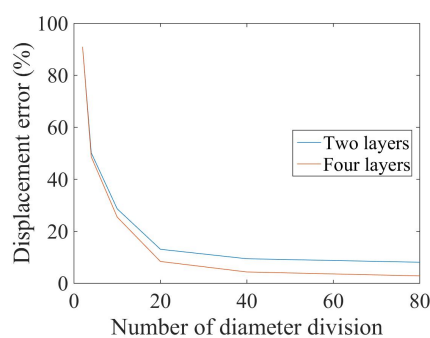


Figure 307.69: 8NodeBrick circular plate with edge simply supported: Displacement error versus Number of side division

307.2.12 Verification of 8NodeBrick Finite Element for Boussinesq Problem

307.2.12.1 Introduction

The Boussinesq problem is finding the displacement distribution in the isotropic linearly elastic half-space, subject to a concentrated load applied on the surface and perpendicular to it. The Boussinesq problem diagram is shown in Fig.(307.166).

Boussinesq problem is widely used in geotechnical engineering, especially when designing a foundation which transfers the superstructure load to the soil. To estimate the foundation settlements, it is important to have a reliable numerical solution for the Boussinesq problem.

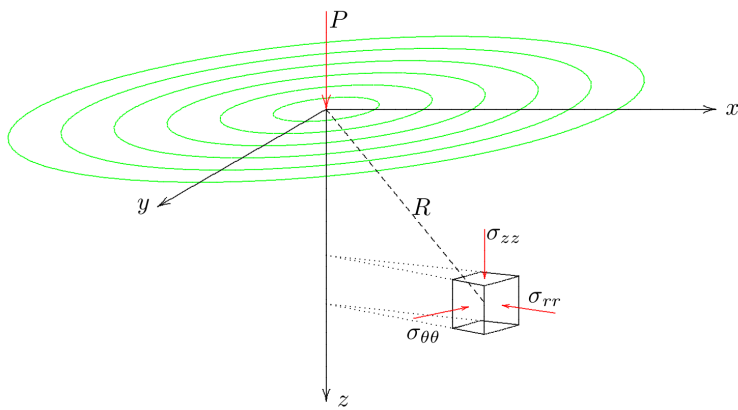


Figure 307.70: Boussinesq problem description. (Figure Reference: Verruijt, Arnold, and Stefan Van Baars. Soil mechanics. Delft, 2007.)

In 1885, the French scientist Joseph Boussinesq solved the analytic solutions of displacements in the homogeneous isotropic linear elastic half space. In general, the vertical displacement of the surface is

$$z = 0 : \quad u_z = \frac{P(1 - \nu^2)}{\pi E R} \quad (307.41)$$

where P is the vertical load, ν is the Poisson's ratio, E is the elastic modulus, and R is the distance from the measured point to the loading point.

In this section, the Real-ESSI numerical solution is verified by the analytic solution for the Boussinesq problem.

307.2.12.2 Description of the Verification Model

Since the problem is cylindrical symmetry, a quarter of the entire cube was employed to represent the whole cube. The reduced model was shown in Fig.(307.167).

The side length is 20 meters and the load P is 1N. The elastic modulus $E = 1 \times 10^3 Pa$ and the Poisson's ratio $\nu = 0.0$.

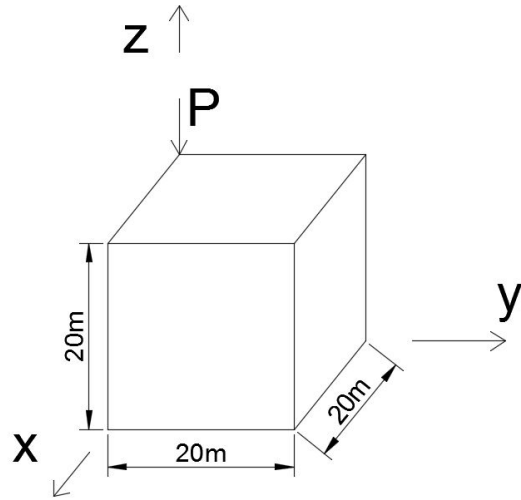


Figure 307.71: Reduced model (One quarter model) for the point load on the half space

The boundary conditions are shown in Fig.(307.72) and (307.73).

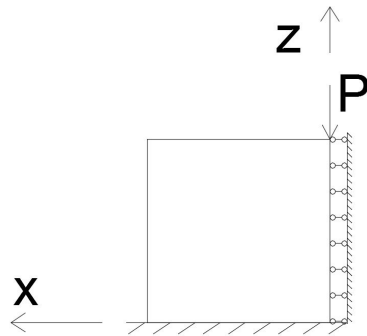


Figure 307.72: X-Z view for the reduced model

307.2.12.3 Results

Analytic solution for this model

According to the previous introduction, the analytic solution on the surface for this problem is

$$z = 0 : \quad u_z = \frac{P(1 - \nu^2)}{\pi E R} = \frac{1}{10^3 \pi} \frac{1}{R} \quad (307.42)$$

On the face $x = 0$, the distance R on the surface is actually the value of y , therefore, the analytic

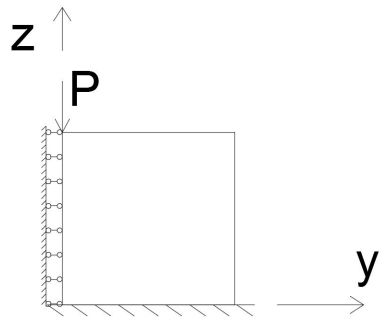


Figure 307.73: Y-Z view for the reduced model

solution is

$$u_z = \frac{1}{10^3 \pi R} = \frac{1}{10^3 \pi} \frac{1}{y} \quad (307.43)$$

As long as the y values are substituted, the displacement u_z is obtained immediately.

Real-ESSI solution with 8NodeBrickLT

In Real-ESSI, 8NodeBrickLT elements were used to simulate this model. Each element is $2m \times 2m \times 2m$. Since the model is $20m \times 20m \times 20m$, the element number is $10 \times 10 \times 10 = 1000$. The vertical displacement at the surface was recorded.

Since the model is symmetric, when the results were plotted, the other half results were obtained by symmetry.

Comparison between the analytic and 8NodeBrickLT solution

The Real-ESSI and analytic results were plotted in Fig.(307.74). Note that the analytic solution for location $y = 0$ is infinity, which was not plotted in the figure below.

307.2.12.4 Error Analysis

1. Mismatch at the loading point.

First of all, when $x = 0$ at the loading point, the analytic solution is infinite. From the perspective of practical engineering, this analytic solution is flawed because the displacement cannot be infinite. The infinite solution is due to the elastic assumption. In consideration of the plasticity, the analytic solution will not be infinite.

In Real-ESSI, the displacement at the loading point is not infinite because the infinite value is averaged by the integration during the finite element calculation. Also, at the loading point,

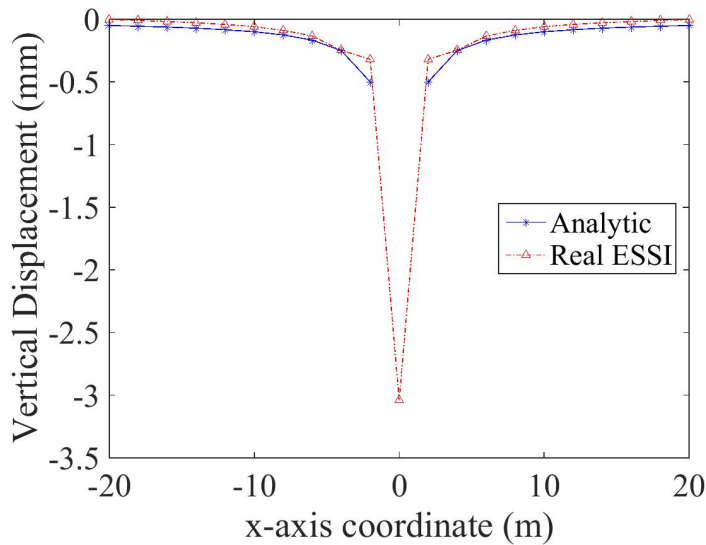


Figure 307.74: Comparison between analytic solution and Real-ESSI 8NodeBrickLT solution

27NodeBrickLT has a much larger displacement than that of 8NodeBrickLT. This is because 27NodeBrickLT has a relatively denser mesh than 8NodeBrickLT. So the maximum value at the loading point is higher than that of 8NodeBrickLT.

2. Mismatch at other locations.

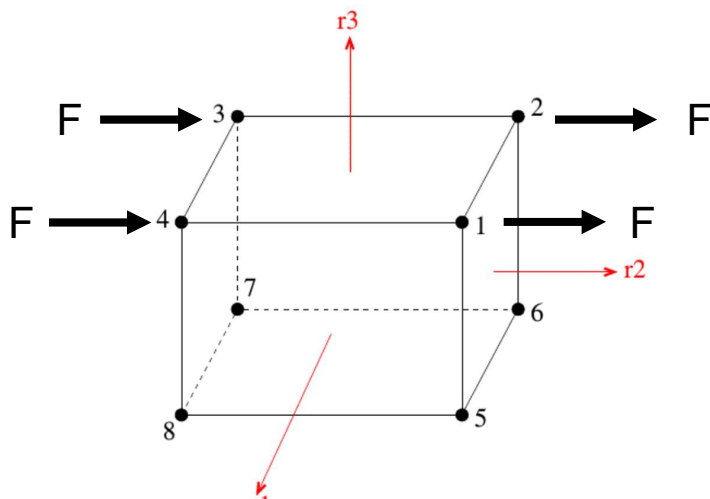
Except at the loading point, the analytic solution is not exactly equal to the numerical solution at other locations. This is because the verification example employs a simplified bounded cube to represent unbounded half space. The original analytic solution is for the half space, which is not true for the verification model. Not only the horizontal space but also the bottom space are removed from the model. This means the analytic solution is not perfect for this bounded cube. However, since the cube is very great, the analytic solution is similar to the Real-ESSI numerical solution. In addition, the brick elements are also verified by other models, like beam, plate and shells.

307.2.13 Verification of 8NodeBrick Finite Element for Collapsed Brick Shapes

307.2.13.1 Test procedure

With reference to the “patch test” put forward by Taylor et al. (1986), the test procedures are:

- A standard solution is given by testing two different loading modes on a single normal 8 node brick element: (1) Pure confinement loading, where same pressure are applied on three different directions. (2) Simple shearing, where shearing force is applied on four nodes of top layer, while four nodes on bottom layer are totally fixed. Linear elastic material is adopted here with Young's modulus $E = 125\text{MPa}$ and Poisson's ratio $\mu = 0.25$. The setup of standard test is shown in Figure 307.75.



Element # 1 with nodes (1, 2, 3, 4, 5, 6, 7, 8)

Figure 307.75: Setup of standard 8-node element.

- Build the same geometric model with collapsed 8 node brick elements and conduct numerical simulation under the same loading and boundary conditions as first step.

Specifically, the geometric configure for 7-node collapsed element is shown in Figure 307.76, where the cubic consists of two 7-node collapsed elements. A dummy node 11 is generated at the same location as node 2.

The geometric configuration for 6-node collapsed element is shown in Figure 307.77. Again the cubic is composed of two 6-node collapsed elements. Two dummy Real-ESSI nodes 9 and 10 are

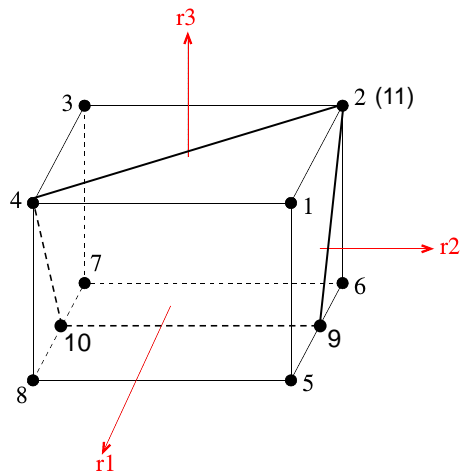


Figure 307.76: Geometric configuration of numerical test for 7-node collapsed element.

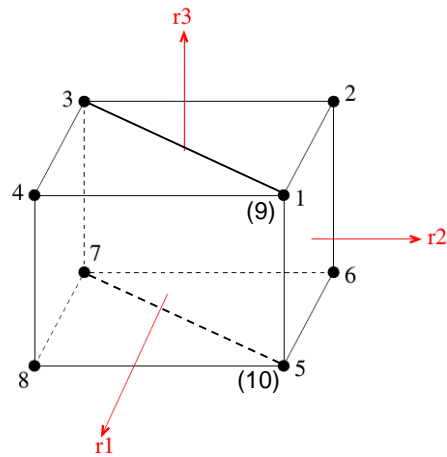
generated at the same location with original node 1 and 2.

And Figure 307.78 gives the geometric configuration of 5-node collapsed element, where the cubic is divided into 3 5-node elements.

- Compare the response of models in step 1 and step 2. If the difference is small enough, the strategy described in section ?? is feasible and valid.

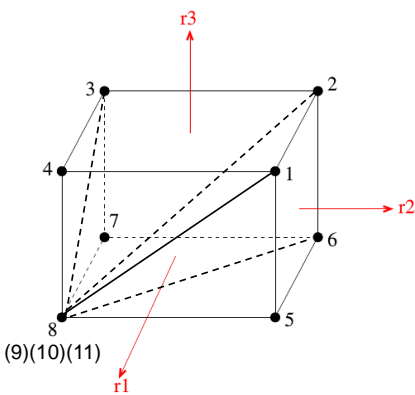
307.2.13.2 Test result

The comparison of displacement response for confinement loading is shown in Figure 307.79. Figure 307.80 demonstrates the test results of simple shearing loading. It can be seen that the simulation results of these types of collapsed element are close to result of standard 8 node brick element. The line of 6 node collapsed element is almost overlap with the line of standard test. Collapsed 7-node element and 5-node element experience certain decrease of accuracy. The main error reflects on the decrease of stiffness. Both bulk modulus and shear modulus of 7-node element and 5-node element are around 7% lower than the standard 8-node element.



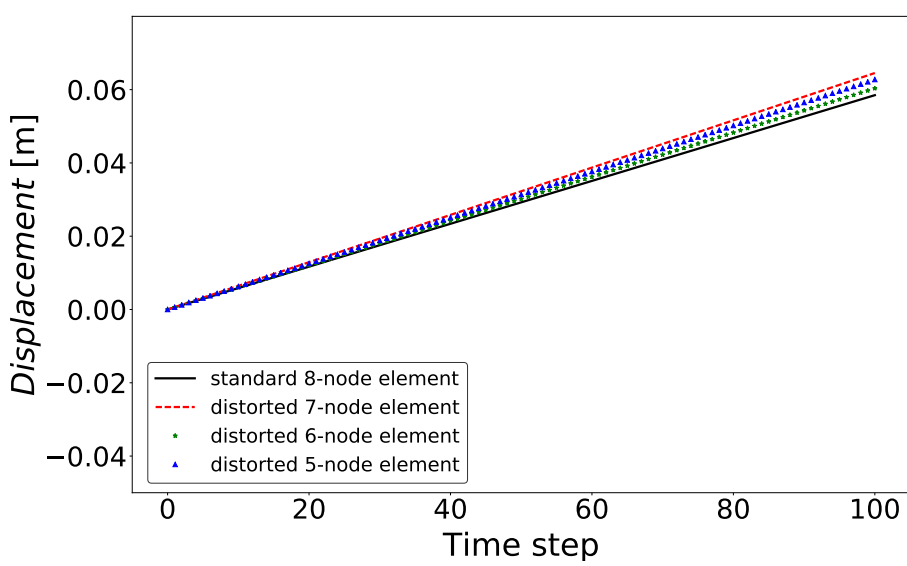
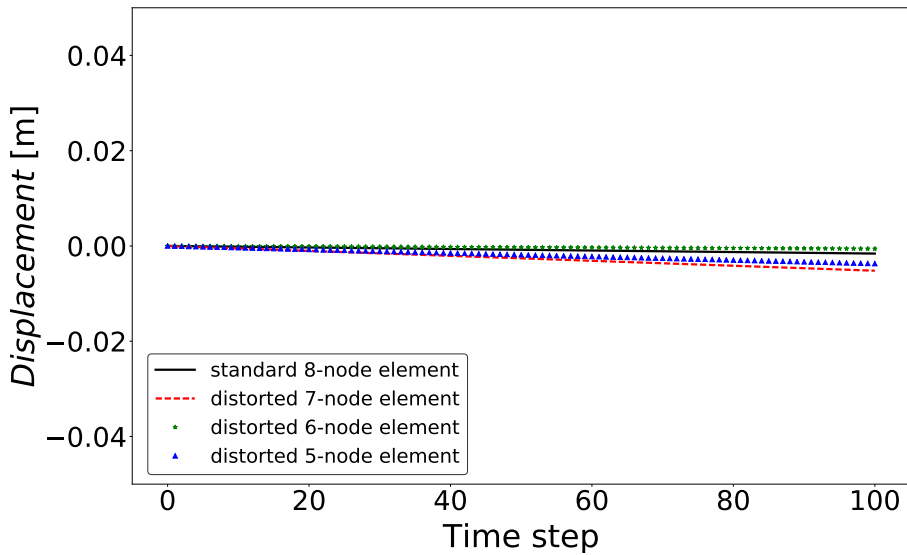
Element # 1 (1, 9, 3, 4, 5, 10, 7, 8)
 Element # 2 (9, 2, 3, 1, 10, 6, 7, 5)

Figure 307.77: Geometric configuration of numerical test for 6-node collapsed element.



Element # 1 (8, 9, 10, 11, 4, 3, 2, 1)
 Element # 2 (8, 9, 10, 11, 2, 3, 7, 6)
 Element # 3 (8, 9, 10, 11, 1, 2, 6, 5)

Figure 307.78: Geometric configuration of numerical test for 5-node collapsed element.



307.2.14 Verification of 27 node brick cantilever beam (static)

Problem description: Length=6m, Width=1m, Height=1m, Force=100N, E=1E8Pa, $\nu = 0.0$. Use the shear deformation coefficient $\kappa = 1.2$. The force direction was shown in Figure (307.81).

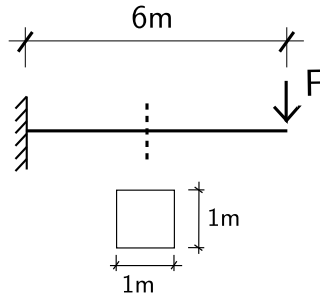


Figure 307.81: Problem description for cantilever beams.

Theoretical displacement (bending and shear deformation):

$$d = \frac{FL^3}{3EI} + \frac{FL}{GA_\nu} = \frac{FL^3}{3E \frac{bh^3}{12}} + \frac{FL}{\frac{E}{2(1+\nu)} \frac{bh}{\kappa}} = \frac{100N \times 6^3 m^3}{3 \times 10^8 N/m^2 \times \frac{1}{12} m^4} + \frac{100N \times 6m}{\frac{10}{2} \times 10^7 N/m^2 \times 1m^2 \times \frac{5}{6}} = 8.64 \times 10^{-4} m + 0.144 \times 10^{-4} m = 8.784 \times 10^{-4} m \quad (307.44)$$

Numerical model:

The 27NodeBrick elements are shown in Figure (307.85).

All the Real-ESSI results are listed in Table (307.23).

Table 307.23: Results for 27NodeBrick cantilever beams of different element numbers.

Element number	1	2	6
27NodeBrick	7.07E-04 m	8.50E-04 m	8.75E-04 m
Error	19.52%	3.19%	0.34%

The errors are plotted in Figure (307.88).

The Real-ESSI model fei/DSL files for the table above are [HERE](#).

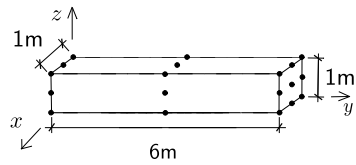


Figure 307.82: One 27NodeBrick element.

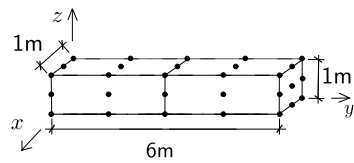


Figure 307.83: Two 27NodeBrick elements.

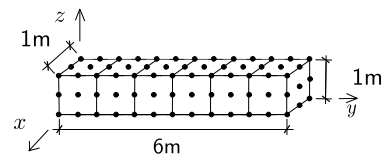


Figure 307.84: Six 27NodeBrick elements.

Figure 307.85: 27NodeBrick elements for cantilever beams.

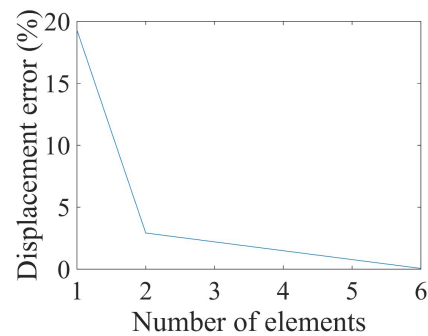


Figure 307.86: Error scale 0% - 20%.

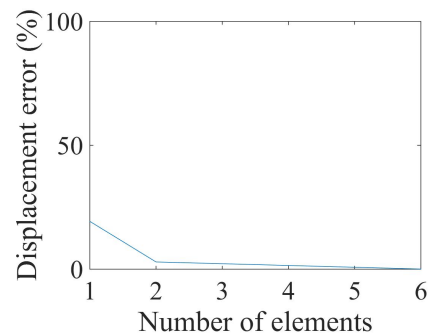


Figure 307.87: Error scale 0% - 100%.

Figure 307.88: 27NodeBrick cantilever beam for different element number: Displacement error versus Number of elements

307.2.15 Verification of 27NodeBrick cantilever beam for different Poisson's ratio

Problem description: Length=6m, Width=1m, Height=1m, Force=100N, E=1E8Pa, $\nu = 0.0 - 0.49$.

The force direction was shown in Figure (307.89).

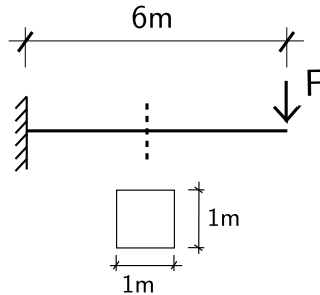


Figure 307.89: Problem description for cantilever beams of different Poisson's ratios.

The theoretical solution for $\nu = 0.0$ was calculated below, while the solution for other Poisson's ratio is calculated by the similar process.

Theoretical displacement (bending and shear deformation):

$$\begin{aligned}
 d &= \frac{FL^3}{3EI} + \frac{FL}{GA_v} \\
 &= \frac{FL^3}{3E \frac{bh^3}{12}} + \frac{FL}{\frac{E}{2(1+\nu)} \frac{bh}{\kappa}} \\
 &= \frac{100N \times 6^3 m^3}{3 \times 10^8 N/m^2 \times \frac{1}{12} m^4} + \frac{100N \times 6m}{\frac{10}{2} \times 10^7 N/m^2 \times 1m^2 \times \frac{5}{6}} \\
 &= 8.64 \times 10^{-4} m + 0.144 \times 10^{-4} m \\
 &= 8.784 \times 10^{-4} m
 \end{aligned} \tag{307.45}$$

The rotation angle at the end:

$$\theta = \frac{FL^2}{2EI} = \frac{100N \times 6^2 m^2}{2 \times 10^8 N/m^2 \times \frac{1}{12} m^4} = 2.16 \times 10^{-4} rad = 0.0124^\circ \tag{307.46}$$

The 27NodeBrick elements for cantilever beams of different Poisson's ratios are shown in Figure (307.90).

All the displacement results are listed in Table (307.24).

The errors are plotted in Figure (307.93).

The angle results are listed in Table (307.27).

The errors are plotted in Figure (307.96).

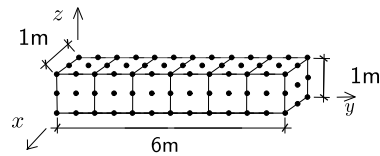


Figure 307.90: 27NodeBrick elements for cantilever beams of different Poisson's ratios.

Table 307.24: Displacement results for 27NodeBrick cantilever beams with element side length 1 m.

Poisson's ratio	27NodeBrick displacement	Theory displacement (bending)	Theory displacement (shear)	Theory displacement(all)	Error
0.00	8.755E-04 m	8.640E-04 m	1.440E-05 m	8.784E-04 m	0.34%
0.05	8.757E-04 m	8.640E-04 m	1.512E-05 m	8.791E-04 m	0.39%
0.10	8.751E-04 m	8.640E-04 m	1.586E-05 m	8.799E-04 m	0.54%
0.15	8.735E-04 m	8.640E-04 m	1.659E-05 m	8.806E-04 m	0.80%
0.20	8.708E-04 m	8.640E-04 m	1.734E-05 m	8.813E-04 m	1.19%
0.25	8.667E-04 m	8.640E-04 m	1.808E-05 m	8.821E-04 m	1.74%
0.30	8.608E-04 m	8.640E-04 m	1.884E-05 m	8.828E-04 m	2.50%
0.35	8.520E-04 m	8.640E-04 m	1.959E-05 m	8.836E-04 m	3.57%
0.40	8.385E-04 m	8.640E-04 m	2.035E-05 m	8.844E-04 m	5.18%
0.45	8.147E-04 m	8.640E-04 m	2.111E-05 m	8.851E-04 m	7.96%
0.49	7.711E-04 m	8.640E-04 m	2.173E-05 m	8.857E-04 m	12.94%

The Real-ESSI model fei/DSL files for the table above are [HERE](#).

Then, different values of elastic modulus were also tried. The errors are plotted below.

According to Fig.(307.97)), the different values of elastic modulus will not influence the error.

However, the different Poisson's ratio will influence the error. The error will increase with the Poisson's ratio increase.

Table 307.25: Displacement results for 27NodeBrick cantilever beams with element side length 0.5 m.

Poisson's ratio	27NodeBrick displacement	Theory displacement (bending)	Theory displacement (shear)	Theory displacement(all)	Error
0.00	8.804E-04 m	8.640E-04 m	1.440E-05 m	8.784E-04 m	0.23%
0.05	8.808E-04 m	8.640E-04 m	1.512E-05 m	8.791E-04 m	0.19%
0.10	8.805E-04 m	8.640E-04 m	1.586E-05 m	8.799E-04 m	0.08%
0.15	8.796E-04 m	8.640E-04 m	1.659E-05 m	8.806E-04 m	0.12%
0.20	8.778E-04 m	8.640E-04 m	1.734E-05 m	8.813E-04 m	0.40%
0.25	8.752E-04 m	8.640E-04 m	1.808E-05 m	8.821E-04 m	0.78%
0.30	8.715E-04 m	8.640E-04 m	1.884E-05 m	8.828E-04 m	1.28%
0.35	8.663E-04 m	8.640E-04 m	1.959E-05 m	8.836E-04 m	1.95%
0.40	8.588E-04 m	8.640E-04 m	2.035E-05 m	8.844E-04 m	2.89%
0.45	8.465E-04 m	8.640E-04 m	2.111E-05 m	8.851E-04 m	4.36%
0.49	8.248E-04 m	8.640E-04 m	2.173E-05 m	8.857E-04 m	6.88%

Table 307.26: Displacement results for 27NodeBrick cantilever beams with element side length 0.25 m.

Poisson's ratio	27NodeBrick displacement	Theory displacement (bending)	Theory displacement (shear)	Theory displacement(all)	Error
0.00	8.797E-04 m	8.640E-04 m	1.440E-05 m	8.784E-04 m	0.15%
0.05	8.801E-04 m	8.640E-04 m	1.512E-05 m	8.791E-04 m	0.11%
0.10	8.799E-04 m	8.640E-04 m	1.586E-05 m	8.799E-04 m	0.01%
0.15	8.792E-04 m	8.640E-04 m	1.659E-05 m	8.806E-04 m	0.16%
0.20	8.778E-04 m	8.640E-04 m	1.734E-05 m	8.813E-04 m	0.40%
0.25	8.758E-04 m	8.640E-04 m	1.808E-05 m	8.821E-04 m	0.71%
0.30	8.730E-04 m	8.640E-04 m	1.884E-05 m	8.828E-04 m	1.12%
0.35	8.692E-04 m	8.640E-04 m	1.959E-05 m	8.836E-04 m	1.63%
0.40	8.641E-04 m	8.640E-04 m	2.035E-05 m	8.844E-04 m	2.29%
0.45	8.567E-04 m	8.640E-04 m	2.111E-05 m	8.851E-04 m	3.21%
0.49	8.452E-04 m	8.640E-04 m	2.173E-05 m	8.857E-04 m	4.58%

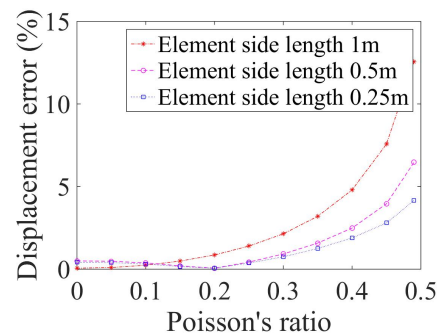


Figure 307.91: Error scale 0% - 15%.

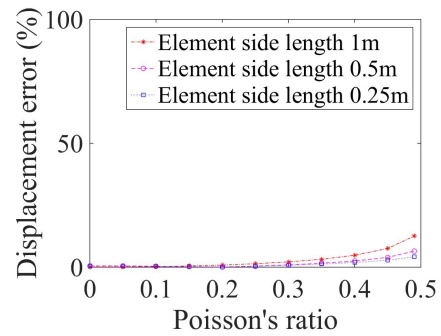


Figure 307.92: Error scale 0% - 100%.

Figure 307.93: 27NodeBrick cantilever beam for different Poisson's ratio' Displacement error versus Poisson's ratio

Table 307.27: Rotation angle results for 27NodeBrick cantilever beams with element side length 1 m.

Poisson's ratio	27NodeBrick angle (unit:°)	Theory angle (unit:°)	Error
0.00	1.238E-02	1.24E-02	0.19%
0.05	1.237E-02	1.24E-02	0.24%
0.10	1.236E-02	1.24E-02	0.34%
0.15	1.233E-02	1.24E-02	0.53%
0.20	1.230E-02	1.24E-02	0.80%
0.25	1.225E-02	1.24E-02	1.18%
0.30	1.219E-02	1.24E-02	1.70%
0.35	1.210E-02	1.24E-02	2.45%
0.40	1.196E-02	1.24E-02	3.55%
0.45	1.172E-02	1.24E-02	5.47%
0.49	1.130E-02	1.24E-02	8.89%

Table 307.28: Rotation angle results for 27NodeBrick cantilever beams with element side length 0.5 m.

Poisson's ratio	27NodeBrick angle (unit:°)	Theory angle (unit:°)	Error
0.00	1.242E-02	1.24E-02	0.12%
0.05	1.241E-02	1.24E-02	0.11%
0.10	1.241E-02	1.24E-02	0.06%
0.15	1.239E-02	1.24E-02	0.05%
0.20	1.237E-02	1.24E-02	0.21%
0.25	1.235E-02	1.24E-02	0.44%
0.30	1.231E-02	1.24E-02	0.74%
0.35	1.226E-02	1.24E-02	1.16%
0.40	1.218E-02	1.24E-02	1.76%
0.45	1.206E-02	1.24E-02	2.76%
0.49	1.183E-02	1.24E-02	4.63%

Table 307.29: Rotation angle results for 27NodeBrick cantilever beams with element side length 0.25 m.

Poisson's ratio	27NodeBrick angle(unit: circ)	Theory angle (unit: circ)	Error
0.00	1.242E-02	1.24E-02	0.17%
0.05	1.242E-02	1.24E-02	0.15%
0.10	1.241E-02	1.24E-02	0.09%
0.15	1.240E-02	1.24E-02	0.02%
0.20	1.238E-02	1.24E-02	0.17%
0.25	1.235E-02	1.24E-02	0.38%
0.30	1.232E-02	1.24E-02	0.64%
0.35	1.228E-02	1.24E-02	0.98%
0.40	1.222E-02	1.24E-02	1.42%
0.45	1.214E-02	1.24E-02	2.06%
0.49	1.202E-02	1.24E-02	3.08%

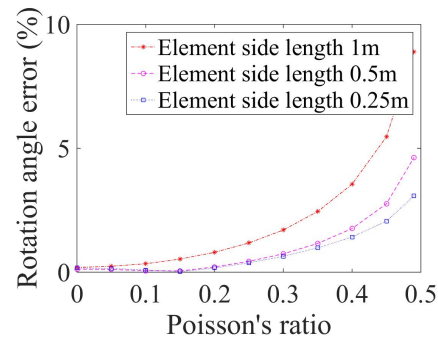


Figure 307.94: Error scale 0% - 10%.

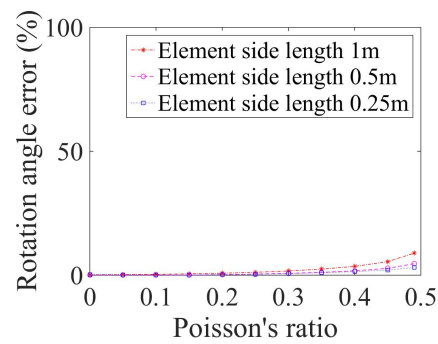


Figure 307.95: Error scale 0% - 100%.

Figure 307.96: 27NodeBrick cantilever beam for different Poisson's ratio' Rotation angle error versus Poisson's ratio

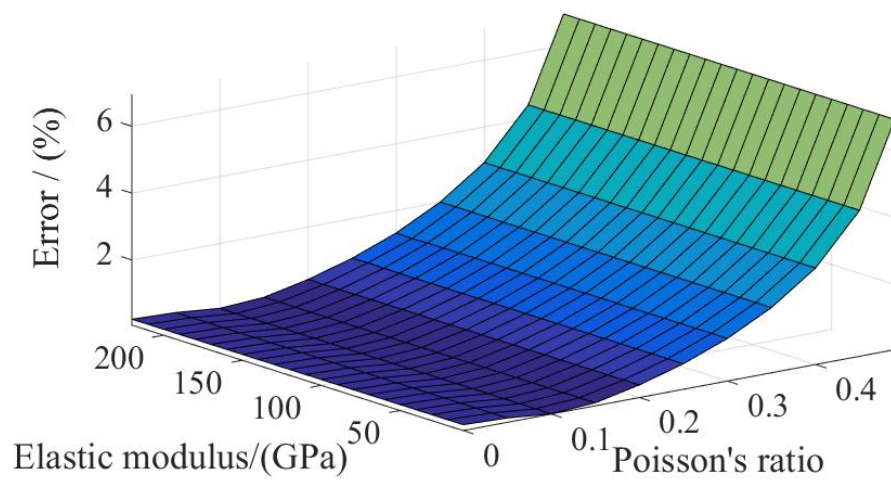


Figure 307.97: The influence of Poisson's ratio and elastic modulus on the errors

307.2.16 Test of irregular shaped 27NodeBrick cantilever beams

Cantilever model was used as an example. Three different shapes are tested.

In the first test, the upper two nodes of each element were moved one half element size along the y -axis, while the lower two nodes were kept at the same location. The element shape was shown in Figure (307.98).

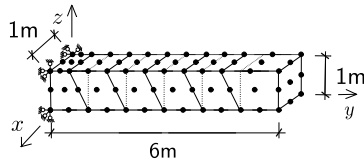


Figure 307.98: 27NodeBrick cantilever beams for irregular Shape 1.

In the second test, the upper two nodes of each element were moved 90% element size along the y -axis, while the lower two nodes were moved 90% element size in the other direction along the y -axis. The element shape was shown in Figure (307.99).

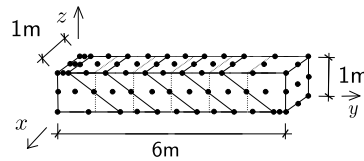


Figure 307.99: 27NodeBrick cantilever beams for irregular Shape 2.

In the third test, the upper two nodes of each element are moved one half element size with different directions along the y -axis, while the lower two nodes were kept at the same location. The element shape was shown in Figure (307.100).

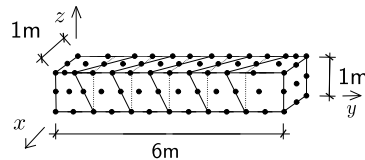


Figure 307.100: 27NodeBrick cantilever beams for irregular Shape 3.

The boundary conditions are shown in Figure (307.103), (307.106) and (307.109).

The Real-ESSI results are listed in Table (307.30).

The errors are listed in Table (307.31) and (307.32).

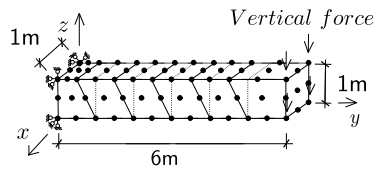


Figure 307.101: Veritical force.

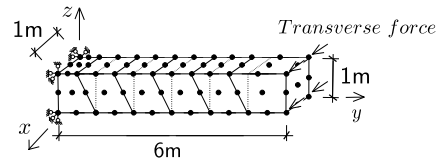


Figure 307.102: Horizontal force.

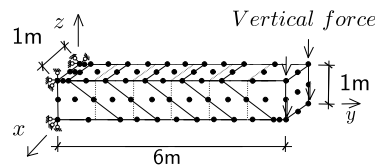
Figure 307.103: 27NodeBrick cantilever beam boundary conditions for irregular Shape 1.

Figure 307.104: Veritical force.

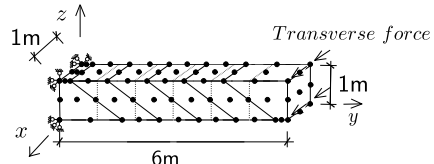


Figure 307.105: Horizontal force.

Figure 307.106: 27NodeBrick cantilever beam boundary conditions for irregular Shape 2.

Table 307.30: Results for 27NodeBrick cantilever beams of irregular shapes.

Displacements for irregular shaped element					
Element Type	Force direction	Normal shape	Shape 1	Shape 2	Shape 3
27NodeBrick	Vertical (z)	8.755E-04 m	8.819E-04 m	8.709E-04 m	8.837E-04 m
27NodeBrick	Transverse (y)	8.755E-04 m	8.831E-04 m	8.462E-04 m	8.824E-04 m
Theoretical	-	8.784E-04 m	8.784E-04 m	8.784E-04 m	8.784E-04 m

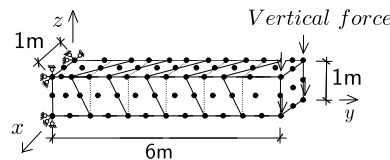


Figure 307.107: Veritical force.

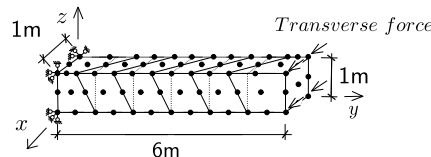


Figure 307.108: Horizontal force.

Figure 307.109: 27NodeBrick cantilever beam boundary conditions for irregular Shape 3.

Table 307.31: Errors for irregular shaped 27NodeBrick compared to theoretical solution.

Errors for irregular shaped element, compared to theoretical solutions					
Element Type	Force direction	Normal shape	Shape 1	Shape 2	Shape 3
27NodeBrick	Vertical (z)	0.34%	0.40%	0.85%	0.60%
27NodeBrick	Transverse (y)	0.34%	0.54%	3.67%	0.46%

Table 307.32: Errors for irregular shaped 27NodeBrick compared to normal shape.

Errors for irregular shaped element, compared to normal shape					
Element Type	Force direction	Normal shape	Shape 1	Shape 2	Shape 3
27NodeBrick	Vertical (z)	0.00%	0.74%	0.52%	0.94%
27NodeBrick	Transverse (y)	0.00%	0.87%	3.34%	0.79%

The Real-ESSI model fei/DSL files for the table above are [HERE](#).

Then, the beam was divided into small elements.

Problem description: Length=12m, Width=2m, Height=2m, Force=400N/m, E=1E8Pa, $\nu = 0.0$.

Use the shear deformation coefficient $\kappa = 1.2$. The force direction was shown in Figure (307.110).

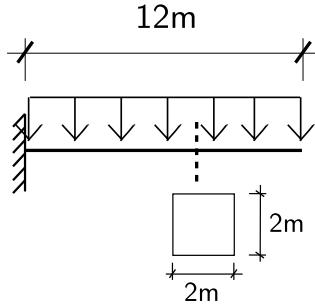


Figure 307.110: Problem description for cantilever beams under uniform pressure .

Theoretical displacement (bending and shear deformation):

$$\begin{aligned}
 d &= \frac{qL^4}{8EI} + \frac{q\frac{L^2}{2}}{GA_v} \\
 &= \frac{qL^4}{8E \frac{bh^3}{12}} + \frac{q\frac{L^2}{2}}{\frac{E}{2(1+\nu)} \frac{bh}{\kappa}} \\
 &= \frac{400N/m \times 12^4 m^4}{8 \times 10^8 N/m^2 \times \frac{2^4}{12} m^4} + \frac{400N/m \times \frac{12^2}{2} m^2}{\frac{10^8}{2} N/m^2 \times 2m \times 2m \times \frac{5}{6}} \\
 &= 7.776 \times 10^{-3} m + 1.728 \times 10^{-4} m \\
 &= 7.9488 \times 10^{-3} m
 \end{aligned} \tag{307.47}$$

The Real-ESSI displacement results are listed in Table (307.33).

Table 307.33: Results for 27NodeBrick cantilever beams of irregular shapes with more elements.

Element Type	Shape	Force direction	Number of division		
			1	2	4
27NodeBrick	shape1	Vertical (z)	7.913E-03 m	7.946E-03 m	7.948E-03 m
27NodeBrick	shape1	Transverse (y)	7.903E-03 m	7.946E-03 m	7.948E-03 m
27NodeBrick	shape2	Vertical (z)	7.741E-03 m	7.930E-03 m	7.947E-03 m
27NodeBrick	shape2	Transverse (y)	7.371E-03 m	7.894E-03 m	7.944E-03 m
27NodeBrick	shape3	Vertical (z)	1.982E-03 m	7.946E-03 m	7.948E-03 m
27NodeBrick	shape3	Transverse (y)	1.979E-03 m	7.947E-03 m	7.948E-03 m
Theoretical solution			7.9488E-03 m	7.9488E-03 m	7.9488E-03 m

The error are listed in Table (307.34).

The errors are shown in Figures (307.113), (307.116) and (307.119).

The Real-ESSI model fei/DSL files for the table above are [HERE](#).

Table 307.34: Errors for 27NodeBrick cantilever beams of irregular shapes with more elements.

Element Type	Shape	Force direction	Number of division		
			1	2	4
27NodeBrick	shape1	Vertical (z)	0.45%	0.04%	0.01%
27NodeBrick	shape1	Transverse (y)	0.32%	0.03%	0.01%
27NodeBrick	shape2	Vertical (z)	2.61%	0.23%	0.03%
27NodeBrick	shape2	Transverse (y)	7.27%	0.69%	0.06%
27NodeBrick	shape3	Vertical (z)	75.06%	0.04%	0.01%
27NodeBrick	shape3	Transverse (y)	75.11%	0.03%	0.01%

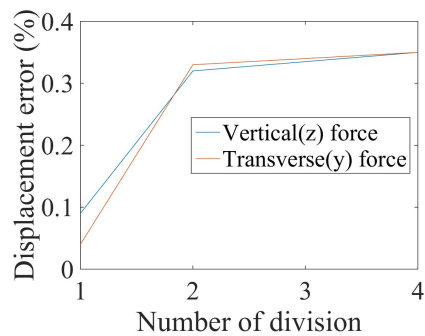


Figure 307.111: Error scale 0% - 0.4%.

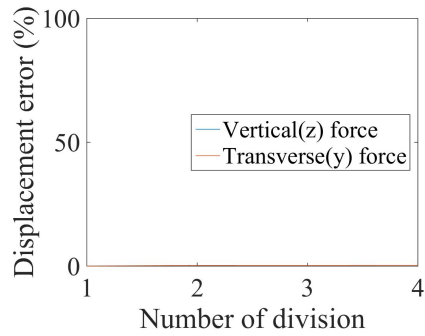


Figure 307.112: Error scale 0% - 100%.

Figure 307.113: 27NodeBrick cantilever beam for irregular Shape 1. Displacement error versus Number of division

$\nu = 0.0$. Use the shear deformation coefficient $\kappa = 1.2$. The force direction was shown in Figure (??).

In this section, the beam was cut into smaller elements with element side length 0.5m and 0.25m respectively. And the element side length of the original models is 1.0m. The numerical models are shown in Figure (307.120), (307.121) and (307.122).

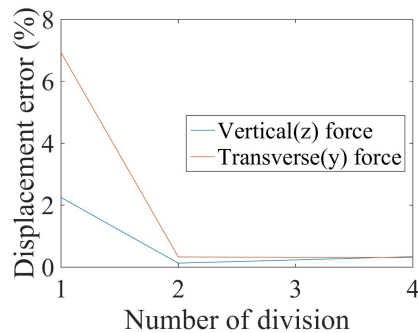


Figure 307.114: Error scale 0% - 8%.

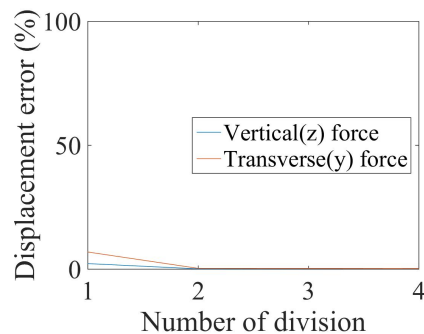


Figure 307.115: Error scale 0% - 100%.

Figure 307.116: 27NodeBrick cantilever beam for irregular Shape 2: Displacement error versus Number of division

Number of division 1:

Number of division 2:

Number of division 4:

The Real-ESSI results are listed in Table (307.35). The theoretical solution is 1.60E-5 m.

Table 307.35: Results for 27NodeBrick clamped beams with more elements.

Element Type	Element side length		
	1 m	0.5 m	0.25 m
27NodeBrick	1.64E-05 m	1.70E-05 m	1.71E-05 m
Error	0.83%	3.25%	3.70%

The errors are plotted in Figure (307.125).

The Real-ESSI model fei/DSL files for the table above are [HERE](#).

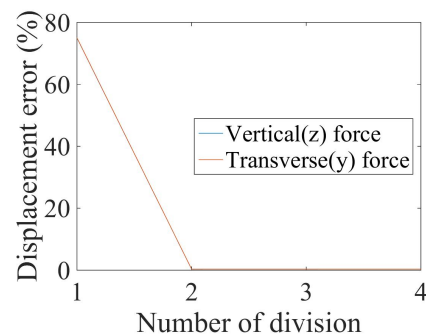


Figure 307.117: Error scale 0% - 80%.

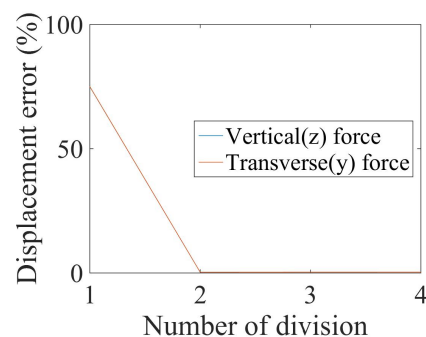


Figure 307.118: Error scale 0% - 100%.

Figure 307.119: 27NodeBrick cantilever beam for irregular Shape 3' Displacement error versus Number of division

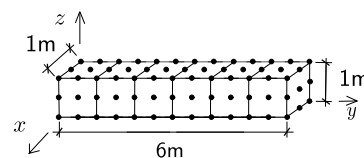


Figure 307.120: 27NodeBrick clamped beams with element side length 1.0m.

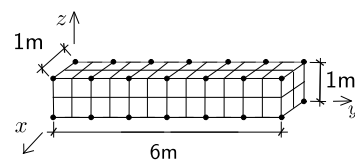


Figure 307.121: 27NodeBrick clamped beams with element side length 0.5m.

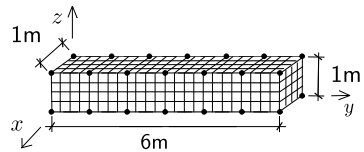


Figure 307.122: 27NodeBrick clamped beams with element side length 0.25m.

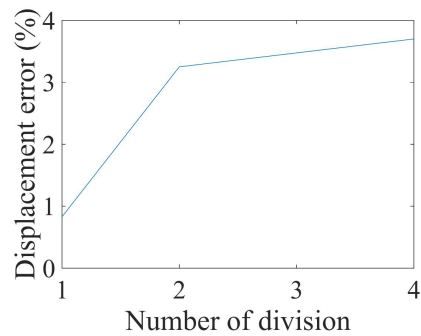


Figure 307.123: Error scale 0% - 4%.

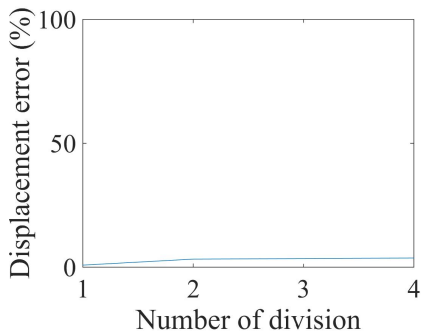


Figure 307.124: Error scale 0% - 100%.

Figure 307.125: 27NodeBrick clamped beam for different element number: Displacement error versus Number of division

307.2.17 Verification of 27NodeBrick stress in cantilever beams

Problem description: Length=6m, Width=1m, Height=1m, Force=100N, E=1E8Pa, $\nu = 0.0$. Use the shear deformation coefficient $\kappa = 1.2$. The force direction was shown in Figure (307.126).

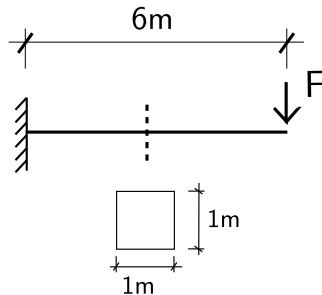


Figure 307.126: Problem description for cantilever beams of stress verification.

The theoretical solution for the stress was calculated below.

The 27NodeBrick elements are shown in Figure (307.127).

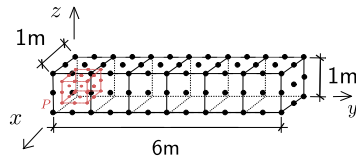


Figure 307.127: 27NodeBrick for cantilever beams of stress verification.

The bending moment at the Gassian Point is

$$M = F(L - P_y) = 100N \times (6 - 0.1127)m = 588.73N \cdot m \quad (307.48)$$

The bending modulus is

$$I = \frac{bh^3}{12} = \frac{1}{12}m^4 \quad (307.49)$$

Therefore, the theoretical stress is

$$\sigma = \frac{M \cdot z}{I} = \frac{588.73N \cdot m \times (0.5 - 0.1127)m}{\frac{1}{12}m^4} = 2736Pa \quad (307.50)$$

To get a better result, the same geometry beam was also cut into small elements. When more elements are used, the theoretical stress was calculated again with the new coordinates. The calculation process is similar to the process above.

The numerical models are shown in Figure (307.128), (307.129) and (307.130).

Number of division 1:

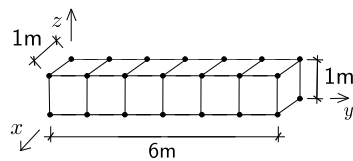


Figure 307.128: 27NodeBrick stress with element side length 1.0m.

Number of division 2:

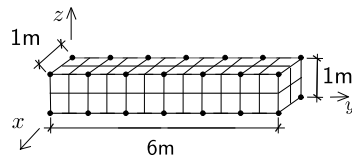


Figure 307.129: 27NodeBrick stress with element side length 0.5m.

Number of division 4:

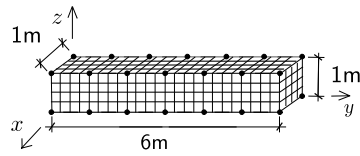


Figure 307.130: 27NodeBrick stress with element side length 0.25m.

All the stress results are listed in Table (307.36).

Table 307.36: Results for 27NodeBrick stress with more elements.

Element Type	Element side length		
	1 m	0.5 m	0.25 m
27NodeBrick	2719.81 Pa	3198.19 Pa	3464.76 Pa
Theoretical	2736.17 Pa	3164.27 Pa	3381.18 Pa
Error	0.60%	1.07%	2.47%

The Real-ESSI model fei/DSL files for the table above are [HERE](#).

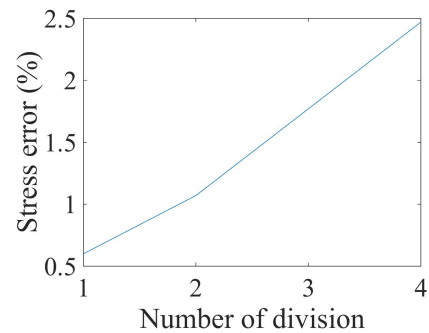


Figure 307.131: Error scale 0% - 2.5%.

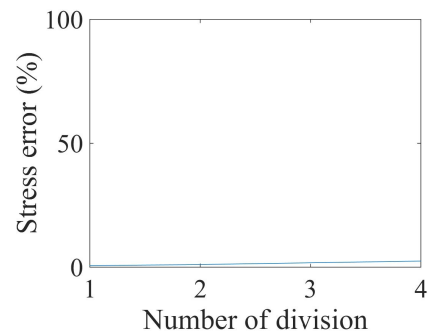


Figure 307.132: Error scale 0% - 100%.

Figure 307.133: 27NodeBrick cantilever beams for stress verification: Stress error versus Number of division

307.2.18 Verification of 27NodeBrick square plate with four edges clamped

Problem description: Length=20m, Width=20m, Height=1m, Force=100N, E=1E8Pa, $\nu = 0.3$.

The four edges are clamped.

The load is the uniform normal pressure on the whole plate.

The plate flexural rigidity is

$$D = \frac{Eh^3}{12(1-\nu^2)} = \frac{10^8 N/m^2 \times 1^3 m^3}{12 \times (1 - 0.3^2)} = 9.1575 \times 10^6 N \cdot m \quad (307.51)$$

The theoretical solution is

$$d = \alpha_c \frac{qa^4}{D} = 0.00406 \times \frac{100N/m^2 \times 20^4 m^4}{9.1575 \times 10^6 N \cdot m} = 2.2015 \times 10^{-3} m \quad (307.52)$$

where α_c is a coefficient, which depends on the ratio of plate length to width. In this problem, the coefficient⁸ α_c is 0.00406.

The 27NodeBrick are shown in Figure (307.134) - (307.139).

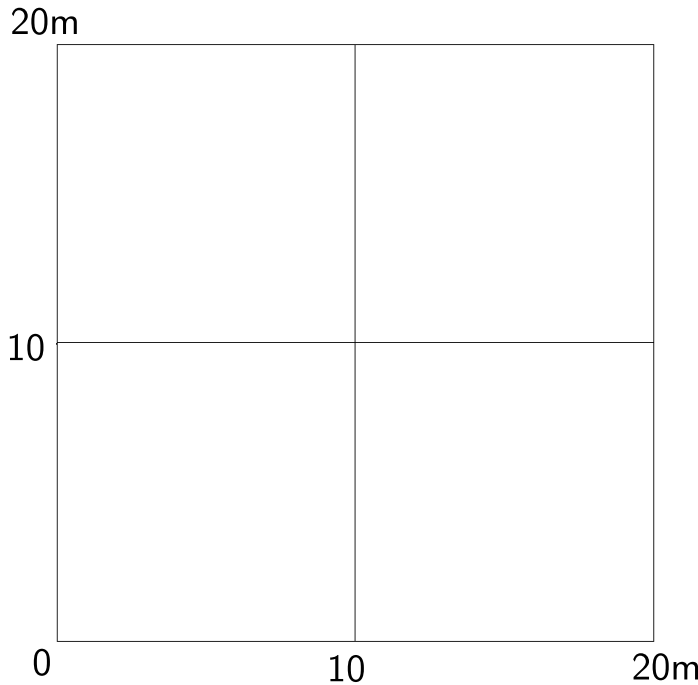


Figure 307.134: 27NodeBrick edge clamped square plate with element side length 10m.

The results were listed in Table (307.37).

⁸Stephen Timoshenko, Theory of plates and shells (2nd edition). MrGRAW-Hill Inc, page120, 1959.

⁹This model run out of memory on machine cml01 (memory: 23.5GB). This model has 233,289 nodes with 3 dofs, which may require 40GB memory.

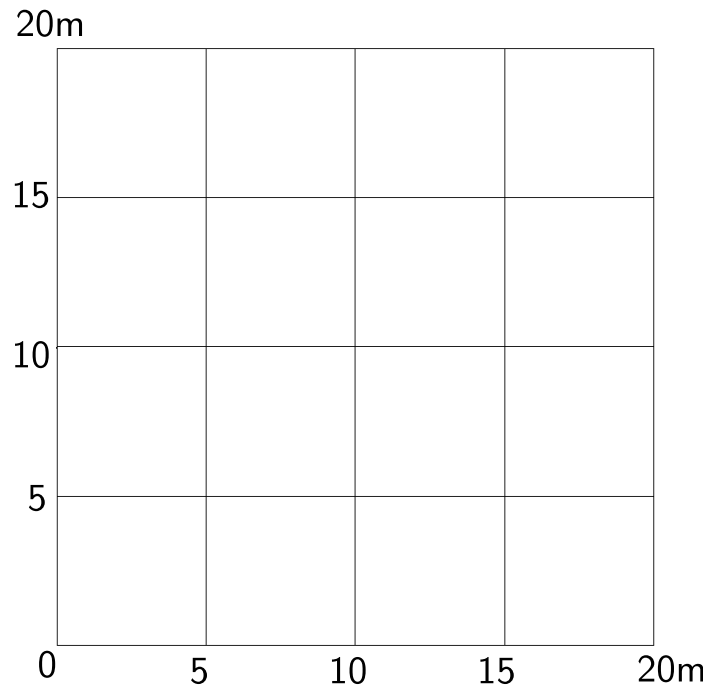


Figure 307.135: 27NodeBrick edge clamped square plate with element side length 5m.

Table 307.37: Results for 27NodeBrick square plate with four edges clamped.

Element type	27NodeBrick	27NodeBrick	27NodeBrick	Theoretical displacement
Number of layers	1layer	2layers	4layers	
Element side length	Height:1.00m	Height:0.50m	Height:0.25m	
10m	4.82E-004 m	4.82E-004 m	4.82E-004 m	2.20E-03 m
5m	1.97E-003 m	1.98E-003 m	1.98E-003 m	2.20E-03 m
2m	2.25E-003 m	2.26E-003 m	2.26E-003 m	2.20E-03 m
1m	2.28E-003 m	2.29E-003 m	2.29E-003 m	2.20E-03 m
0.5m	2.29E-003 m	2.30E-003 m	2.30E-003 m	2.20E-03 m
0.25m	2.29E-003 m	2.30E-003 m	- ⁹	2.20E-03 m

The errors were listed in Table (307.38).

The errors were plotted in Figure (307.140).

The Real-ESSI model fei/DSL files for the table above are [HERE](#).

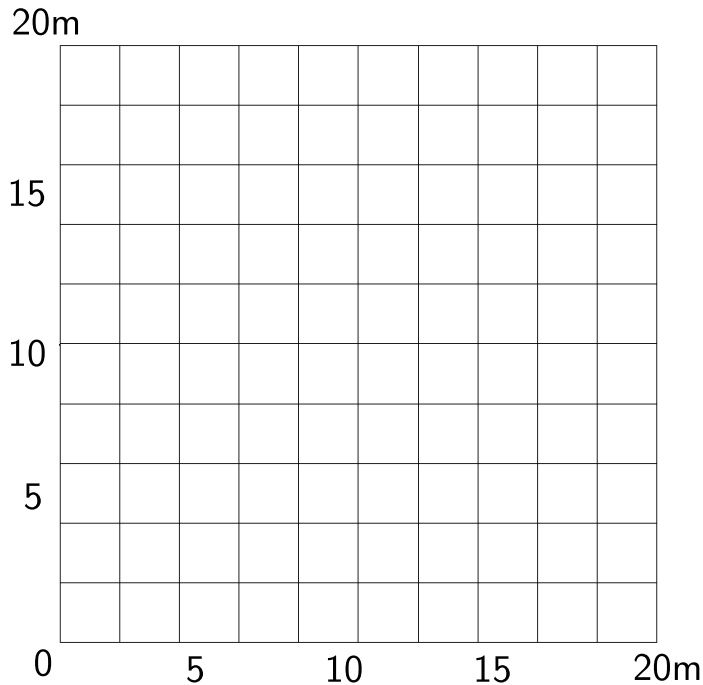


Figure 307.136: 27NodeBrick edge clamped square plate with element side length 2m.

Table 307.38: Errors for 27NodeBrick square plate with four edges clamped.

Element type	27NodeBrick	27NodeBrick	27NodeBrick
Number of layers	1layer	2layers	4layers
Element side length	Height:1.00m	Height:0.50m	Height:0.25m
10m	78.11%	78.10%	78.10%
5m	10.67%	10.19%	10.16%
2m	2.23%	2.79%	2.83%
1m	3.56%	4.16%	4.22%
0.5m	3.96%	4.58%	4.65%
0.25m	4.08%	4.70%	-

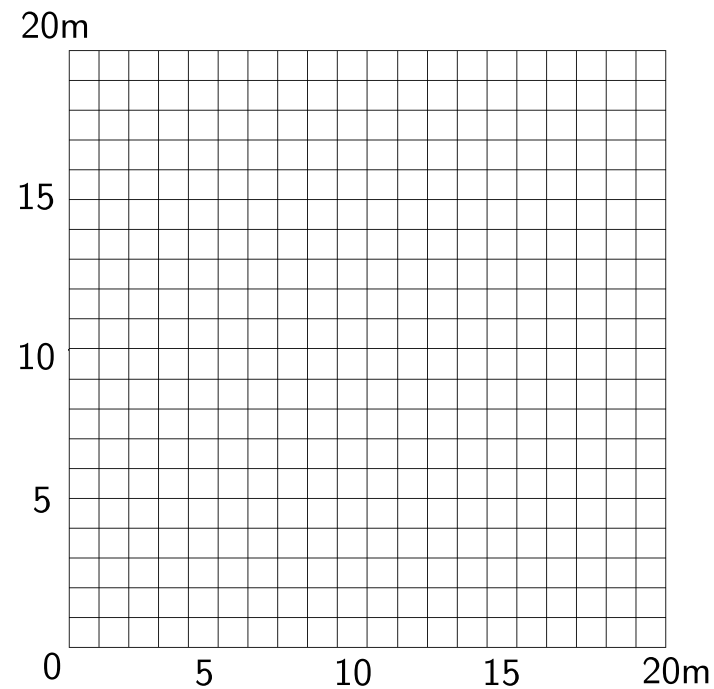


Figure 307.137: 27NodeBrick edge clamped square plate with element side length 1m.

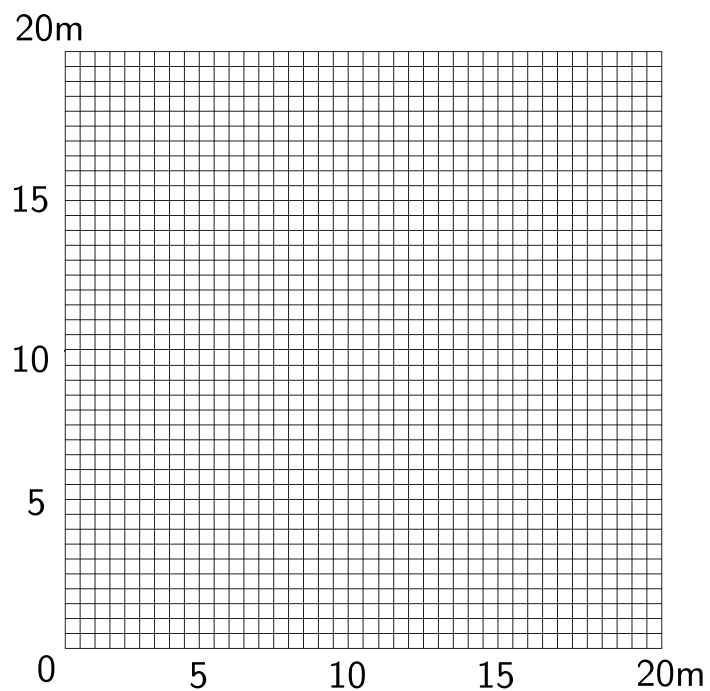


Figure 307.138: 27NodeBrick edge clamped square plate with element side length 0.5m.

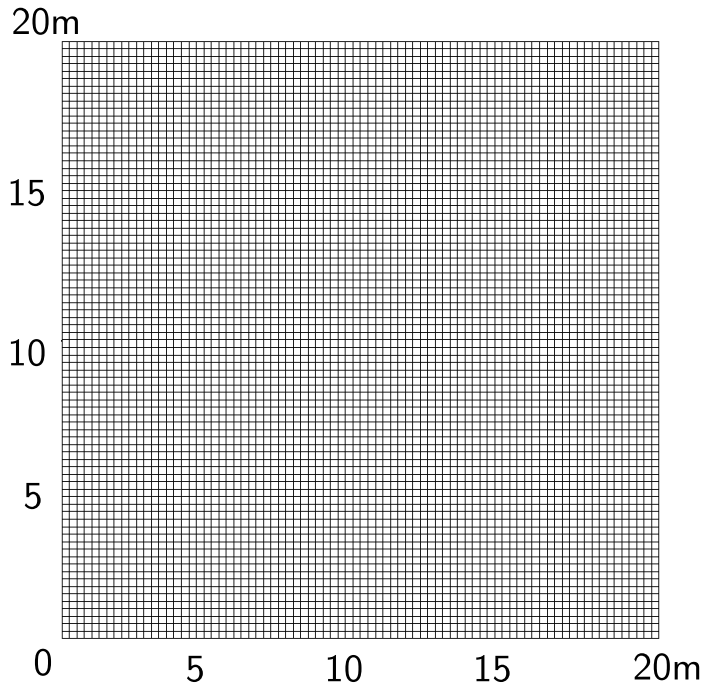


Figure 307.139: 27NodeBrick edge clamped square plate with element side length 0.25m.

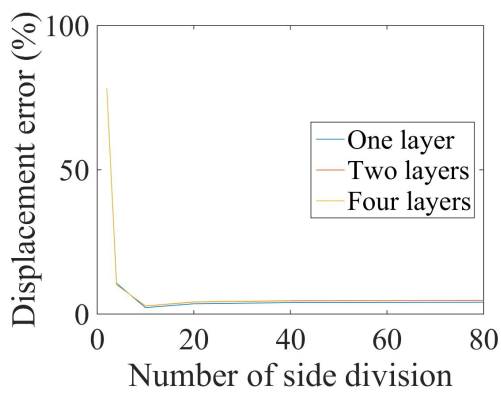


Figure 307.140: 27NodeBrick square plate with edge clamped' Displacement error versus Number of side division

307.2.19 Verification of 27NodeBrick square plate with four edges simply supported

Problem description: Length=20m, Width=20m, Height=1m, Force=100N, E=1E8Pa, $\nu = 0.3$.

The four edges are simply supported.

The load is the uniform normal pressure on the whole plate.

The plate flexural rigidity is

$$D = \frac{Eh^3}{12(1-\nu^2)} = \frac{10^8 N/m^2 \times 1^3 m^3}{12 \times (1 - 0.3^2)} = 9.1575 \times 10^6 N \cdot m \quad (307.53)$$

The theoretical solution is

$$d = \alpha_s \frac{qa^4}{D} = 0.00126 \times \frac{100 N/m^2 \times 20^4 m^4}{9.1575 \times 10^6 N \cdot m} = 7.0936 \times 10^{-3} m \quad (307.54)$$

where α_s is a coefficient, which depends on the ratio of plate length to width. In this problem, the coefficient¹⁰ α_s is 0.00126.

The 27NodeBrick were shown in Figure (307.141) - (307.146).

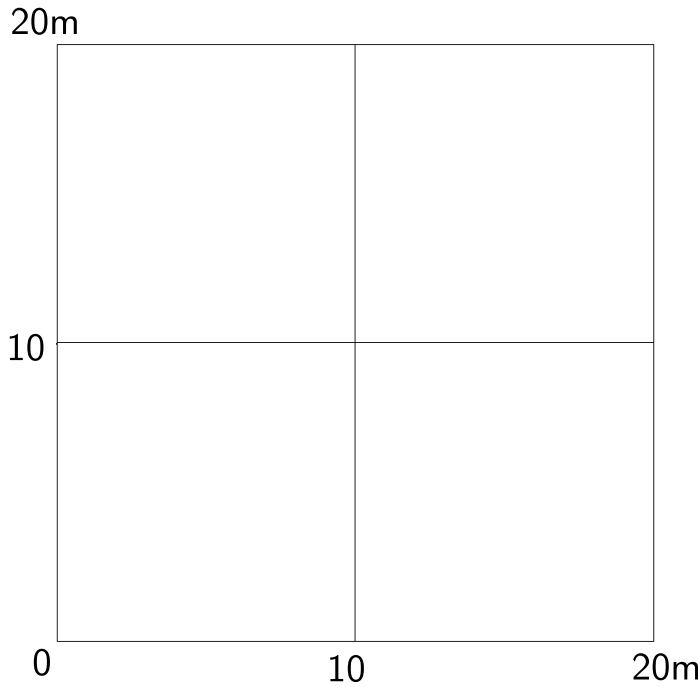


Figure 307.141: 27NodeBrick edge simply supported square plate with element side length 10m.

The results were listed in Table (307.39).

¹⁰Stephen Timoshenko, Theory of plates and shells (2nd edition). MrGRAW-Hill Inc, page202, 1959.

¹¹This model run out of memory on machine cml01 (memory: 23.5GB). This model has 233,289 nodes with 3 dofs, which may require 40GB memory.

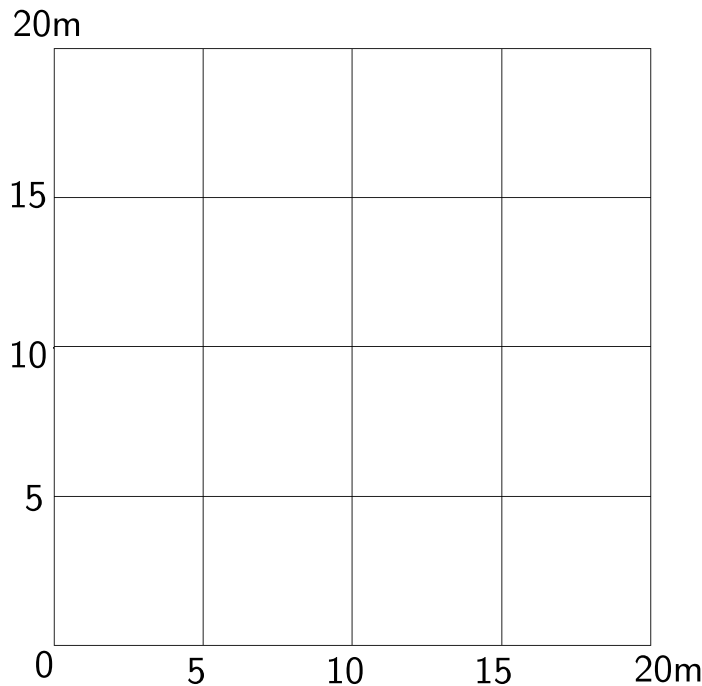


Figure 307.142: 27NodeBrick edge simply supported square plate with element side length 5m.

Table 307.39: Results for 27NodeBrick square plate with four edges simply supported.

Element type	27NodeBrick	27NodeBrick	Theoretical displacement
Number of layers	2layers	4layers	
Element side length	Height:0.50m	Height:0.25m	
10m	6.54E-003 m	6.54E-003 m	7.09E-03 m
5m	7.24E-003 m	7.24E-003 m	7.09E-03 m
2m	7.44E-003 m	7.44E-003 m	7.09E-03 m
1m	7.49E-003 m	7.49E-003 m	7.09E-03 m
0.5m	7.50E-003 m	7.50E-003 m	7.09E-03 m
0.25m	7.51E-003 m	- ¹¹	7.09E-03 m

The errors were listed in Table (307.40).

The errors were plotted in Figure (307.149).

The Real-ESSI model fei/DSL files for the table above are [HERE](#).

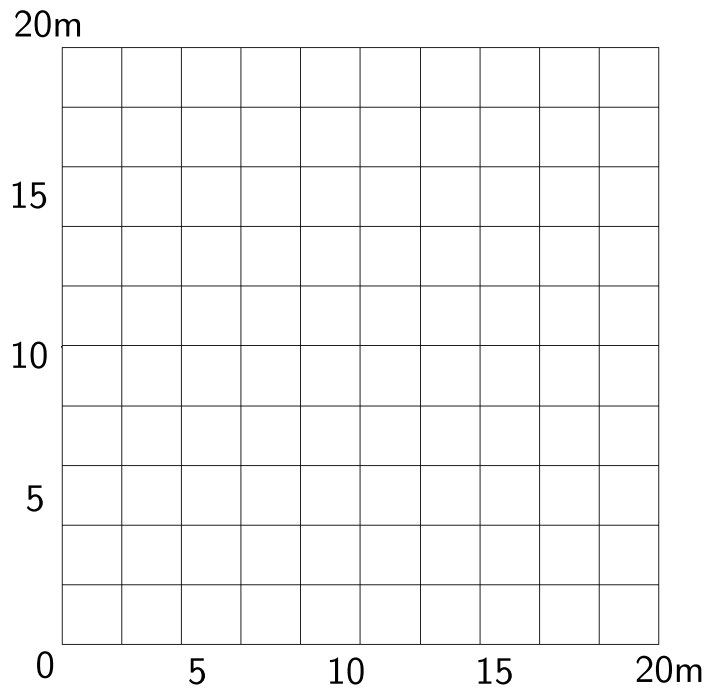


Figure 307.143: 27NodeBrick edge simply supported square plate with element side length 2m.

Table 307.40: Errors for 27NodeBrick square plate with four edges simply supported.

Element type	27NodeBrick	27NodeBrick
Number of layers	2layers	4layers
Element side length	Height:0.50m	Height:0.25m
10m	7.87%	7.85%
5m	2.07%	2.10%
2m	4.85%	4.89%
1m	5.54%	5.58%
0.5m	5.74%	5.79%
0.25m	5.80%	-

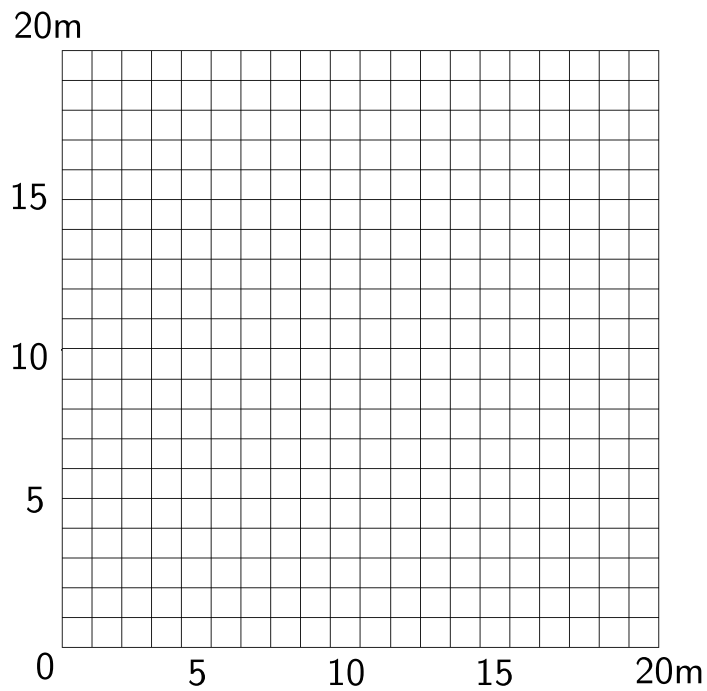


Figure 307.144: 27NodeBrick edge simply supported square plate with element side length 1m.

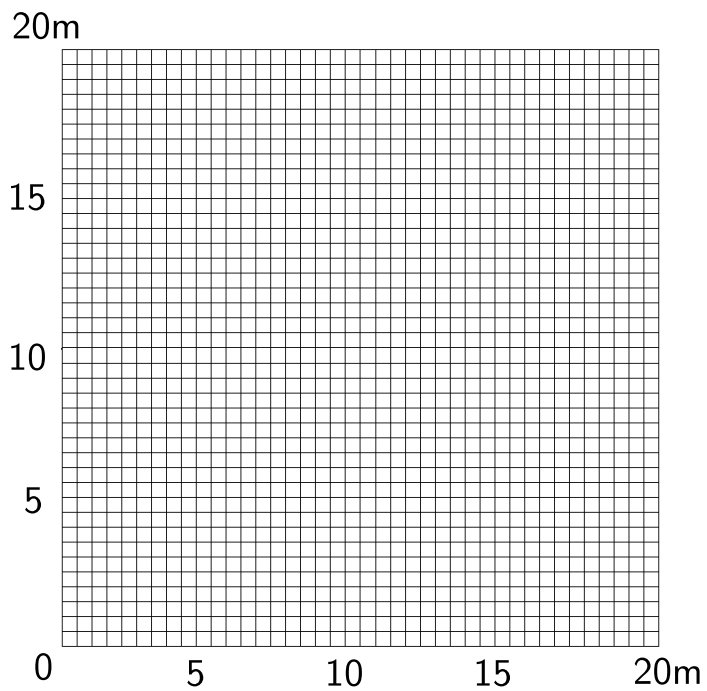


Figure 307.145: 27NodeBrick edge simply supported square plate with element side length 0.5m.

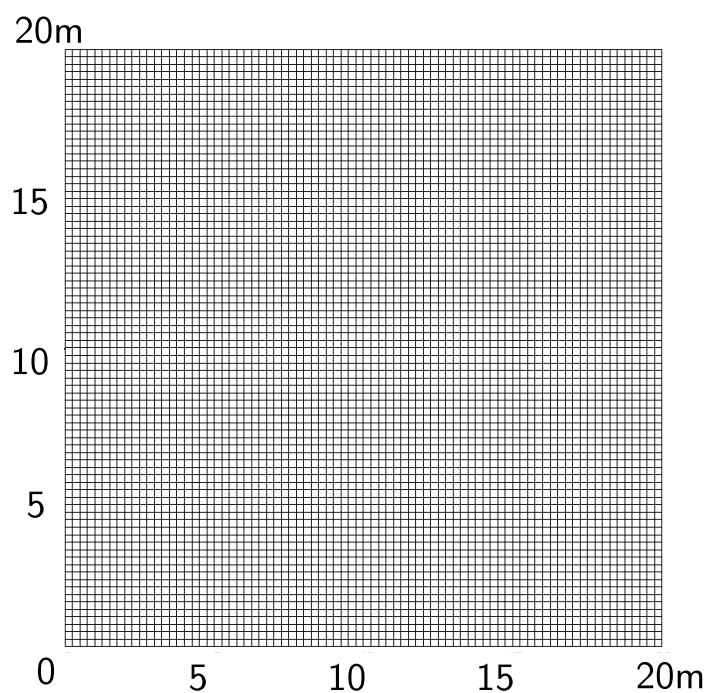


Figure 307.146: 27NodeBrick edge simply supported square plate with element side length 0.25m.

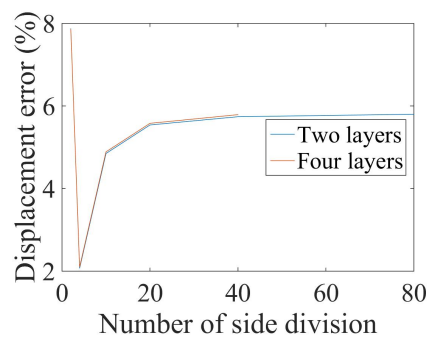


Figure 307.147: Error scale 0% - 8%.

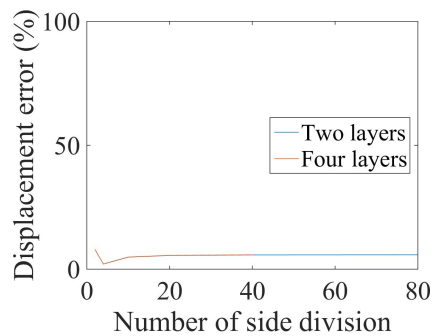


Figure 307.148: Error scale 0% - 100%.

Figure 307.149: 27NodeBrick square plate with edge simply supported' Displacement error versus Number of side division

307.2.20 Verification of 27NodeBrick circular plate with all edges clamped

Problem description: Diameter=20m, Height=1m, Force=100N, E=1E8Pa, $\nu = 0.3$.

The four edges are clamped.

The load is the uniform normal pressure on the whole plate.

The plate flexural rigidity is

$$D = \frac{Eh^3}{12(1-\nu^2)} = \frac{10^8 N/m^2 \times 1^3 m^3}{12 \times (1 - 0.3^2)} = 9.1575 \times 10^6 N \cdot m \quad (307.55)$$

The theoretical solution¹² is

$$d = \frac{qa^4}{64D} = \frac{100N/m^2 \times 10^4 m^4}{64 \times 9.1575 \times 10^6 N \cdot m} = 1.7106 \times 10^{-3} m \quad (307.56)$$

The 27NodeBrick were shown in Figure (307.150) - (307.155).

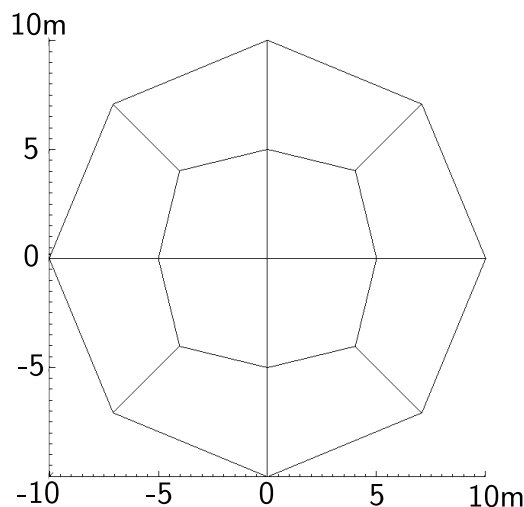


Figure 307.150: 27NodeBrick edge clamped circular plate with element side length 10m.

The results were listed in Table (307.41).

The errors were listed in Table (307.42).

The errors were shown in Figure (307.156).

The Real-ESSI model fei/DSL files for the table above are [HERE](#).

¹²Stephen Timoshenko, Theory of plates and shells (2nd edition). MrGRAW-Hill Inc, page55, 1959.

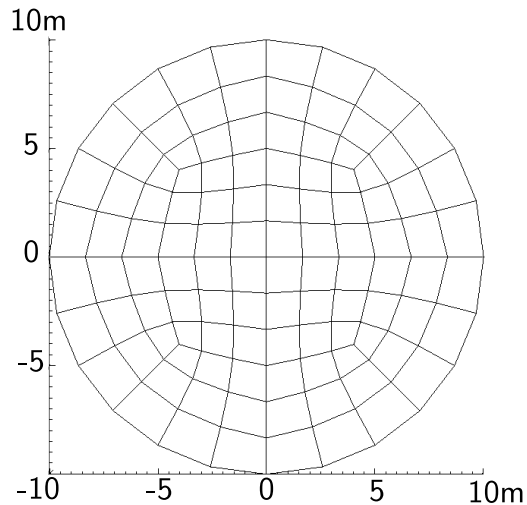


Figure 307.151: 27NodeBrick edge clamped circular plate with element side length 5m.

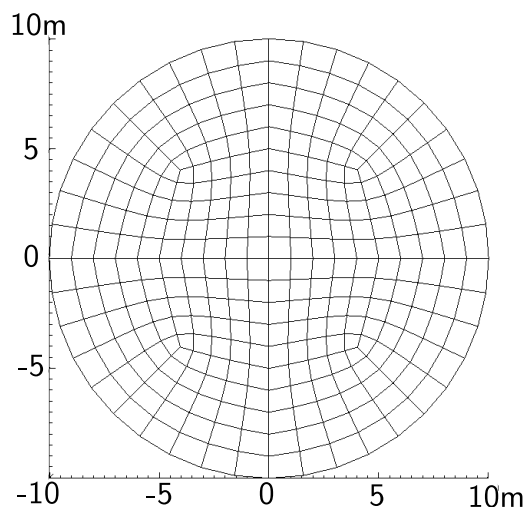


Figure 307.152: 27NodeBrick edge clamped circular plate with element side length 2m.

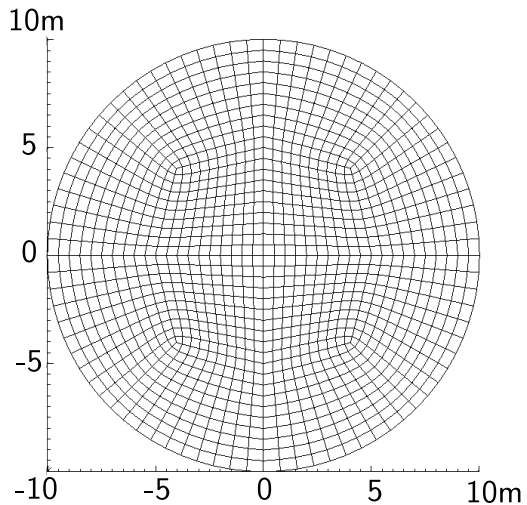


Figure 307.153: 27NodeBrick edge clamped circular plate with element side length 1m.

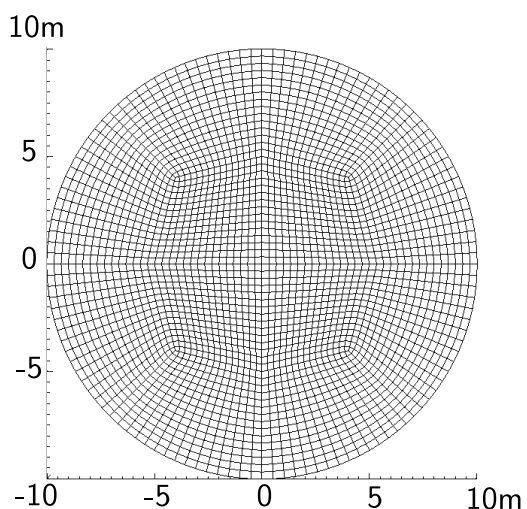


Figure 307.154: 27NodeBrick edge clamped circular plate with element side length 0.5m.

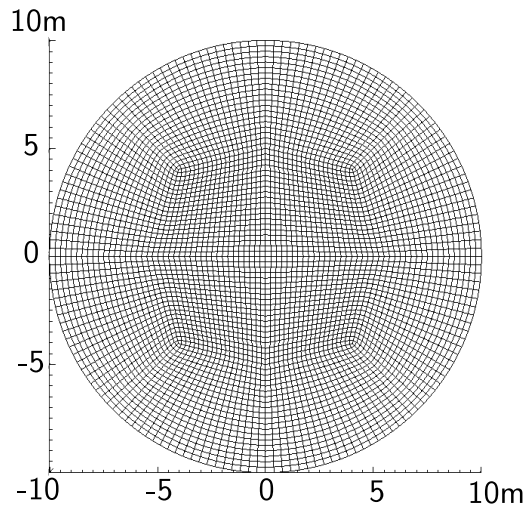


Figure 307.155: 27NodeBrick edge clamped circular plate with element side length 0.25m.

Table 307.41: Results for 27NodeBrick circular plate with four edges clamped.

Element type	27NodeBrick	27NodeBrick	27NodeBrick	Theoretical displacement
Number of layers	1layer	2layers	4layers	
Number of diameter divisions	Height:1.00m	Height:0.50m	Height:0.25m	
4	2.777E-03 m	2.788E-03 m	2.789E-03 m	1.706E-03 m
12	2.772E-03 m	2.786E-03 m	2.787E-03 m	1.706E-03 m
20	2.545E-03 m	2.556E-03 m	2.558E-03 m	1.706E-03 m
40	1.758E-03 m	1.768E-03 m	1.769E-03 m	1.706E-03 m
60	1.762E-03 m	1.772E-03 m	1.773E-03 m	1.706E-03 m
80	1.763E-03 m	1.773E-03 m	1.774E-03 m	1.706E-03 m

Table 307.42: Errors for 27NodeBrick circular plate with four edges clamped.

Element type	27NodeBrick	27NodeBrick	27NodeBrick
Number of layers	1layer	2layers	4layers
Number of diameter divisions	Height:1.00m	Height:0.50m	Height:0.25m
4	62.75%	63.42%	63.47%
12	62.46%	63.27%	63.34%
20	49.14%	49.82%	49.91%
40	3.03%	3.62%	3.68%
60	3.25%	3.83%	3.91%
80	3.32%	3.91%	3.99%

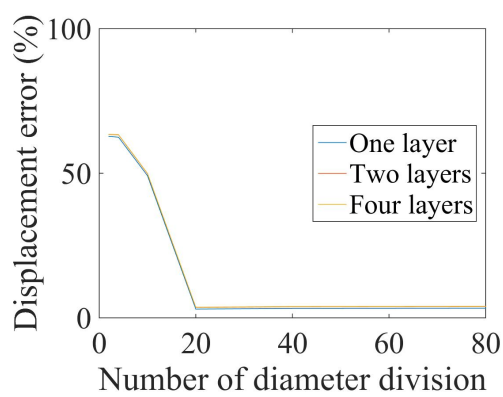


Figure 307.156: 27NodeBrick circular plate with edge clamped' Displacement error versus Number of side division

307.2.21 Verification of 27NodeBrick circular plate with all edges simply supported

Problem description: Diameter=20m, Height=1m, Force=100N, E=1E8Pa, $\nu = 0.3$.

The four edges are simply supported.

The load is the uniform normal pressure on the whole plate.

The plate flexural rigidity is

$$D = \frac{Eh^3}{12(1-\nu^2)} = \frac{10^8 N/m^2 \times 1^3 m^3}{12 \times (1 - 0.3^2)} = 9.1575 \times 10^6 N \cdot m \quad (307.57)$$

The theoretical solution¹³ is

$$d = \frac{(5 + \nu)qa^4}{64(1 + \nu)D} = \frac{(5 + 0.3) \times 100N/m^2 \times 10^4 m^4}{64 \times (1 + 0.3) \times 9.1575 \times 10^6 N \cdot m} = 6.956 \times 10^{-3} m \quad (307.58)$$

The 27NodeBrick were shown in Figure (307.157) - (307.162).

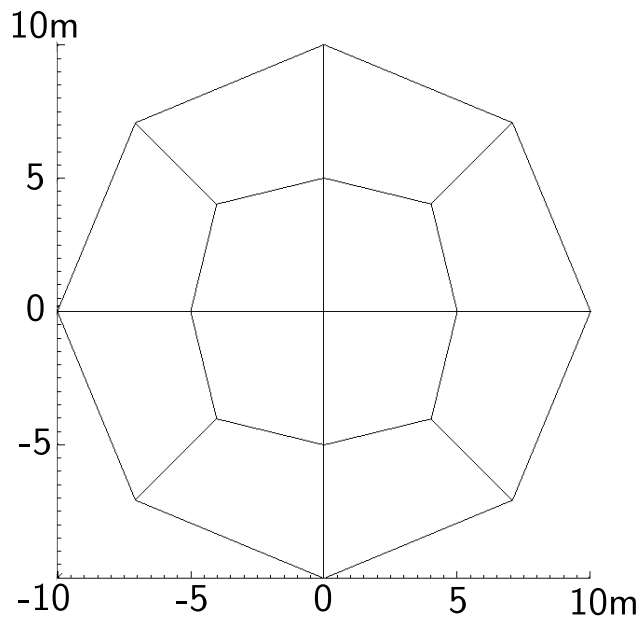


Figure 307.157: 27NodeBrick edge simply supported circular plate with element side length 10m.

The results were listed in Table (307.43).

The errors were listed in Table (307.44).

The errors were plotted in Figure (307.165).

The Real-ESSI model fei/DSL files for the table above are [HERE](#).

¹³Stephen Timoshenko, Theory of plates and shells (2nd edition). MrGRAW-Hill Inc, page55, 1959.

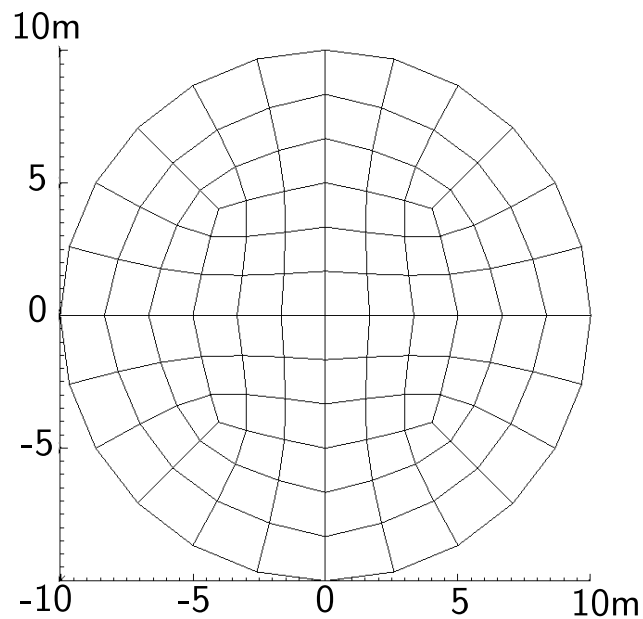


Figure 307.158: 27NodeBrick edge simply supported circular plate with element side length 5m.

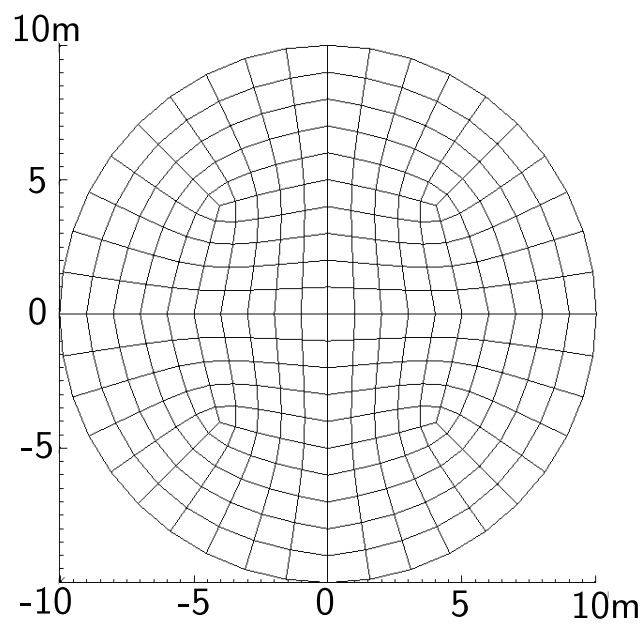


Figure 307.159: 27NodeBrick edge simply supported circular plate with element side length 2m.

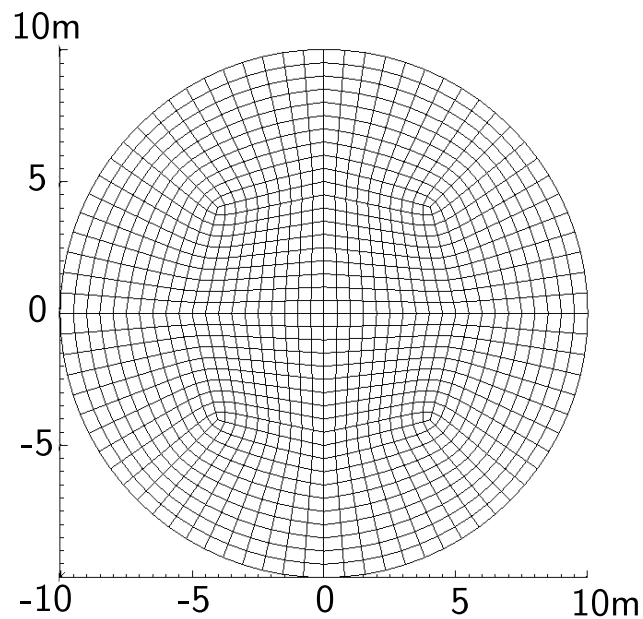


Figure 307.160: 27NodeBrick edge simply supported circular plate with element side length 1m.

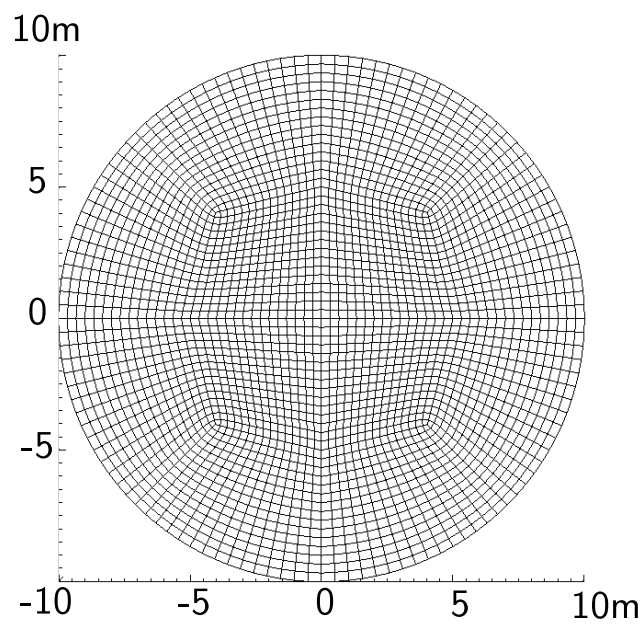


Figure 307.161: 27NodeBrick edge simply supported circular plate with element side length 0.5m.

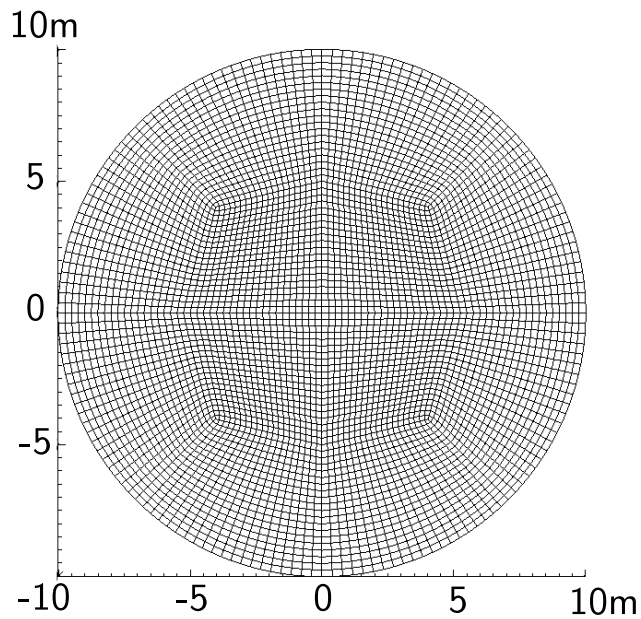


Figure 307.162: 27NodeBrick edge simply supported circular plate with element side length 0.25m.

Table 307.43: Results for 27NodeBrick circular plate with four edges simply supported.

Element type	27NodeBrick	27NodeBrick	Theoretical displacement
Number of layers	2layers	4layers	
Number of diameter divisions	Height:0.50m	Height:0.25m	
4	7.259E-03 m	7.261E-03 m	6.956E-03 m
12	7.083E-03 m	7.084E-03 m	6.956E-03 m
20	7.064E-03 m	7.065E-03 m	6.956E-03 m
40	7.018E-03 m	7.019E-03 m	6.956E-03 m
60	7.029E-03 m	7.030E-03 m	6.956E-03 m
80	7.032E-03 m	7.034E-03 m	6.956E-03 m

Table 307.44: Errors for 27NodeBrick circular plate with four edges simply supported.

Element type	27NodeBrick	27NodeBrick
Number of layers	2layers	4layers
Number of diameter divisions	Height:0.50m	Height:0.25m
4	4.36%	4.38%
12	1.82%	1.83%
20	1.56%	1.57%
40	0.88%	0.90%
60	1.04%	1.06%
80	1.09%	1.11%

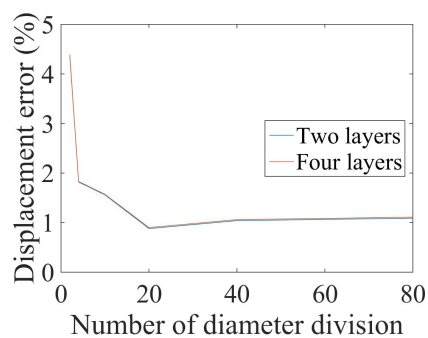


Figure 307.163: Error scale 0% - 5%.

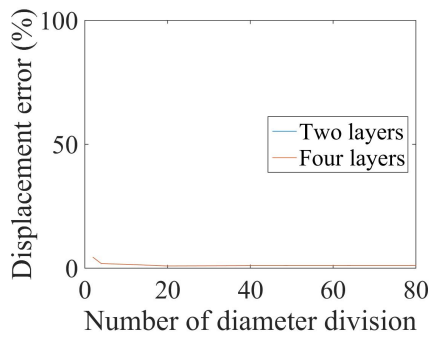


Figure 307.164: Error scale 0% - 100%.

Figure 307.165: 27NodeBrick circular plate with edge simply supported Displacement error versus Number of side division.

307.2.22 Verification of 27NodeBrick Finite Element for Boussinesq Problem

307.2.22.1 Introduction

The Boussinesq problem is finding the displacement distribution in the isotropic linearly elastic half-space, subject to a concentrated load applied on the surface and perpendicular to it. The Boussinesq problem diagram is shown in Fig.(307.166).

Boussinesq problem is widely used in geotechnical engineering, especially when designing a foundation which transfers the superstructure load to the soil. To estimate the foundation settlements, it is important to have a reliable numerical solution for the Boussinesq problem.

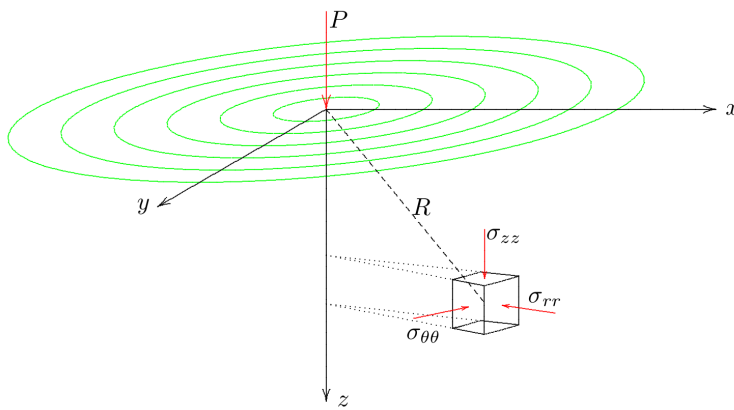


Figure 307.166: Boussinesq problem description (Figure Reference: Verruijt, Arnold, and Stefan Van Baars. Soil mechanics. Delft, 2007.)

In 1885, the French scientist Joseph Boussinesq solved the analytic solutions of displacements in the homogeneous isotropic linear elastic half space. In general, the vertical displacement of the surface is

$$z = 0 : \quad u_z = \frac{P(1 - \nu^2)}{\pi E R} \quad (307.59)$$

where P is the vertical load, ν is the Poisson's ratio, E is the elastic modulus, and R is the distance from the measured point to the loading point.

In this section, the Real-ESSI numerical solution is verified by the analytic solution for the Boussinesq problem.

307.2.22.2 Description of the Verification Model

Since the problem is cylindrical symmetry, a quarter of the entire cube was employed to represent the whole cube. The reduced model was shown in Fig.(307.167).

The side length is 20 meters and the load P is 1N. The elastic modulus $E = 1 \times 10^3 Pa$ and the Poisson's ratio $\nu = 0.0$.

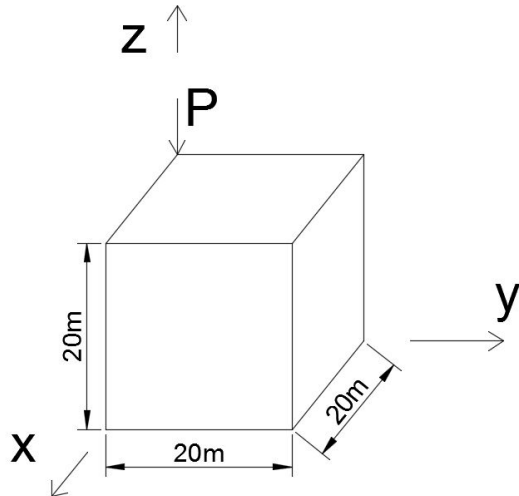


Figure 307.167: Reduced model (One quarter model) for the point load on the half space

The boundary conditions are shown in Fig.(307.168) and (307.169).

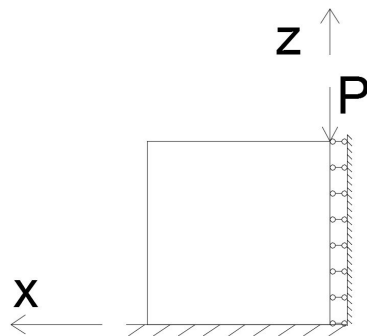


Figure 307.168: X-Z view for the reduced model

307.2.22.3 Results

Analytic solution for this model

According to the previous introduction, the analytic solution on the surface for this problem is

$$z = 0 : \quad u_z = \frac{P(1 - \nu^2)}{\pi E R} = \frac{1}{10^3 \pi} \frac{1}{R} \quad (307.60)$$

On the face $x = 0$, the distance R on the surface is actually the value of y , therefore, the analytic

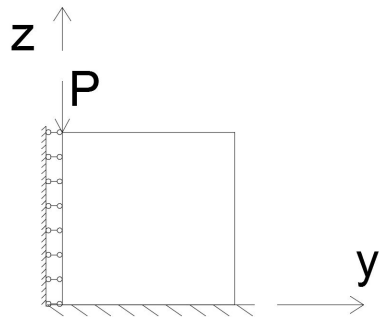


Figure 307.169: Y-Z view for the reduced model

solution is

$$u_z = \frac{1}{10^3 \pi R} = \frac{1}{10^3} \frac{1}{y} \quad (307.61)$$

As long as the y values are substituted, the displacement u_z is obtained immediately.

Real-ESSI solution with 27NodeBrickLT

In Real-ESSI, 27NodeBrickLT elements were used to simulate this model. Each element is $2m \times 2m \times 2m$. Since the model is $20m \times 20m \times 20m$, the element number is $10 \times 10 \times 10 = 1000$. The vertical displacement at the surface was recorded.

Since the model is symmetric, when the results were plotted, the other half results were achieved by symmetry.

Comparison between the analytic and 27NodeBrickLT solution

The Real-ESSI and analytic results were plotted in Fig.(307.170). Note that the analytic solution for location $y = 0$ is infinity, which was not plotted in the figure below.

307.2.22.4 Error Analysis

1. Mismatch at the loading point.

First of all, when $x = 0$ at the loading point, the analytic solution is infinite. From the perspective of practical engineering, this analytic solution is flawed because the displacement cannot be infinite. The infinite solution is due to the elastic assumption. In consideration of the plasticity, the analytic solution will not be infinite.

In Real-ESSI, the displacement at the loading point is not infinite because the infinite value is averaged by the integration during the finite element calculation. Also, at the loading point,

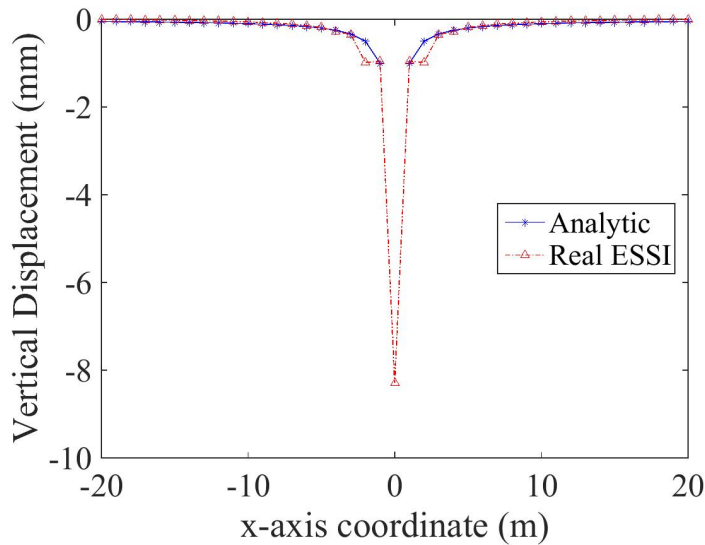


Figure 307.170: Comparison between analytic solution and Real-ESSI 27NodeBrickLT solution

27NodeBrickLT has a much larger displacement than that of 8NodeBrickLT. This is because 27NodeBrickLT has a relatively denser mesh than 8NodeBrickLT. So the maximum value at the loading point is higher than that of 8NodeBrickLT.

2. Mismatch at other locations.

Except at the loading point, the analytic solution is not exactly equal to the numerical solution at other locations. This is because the verification example employs a simplified bounded cube to represent unbounded half space. The original analytic solution is for the half space, which is not true for the verification model. Not only the horizontal space but also the bottom space are removed from the model. This means the analytic solution is not perfect for this bounded cube. However, since the cube is very great, the analytic solution is similar to the Real-ESSI numerical solution. In addition, the brick elements are also verified by other models, like beam, plate and shells.

307.3 Verification of Dynamic, Single Phase Solid Modeling and Simulation

Chapter 308

Verification and Validation for Static and Dynamic Behavior of Structural Elements

(1986-2011-2015-2017-2019-2021-)

(In collaboration with Prof. José Abell, Dr. Yuan Feng, and Prof. Han Yang)

308.1 Chapter Summary and Highlights

308.2 Verification of Static, Beam-Column Finite Element Modeling and Simulation

308.3 Bernoulli Beam Elements with 12DOFs and 9DOFs

Figures 308.1 and 308.2

308.3.1 FEM Model



Figure 308.1: Finite element model for static analysis



Figure 308.2: Finite element model for dynamic analysis

308.3.2 Static Analysis

Figures 308.3

$$E = 5 \text{ Pa}$$

$$I = 16 \text{ m}^4$$

$$L = 2 \text{ m}$$

$$P = 1 \text{ N}$$

$$\Delta = \frac{PL^3}{3EI} = 0.033 \text{ m}$$

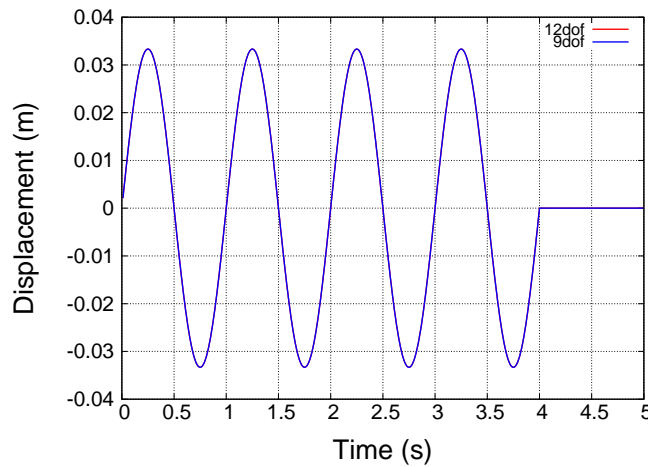


Figure 308.3: Comparison of static displacements (pseudo time) of the top nodes, Force time history applied to the top node

308.3.3 Dynamic Analysis

Figures 308.4 and 308.5

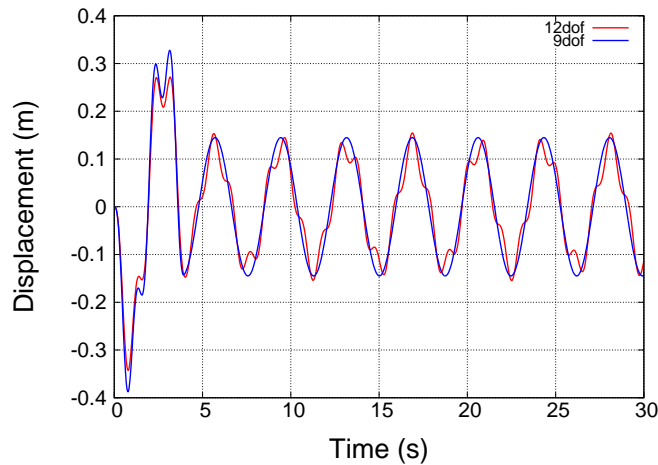


Figure 308.4: Comparison of displacement time histories of the top nodes, Displacement time history applied to the node with 6DOF, mass comes from beam density

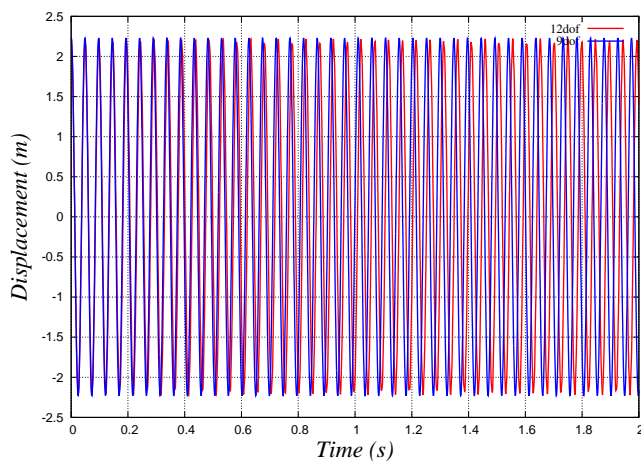


Figure 308.5: Comparison of free vibration displacement time histories of the top nodes, mass comes from beam density

308.3.4 Bernoulli Beam, Comparison of Eigen Frequencies

Table 308.1

Table 308.1: Comparison of eigen frequencies between models of using 9DOF beam and 12DOF beam

Mode	9DOF	12DOF
1	0.264559	0.264236
2	0.268474	0.268064
3	0.308202	0.308202

308.4 Timoshenko Beam

Models used:

- Model with 27-node-brick model is used as the benchmark. The model is $10\text{m} \times 10\text{m} \times 60\text{m}$, each element is $2\text{m} \times 2\text{m} \times 2\text{m}$, so there are $5 \times 5 \times 30 = 750$ elements in total.
- Model with 5 Timoshenko beams are used to test the performance of the Timoshenko element. Material properties and cross-section properties are kept the same as those of the brick model. Various values of the shear correction factor are tested.
- Model with 5 Bernoulli beam elements is also tested.
- For both beam models, consistent mass is used.

Input files for all the models shown are available [HERE](#).

Figures of models are shown below:

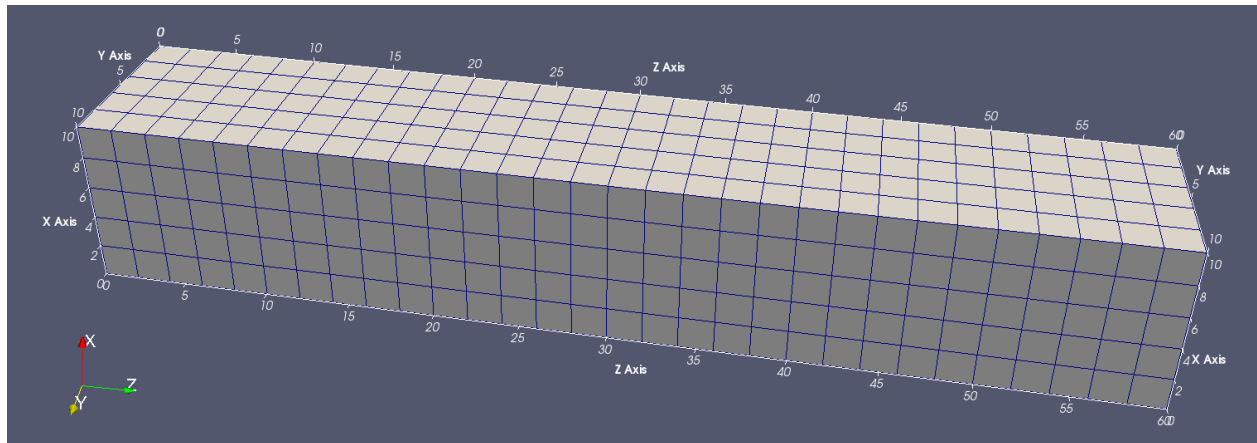


Figure 308.6: Cantilever model made of 27-node-brick elements.

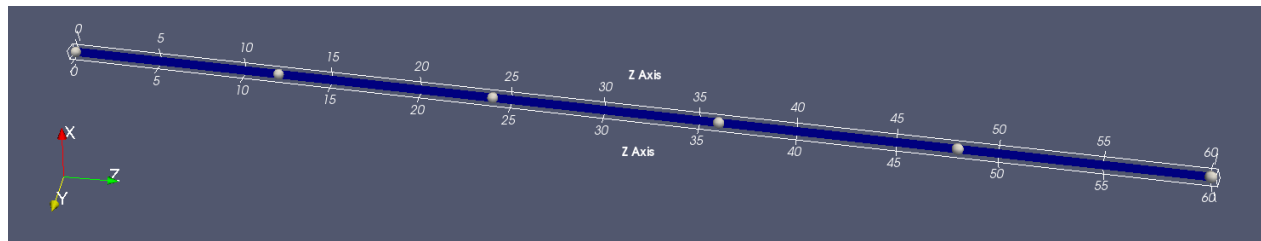


Figure 308.7: Cantilever model made of multiple Timoshenko or Bernoulli elements.

Eigenanalysis results are shown in the following table and figures.

Table 308.2: Comparison of eigenfrequencies for 27-node-brick, Timoshenko beam with different shear correction factors, and Bernoulli beam models.

Eigenmode		Eigenfrequency (Hz)				
		27-Node-Brick	Timoshenko (shear factor=1)	Timoshenko (shear factor=2)	Timoshenko (shear factor=100)	Bernoulli
Bending (1st)	1	1.63364	1.63375	1.64358	1.65336	1.65356
	2	1.63364	1.63375	1.64358	1.65336	1.65356
Bending (2nd)	3	9.23543	9.36137	9.6899	10.0443	10.0519
	4	9.23543	9.36137	9.6899	10.0443	10.0519
Torsion (1st)	5	9.30771	10.1473	10.1473	10.1473	10.1473
Axial (1st)	6	15.4575	15.5002	15.5002	15.5002	15.5002
Bending (3rd)	7	22.8703	23.7943	25.246	26.9177	26.9542
	8	22.8703	23.7943	25.246	26.9177	26.9542
Torsion (2nd)	9	27.9199	31.4476	31.4476	31.4476	31.4476

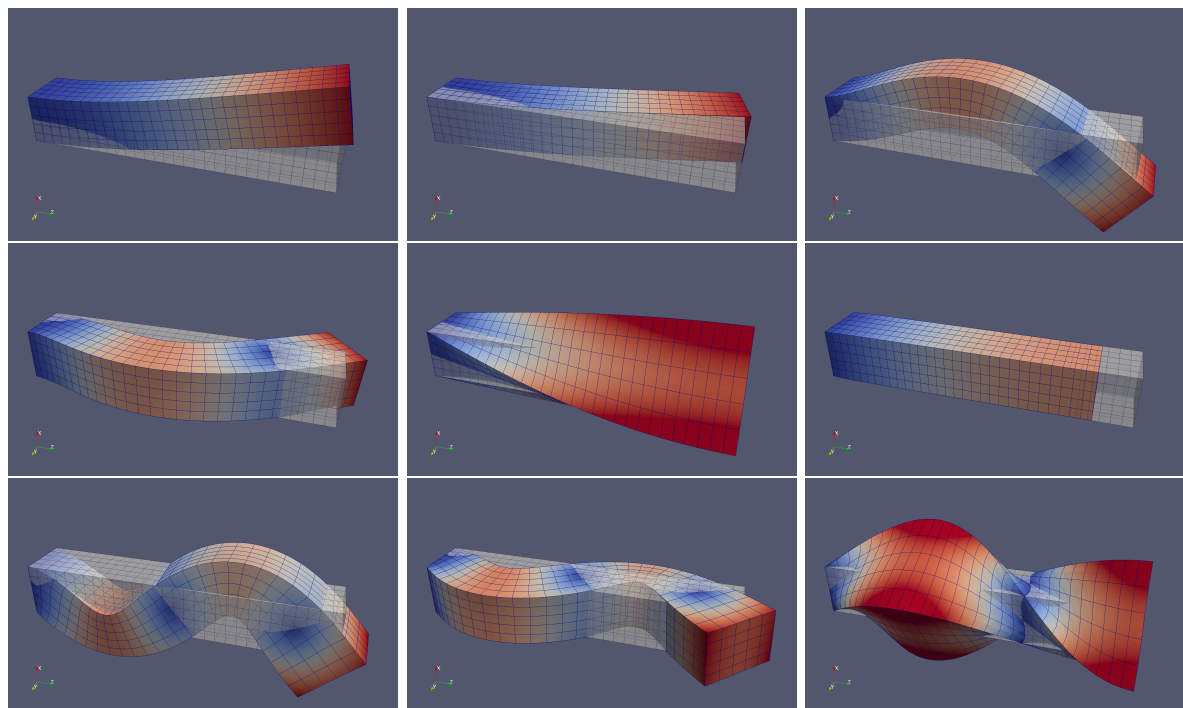


Figure 308.8: First 9 eigenmodes of the cantilever model made of 27-node-brick elements.

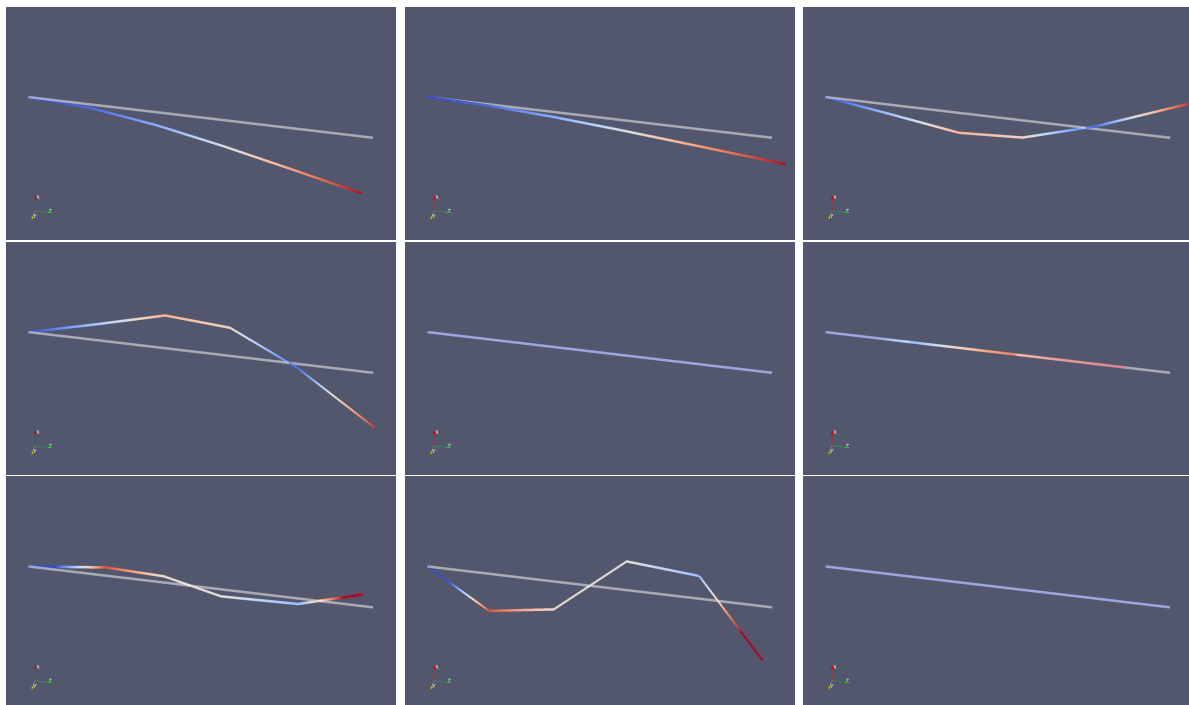


Figure 308.9: First 9 eigenmodes of the cantilever model made of Timoshenko beam elements.

308.5 Verification of Shell (Felippa-ANDES) Finite Element Modeling and Simulation

The verification and validation of the behavior of the ANDES (Assumed Natural Deviatoric Strain) shell finite element implemented in essi is described in this section. The verification is split up into several cases intended to test different aspects of the implementation. The tests are based on well-known closed form solutions to elasticity problems which can be modelled using shells. Further, the verification is divided into static and dynamic tests.

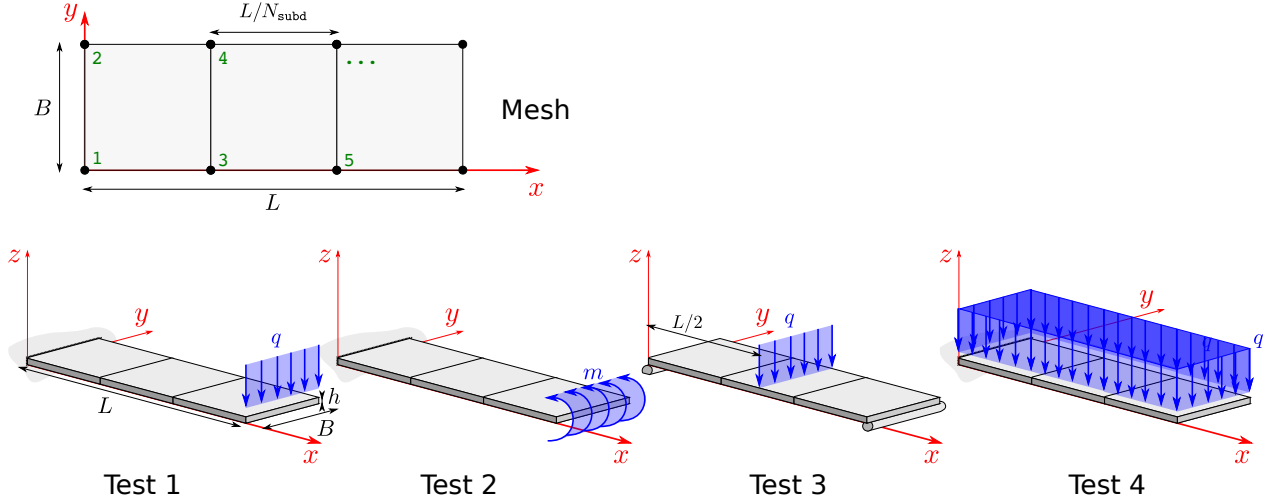
308.5.1 Static Tests

The purpose of the static tests is to verify that the stiffness matrices generated by the 4 Node ANDES Shell are useful to approximate well known cases of solutions to beam theory.

Tests are done to verify the bending component and the membrane component independently, because the behaviour of both is assumed de-coupled in this linear implementation.

308.5.1.1 Bending Component Verification

These tests compare the bending performance of a simple mesh of ANDES shells for the case of simple (Bernoulli) beam examples.



Test 1: Concentrated transversal tip load

The test file for this case can be found in
 (ESSI SOURCE FOLDER)/Verification_Examples/...
 .../Static_and_Dynamic_Behavior_of_Structural_Elements/...
 .../Shell_ANDES/static/Test_shell_andes_1_bending_transverse.fei

For a prismatic beam made of a homogeneous elastic isotropic material of modulus of elasticity E , cross section I and length L we have that, under Bernoulli-Euler theory, the displacement at the tip due to a concentrated load P is

$$\delta_{\text{tip}} = \frac{PL^3}{3EI}$$

and for this test case's geometry

$$\delta_{\text{tip}} = \frac{qBL^3}{3EBh^3/12} = \frac{4qL^3}{Eh^3}$$

With the purpose of measuring the errors as percent agreement with the theoretical results, the load q is computed such that the tip displacement is 100 units. Thus, in terms of the geometry of the problem.

$$q = 100 \times \frac{Eh^3}{4L^3}$$

This force is translated into nodal equivalent forces by applying half the total load qB to each tip node in the vertical direction and fixing the x direction rotational degrees of freedom for the tip nodes.

The parameters chosen for this case are

```

1 h = 1*m; // Shell thickness
2 Eshell = 1*N/m^2; // Elastic modulus
3 nu = 0.0; // Poisson's ratio
4 L = 1*m; // Beam length
5 B = 0.2*m; // Beam width
6 rho = 0*kg/m^3; // Mass density

```

For different number of subdivisions, here are the results of the tip displacement.

N_{subd}	u_z	N_{subd}	u_z	N_{subd}	u_z
2	96.2118	42	100.009	83	100.002
7	100.096	48	100.007	89	100.002
13	100.068	54	100.006	95	100.002
19	100.039	60	100.005	101	100.002
25	100.024	66	100.004	107	100.001
31	100.016	72	100.003	112	100.001
37	100.012	77	100.003		

The element displays sensitivity to the aspect ratio of its sides. Indeed, choosing a different set of parameters

```

1 h = 1*m; // Shell thickness
2 Eshell = 1*N/m^2; // Elastic modulus
3 nu = 0.0; // Poisson's ratio
4 L = 1*m; // Beam length
5 B = 0.2*m; // Beam width
6 rho = 0*kg/m^3; // Mass density

```

yields slightly different results

N_{subd}	u_z	N_{subd}	u_z	N_{subd}	u_z
2	93.7897	42	99.9958	83	100.001
7	99.5267	48	99.998	89	100.001
13	99.8587	54	99.9993	95	100.001
19	99.9409	60	100.	101	100.001
25	99.9713	66	100.001	107	100.001
31	99.985	72	100.001	112	100.001
37	99.992	77	100.001		

Test 2: Concentrated tip moment

The test file for this case can be found in

(ESSI SOURCE FOLDER)/Verification_Examples/...

.../Static_and_Dynamic_Behavior_of_Structural_Elements/...

.../Shell_ANDES/static/Test_shell_andes_2_bending_transverse.fei

Analogous to the previous test, for a cantilever beam with a tip moment the tip rotation is

$$\theta_{\text{tip}} = \frac{ML}{EI}$$

and for this test case's geometry

$$\theta_{\text{tip}} = \frac{mBL}{EBh^3/12} = \frac{12mL}{Eh^3}$$

In this case, the parameters are selected such that this tip rotation is of 100 units. Execution of the test case shows that with $N_{\text{subd}} = 2$ the theoretical value is met with 100% accuracy. This is because the moment field is constant inside the beam and the elements are capable of reproducing this field with accuracy.

Test 3: Concentrated mid-span transversal load

This case is similar to test case 1. The accuracy for 2 elements is 96.2% agreement with the theoretical solution. For $N_{\text{subd}} = 4$ (4 elements total) the accuracy climbs to 99.7%. The test file for this case can be found in

```
(ESSI SOURCE FOLDER)/Verification_Examples/...
.../Static_and_Dynamic_Behavior_of_Structural_Elements/...
.../Shell_ANDES/static/Test_shell_andes_3_bending_transverse.fei
```

Test 4: Transversal distributed load

The distributed load is generated by accelerating the beam transversally with an acceleration which produces a 100 (unit) displacement. This provides an indirect test to the mass matrix which will be further tested in dynamic tests. The uniformly distributed load q which produces the δ_{tip} unit displacement and the corresponding tip rotation are

$$q = 8 \frac{EI}{L^4} \delta_{\text{tip}} \quad \text{and} \quad \theta_{y\text{tip}} = \frac{4}{3L} \delta_{\text{tip}}$$

from this value, the required acceleration is computed as

$$a = \frac{q}{\rho BH}$$

where ρ is the unit-weight of the material used to compute the mass matrix.

For two subdivisions (6 nodes) the results of the two nodes located at the tip of the beam are

```
1 Node : 5
2 ux = 0.000000, rx = 30.550500
3 uy = 0.000000, ry = -133.333000
4 uz = 102.541000, rz = 0.000000
5 Node : 6
6 ux = 0.000000, rx = -30.550500
7 uy = 0.000000, ry = -133.333000
8 uz = 102.541000, rz = 0.000000
```

First, a 2.5% accuracy is reached in the tip displacement. Second, it is noteworthy to mention that the current formulation of the mass matrix will produce rotations around the x axis for the nodes. One reason for this is that the chosen mass matrix is not consistent with the stiffness matrix instead, it is borrowed from a similar element ^{1 2 3}. The reason behind this decision is the fact that the very accurate ANDES stiffness formulation lacks a displacement interpolation scheme which is necessary to produce

¹The First ANDES Elements: 9-DOF Plate Bending Triangles Carmello Militello & Carlos A. Felippa December 1989 Report No. CU-CSSC-89-22

²Chapter 32 of Felippa's Lecture Notes Finite element templates for bending

³C. A. Felippa and P. G. Bergan, A triangular plate bending element based on an energy-orthogonal free formulation, Comp. Meth. Appl. Mech. Engrg., 61, 129{160, 1987.

a consistent mass matrix. Furthermore, restraining these x roation degrees of freedom does not lead to an improved solution.

For 4 subdivisions, the results at the tip are:

```

1 Node : 9
2 ux = 0.000000, rx = 31.671000
3 uy = 0.000000, ry = -133.333000
4 uz = 100.891000, rz = 0.000000
5 Node : 10
6 ux = 0.000000, rx = -31.671000
7 uy = 0.000000, ry = -133.333000
8 uz = 100.891000, rz = 0.000000

```

and for 20.

```

1 Node : 41
2 ux = 0.000000, rx = 32.095800
3 uy = 0.000000, ry = -133.333000
4 uz = 100.039000, rz = 0.000000
5 Node : 42
6 ux = 0.000000, rx = -32.095800
7 uy = 0.000000, ry = -133.333000
8 uz = 100.039000, rz = 0.000000

```

and back to 2 subdivisions but this time with an aspect ratio $L/B = 2$, by changing B so that the expected tip displacement remains the same, we get

```

1 Node : 5
2 ux = 0.000000, rx = 3.890200
3 uy = 0.000000, ry = -133.333000
4 uz = 99.810100, rz = 0.000000
5 Node : 6
6 ux = 0.000000, rx = -3.890200
7 uy = 0.000000, ry = -133.333000
8 uz = 99.810100, rz = 0.000000

```

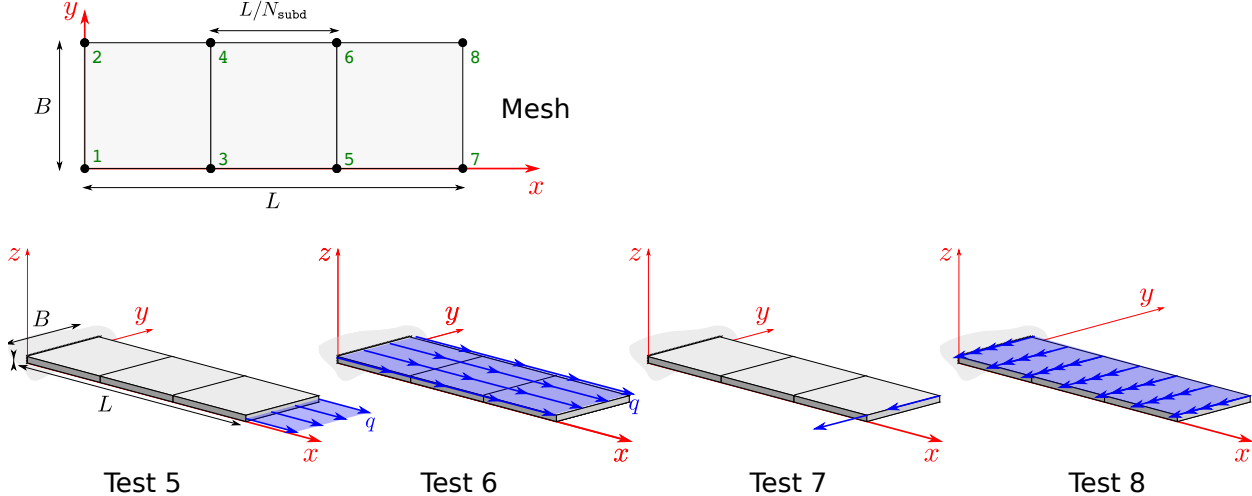
which shows that the effect of the inconsistent mass matrix is ameliorated for elements with a better aspect ratio. The elements in this case are square in shape since $L/B = 2$ and $N_{\text{subd}} = 2$.

In conclusion increasing accuracy for bending problems not only involves making the elements smaller but also improving their aspect ratio. This is especially critical in dynamic problems (or self weight problems). The test file for this case can be found in

```
(ESSI SOURCE FOLDER)/Verification_Examples/...
.../Static_and_Dynamic_Behavior_of_Structural_Elements/...
.../Shell_ANDES/static/Test_shell_andes_4_bending_transverse.fei
```

308.5.1.2 Membrane Component Verification

These tests compare the performance of the membrane component of the ANDES Shell by modelling simple beams and comparing the approximation with Bernoulli-beam theoretical results.



Test 5: Longitudinal tip load

The parameters used to test this case are,

```

1 h = 0.2*m; // Shell thickness
2 Eshell = 1*N/m^2; // Elastic modulus
3 nu = 0.0; // Poisson's ratio
4 L = 30*m; // Beam length
5 B = 3*m; // Beam width
6 rho = 0.0*kg/m^3; // Mass density
7 delta_tip = 100*m; // Target tip displacement
8
9 Nsubd = 2; // Number of side subdivisions

```

the tip load was computed to give $\delta_{tip} = 100$ from

$$F_{tip} = \frac{AE}{L} \delta_{tip}$$

Additionally, the tip rotation degrees of freedom about z axis (rz) were fixed to enforce the uniform loading condition. The results for 2 subdivisions observed at the two tip nodes is

```

1 Node : 5
2 ux = 100.000000, rx = 0.000000
3 uy = -0.000000, ry = 0.000000
4 uz = 0.000000, rz = 0.000000
5 Node : 6
6 ux = 100.000000, rx = 0.000000
7 uy = -0.000000, ry = 0.000000
8 uz = 0.000000, rz = 0.000000

```

The test file for this case can be found in (ESSI SOURCE FOLDER)/Verification_Examples/...
 .../Static_and_Dynamic_Behavior_of_Structural_Elements/...
 .../Shell_ANDES/static/Test_shell_andes_5_membrane_axial.fei

Test 6: Longitudinal self-weight load

As in test 4, the distributed load for this test was generated by using an acceleration field with a magnitude such that it generates 100 units of displacement in DOF ux . The required body force q (per unit length) is derived from linear elasticity to be

$$q = \frac{2EA}{L^2} \delta_{tip}$$

from which the acceleration is found to be given by $a = \frac{q}{\rho BH}$. The tip nodes were fixed to move only in the x direction. The model parameters used for this test are,

```

1 h = 1*m; // Shell thickness
2 Eshell = 1*N/m^2; // Elastic modulus
3 nu = 0.0; // Poisson's ratio
4 L = 1*m; // Beam length
5 B = 1*m; // Beam width
6 rho = 100*kg/m^3; // Mass density
7 delta_tip = 100*m; // Target tip displacement
8
9 Nsubd = 2; // Number of side subdivisions

```

and the tip displacements

```

1 Node : 5
2 ux = 100.000000, rx = 0.000000
3 uy = 0.000000, ry = 0.000000
4 uz = 0.000000, rz = 0.000000
5 Node : 6
6 ux = 100.000000, rx = 0.000000
7 uy = 0.000000, ry = 0.000000
8 uz = 0.000000, rz = 0.000000

```

Which means that in the quadratic displacement field coming from a uniform external load can be captured exactly by this element.

The test file for this case can be found in (ESSI SOURCE FOLDER)/Verification_Examples/...
 .../Static_and_Dynamic_Behavior_of_Structural_Elements/...
 .../Shell_ANDES/static/Test_shell_andes_6_membrane_axial.fei

Test 7: Transversal tip load This test is identical to test 1, except the beam mesh is placed sideways so that the membrane component is used instead of the bending one. Since the membrane part can capture deformation due to shear, the ratio L/B is set to 10 so that this does not affect the results.

```

1 h = 0.2*m; // Shell thickness
2 Eshell = 1*N/m^2; // Elastic modulus
3 nu = 0.0; // Poisson's ratio
4 L = 10*m; // Beam length
5 B = 1.0*m; // Beam height
6 rho = 0*kg/m^3; // Mass density
7 d_tip = 100*m; // Target tip displacement
8
9 Nsubd = 10; // Number of side subdivisions

```

Results at the tip show less than 1% error with theoretical results when shear component is made small.

```

1 Node : 21
2 ux = -7.513920, rx = 0.000000
3 uy = -100.650000, ry = 0.000000
4 uz = 0.000000, rz = -15.072400
5 Node : 22
6 ux = 7.513920, rx = 0.000000
7 uy = -100.650000, ry = 0.000000
8 uz = 0.000000, rz = -15.072400

```

It would be interesting to test this component vs. a beam theory which incorporates deformation due to shear such as Timoshenko beams.

The test file for this case can be found in (ESSI SOURCE FOLDER)/Verification_Examples/...
.../Static_and_Dynamic_Behavior_of_Structural_Elements/...
.../Shell_ANDES/static/Test_shell_andes_7_membrane_transverse.fei

Test 8: Transversal self-weight load This test is analogous to test 4, except the membrane component is being tested instead of the bending. Again, the L/B ratio is kept at 10 to avoid shear deformation creeping into the results perceptively.

```

1 h = 1*m; // Shell thickness
2 Eshell = 1*N/m^2; // Elastic modulus
3 nu = 0.0; // Poisson's ratio
4 L = 10*m; // Beam length
5 B = 0.5*m; // Beam width
6 rho = 100*kg/m^3; // Mass density
7 delta_tip = 100*m; // Target tip displacement
8
9 Nsubd = 10; // Number of side subdivisions

```

Displacement results at the tip nodes show less than 1% error when compared to Bernoulli beam theory.

```

1 Node : 21
2 ux = 3.325110, rx = 0.000000
3 uy = 99.780900, ry = 0.000000
4 uz = 0.000000, rz = 13.301200

```

```
5 Node : 22
6 ux = -3.325110, rx = 0.000000
7 uy = 99.780900, ry = 0.000000
8 uz = 0.000000, rz = 13.301200
```

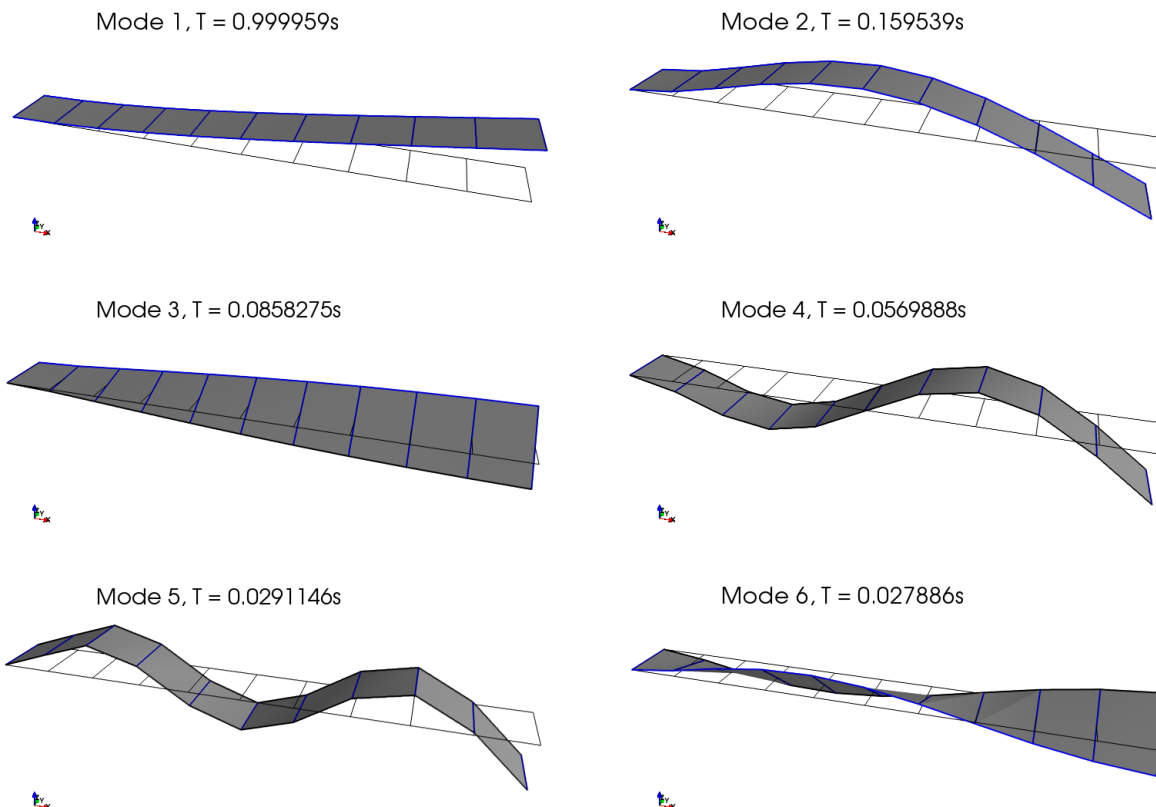
The test file for this case can be found in (ESSI SOURCE FOLDER)/Verification_Examples/...
.../Static_and_Dynamic_Behavior_of_Structural_Elements/...
.../Shell_ANDES/static/Test_shell_andes_8_membrane_transverse.fei

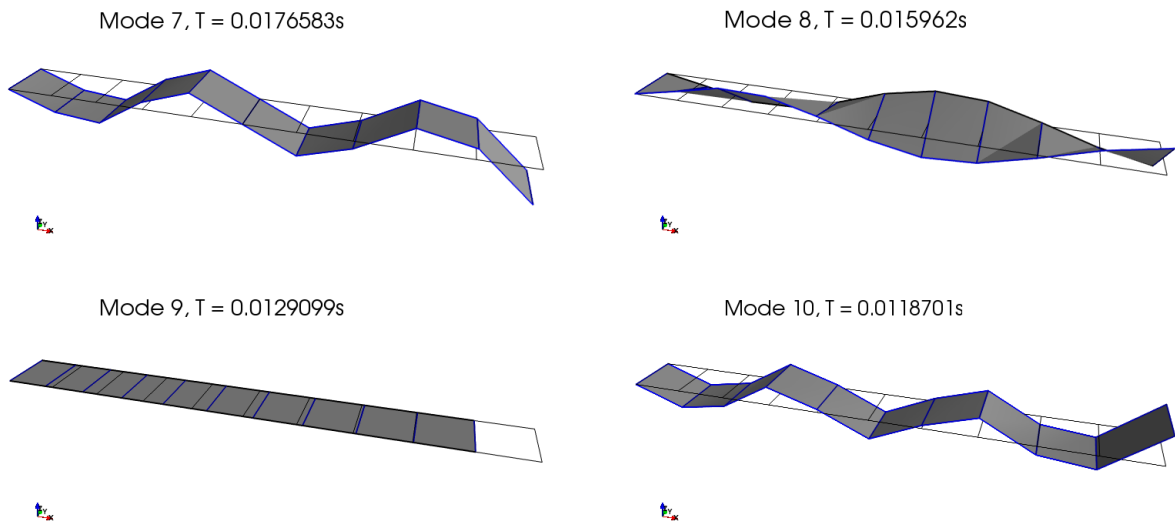
308.5.2 Dynamic Tests

The purpose of the dynamic tests is to verify that the mass matrix adopted for these elements (which is not consistent with the stiffness) is adequate for Dynamic analysis. Also tested herein are the geometric transformations.

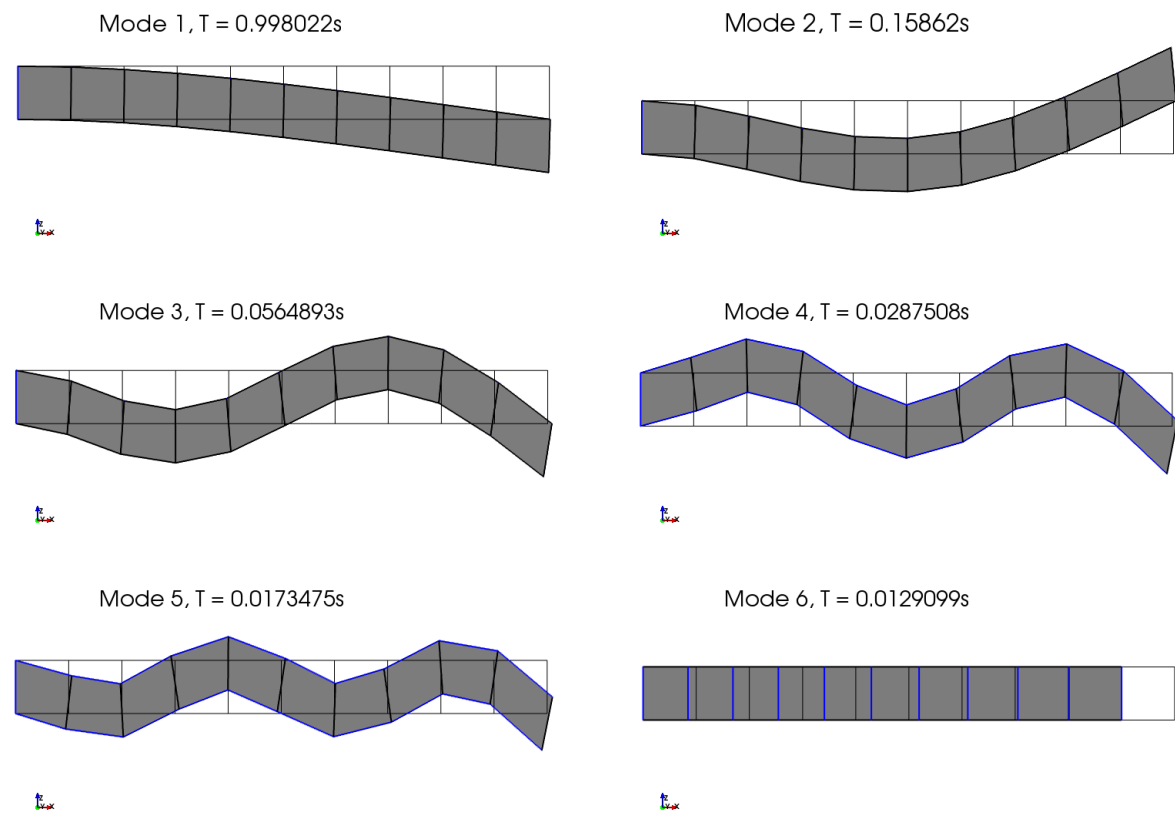
Again, the tests are divided into bending and membrane components which are tested independently. Also, an eigenvalue analysis is performed to verify accordance with theoretical results for continuous Bernoulli beams. Finally, geometric transformations are tested by performing an eigenvalue analysis for the same (unrestrained) beam in different orientations (pitch, yaw and roll) which should have invariant eigenvalues.

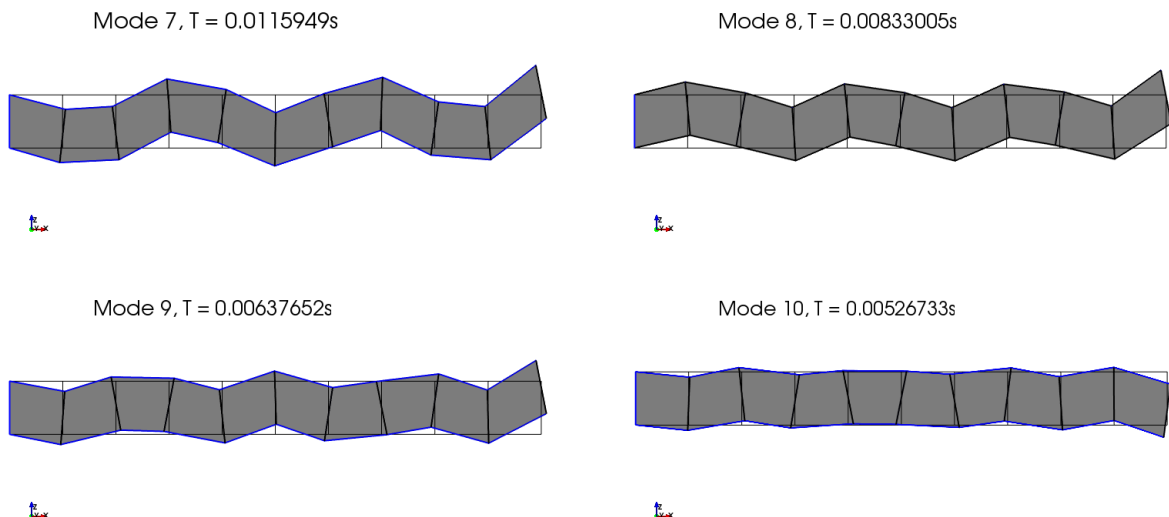
308.5.2.1 Bending Component





308.5.2.2 Membrane Component





308.5.2.3 Geometric Transformations

308.6 Verification of 4NodeANDES elements

308.6.1 Verification of 4NodeANDES cantilever beams

Problem description: Length=6m, Width=1m, Height=1m, Force=100N, E=1E8Pa, $\nu = 0.0$. Use the shear deformation coefficient $\kappa = 1.2$. The force direction was shown in Figure (308.10).

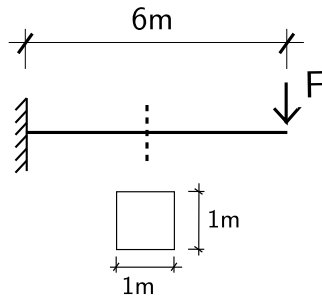


Figure 308.10: Problem description for cantilever beams.

Theoretical displacement (bending and shear deformation):

$$\begin{aligned}
 d &= \frac{FL^3}{3EI} + \frac{FL}{GA_y} \\
 &= \frac{FL^3}{3E \frac{bh^3}{12}} + \frac{FL}{\frac{E}{2(1+\nu)} \frac{bh}{\kappa}} \\
 &= \frac{100N \times 6^3 m^3}{3 \times 10^8 N/m^2 \times \frac{1}{12} m^4} + \frac{100N \times 6m}{\frac{10}{2} \times 10^7 N/m^2 \times 1m^2 \times \frac{5}{6}} \\
 &= 8.64 \times 10^{-4} m + 0.144 \times 10^{-4} m \\
 &= 8.784 \times 10^{-4} m
 \end{aligned} \tag{308.1}$$

4NodeANDES element model:

- Force direction: perpendicular to plane (bending)

When the force direction is perpendicular to the plane, only the bending deformation is calculated in 4NodeANDES elements.

The 4NodeANDES elements were shown in Figure (308.14).

- Force direction: inplane force

When the force direction is inplane, both the bending and shear deformation are calculated in 4NodeANDES elements.

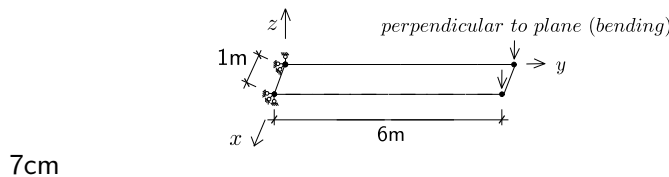


Figure 308.11: One 4NodeANDES element.

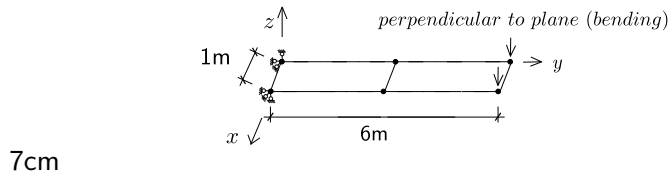


Figure 308.12: Two 4NodeANDES elements.

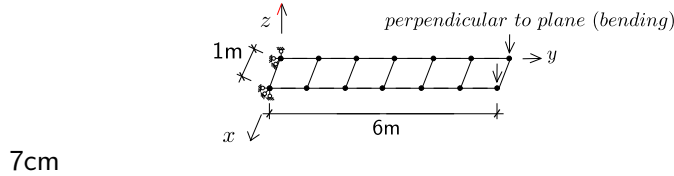


Figure 308.13: Six 4NodeANDES elements.

Figure 308.14: 4NodeANDES elements for cantilever beams under force perpendicular to plane.

The 4NodeANDES elements under inplane force were shown in Figure (308.18).

The Real-ESSI results for the force perpendicular to plane (bending) were listed in Table (308.3).

The theoretical solution is $8.784E-04\ m$. The Real-ESSI results for the inplane force were listed in Table

Table 308.3: Results for 4NodeANDES cantilever beams under the force perpendicular to plane (bending).

Element number	1	2	6
4NodeANDES	$6.56E-04\ m$	$8.27E-04\ m$	$8.86E-04\ m$
Error	25.34%	5.87%	0.83%

(308.4).

The theoretical solution is $8.784E-04\ m$.

The errors were plotted in Figure (308.21).

The Real-ESSI model fei/DSL files for the table above are [HERE](#).

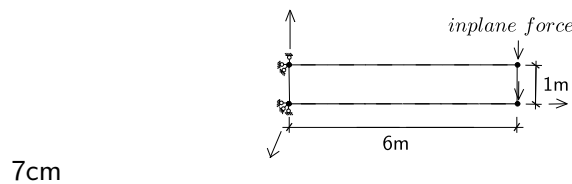


Figure 308.15: One 4NodeANDES element.

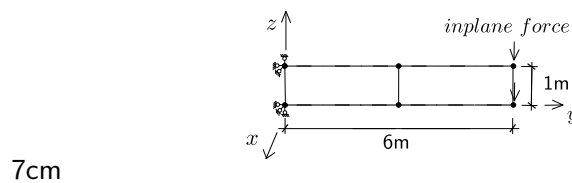


Figure 308.16: Two 4NodeANDES elements.

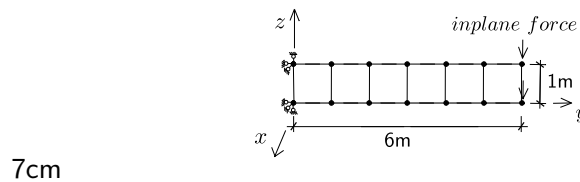


Figure 308.17: Six 4NodeANDES elements.

Figure 308.18: 4NodeANDES elements for cantilever beams under inplane force.

Table 308.4: Results for 4NodeANDES cantilever beams under the inplane force.

Element number	1	2	6
4NodeANDES	6.70E-04 m	8.27E-04 m	8.64E-04 m
Error	23.77%	5.89%	1.65%

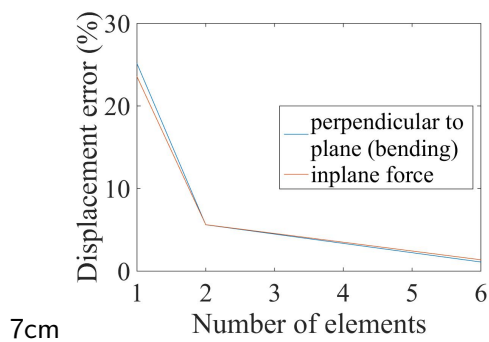


Figure 308.19: Error scale 0% - 30%.

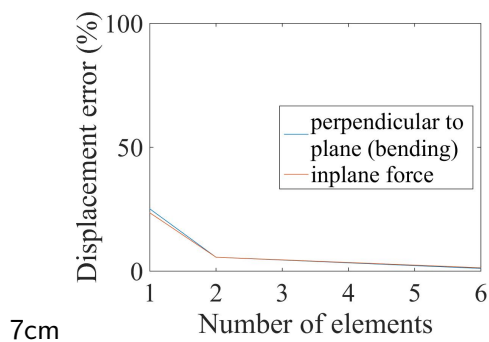


Figure 308.20: Error scale 0% - 100%.

Figure 308.21: 4NodeANDES cantilever beam for different element number: Displacement error versus Number of elements

308.6.2 Verification of 4NodeANDES cantilever beam for different Poisson's ratio

Problem description: Length=6m, Width=1m, Height=1m, Force=100N, E=1E8Pa, $\nu = 0.0 - 0.49$. The force direction was shown in Figure (308.22).

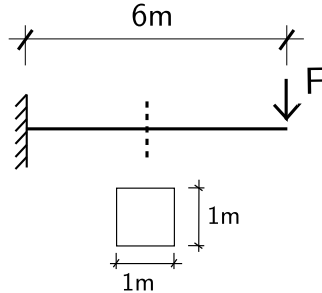


Figure 308.22: Problem description for cantilever beams of different Poisson's ratios.

The theoretical solution for $\nu = 0.0$ was calculated below, while the solution for other Poisson's ratio were calculated by the similar process.

Theoretical displacement (bending and shear deformation):

$$\begin{aligned}
 d &= \frac{FL^3}{3EI} + \frac{FL}{GA_v} \\
 &= \frac{FL^3}{3E \frac{bh^3}{12}} + \frac{FL}{\frac{E}{2(1+\nu)} \frac{bh}{\kappa}} \\
 &= \frac{100N \times 6^3 m^3}{3 \times 10^8 N/m^2 \times \frac{1}{12} m^4} + \frac{100N \times 6m}{\frac{10}{2} \times 10^7 N/m^2 \times 1m^2 \times \frac{5}{6}} \\
 &= 8.64 \times 10^{-4} m + 0.144 \times 10^{-4} m \\
 &= 8.784 \times 10^{-4} m
 \end{aligned} \tag{308.2}$$

The rotation angle at the end:

$$\theta = \frac{FL^2}{2EI} = \frac{100N \times 6^2 m^2}{2 \times 10^8 N/m^2 \times \frac{1}{12} m^4} = 2.16 \times 10^{-4} rad = 0.0124^\circ \tag{308.3}$$

The 4NodeANDES elements for cantilever beams of different Poisson's ratios were shown in Figure (308.23) and (308.24):

The Real-ESSI results for the force perpendicular to plane (bending) were listed in Table (308.5) - (308.7).

The errors were plotted in Figure (308.27).

The Real-ESSI results for the inplane force were listed in Table (308.8) - (308.10).

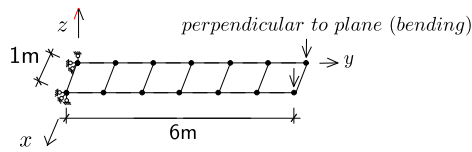


Figure 308.23: 4NodeANDES elements for different Poisson's ratios under the force perpendicular to plane (bending).

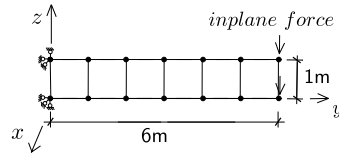


Figure 308.24: 4NodeANDES elements for different Poisson's ratios under the inplane force.

Table 308.5: Displacement error results for 4NodeANDES with element side length 1 m under the force perpendicular to plane (bending).

Poisson's ratio	4NodeANDES displacement	Theory displacement (bending)	Theory displacement (shear)	Theory displacement(all)	Error
0.00	8.639E-04 m	8.640E-04 m	1.440E-05 m	8.784E-04 m	1.38%
0.05	8.635E-04 m	8.640E-04 m	1.512E-05 m	8.791E-04 m	1.49%
0.10	8.622E-04 m	8.640E-04 m	1.586E-05 m	8.799E-04 m	1.71%
0.15	8.599E-04 m	8.640E-04 m	1.659E-05 m	8.806E-04 m	2.04%
0.20	8.566E-04 m	8.640E-04 m	1.734E-05 m	8.813E-04 m	2.48%
0.25	8.522E-04 m	8.640E-04 m	1.808E-05 m	8.821E-04 m	3.05%
0.30	8.466E-04 m	8.640E-04 m	1.884E-05 m	8.828E-04 m	3.75%
0.35	8.398E-04 m	8.640E-04 m	1.959E-05 m	8.836E-04 m	4.59%
0.40	8.315E-04 m	8.640E-04 m	2.035E-05 m	8.844E-04 m	5.60%
0.45	8.216E-04 m	8.640E-04 m	2.111E-05 m	8.851E-04 m	6.78%
0.49	8.124E-04 m	8.640E-04 m	2.173E-05 m	8.857E-04 m	7.88%

The errors were plotted in Figure (308.27).

plane(bending)'

The angle results for the force perpendicular to plane (bending) were listed in Table (308.11).

The errors were plotted in Figure (308.33).

Table 308.6: Displacement error results for 4NodeANDES with element side length 0.5 m under the force perpendicular to plane (bending).

Poisson's ratio	4NodeANDES displacement	Theory displacement (bending)	Theory displacement (shear)	Theory displacement(all)	Error
0.00	8.724E-04 m	8.640E-04 m	1.440E-05 m	8.784E-04 m	0.68%
0.05	8.724E-04 m	8.640E-04 m	1.512E-05 m	8.791E-04 m	0.76%
0.10	8.717E-04 m	8.640E-04 m	1.586E-05 m	8.799E-04 m	0.93%
0.15	8.703E-04 m	8.640E-04 m	1.659E-05 m	8.806E-04 m	1.17%
0.20	8.682E-04 m	8.640E-04 m	1.734E-05 m	8.813E-04 m	1.49%
0.25	8.652E-04 m	8.640E-04 m	1.808E-05 m	8.821E-04 m	1.91%
0.30	8.615E-04 m	8.640E-04 m	1.884E-05 m	8.828E-04 m	2.42%
0.35	8.569E-04 m	8.640E-04 m	1.959E-05 m	8.836E-04 m	3.02%
0.40	8.514E-04 m	8.640E-04 m	2.035E-05 m	8.844E-04 m	3.73%
0.45	8.449E-04 m	8.640E-04 m	2.111E-05 m	8.851E-04 m	4.54%
0.49	8.388E-04 m	8.640E-04 m	2.173E-05 m	8.857E-04 m	5.30%

Table 308.7: Displacement error results for 4NodeANDES with element side length 0.25 m under the force perpendicular to plane (bending).

Poisson's ratio	4NodeANDES displacement	Theory displacement (bending)	Theory displacement (shear)	Theory displacement(all)	Error
0.00	8.640E-04 m	8.640E-04 m	1.440E-05 m	8.784E-04 m	1.64%
0.05	8.637E-04 m	8.640E-04 m	1.512E-05 m	8.791E-04 m	1.75%
0.10	8.627E-04 m	8.640E-04 m	1.586E-05 m	8.799E-04 m	1.95%
0.15	8.611E-04 m	8.640E-04 m	1.659E-05 m	8.806E-04 m	2.21%
0.20	8.588E-04 m	8.640E-04 m	1.734E-05 m	8.813E-04 m	2.56%
0.25	8.559E-04 m	8.640E-04 m	1.808E-05 m	8.821E-04 m	2.97%
0.30	8.523E-04 m	8.640E-04 m	1.884E-05 m	8.828E-04 m	3.46%
0.35	8.480E-04 m	8.640E-04 m	1.959E-05 m	8.836E-04 m	4.03%
0.40	8.429E-04 m	8.640E-04 m	2.035E-05 m	8.844E-04 m	4.69%
0.45	8.370E-04 m	8.640E-04 m	2.111E-05 m	8.851E-04 m	5.44%
0.49	8.316E-04 m	8.640E-04 m	2.173E-05 m	8.857E-04 m	6.11%

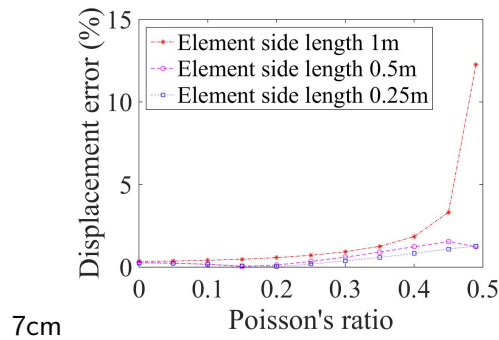


Figure 308.25: Error scale 0% - 15%.

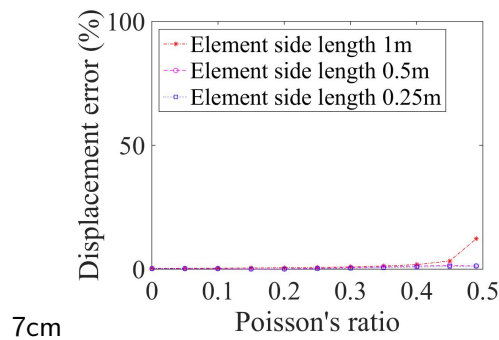


Figure 308.26: Error scale 0% - 100%.

Figure 308.27: 4NodeANDES cantilever beam for force perpendicular to the plane(bending)
Displacement error versus Poisson's ratio

The Real-ESSI results for the inplane force were listed in Table (308.14 - (308.16)).

The errors were plotted in Figure (308.33).

The Real-ESSI model fei/DSL files for the table above are [HERE](#).

Table 308.8: Displacement error results for 4NodeANDES with element side length 1 m under the inplane force.

Poisson's ratio	4NodeANDES displacement	Theory displacement (bending)	Theory displacement (shear)	Theory displacement(all)	Error
0.00	8.790E-04 m	8.640E-04 m	1.440E-05 m	8.784E-04 m	0.07%
0.05	8.799E-04 m	8.640E-04 m	1.512E-05 m	8.791E-04 m	0.09%
0.10	8.809E-04 m	8.640E-04 m	1.586E-05 m	8.799E-04 m	0.12%
0.15	8.821E-04 m	8.640E-04 m	1.659E-05 m	8.806E-04 m	0.17%
0.20	8.835E-04 m	8.640E-04 m	1.734E-05 m	8.813E-04 m	0.25%
0.25	8.853E-04 m	8.640E-04 m	1.808E-05 m	8.821E-04 m	0.37%
0.30	8.878E-04 m	8.640E-04 m	1.884E-05 m	8.828E-04 m	0.56%
0.35	8.913E-04 m	8.640E-04 m	1.959E-05 m	8.836E-04 m	0.87%
0.40	8.971E-04 m	8.640E-04 m	2.035E-05 m	8.844E-04 m	1.44%
0.45	9.107E-04 m	8.640E-04 m	2.111E-05 m	8.851E-04 m	2.89%
0.49	9.901E-04 m	8.640E-04 m	2.173E-05 m	8.857E-04 m	11.79%

Table 308.9: Displacement error results for 4NodeANDES with element side length 0.5 m under the inplane force.

Poisson's ratio	4NodeANDES displacement	Theory displacement (bending)	Theory displacement (shear)	Theory displacement(all)	Error
0.00	8.784E-04 m	8.640E-04 m	1.440E-05 m	8.784E-04 m	0.00%
0.05	8.788E-04 m	8.640E-04 m	1.512E-05 m	8.791E-04 m	0.04%
0.10	8.787E-04 m	8.640E-04 m	1.586E-05 m	8.799E-04 m	0.13%
0.15	8.782E-04 m	8.640E-04 m	1.659E-05 m	8.806E-04 m	0.27%
0.20	8.772E-04 m	8.640E-04 m	1.734E-05 m	8.813E-04 m	0.47%
0.25	8.759E-04 m	8.640E-04 m	1.808E-05 m	8.821E-04 m	0.70%
0.30	8.742E-04 m	8.640E-04 m	1.884E-05 m	8.828E-04 m	0.98%
0.35	8.722E-04 m	8.640E-04 m	1.959E-05 m	8.836E-04 m	1.29%
0.40	8.699E-04 m	8.640E-04 m	2.035E-05 m	8.844E-04 m	1.63%
0.45	8.679E-04 m	8.640E-04 m	2.111E-05 m	8.851E-04 m	1.94%
0.49	8.709E-04 m	8.640E-04 m	2.173E-05 m	8.857E-04 m	1.67%

Table 308.10: Displacement error results for 4NodeANDES with element side length 0.25 m under the inplane force.

Poisson's ratio	4NodeANDES displacement	Theory displacement (bending)	Theory displacement (shear)	Theory displacement(all)	Error
0.00	8.782E-04 m	8.640E-04 m	1.440E-05 m	8.784E-04 m	0.02%
0.05	8.786E-04 m	8.640E-04 m	1.512E-05 m	8.791E-04 m	0.06%
0.10	8.788E-04 m	8.640E-04 m	1.586E-05 m	8.799E-04 m	0.12%
0.15	8.786E-04 m	8.640E-04 m	1.659E-05 m	8.806E-04 m	0.23%
0.20	8.781E-04 m	8.640E-04 m	1.734E-05 m	8.813E-04 m	0.37%
0.25	8.774E-04 m	8.640E-04 m	1.808E-05 m	8.821E-04 m	0.53%
0.30	8.763E-04 m	8.640E-04 m	1.884E-05 m	8.828E-04 m	0.74%
0.35	8.750E-04 m	8.640E-04 m	1.959E-05 m	8.836E-04 m	0.97%
0.40	8.734E-04 m	8.640E-04 m	2.035E-05 m	8.844E-04 m	1.24%
0.45	8.717E-04 m	8.640E-04 m	2.111E-05 m	8.851E-04 m	1.52%
0.49	8.706E-04 m	8.640E-04 m	2.173E-05 m	8.857E-04 m	1.71%

Table 308.11: Rotation angle results for element side length 1 m under the force perpendicular to plane (bending).

Poisson's ratio	4NodeANDES angle (unit: $^{\circ}$)	Theory angle (unit: $^{\circ}$)	Error
0.00	1.238E-02	1.240E-02	0.19%
0.05	1.237E-02	1.240E-02	0.23%
0.10	1.236E-02	1.240E-02	0.34%
0.15	1.234E-02	1.240E-02	0.52%
0.20	1.230E-02	1.240E-02	0.78%
0.25	1.226E-02	1.240E-02	1.12%
0.30	1.221E-02	1.240E-02	1.54%
0.35	1.214E-02	1.240E-02	2.07%
0.40	1.206E-02	1.240E-02	2.70%
0.45	1.197E-02	1.240E-02	3.46%
0.49	1.188E-02	1.240E-02	4.16%

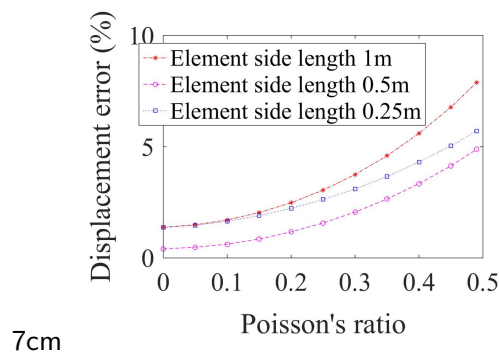


Figure 308.28: Error scale 0% - 10%.

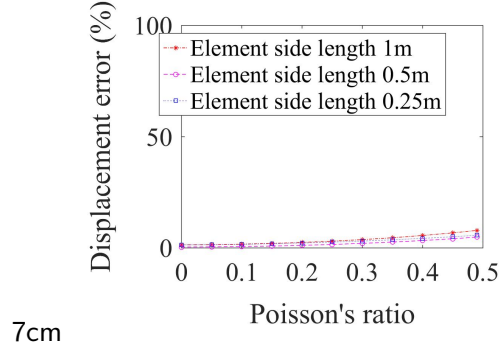


Figure 308.29: Error scale 0% - 100%.

Figure 308.30: 4NodeANDES cantilever beam for inplane force' Displacement error versus Poisson's ratio

Table 308.12: Rotation angle results for element side length 0.5 m the force perpendicular to plane (bending).

Poisson's ratio	4NodeANDES angle (unit: $^{\circ}$)	Theory angle (unit: $^{\circ}$)	Error
0.00	1.239E-02	1.240E-02	0.10%
0.05	1.238E-02	1.240E-02	0.13%
0.10	1.237E-02	1.240E-02	0.22%
0.15	1.236E-02	1.240E-02	0.36%
0.20	1.233E-02	1.240E-02	0.55%
0.25	1.230E-02	1.240E-02	0.81%
0.30	1.226E-02	1.240E-02	1.13%
0.35	1.221E-02	1.240E-02	1.52%
0.40	1.216E-02	1.240E-02	1.97%
0.45	1.209E-02	1.240E-02	2.51%
0.49	1.203E-02	1.240E-02	3.00%

Table 308.13: Rotation angle results for element side length 0.25 m under the force perpendicular to plane (bending).

Poisson's ratio	4NodeANDES angle (unit: $^{\circ}$)	Theory angle (unit: $^{\circ}$)	Error
0.00	1.238E-02	1.240E-02	0.19%
0.05	1.237E-02	1.240E-02	0.21%
0.10	1.237E-02	1.240E-02	0.28%
0.15	1.235E-02	1.240E-02	0.39%
0.20	1.233E-02	1.240E-02	0.56%
0.25	1.230E-02	1.240E-02	0.78%
0.30	1.227E-02	1.240E-02	1.05%
0.35	1.223E-02	1.240E-02	1.38%
0.40	1.218E-02	1.240E-02	1.77%
0.45	1.212E-02	1.240E-02	2.23%
0.49	1.207E-02	1.240E-02	2.64%

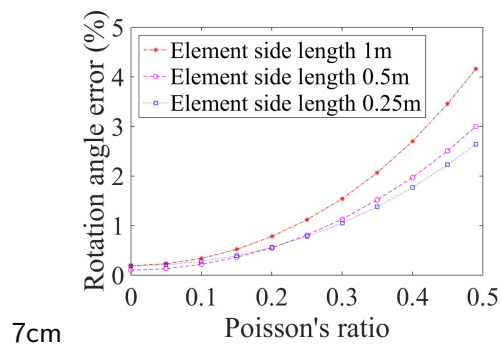


Figure 308.31: Error scale 0% - 5%.

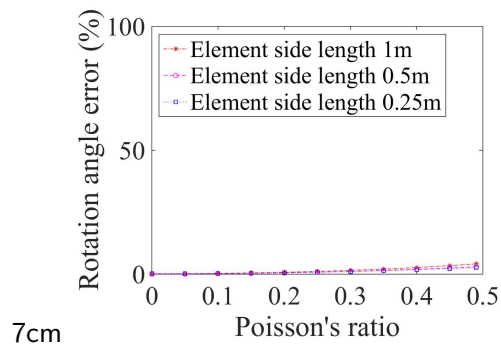


Figure 308.32: Error scale 0% - 100%.

Figure 308.33: 4NodeANDES cantilever beam for force perpendicular to the plane(bending)
Rotation angle error versus Poisson's ratio

Table 308.14: Rotation angle results for element side length 1 m under the inplane force.

Poisson's ratio	4NodeANDES angle (unit: $^{\circ}$)	Theory angle (unit: $^{\circ}$)	Error
0.00	1.254E-02	1.240E-02	1.14%
0.05	1.255E-02	1.240E-02	1.19%
0.10	1.256E-02	1.240E-02	1.26%
0.15	1.257E-02	1.240E-02	1.35%
0.20	1.258E-02	1.240E-02	1.47%
0.25	1.260E-02	1.240E-02	1.64%
0.30	1.263E-02	1.240E-02	1.89%
0.35	1.269E-02	1.240E-02	2.30%
0.40	1.278E-02	1.240E-02	3.08%
0.45	1.305E-02	1.240E-02	5.28%
0.49	1.506E-02	1.240E-02	21.43%

Table 308.15: Rotation angle results for element side length 0.5 m under the inplane force.

Poisson's ratio	4NodeANDES angle (unit: $^{\circ}$)	Theory angle (unit: $^{\circ}$)	Error
0.00	1.271E-02	1.240E-02	2.51%
0.05	1.272E-02	1.240E-02	2.56%
0.10	1.272E-02	1.240E-02	2.58%
0.15	1.272E-02	1.240E-02	2.60%
0.20	1.273E-02	1.240E-02	2.63%
0.25	1.273E-02	1.240E-02	2.67%
0.30	1.274E-02	1.240E-02	2.77%
0.35	1.277E-02	1.240E-02	2.98%
0.40	1.283E-02	1.240E-02	3.47%
0.45	1.299E-02	1.240E-02	4.79%
0.49	1.361E-02	1.240E-02	9.78%

Table 308.16: Rotation angle results for element side length 0.25 m under the inplane force.

Poisson's ratio	4NodeANDES angle (unit: $^{\circ}$)	Theory angle (unit: $^{\circ}$)	Error
0.00	1.268E-02	1.240E-02	2.24%
0.05	1.268E-02	1.240E-02	2.27%
0.10	1.268E-02	1.240E-02	2.30%
0.15	1.269E-02	1.240E-02	2.31%
0.20	1.269E-02	1.240E-02	2.33%
0.25	1.269E-02	1.240E-02	2.35%
0.30	1.270E-02	1.240E-02	2.41%
0.35	1.271E-02	1.240E-02	2.53%
0.40	1.275E-02	1.240E-02	2.83%
0.45	1.284E-02	1.240E-02	3.58%
0.49	1.312E-02	1.240E-02	5.77%

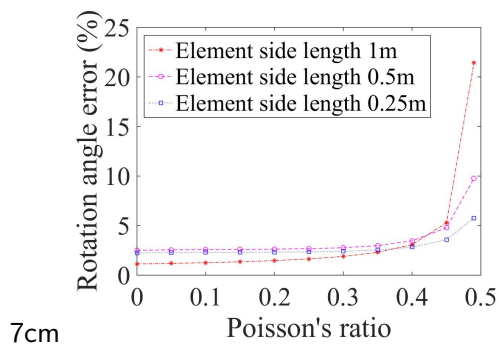


Figure 308.34: Error scale 0% - 25%.

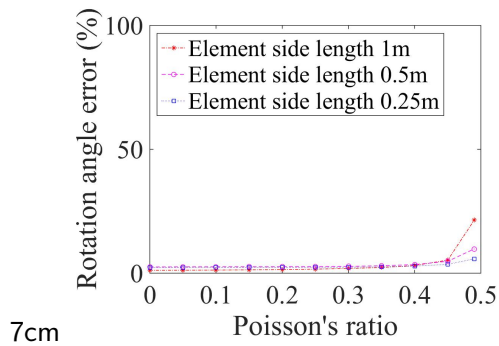


Figure 308.35: Error scale 0% - 100%.

Figure 308.36: 4NodeANDES cantilever beam for inplane force' Rotation angle error versus Poisson's ratio

308.6.3 Test of irregular shaped 4NodeANDES cantilever beams

Cantilever model was used as an example. Three different shapes were tested.

In the first test, the upper two nodes of each element were moved one half element size along the $y-axis$, while the lower two nodes were kept at the same location. The element shape was shown in Figure (308.39).

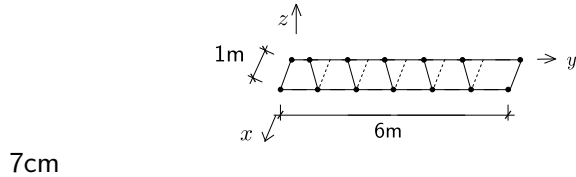


Figure 308.37: Horizontal plane.

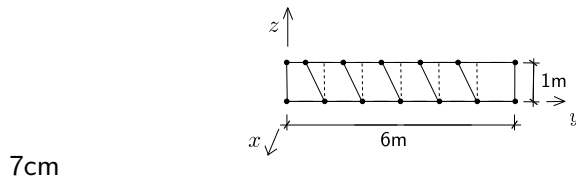


Figure 308.38: Vertical plane.

Figure 308.39: 4NodeANDES cantilever beam for irregular Shape 1.

In the second test, the upper nodes of each element were moved 50% element size along the $y-axis$, while the lower nodes were moved 50% element size in the other direction along the $y-axis$. The element shape was shown in Figure (308.42).

In the third test, the upper two nodes of each element were moved 90% element size with different directions along the $y-axis$, while the lower nodes were moved 90% element size in the other direction along the $y-axis$. The element shape was shown in Figure (308.45).

The boundary conditions were shown in Figures (308.48), (308.51) and (308.54).

The Real-ESSI results were listed in Table (308.17).

The errors were listed in Tables (308.18) and (308.19).

The Real-ESSI model fei/DSL files for the table above are [HERE](#).

Then, the beam was divided into small elements.

Problem description: Length=6m, Width=1m, Height=1m, Force=100N, E=1E8Pa, $\nu = 0.0$. Use the shear deformation coefficient $\kappa = 1.2$. The force direction was shown in Figure (308.55).

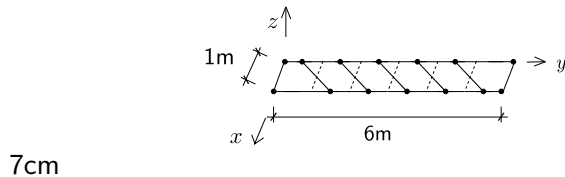


Figure 308.40: Horizontal plane.

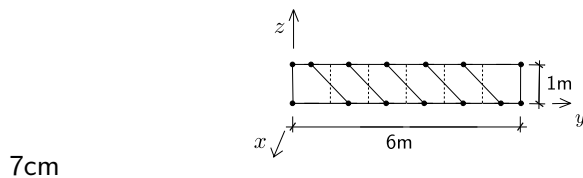


Figure 308.41: Veritical plane.

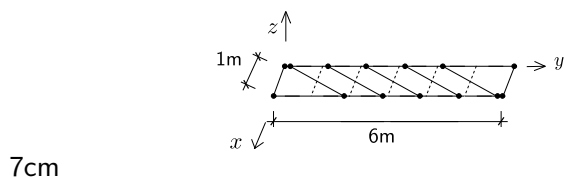
Figure 308.42: 4NodeANDES cantilever beam for irregular Shape 2.

Figure 308.43: Horizontal plane.

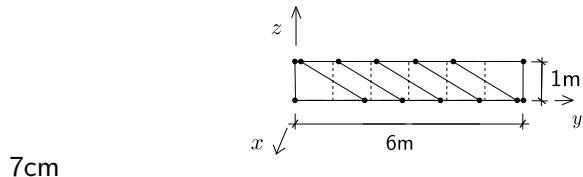


Figure 308.44: Veritical plane.

Figure 308.45: 4NodeANDES cantilever beam for irregular Shape 3.

Theoretical displacement (bending and shear deformation):

$$\begin{aligned}
 d &= \frac{qL^4}{8EI} + \frac{q\frac{L^2}{2}}{GA_y} \\
 &= \frac{qL^4}{8E\frac{bh^3}{12}} + \frac{q\frac{L^2}{2}}{\frac{E}{2(1+\nu)}\frac{bh}{\kappa}} \\
 &= \frac{400N/m \times 12^4 m^4}{8 \times 10^8 N/m^2 \times \frac{24}{12} m^4} + \frac{400N/m \times \frac{12^2}{2} m^2}{\frac{10^8}{2} N/m^2 \times 2m \times 2m \times \frac{5}{6}} \\
 &= 7.776 \times 10^{-3} m + 1.728 \times 10^{-4} m \\
 &= 7.9488 \times 10^{-3} m
 \end{aligned} \tag{308.4}$$

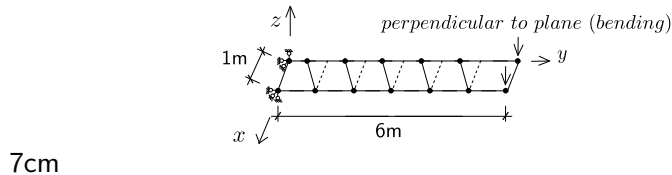


Figure 308.46: Horizontal plane.

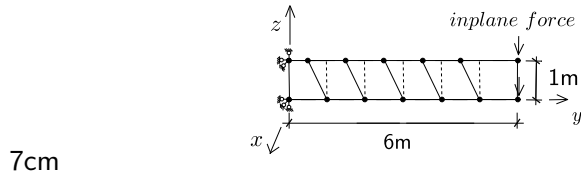


Figure 308.47: Veritical plane.

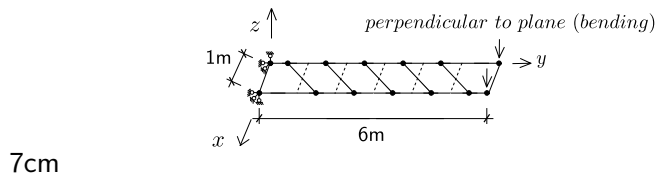
Figure 308.48: 4NodeANDES cantilever beam boundary conditions for irregular Shape 1.

Figure 308.49: Horizontal plane.

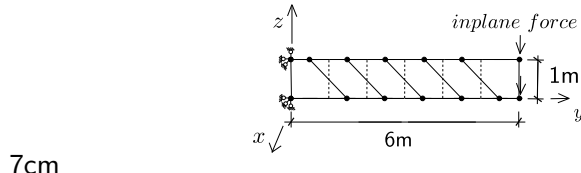


Figure 308.50: Veritical plane.

Figure 308.51: 4NodeANDES cantilever beam boundary conditions for irregular Shape 2.

The Real-ESSI displacement results were listed in Table (308.20).

The error were listed in Table (308.21).

The errors were shown in Figures (308.58), (308.61) and (308.64).

The Real-ESSI model fei/DSL files for the table above are [HERE](#).

In this section, the beam was cut into smaller elements with element side length 0.5m and 0.25m respectively. And the element side length of the original models is 1.0m. The numerical models were shown in Figure (308.67), (308.70) and (308.73).

Number of division 1:

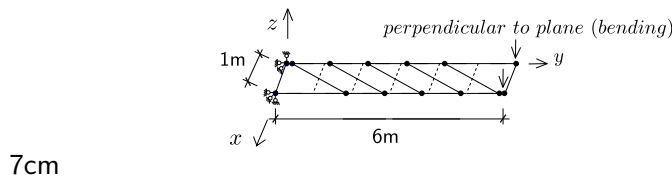


Figure 308.52: Horizontal plane.

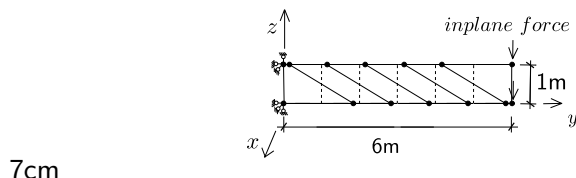


Figure 308.53: Veritical plane.

Figure 308.54: 4NodeANDES cantilever beam boundary conditions for irregular Shape 3.

Table 308.17: Results for 4NodeANDES cantilever beams of irregular shapes.

Displacements for irregular shaped element					
Element Type	Force direction	Normal shape	Shape 1	Shape 2	Shape 3
4NodeANDES	perpendicular to plane (bending)	8.639E-04 m	8.602E-04 m	8.534E-04 m	7.851E-04 m
4NodeANDES	inplane force	8.857E-04 m	7.036E-04 m	4.263E-04 m	1.909E-04 m
Theoretical	-	8.784E-04 m	8.784E-04 m	8.784E-04 m	8.784E-04 m

Table 308.18: Errors for irregular shaped 4NodeANDES compared to theoretical solution.

Errors for irregular shaped element, compared to theoretical solutions					
Element Type	Force direction	Normal shape	Shape 1	Shape 2	Shape 3
4NodeANDES	perpendicular to plane (bending)	1.65%	2.07%	2.85%	10.63%
4NodeANDES	inplane force	0.83%	19.90%	51.47%	78.27%

Number of division 2:

Number of division 4:

The Real-ESSI results for the force perpendicular to plane (bending) were listed in Table (308.22).

The theoretical solution is 1.60E-5 m.

The Real-ESSI results for the inplane force were listed in Table (308.23). The theoretical solution is 1.60E-5 m.

Table 308.19: Errors for irregular shaped 4NodeANDES compared to normal shape.

Errors for irregular shaped element, compared to normal shape					
Element Type	Force direction	Normal shape	Shape 1	Shape 2	Shape 3
4NodeANDES	perpendicular to plane (bending)	0.00%	0.42%	1.22%	9.12%
4NodeANDES	inplane force	0.00%	20.56%	51.87%	78.45%

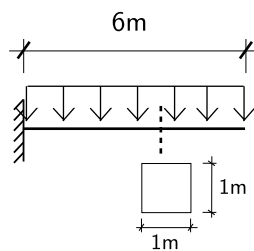


Figure 308.55: Problem description for cantilever beams under uniform pressure .

Table 308.20: Results for 4NodeANDES cantilever beams of irregular shapes with more elements.

Element Type	Shape	Force direction	Number of division		
			1	2	4
4NodeANDES	shape1	perpendicular to plane (bending)	7.750E-03 m	7.768E-03 m	7.774E-03 m
4NodeANDES	shape1	inplane force	6.822E-03 m	7.569E-03 m	7.832E-03 m
4NodeANDES	shape2	perpendicular to plane (bending)	7.656E-03 m	7.734E-03 m	7.765E-03 m
4NodeANDES	shape2	inplane force	3.875E-03 m	5.855E-03 m	7.074E-03 m
4NodeANDES	shape3	perpendicular to plane (bending)	6.637E-03 m	7.139E-03 m	7.521E-03 m
4NodeANDES	shape3	inplane force	1.555E-03 m	2.424E-03 m	3.896E-03 m
Theoretical solution			7.9488E-03 m	7.9488E-03 m	7.9488E-03 m

The errors were plotted in Figure (308.76).

The Real-ESSI model fei/DSL files for the table above are [HERE](#).

Table 308.21: Errors for 4NodeANDES cantilever beams of irregular shapes with more elements.

Element Type	Shape	Force direction	Number of division		
			1	2	4
4NodeANDES	shape1	perpendicular to plane (bending)	2.51%	2.28%	2.20%
4NodeANDES	shape1	inplane force	14.18%	4.78%	1.48%
4NodeANDES	shape2	perpendicular to plane (bending)	3.68%	2.71%	2.31%
4NodeANDES	shape2	inplane force	51.25%	26.34%	11.00%
4NodeANDES	shape3	perpendicular to plane (bending)	16.51%	10.19%	5.38%
4NodeANDES	shape3	inplane force	80.44%	69.51%	50.98%

Table 308.22: Results for 4NodeANDES clamped beams under the force perpendicular to plane (bending).

Element Type	Element side length		
	1 m	0.5 m	0.25 m
4NodeANDES	1.347E-05 m	1.35E-05 m	1.35E-05 m
Error	18.36%	18.24%	18.18%

Table 308.23: Results for 4NodeANDES clamped beams under the inplane force.

Element Type	Element side length		
	1 m	0.5 m	0.25 m
4NodeANDES	1.62E-05 m	1.65E-05 m	1.69E-05 m
Error	1.70%	0.12%	2.12%

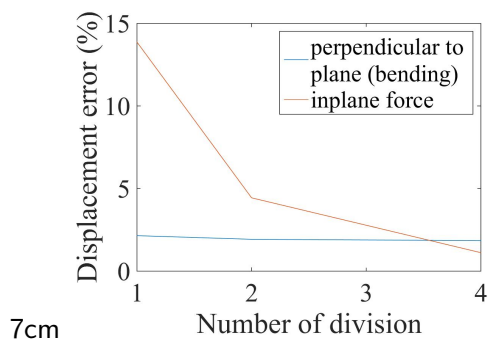


Figure 308.56: Error scale 0% - 15%.

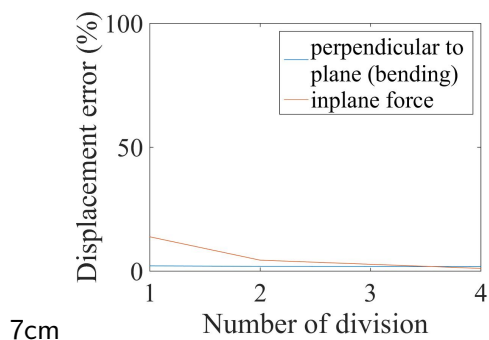


Figure 308.57: Error scale 0% - 100%.

Figure 308.58: 4NodeANDES cantilever beam for irregular Shape 1. Displacement error versus Number of division

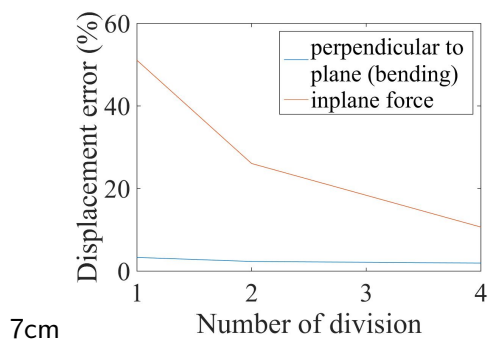


Figure 308.59: Error scale 0% - 60%.

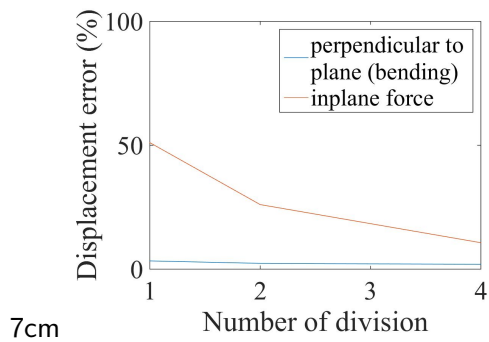


Figure 308.60: Error scale 0% - 100%.

Figure 308.61: 4NodeANDES cantilever beam for irregular Shape 2. Displacement error versus Number of division

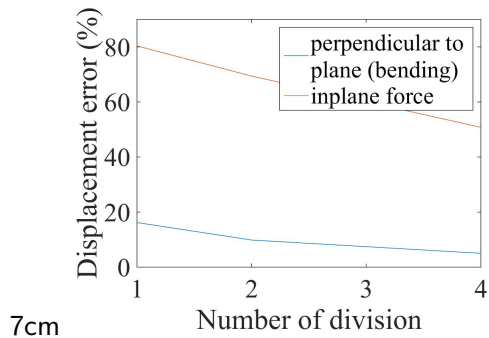


Figure 308.62: Error scale 0% - 80%.

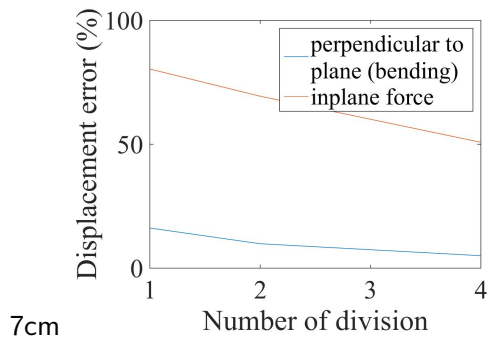


Figure 308.63: Error scale 0% - 100%.

Figure 308.64: 4NodeANDES cantilever beam for irregular Shape 3'. Displacement error versus Number of division

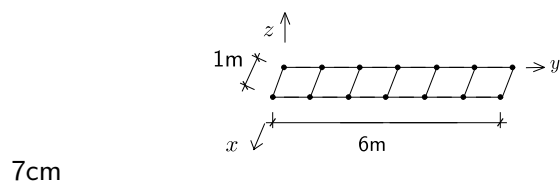


Figure 308.64: Horizontal plane.

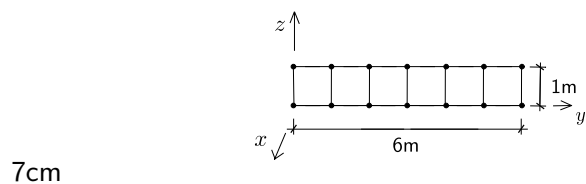


Figure 308.65: Vertical plane.

Figure 308.67: 4NodeANDES clamped beam with element side length 1.0m.

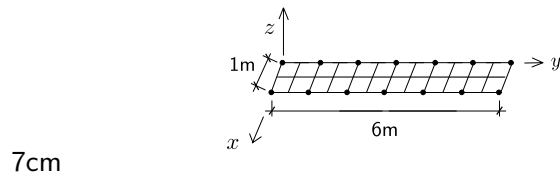


Figure 308.68: Horizontal plane.

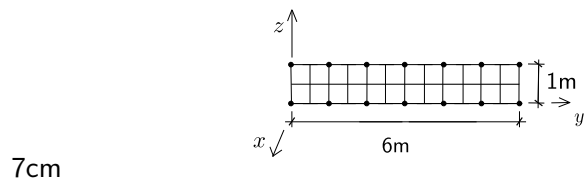


Figure 308.69: Veritical plane.

Figure 308.70: 4NodeANDES clamped beam with element side length 0.5m.

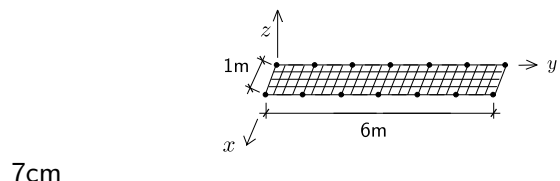


Figure 308.71: Horizontal plane.

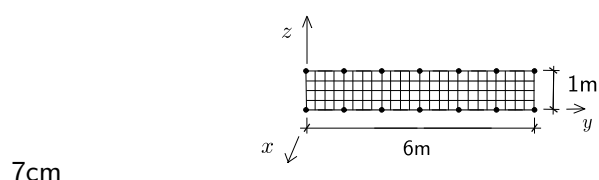


Figure 308.72: Veritical plane.

Figure 308.73: 4NodeANDES clamped beam with element side length 0.25m.

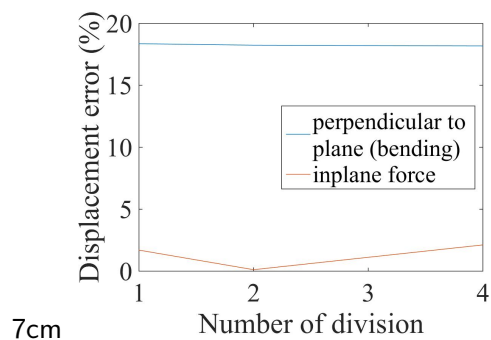


Figure 308.74: Error scale 0% - 20%.

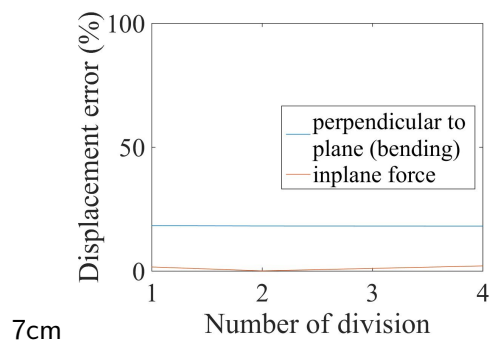


Figure 308.75: Error scale 0% - 100%.

Figure 308.76: 4NodeANDES clamped beam for different element number. Displacement error versus Number of division

308.6.4 Verification of 4NodeANDES square plate with four edges clamped

Problem description: Length=20m, Width=20m, Height=1m, Force=100N, E=1E8Pa, $\nu = 0.3$.

The four edges are clamped.

The load is the uniform normal pressure on the whole plate.

The plate flexural rigidity is

$$D = \frac{Eh^3}{12(1-\nu^2)} = \frac{10^8 N/m^2 \times 1^3 m^3}{12 \times (1 - 0.3^2)} = 9.1575 \times 10^6 N \cdot m \quad (308.5)$$

The theoretical solution is

$$d = \alpha_c \frac{qa^4}{D} = 0.00406 \times \frac{100N/m^2 \times 20^4 m^4}{9.1575 \times 10^6 N \cdot m} = 2.2015 \times 10^{-3} m \quad (308.6)$$

where α_c is a coefficient, which depends on the ratio of plate length to width. In this problem, the coefficient⁴ α_c is 0.00406.

The 4NodeANDES were shown in Figures (308.77) - (308.82).

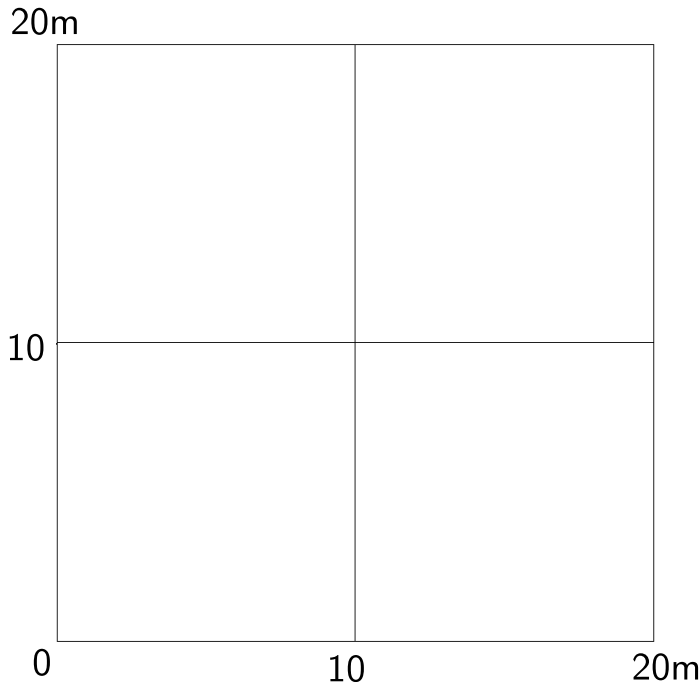


Figure 308.77: 4NodeANDES edge clamped square plate with element side length 10m.

The results were listed in Table (308.24).

The errors were listed in Table (308.25).

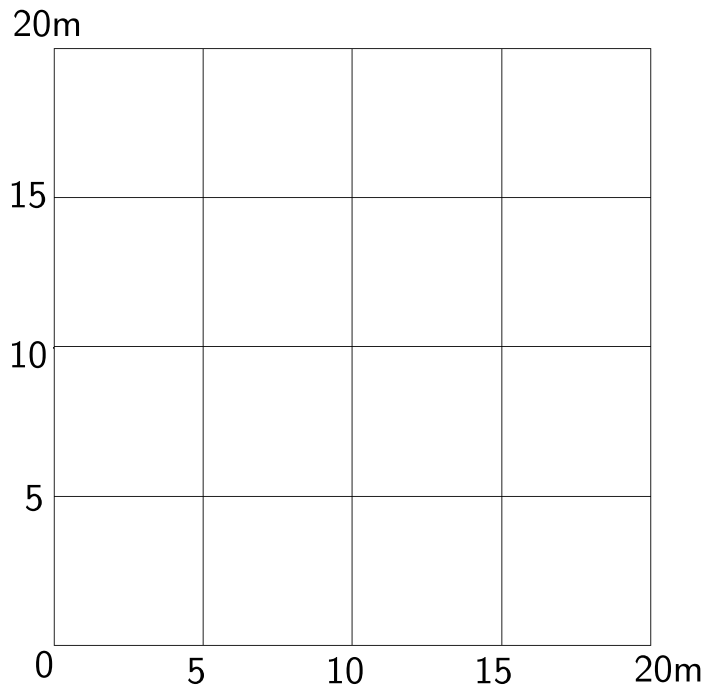


Figure 308.78: 4NodeANDES edge clamped square plate with element side length 5m.

Table 308.24: Results for 4NodeANDES square plate with four edges clamped.

Element type	4NodeANDES	Theoretical displacement
Element side length	Height:1.00m	
10m	2.33E-003 m	2.20E-03 m
5m	2.75E-003 m	2.20E-03 m
2m	2.58E-003 m	2.20E-03 m
1m	2.54E-003 m	2.20E-03 m
0.5m	2.53E-003 m	2.20E-03 m
0.25m	2.53E-003 m	2.20E-03 m

The errors were plotted in Figure (308.85).

The Real-ESSI model fei/DSL files for the table above are [HERE](#).

⁴Stephen Timoshenko, Theory of plates and shells (2nd edition). MrGRAW-Hill Inc, page120, 1959.

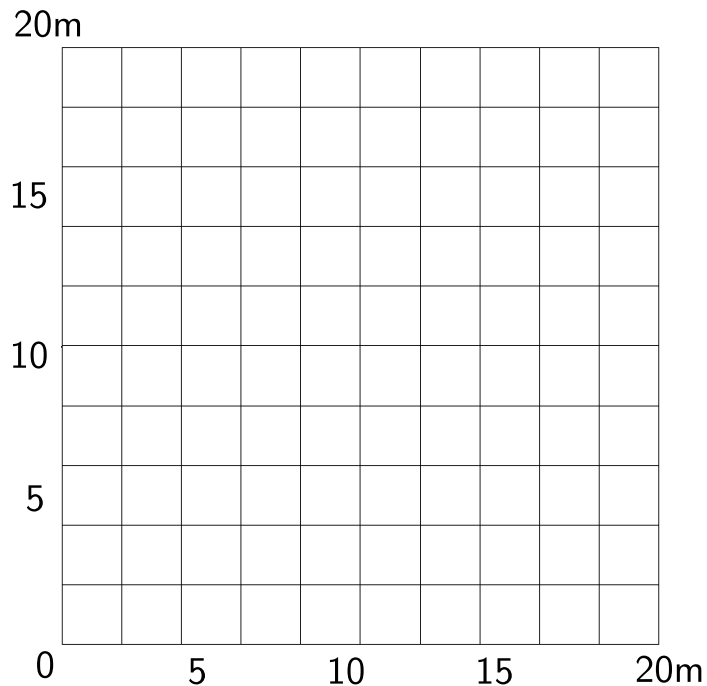


Figure 308.79: 4NodeANDES edge clamped square plate with element side length 2m.

Table 308.25: Errors for 4NodeANDES square plate with four edges clamped.

Element type	4NodeANDES
Element side length	Height:1.00m
10m	5.65%
5m	24.98%
2m	16.97%
1m	15.28%
0.5m	14.84%
0.25m	14.73%

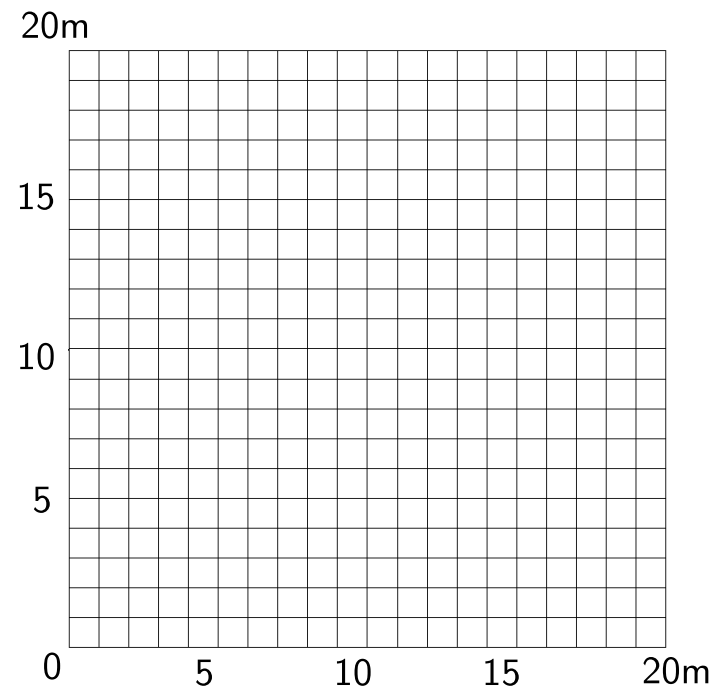


Figure 308.80: 4NodeANDES edge clamped square plate with element side length 1m.

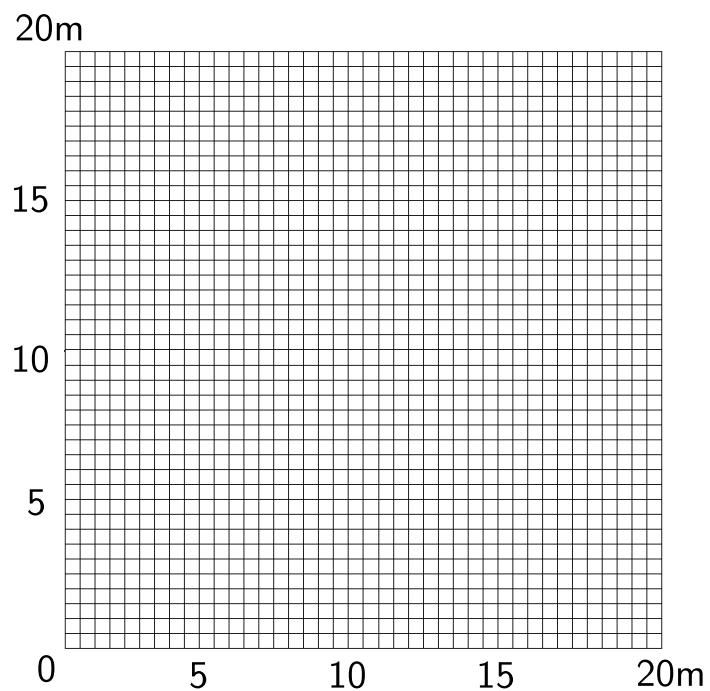


Figure 308.81: 4NodeANDES edge clamped square plate with element side length 0.5m.

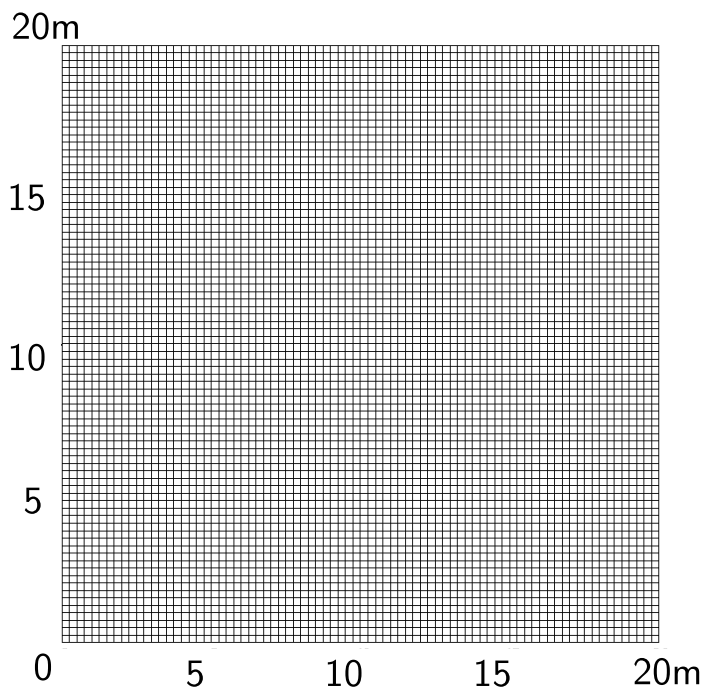


Figure 308.82: 4NodeANDES edge clamped square plate with element side length 0.25m.

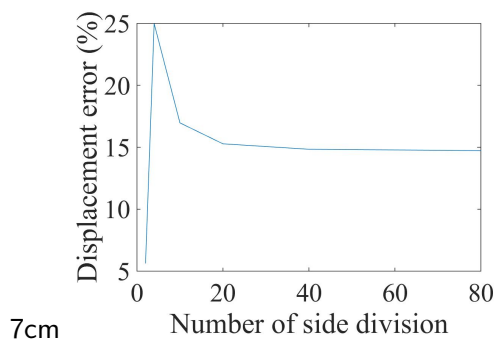


Figure 308.83: Error scale 0% - 25%.

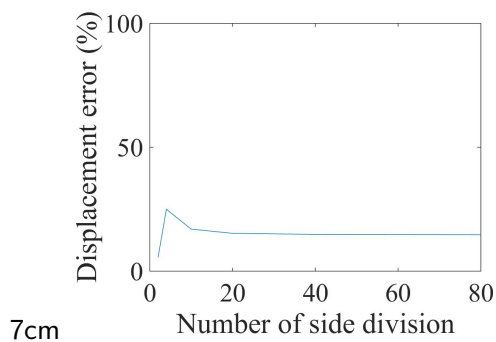


Figure 308.84: Error scale 0% - 100%.

Figure 308.85: 4NodeANDES square plate with edge clamped' Displacement error versus Number of side division

308.6.5 Verification of 4NodeANDES square plate with four edges simply supported

Problem description: Length=20m, Width=20m, Height=1m, Force=100N, E=1E8Pa, $\nu = 0.3$.

The four edges are simply supported.

The load is the uniform normal pressure on the whole plate.

The plate flexural rigidity is

$$D = \frac{Eh^3}{12(1-\nu^2)} = \frac{10^8 N/m^2 \times 1^3 m^3}{12 \times (1 - 0.3^2)} = 9.1575 \times 10^6 N \cdot m \quad (308.7)$$

The theoretical solution is

$$d = \alpha_s \frac{qa^4}{D} = 0.00126 \times \frac{100N/m^2 \times 20^4 m^4}{9.1575 \times 10^6 N \cdot m} = 7.0936 \times 10^{-3} m \quad (308.8)$$

where α_s is a coefficient, which depends on the ratio of plate length to width. In this problem, the coefficient⁵ α_s is 0.00126.

The 4NodeANDES were shown in Figure (308.86) - (308.91).

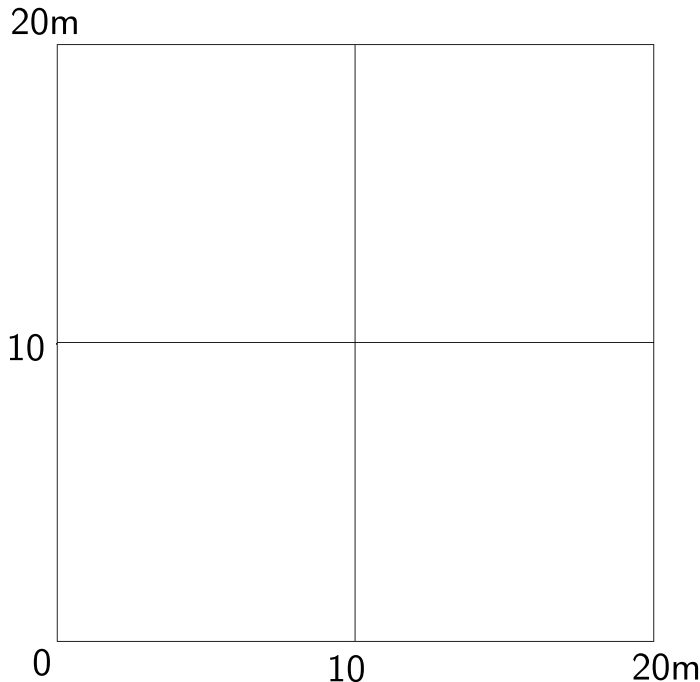


Figure 308.86: 4NodeANDES edge simply supported square plate with element side length 10m.

The results were listed in Table (308.26).

The errors were listed in Table (308.27).

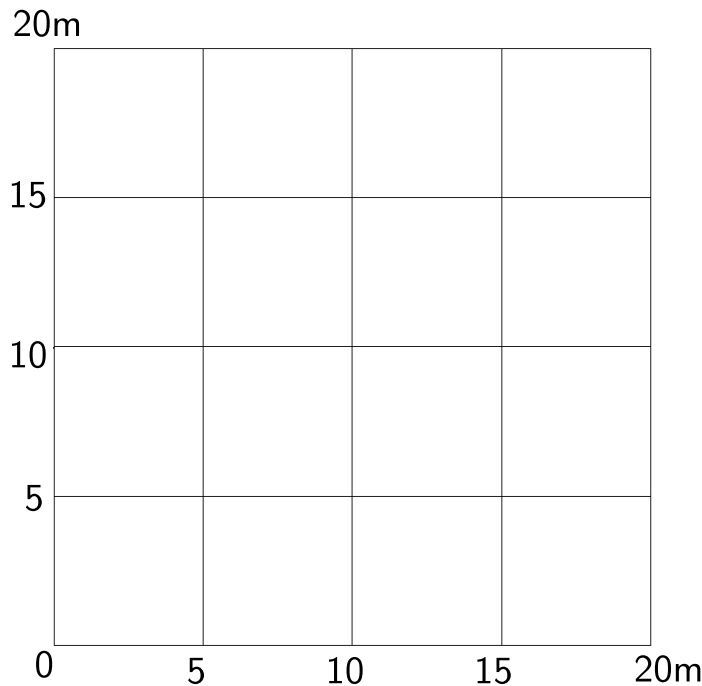


Figure 308.87: 4NodeANDES edge simply supported square plate with element side length 5m.

Table 308.26: Results for 4NodeANDES square plate with four edges simply supported.

Element type	4NodeANDES	Theoretical displacement
Element side length	Height:1.00m	
10m	1.14E-002 m	7.09E-03 m
5m	1.03E-002 m	7.09E-03 m
2m	9.78E-003 m	7.09E-03 m
1m	9.70E-003 m	7.09E-03 m
0.5m	9.68E-003 m	7.09E-03 m
0.25m	9.67E-003 m	7.09E-03 m

The errors were plotted in Figure (308.94).

The Real-ESSI model fei/DSL files for the table above are [HERE](#).

⁵Stephen Timoshenko, Theory of plates and shells (2nd edition). MrGRAW-Hill Inc, page202, 1959.

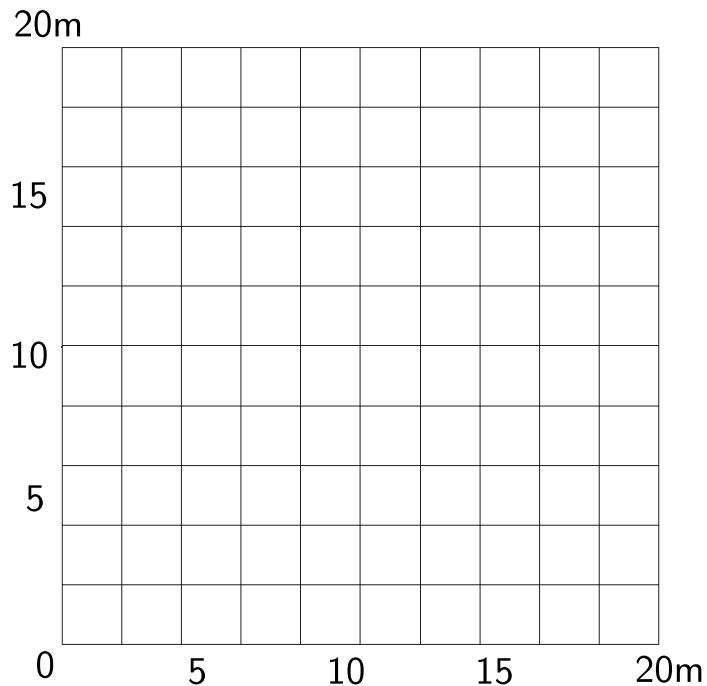


Figure 308.88: 4NodeANDES edge simply supported square plate with element side length 2m.

Table 308.27: Errors for 4NodeANDES square plate with four edges simply supported.

Element type	4NodeANDES
Element side length	Height:1.00m
10m	60.34%
5m	45.14%
2m	37.83%
1m	36.69%
0.5m	36.40%
0.25m	36.32%

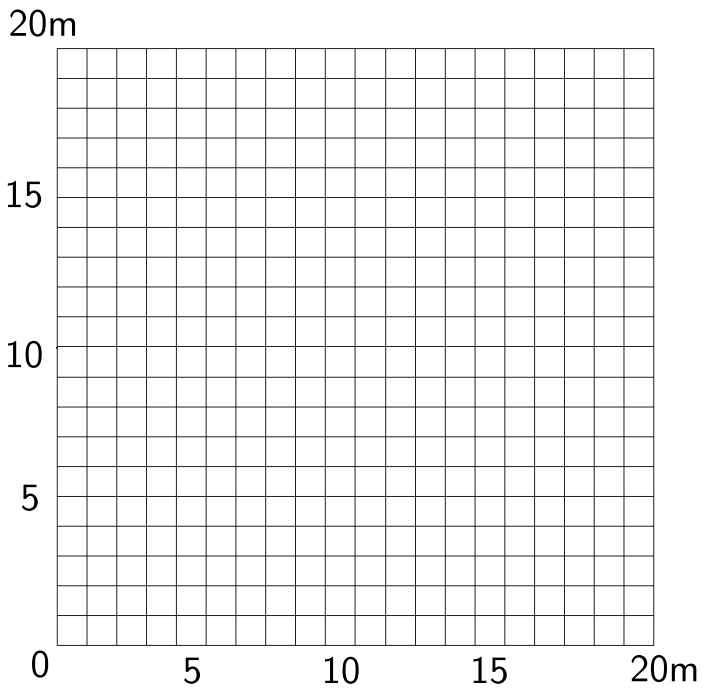


Figure 308.89: 4NodeANDES edge simply supported square plate with element side length 1m.

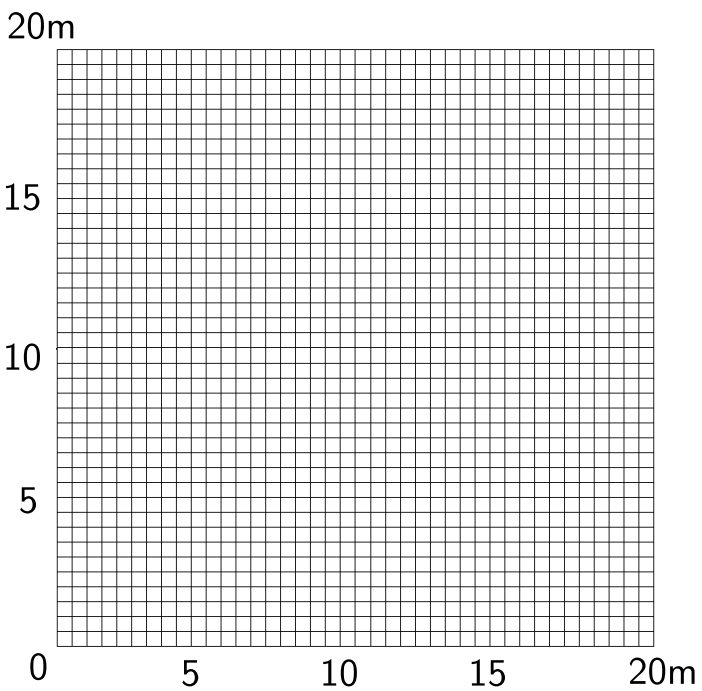


Figure 308.90: 4NodeANDES edge simply supported square plate with element side length 0.5m.

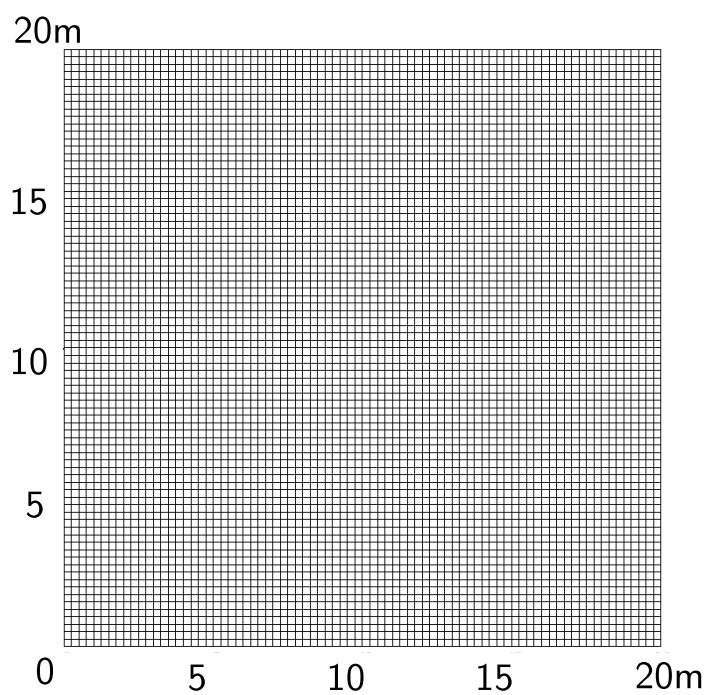


Figure 308.91: 4NodeANDES edge simply supported square plate with element side length 0.25m.

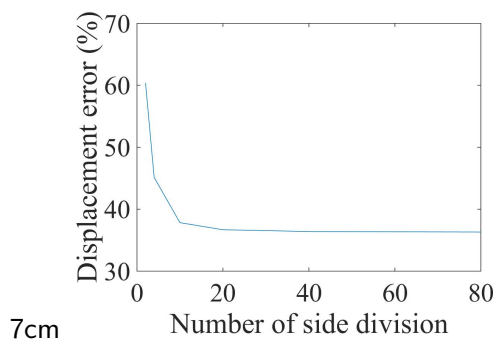


Figure 308.92: Error scale 0% - 70%.

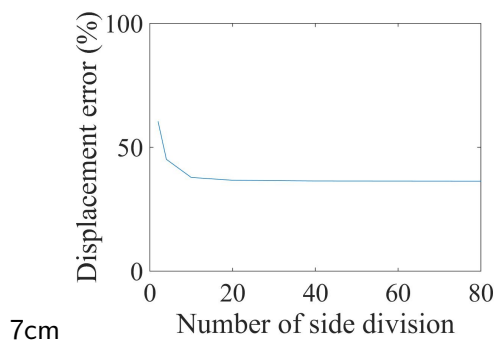


Figure 308.93: Error scale 0% - 100%.

Figure 308.94: 4NodeANDES square plate with edge simply supported: Displacement error versus Number of side division

308.6.6 Verification of 4NodeANDES circular plate with all edges clamped

Problem description: Diameter=20m, Height=1m, Force=100N, E=1E8Pa, $\nu = 0.3$.

The four edges are clamped.

The load is the uniform normal pressure on the whole plate.

The plate flexural rigidity is

$$D = \frac{Eh^3}{12(1-\nu^2)} = \frac{10^8 N/m^2 \times 1^3 m^3}{12 \times (1 - 0.3^2)} = 9.1575 \times 10^6 N \cdot m \quad (308.9)$$

The theoretical solution⁶ is

$$d = \frac{qa^4}{64D} = \frac{100N/m^2 \times 10^4 m^4}{64 \times 9.1575 \times 10^6 N \cdot m} = 1.7106 \times 10^{-3} m \quad (308.10)$$

The 4NodeANDES were shown in Figures (308.95) - (308.100).

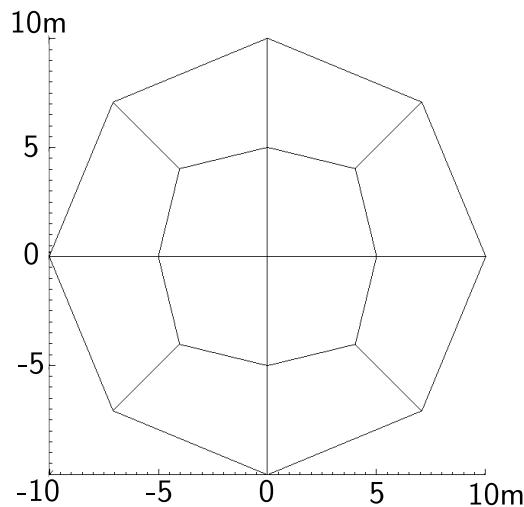


Figure 308.95: 4NodeANDES edge clamped circular plate with element side length 10m.

The results were listed in Table (308.28).

The errors were listed in Table (308.29).

The errors were shown in Figure (308.103).

The Real-ESSI model fei/DSL files for the table above are [HERE](#).

⁶Stephen Timoshenko, Theory of plates and shells (2nd edition). MrGRAW-Hill Inc, page55, 1959.

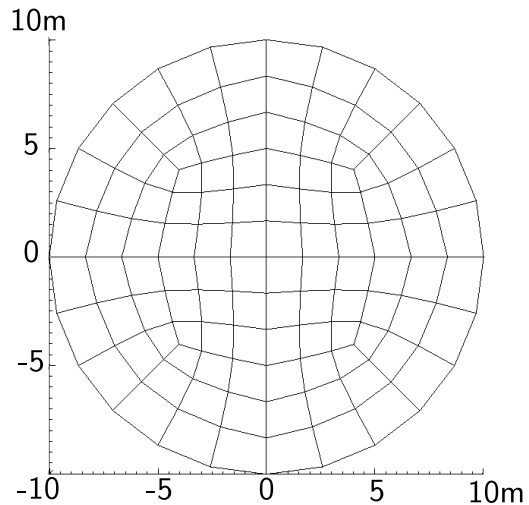


Figure 308.96: 4NodeANDES edge clamped circular plate with element side length 5m.

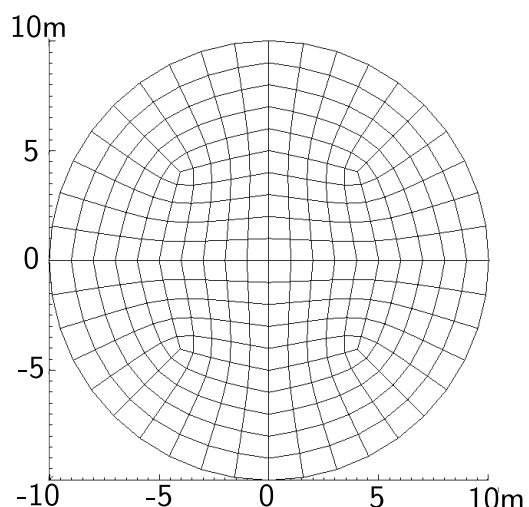


Figure 308.97: 4NodeANDES edge clamped circular plate with element side length 2m.

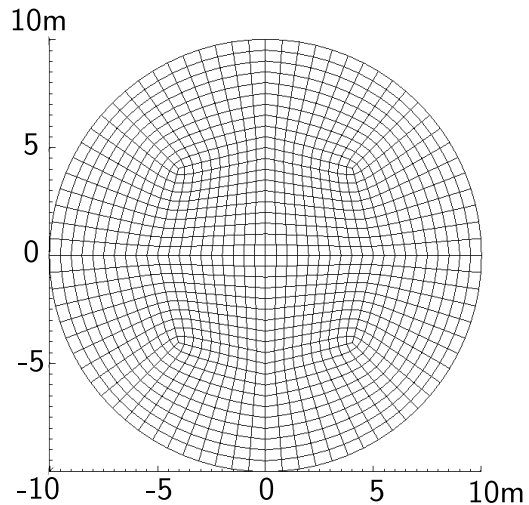


Figure 308.98: 4NodeANDES edge clamped circular plate with element side length 1m.

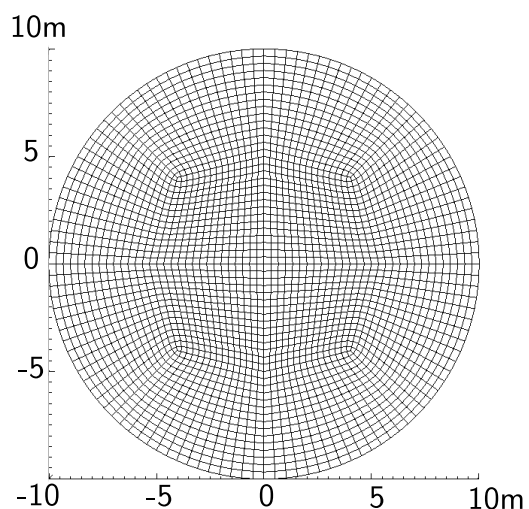


Figure 308.99: 4NodeANDES edge clamped circular plate with element side length 0.5m.

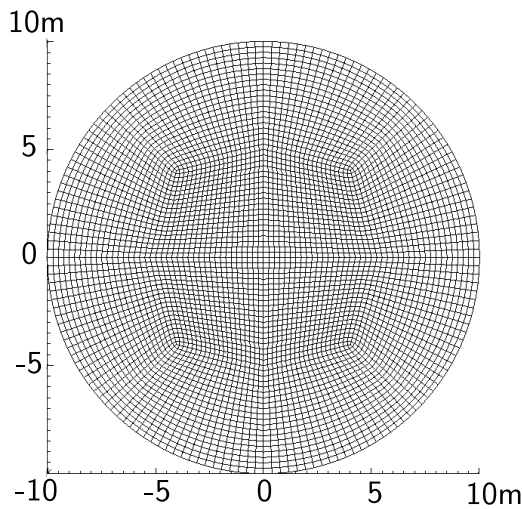


Figure 308.100: 4NodeANDES edge clamped circular plate with element side length 0.25m.

Table 308.28: Results for 4NodeANDES circular plate with four edges clamped.

Element type	4NodeANDES	Theoretical displacement
Element side length	Height:1.00m	
10m	1.69E-003 m	1.706E-03 m
5m	1.97E-003 m	1.706E-03 m
2m	1.97E-003 m	1.706E-03 m
1m	1.96E-003 m	1.706E-03 m
0.5m	1.96E-003 m	1.706E-03 m
0.25m	1.96E-003 m	1.706E-03 m

Table 308.29: Errors for 4NodeANDES circular plate with four edges clamped.

Element type	4NodeANDES
Element side length	Height:1.00m
10m	0.71%
5m	15.43%
2m	15.31%
1m	15.16%
0.5m	15.13%
0.25m	15.12%

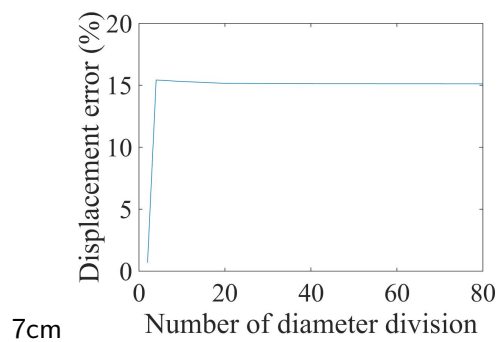


Figure 308.101: Error scale 0% - 20%.

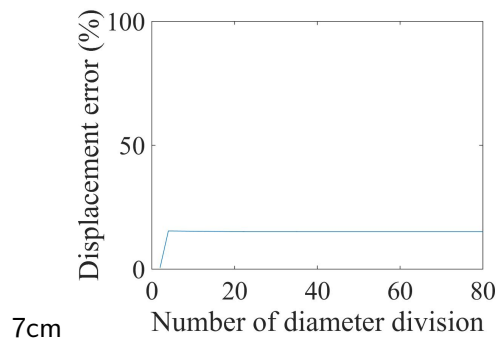


Figure 308.102: Error scale 0% - 100%.

Figure 308.103: 4NodeANDES circular plate with edge clamped: Displacement error versus Number of side division

308.6.7 Verification of 4NodeANDES circular plate with all edges simply supported

Problem description: Diameter=20m, Height=1m, Force=100N, E=1E8Pa, $\nu = 0.3$.

The four edges are simply supported.

The load is the uniform normal pressure on the whole plate.

The plate flexural rigidity is

$$D = \frac{Eh^3}{12(1-\nu^2)} = \frac{10^8 N/m^2 \times 1^3 m^3}{12 \times (1 - 0.3^2)} = 9.1575 \times 10^6 N \cdot m \quad (308.11)$$

The theoretical solution⁷ is

$$d = \frac{(5 + \nu)qa^4}{64(1 + \nu)D} = \frac{(5 + 0.3) \times 100N/m^2 \times 10^4 m^4}{64 \times (1 + 0.3) \times 9.1575 \times 10^6 N \cdot m} = 6.956 \times 10^{-3} m \quad (308.12)$$

The 4NodeANDES were shown in Figure (308.104) - (308.109).

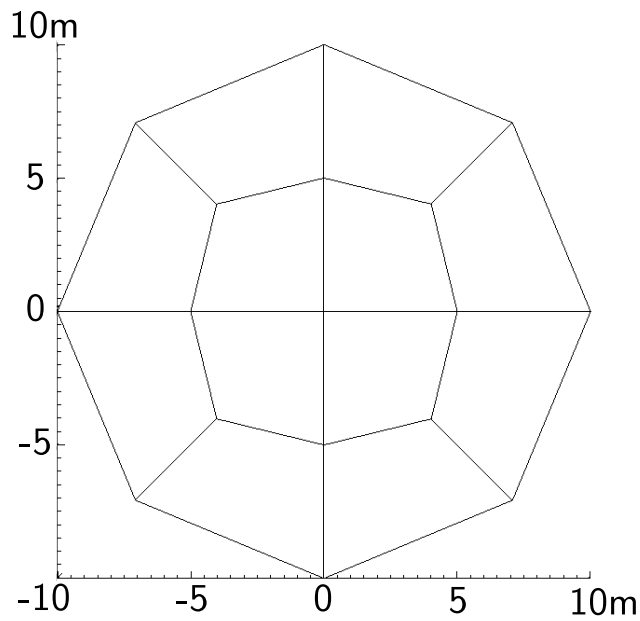


Figure 308.104: 4NodeANDES edge simply supported circular plate with element side length 10m.

The results were listed in Table (308.30).

The errors were listed in Table (308.31).

The errors were plotted in Figure (308.112).

The Real-ESSI model fei/DSL files for the table above are [HERE](#).

⁷Stephen Timoshenko, Theory of plates and shells (2nd edition). MrGRAW-Hill Inc, page55, 1959.

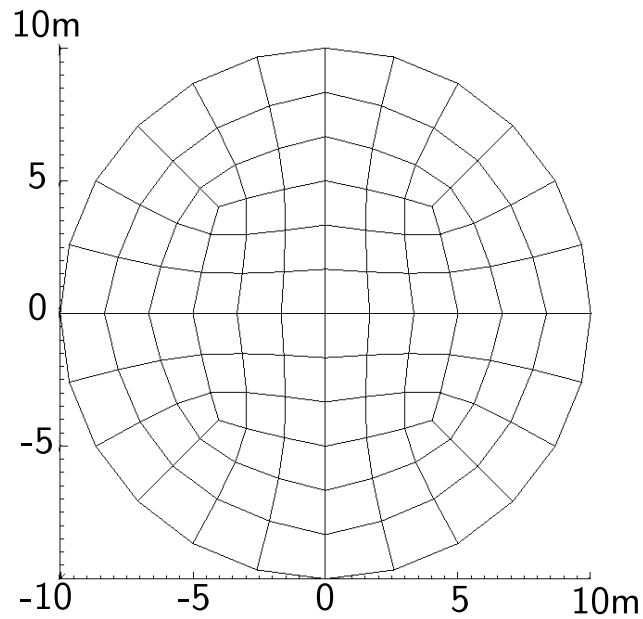


Figure 308.105: 4NodeANDES edge simply supported circular plate with element side length 5m.

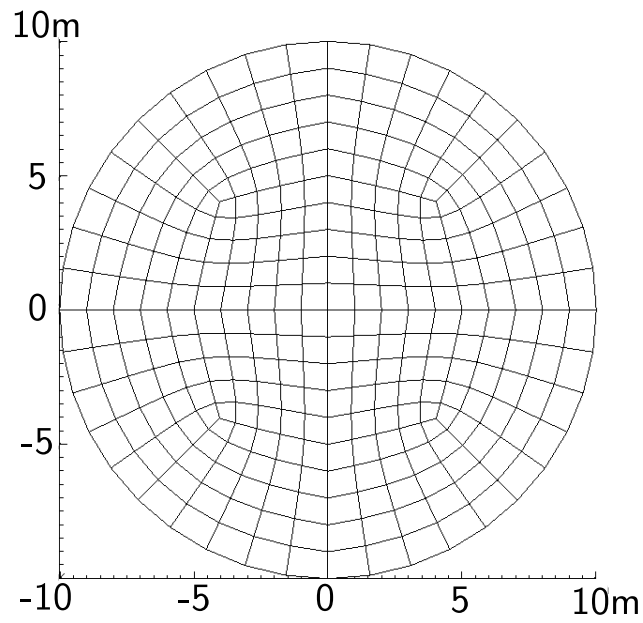


Figure 308.106: 4NodeANDES edge simply supported circular plate with element side length 2m.

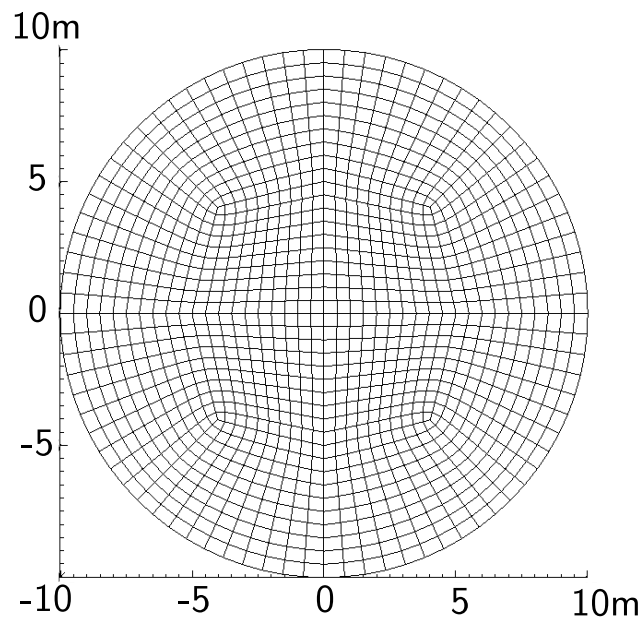


Figure 308.107: 4NodeANDES edge simply supported circular plate with element side length 1m.

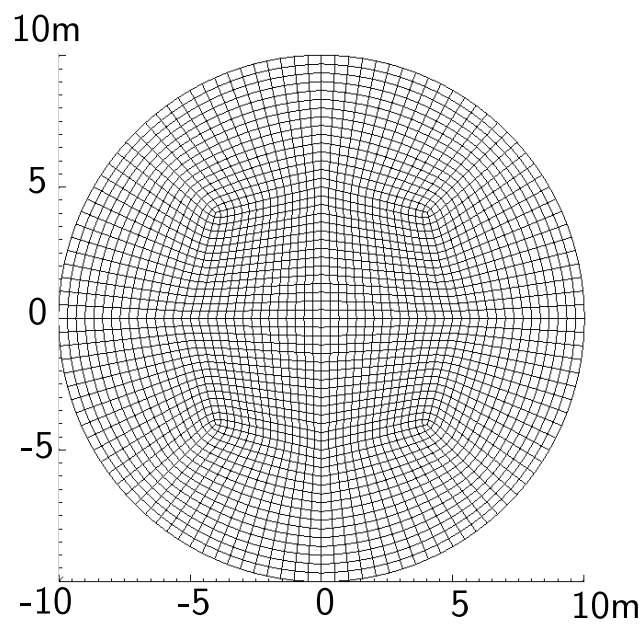


Figure 308.108: 4NodeANDES edge simply supported circular plate with element side length 0.5m.

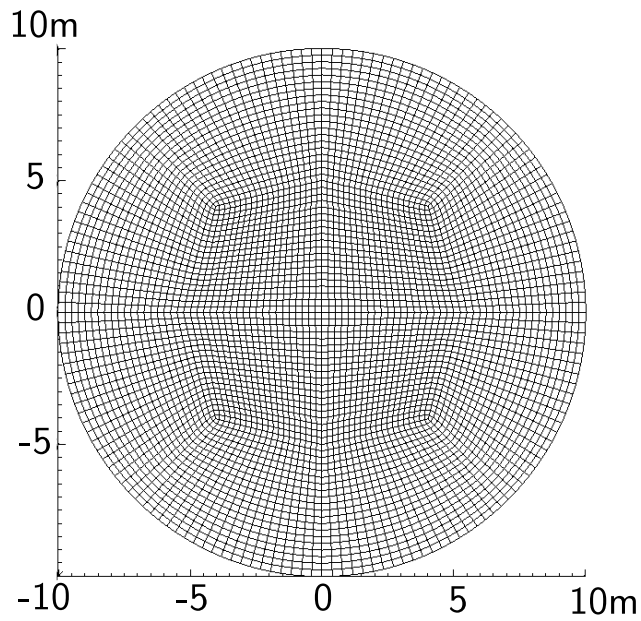


Figure 308.109: 4NodeANDES edge simply supported circular plate with element side length 0.25m.

Table 308.30: Results for 4NodeANDES cicular plate with four edges simply supported.

Element type	4NodeANDES	Theoretical displacement
Element side length	Height:1.00m	
10m	7.50E-003 m	6.956E-03 m
5m	7.29E-003 m	6.956E-03 m
2m	7.25E-003 m	6.956E-03 m
1m	7.23E-003 m	6.956E-03 m
0.5m	7.22E-003 m	6.956E-03 m
0.25m	7.22E-003 m	6.956E-03 m

Table 308.31: Errors for 4NodeANDES circular plate with four edges simply supported.

Element type	4NodeANDES
Element side length	Height:1.00m
10m	7.75%
5m	4.73%
2m	4.15%
1m	3.89%
0.5m	3.84%
0.25m	3.82%

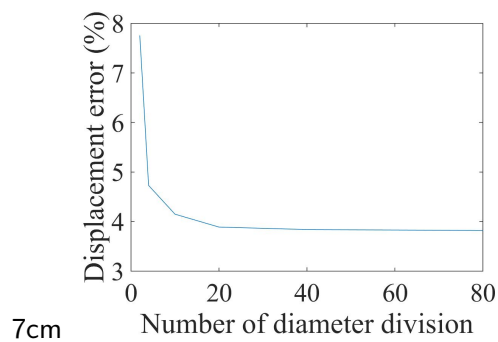


Figure 308.110: Error scale 0% - 8%.

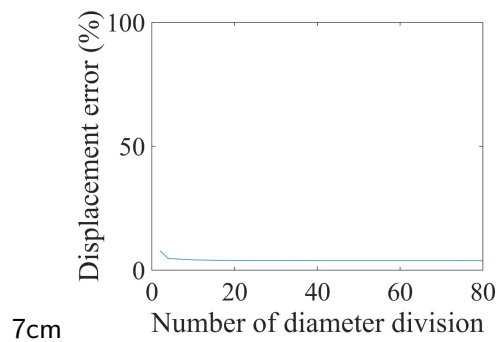


Figure 308.111: Error scale 0% - 100%.

Figure 308.112: 4NodeANDES circular plate with edge simply supported' Displacement error versus Number of side division

Chapter 309

Verification and Validation for Static and Dynamic Behavior of Special Elements (Contacts/Interfaces/Joints, Gap/Frictional, Isolators)

(2010-2011-2016-2017-2019-2021-)

(In collaboration with Prof. Sumeet Kumar Sinha and Dr. Yuan Feng, and Prof. Han Yang)

309.1 Chapter Summary and Highlights

309.2 Verification of Static Penalty Contact/Interface/Joint Element Modeling and Simulation

References for interface elements: [Hird and Russell \(1990\)](#), [AG \(2020\)](#).

This section presents the verification of Penalty Stiffness based Frictional Contact/Interface/Joint Element using analytical simple solutions to verify the numerical solutions obtained by the application of the developed model. The examples show the response of element for different cases. Solution sensitivity on penalty stiffness is also discussed in details for those examples.

Theoretically, the penalty stiffness should be infinite, but for numerical stability of the solution, it can go upto 10^{16} . This is because for a double precision computer, machine epsilon $\epsilon \approx 10^{-16}$ and thus the corresponding displacement for the penalty springs can go low only till 10^{-16} . For all the cases considred below in this cases, the convergence criteria was as $||\delta U|| \leq 10^{-12}$.

309.2.1 Static Normal Contact/Interface/Joint Verification

A Two-bar truss example is considered here to verify the normal contact/interface/joint for different normal loading conditions and different penalty stiffness K_n . This is an example of normal loading on a 1-D contact/interface/joint between two bars separated by an initial gap of $\delta_{in} = 0.1m$. An illustrative diagram of the problem statement is shown below.

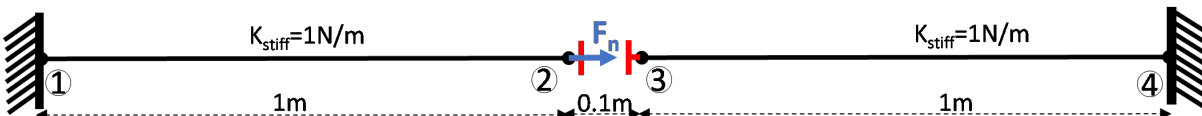


Figure 309.1: Illustration of two bar normal Contact/Interface/Joint problem under monotonic loading with inital gap.

A snapshot of the code for the contact/interface/joint element is shown below. The Real-ESSI model fei/DSL files for this example can be downloaded [HERE](#).

```

1 add element #3 type FrictionalPenaltyContact with nodes (2,3)
2   normal_stiffness =1e10*N/m
3   tangential_stiffness = 1e10*Pa*m
4   normal_damping = 0*kN/m*s
5   tangential_damping = 0*kN/m*s
6   friction_ratio = 0.3
7   contact_plane_vector = (1,0,0);

```

309.2.1.1 Case 1: Monotonic Loading with initial gap $\delta_{in} = 0.1m$

In this case a force of 0.3N is applied to Node 2. From Figure 309.2, the solution converges to the analytical result for $K_n = 100N/m$ i.e 100 times the stiffness of bar element. Please note that, the for penalty stiffness $> 10e15$, the convergence fails (when the bars contact/interface/joint mode changes), as the global stiffness matrix becomes *ill conditions*. Thus, the penalty stiffness cannot be too large.

309.2.1.2 Case 2: Monotonic Loading with no initial gap $\delta_{in} = 0m$

In this case a force of 0.3N is applied to Node 2. From Figure 309.3, the solution again converges to the analytical result for $K_n = 100N/m$ i.e 100 times the stiffness of bar element.

309.2.1.3 Case 3: Cyclic Loading with initial gap $\delta_{in} = 0.1m$

For cyclic loading cases considered below, the loading force F_n applied is shown in Figure 309.4. From Figure 309.5, the solution again converges to the analytical result for $K_n = 100N/m$ i.e 100 times the stiffness of bar element.

309.2.1.4 Case 4: Cyclic Loading with no initial gap $\delta_{in} = 0m$

The same cyclic load shown in Figure 309.4 is again applied for this case. From Figure ??, the solution again converges to the analytical result for $K_n = 100N/m$ i.e 100 times the stiffness of bar element.

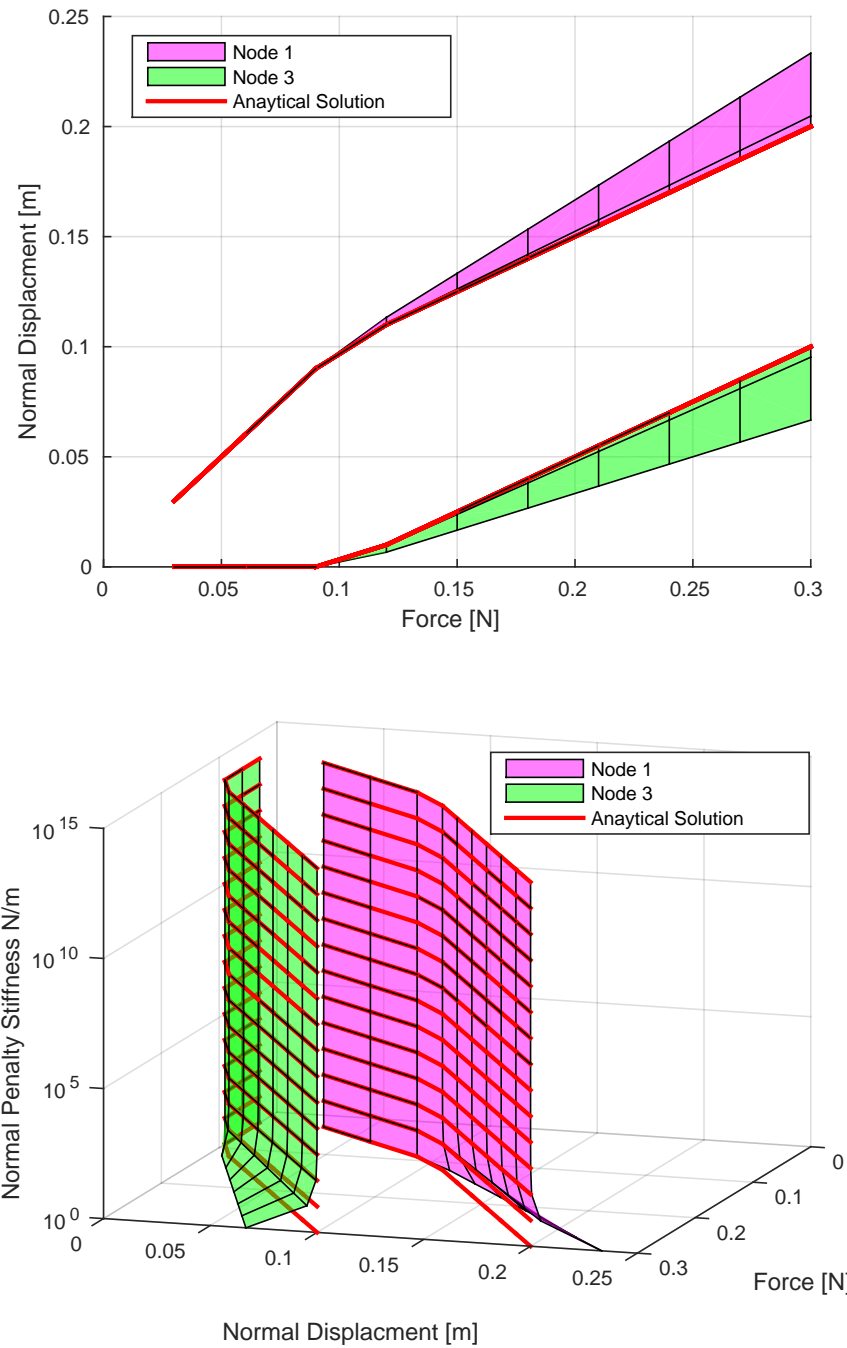


Figure 309.2: Displacements of Node 2 and Node 3 with change in normal penalty stiffness for $\delta_{in} = 0.1m$

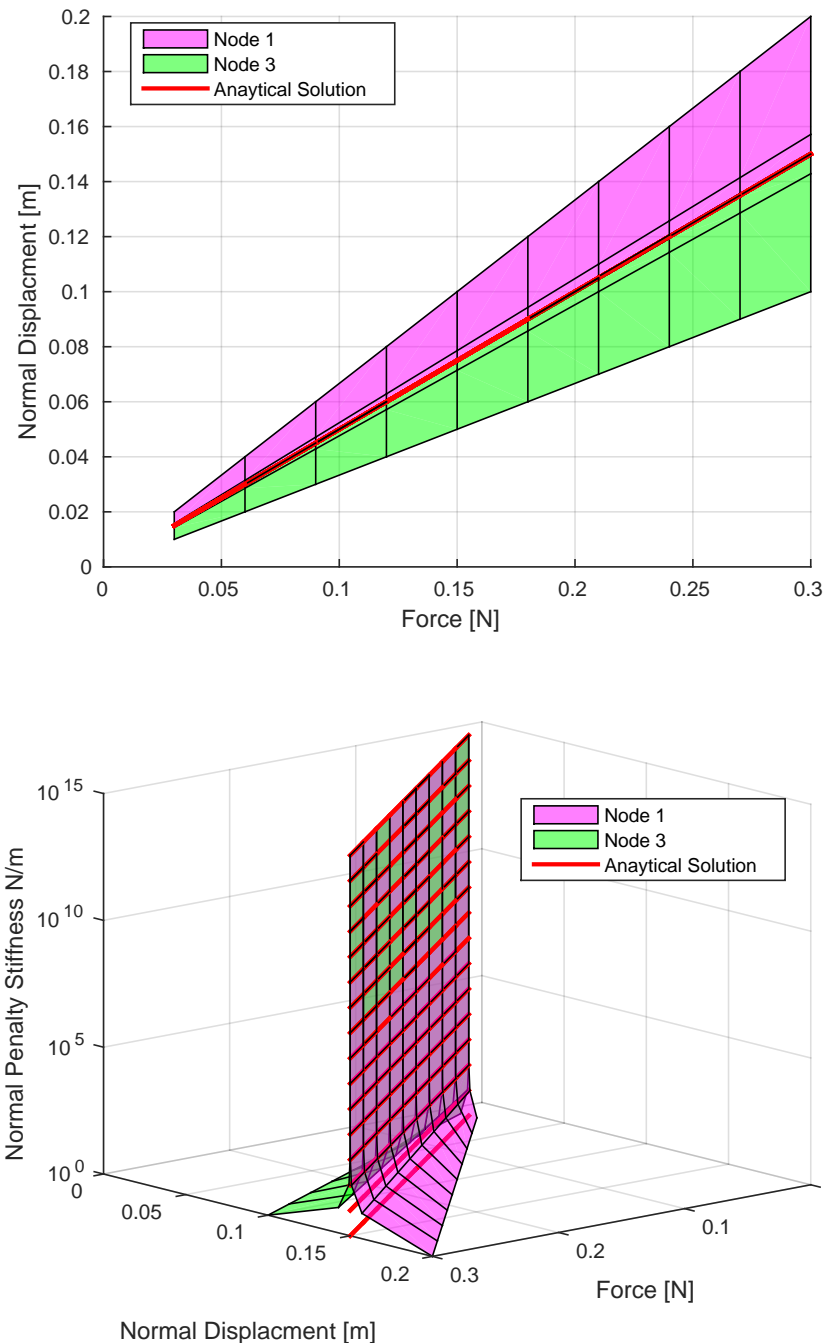


Figure 309.3: Displacements of Node 2 and Node 3 with change in normal penalty stiffness for $\delta_{in} = 0m$

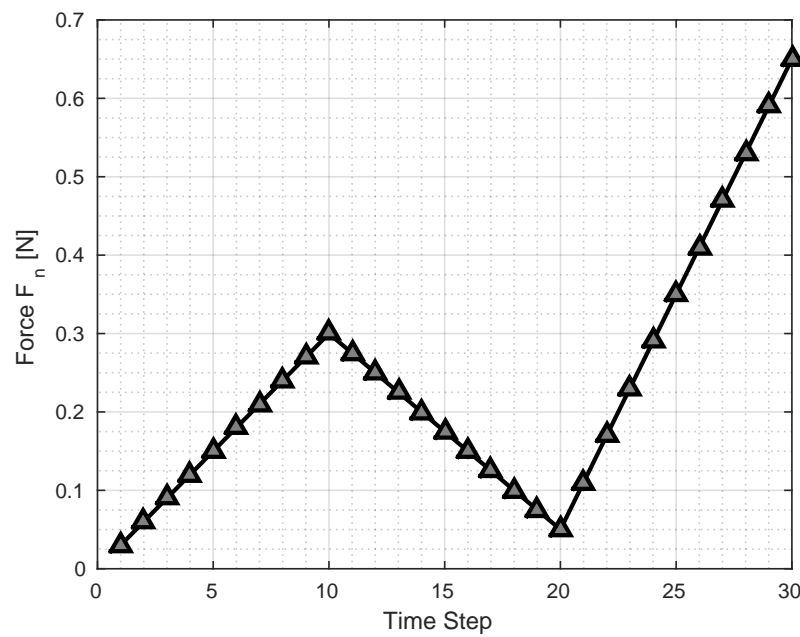


Figure 309.4: Cyclic normal load applied on two bar contact/interface/joint problem.

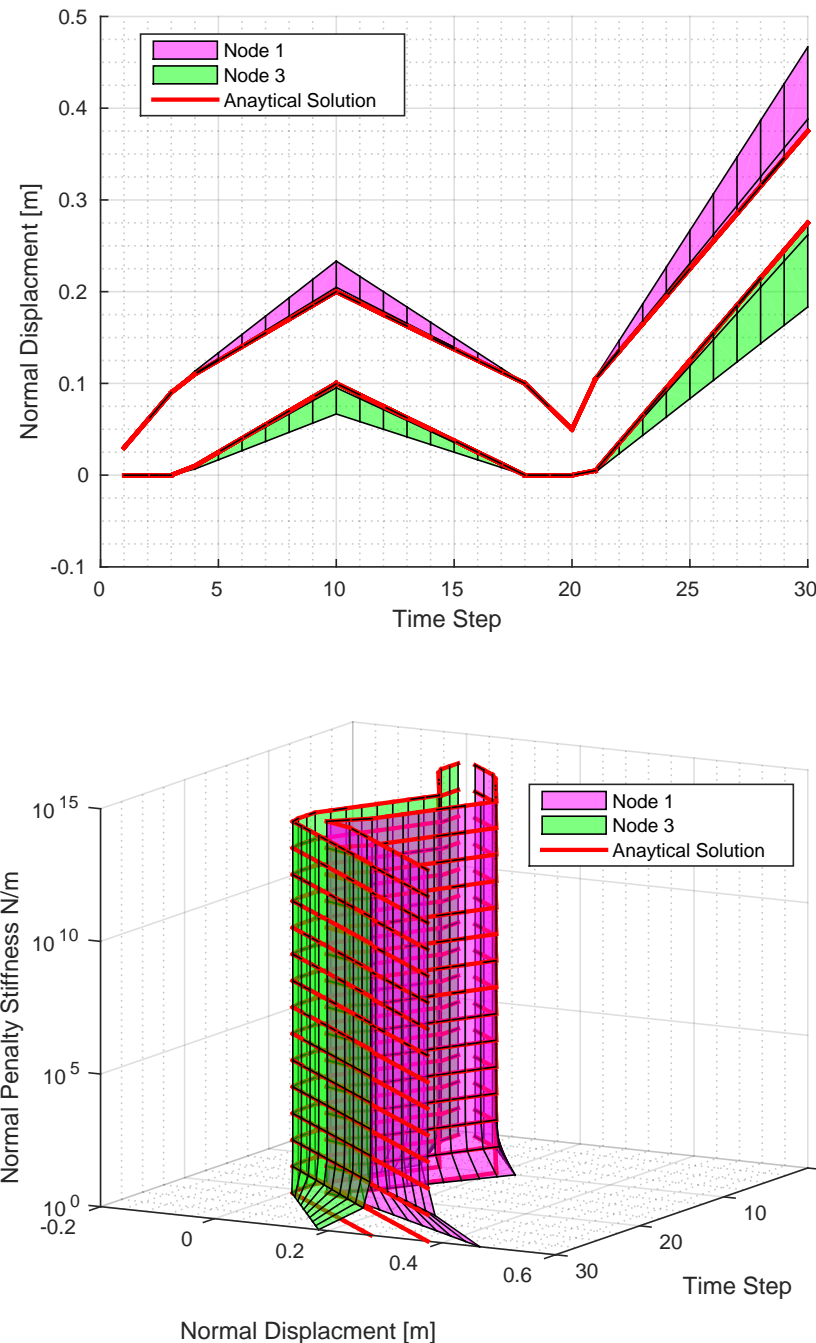


Figure 309.5: Displacements of Node 2 and Node 3 with change in normal penalty stiffness for $\delta_{in} = 0\text{m}$

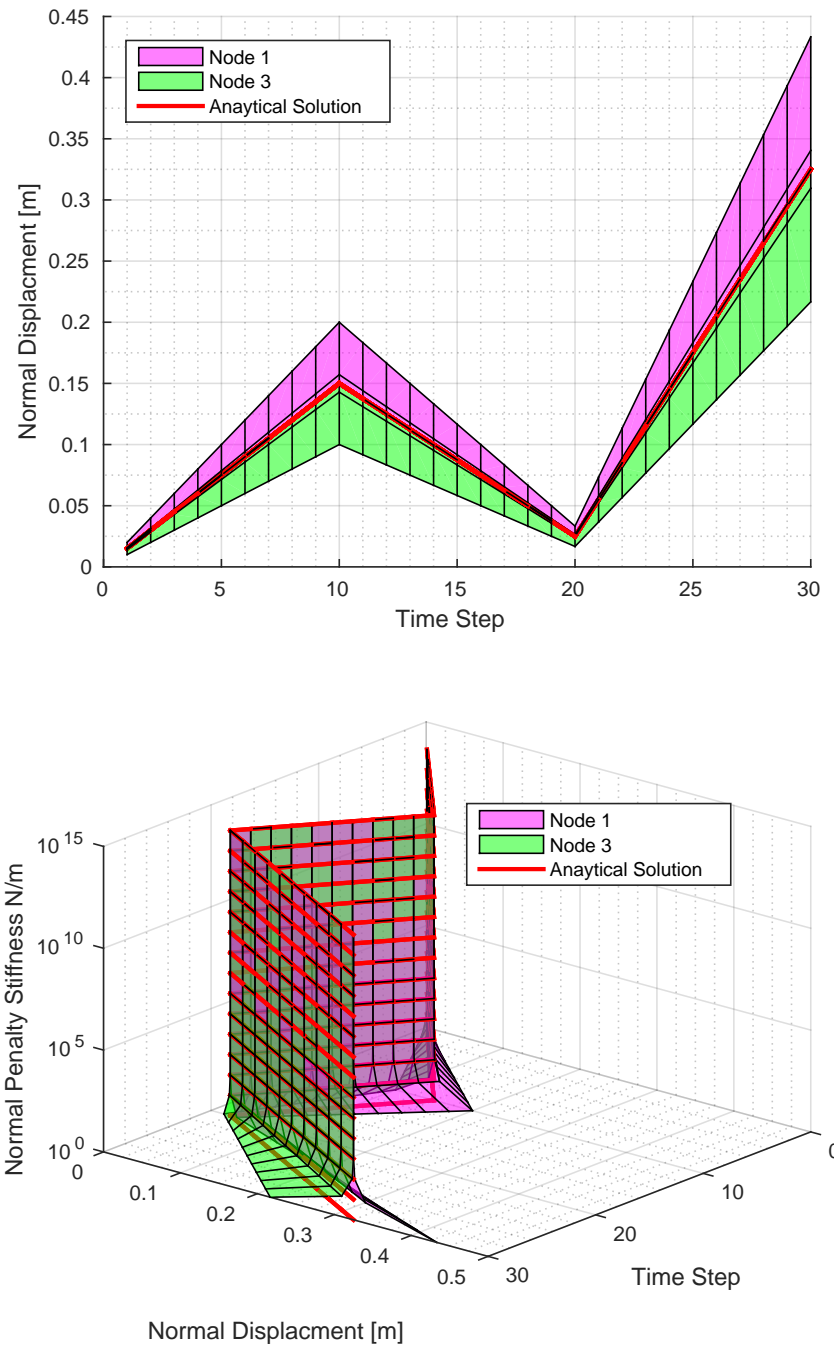


Figure 309.6: Displacements of Node 2 and Node 3 with change in normal penalty stiffness for $\delta_{in} = 0\text{m}$

309.2.2 Static Frictional Tangential Contact/Interface/Joint Verification

A simple 3-D truss example with Normal confinement in z-direction of $F_N = 0.5N$, friction coefficient $\mu = 0.2$ and shear loading of magnitude $F_s = 0.5N$ is considered to verify the tangential behaviour of contact/interface/joint element. Different cases as discussed below are considered.

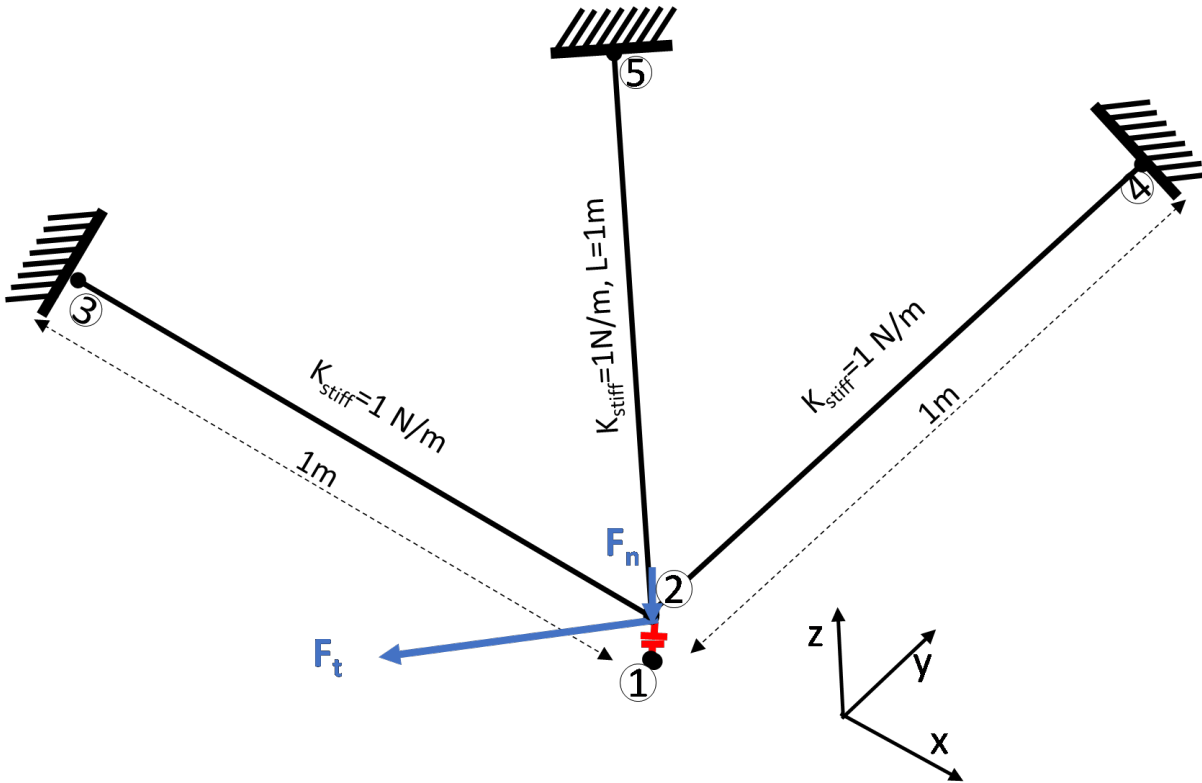


Figure 309.7: Illustration of 3-D three bar contact/interface/joint problem.

A snapshot of the properties of contact/interface/joint element is shown below. The Real-ESSI model fei/DSL files for this example can be downloaded [HERE](#).

```

1 add element #4 type FrictionalPenaltyContact with nodes (1,2)
2   normal_stiffness =1e10*N/m
3   tangential_stiffness = 1e10*Pa*m
4   normal_damping = 0*kN/m*s
5   tangential_damping = 0*kN/m*s
6   friction_ratio = 0.2
7   contact_plane_vector = (0,0,1);

```

309.2.2.1 Case 1: Verification of the yield surface for different loading angles with fixed normal confinement.

A Shear force of magnitude of $F_s = 0.5N$ was applied in 20 steps in different loading directions. The response of the contact/interface/joint element and the displacement of node 2 is shown in Figure 309.8 and Figure 309.9 respectively . It can be observed that the contact/interface/joint element slips at magnitude of force $||F|| - > (F_n = 0.5) * (\mu = 0.2) - > 0.1N$ for all loading angles.

In Figure 309.9, it can be observed that for the first 4 steps, there is no (zero) displacement for node 2 because of the stick case. When the load exceeds 0.1N, slip occurs and node 2 starts to undergo deformation.

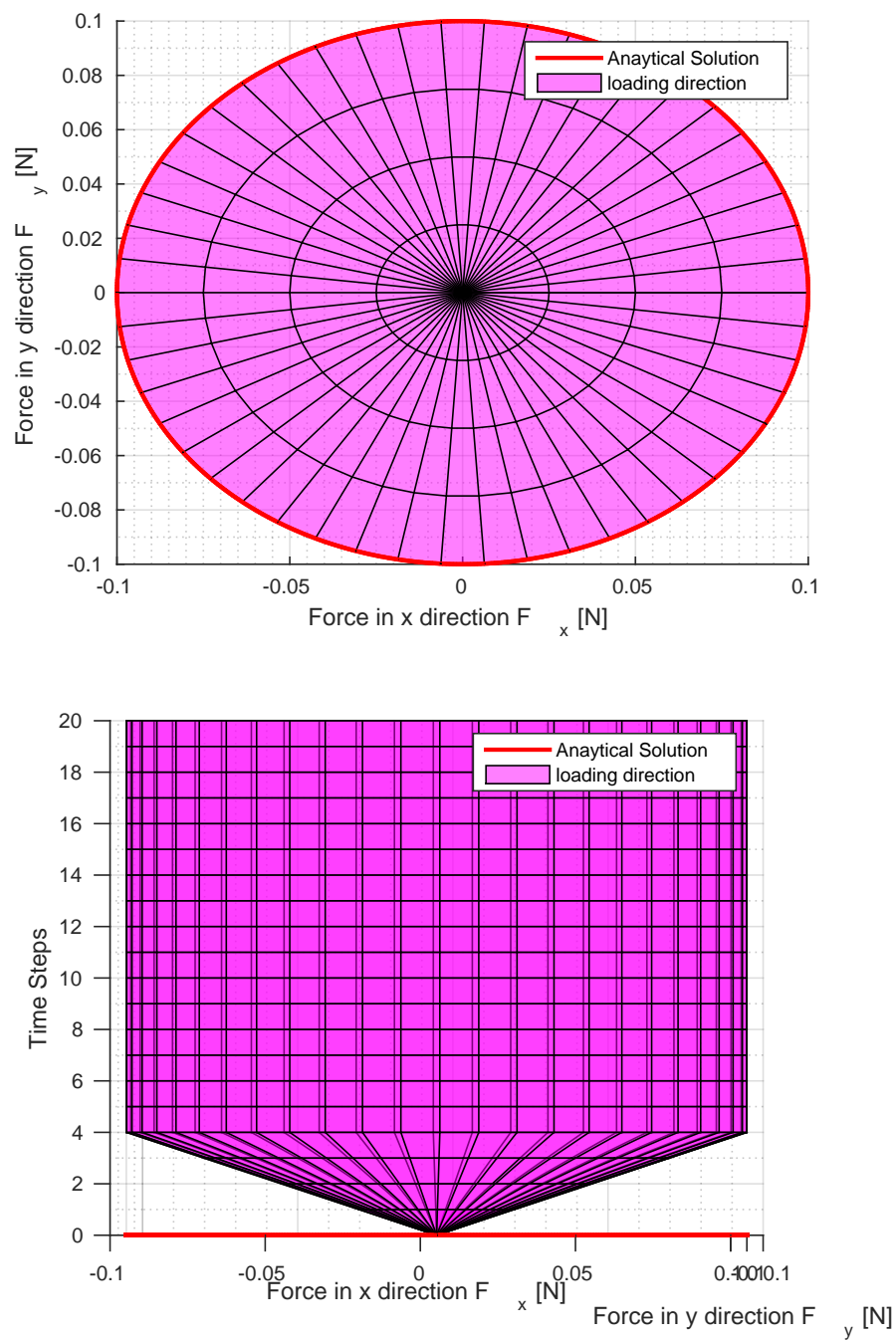


Figure 309.8: Response of contact/interface/joint element for different loading angles for confinement of $0.5N$ and coefficient of friction as 0.2

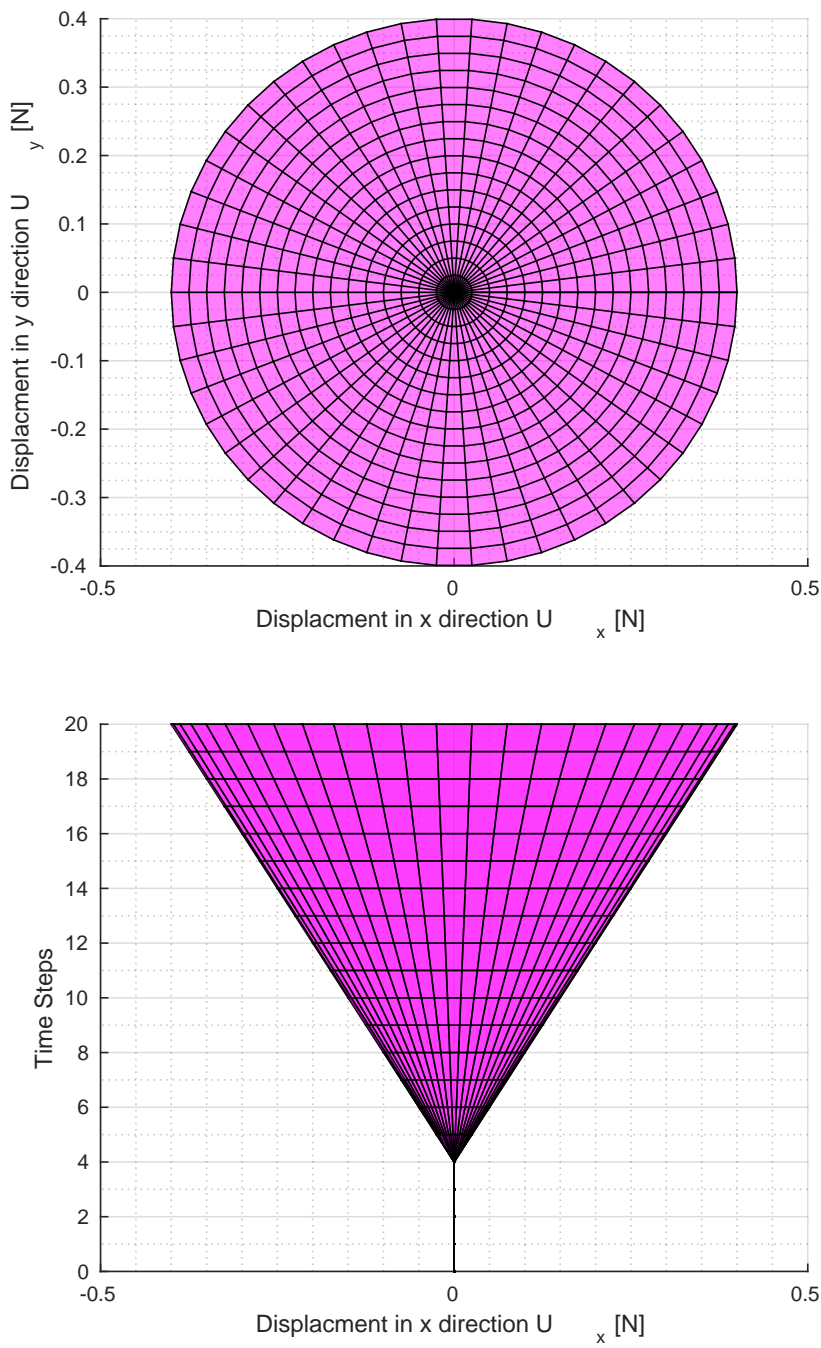


Figure 309.9: Displacement of Node No. 2 in x and y direction for different loading angles for confinement of $0.5N$ and coefficient of friction as 0.2

309.3 Verification of Static and Dynamic Contact/interface/Joint Element Modeling and Simulation

Solution verification of the contact/interface/joint element formulation and its implementation is presented in what follows. Analytical simple solutions for the frictional contact/interface/joint element are used to verify numerical solutions obtained by application of the developed model. The examples provided show the response of the contact element in several situations. Initially, the element is tested by connecting two nodes that each have $3dof$, subsequently, the element is even implemented to simulate a contact/interface/joint between two nodes that each have $7dof$ and two nodes with different dofs: $3dof$ for the first one and $7dof$ for the second one.

The parameters used for the contact/interface/joint element are listed in Table 309.1.

Parameter	Value
C_N [kN/m]	10420
\bar{v}_{max} [m]	0.001
K_T [kN/m]	1e7
μ [-]	0.6

Table 309.1: Contact/interface/joint element parameters.

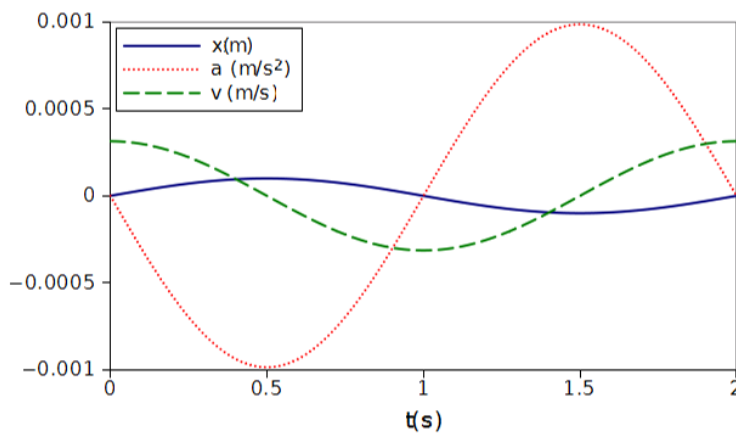


Figure 309.10: Input signal: time history of displacement, acceleration and velocity.

309.3.1 Truss Examples

The first example (Figure 309.11) represents five nodes: 1,2,3,4,5. Nodes 2,3,4,5 are connected by three truss elements and a contact/interface/joint element links node 1 and 2. All degrees of freedom of nodes 1,3,4,5 are fixed, whereas a sine wave displacement time-history (Figure 309.10) is applied to node 2 along x direction and the normal force acting within the contact/interface/joint element is recorded. The results, represented in Figure 309.12, show the normal response of this new contact/interface/joint element. As the timestep decreases, the force-displacement curves tends to be similar to the one represented by (??).

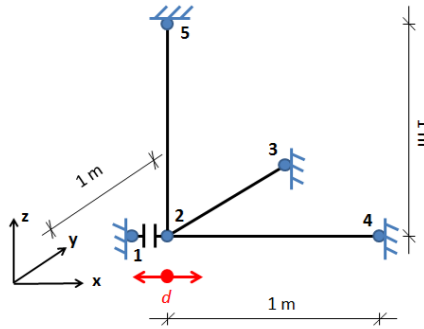


Figure 309.11: System composed of one contact/interface/joint element and three truss elements. A sine wave displacement time-history is applied to node (2).

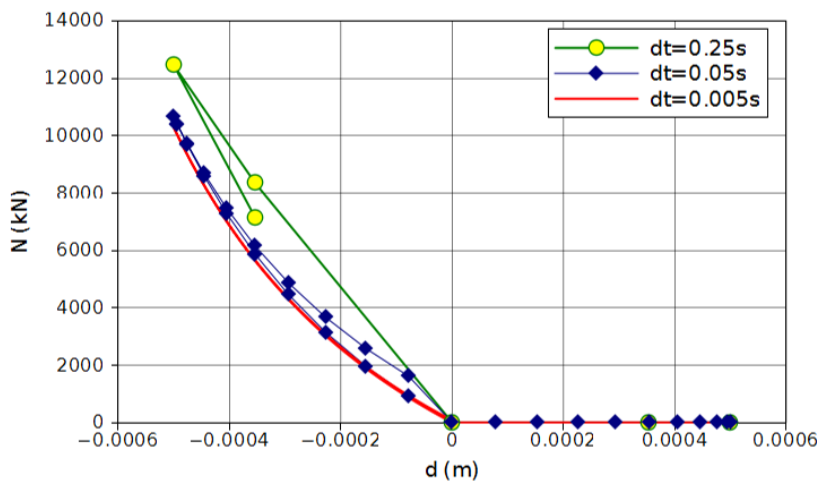


Figure 309.12: Normal force vs normal-relative displacement in contact/interface/joint element.

The second example (Figure 309.13) shows the tangential response of this new contact/interface/joint element. The geometry of the problem is the same as Figure 309.11, but an axial force ($p = 1140 \text{ kN}$), constant in time, and a sine wave time-history displacement are applied to node 2. The results, represented in Figure 309.14, show that the response is not dependent on the timestep used for the analysis. Due to the elastic-perfectly-plastic behavior, associated with Mohr-Coulomb yield criteria, the maximum shear force (t_{max}) that the contact/interface/joint element can sustain is 684 kN , equal to $t_{max} = \mu \cdot p = 0.6 \cdot 1140 \text{ kN}$.

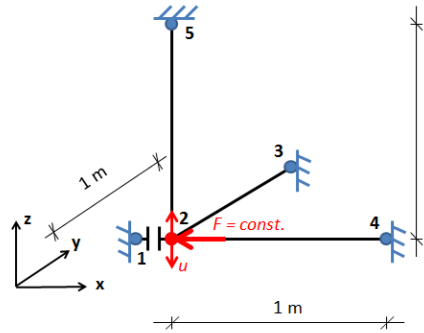


Figure 309.13: Same system used in Figure 309.11. A normal force constant in time ($F = 1140 \text{ kN}$) and a sine wave displacement time history are applied to node (2).

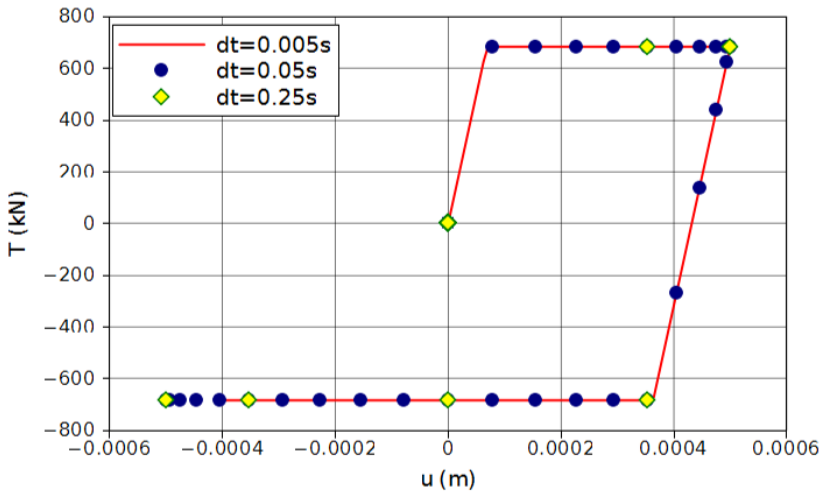


Figure 309.14: $p = 1140 \text{ kN}$. Transversal force in the contact/interface/joint element vs transversal-relative displacement

309.3.2 Single Brick Element Examples

The contact/interface/joint element is now used to connect each node (5,6,7,8) of the bottom face of an eight node hexahedral element (hex8) to the corresponding node attached to the ground (1,2,3,4).

A linear elastic constitutive model is used for the eight node brick and the parameters are listed in Table 309.2.

Parameter	Value
E [kPa]	1.5e10
ν [-]	0.0

Table 309.2: Brick Element Parameters

In the first example (Figure 309.15) the time-history displacement, shown in Figure 309.10, is applied in the vertical direction to each node of the top surface of the brick element (9,10,11,12) and the time-history normal force induced in each contact element is represented in Figure 309.16. It is worth noting that the normal force is positive if the displacement of the top surface is downward, whereas it is zero if the detachment occurs caused by the upward movement.

Through the second example, shown in Figure 309.17, the transversal response of the contact/interface/joint elements is highlighted. The vertical normal force ($F_v = 50\text{kN}$), constant in time, and a horizontal time-history displacement are applied to each node of the top surface and the transversal response is shown in Figure 309.18. As stated in section 309.3.1, the maximum shear force that the contact element can sustain is 30 kN , equal to $t_{max} = \mu \cdot p = 0.6 \cdot 50\text{kN}$.

The third example is focused on the transversal response of the contact/interface/joint element under variable normal forces. In fact, a sine wave time-history horizontal displacement and a vertical force are applied to each node of the top surface of the brick. The normal force is variable in time according to the factor ($Fact(t)$) shown in Figure 309.20 and the vertical force is computed as $F_v(t) = Fact(t) \cdot F_{v,max}$, and $F_{v,max}$ equal to 50 kN . The response of the contact element, shown in Figure 309.21, is independent of the timestep used for the analysis emphasizing the correct numerical implementation.

309.3.3 Double Brick Element Examples

Few other examples are produced taking in consideration two brick elements. The constitutive model used for these two brick elements is linear elastic with the same parameters listed in Table 309.2. Vertical and horizontal time-history displacement are applied to the top surface, shown in Figure 309.22 and Figure 309.23, and variable vertical forces are considered in the example represented in Figure 309.24. The results are the same shown in Figure 309.16, Figure 309.18 and Figure 309.19.

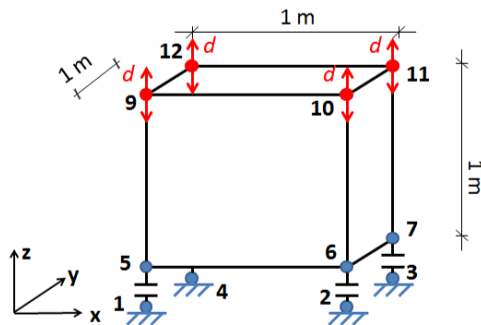


Figure 309.15: Eight-node brick element over four contact/interface/joint elements. A sine wave time-history vertical displacement applied to each node of the top surface.

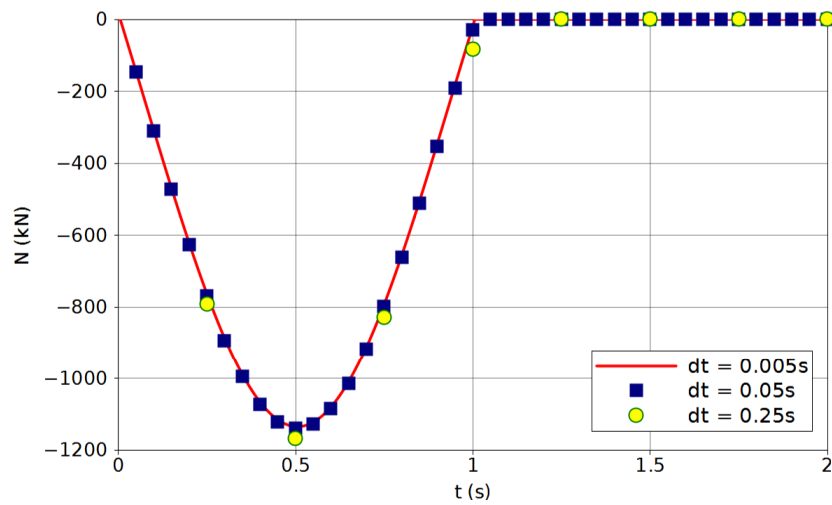


Figure 309.16: Normal force vs time in each contact element.

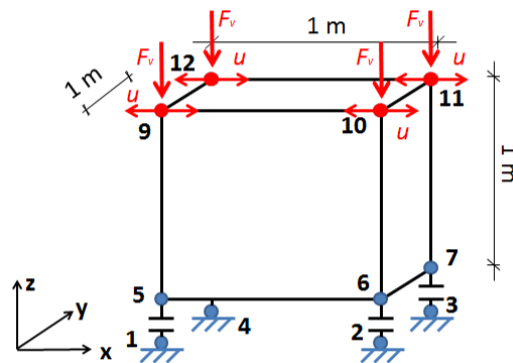


Figure 309.17: Eight-node brick element over four contact/interface/joint elements. $F_v = 50$ kN and a sine wave time-history horizontal displacement applied to each node of the top surface.

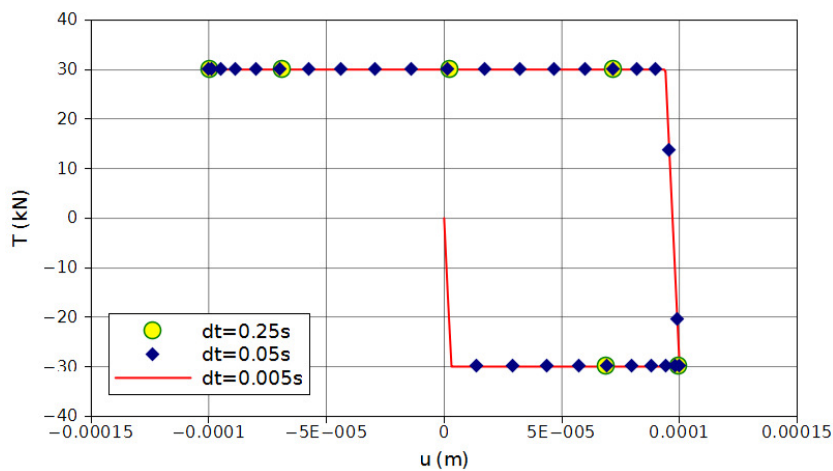


Figure 309.18: Transversal force vs transversal relative-displacement in the contact element with normal force F equal to 50 kN.

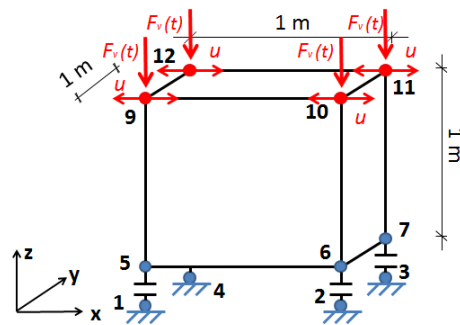


Figure 309.19: Eight-node brick element over four contact/interface/joint elements. Variable vertical force ($F_v(t)$) and a sine wave time-history horizontal displacement applied to each node of the top surface.

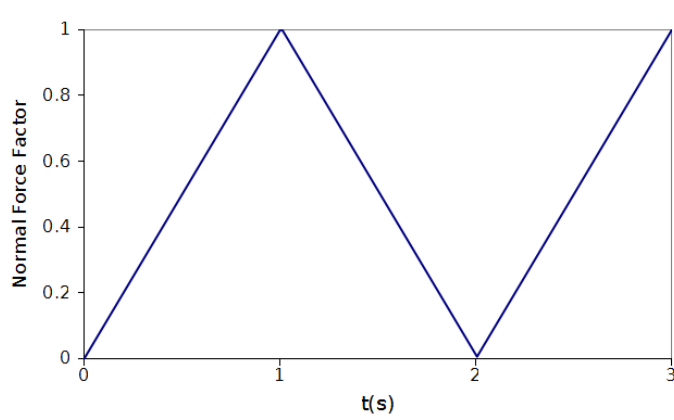


Figure 309.20: Time-history of the normal force factor $Fact(t)$.

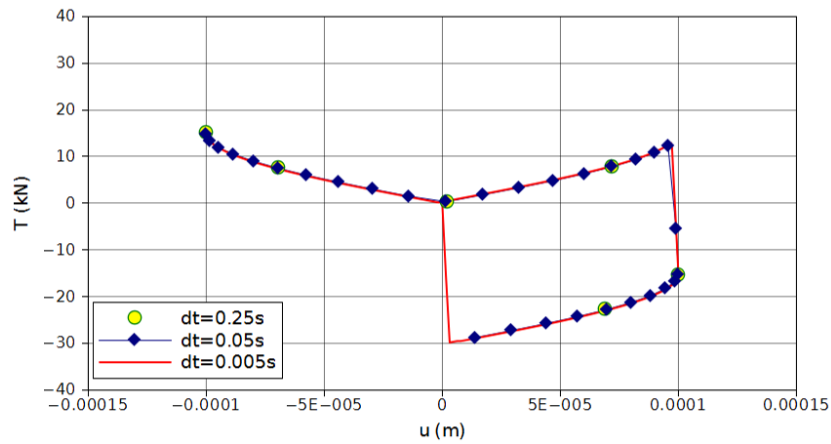


Figure 309.21: Variable normal force. Transversal force vs transversal relative-displacement in each contact element.

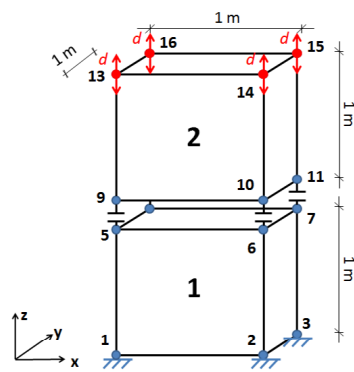


Figure 309.22: Two eight-node brick elements connected by four contact/interface/joint elements. Vertical time-history displacement applied to the nodes of the top surface.

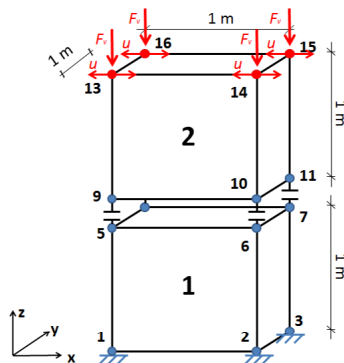


Figure 309.23: Two eight-node brick elements connected by four contact/interface/joint elements. Vertical force, equal to 50 kN and constant in time, and horizontal time-history displacement applied to the nodes of the top surface.

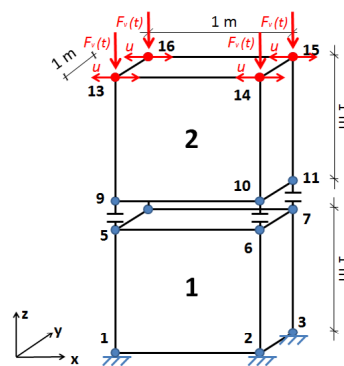


Figure 309.24: Two eight-node brick elements connected by four contact/interface/joint elements. Vertical force, variable in time, and horizontal time-history displacement applied to the nodes of the top surface.

309.4 Verification of Static and Dynamic Coupled (Saturated) Contact/Interface/Joint Element Modeling and Simulation

309.4.1 Dry u-p-U Contact/Interface/Joint

A single brick u - p - U finite element is used to model an oedometric compression shown in Figure 309.25. Horizontal displacements and pore pressure are fixed in each node in order to guarantee the one-dimensional and dry conditions. Since the ground is modeled as an undefeatable and impermeable layer (1,2,3,4), vertical soil and fluid displacements are fixed. The time-history displacement, shown in Figure 309.10, is applied in vertical direction to each node of the top surface (9,10,11,12).

The time-history normal force induced in each contact/interface/joint element is represented in Figure 309.16 and compared with the one obtained with the dry brick element with u formulation, shown in Figure 309.15. It is worth noting that the normal force patterns are perfectly overlapped: this is due to the fact that excess pore pressure is fixed to zero and the oedometric stiffness are the same in the two cases.

Parameter	Symbol	Value
Young's Modulus	E [kPa]	$1.5 \cdot 10^{10}$
Poisson ratio	ν [-]	0.0
Solid particle bulk modulus	K_s [kPa]	$3.6 \cdot 10^7$
Fluid bulk modulus	K_f [kPa]	$2.17 \cdot 10^6$
Solid density	ρ_s [Mg/m ³]	2.7
Fluid density	ρ_f [Mg/m ³]	1.0
Porosity	n [-]	$1.0 \cdot 10^{-8}$
Darcy permeability	K [m/s]	$1.0 \cdot 10^3$

Table 309.3: Soil parameters.

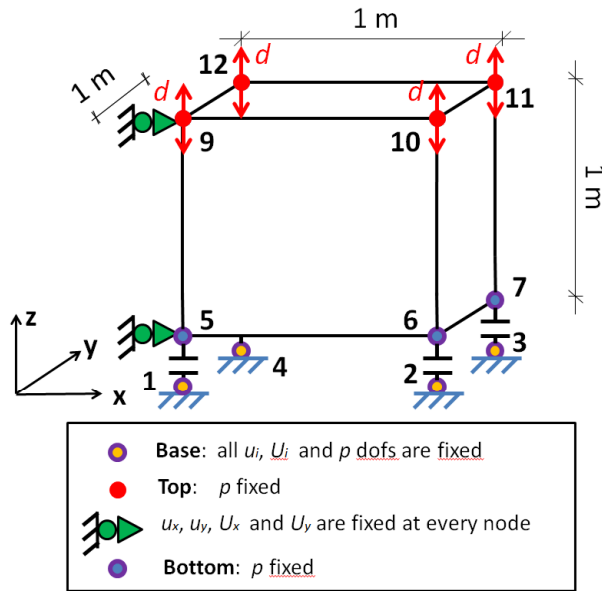


Figure 309.25: Single eight-node brick element. The nodes of the bottom surface are connected to the ground floor through contact/interface/joint elements. Vertical time-history displacement applied to the nodes of the top surface.

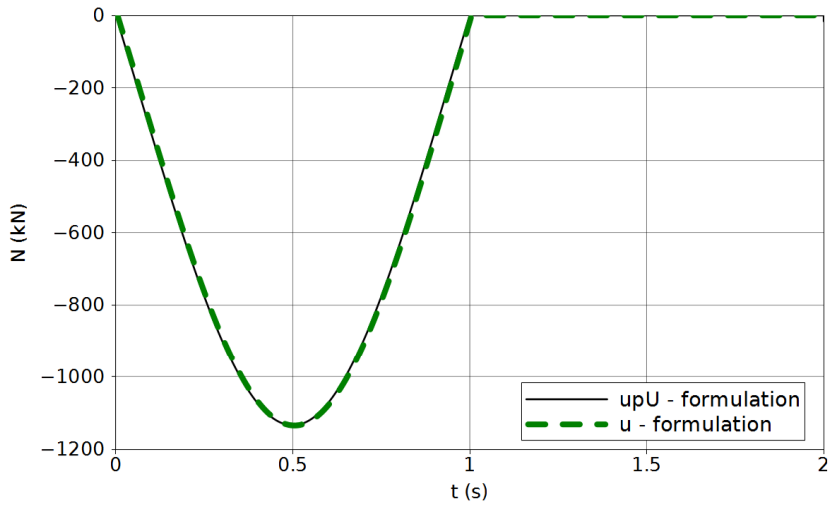


Figure 309.26: Normal force vs time in each contact/interface/joint element. *u-formulation* represents the results shown in Figure 309.16 whereas *upU-formulation* represents the results obtained through the model shown in Figure 309.25.

309.4.2 u-p-U Contact/Interface/Joint

A column of four brick *u-p-U* finite elements is used to model the horizontal layer. The height of the soil column is 1 m and the height of each element has dimensions $1m \cdot 1m \cdot 1m$, illustrated in Figure 309.27.

The following boundary conditions are applied to the model. As the bottom of the column is modeled as an undeformable and impermeable layer, both the solid and fluid displacements are fixed. The pore pressure is kept constant as zero at the top surface of the soil column because of the perfectly drained condition. In order to simulate the 1D compression problem, all the lateral movement of the solid and fluid phase are constrained so that the vertical displacement is the only non-zero displacement. A vertical time-history displacement, shown in Figure 309.10, is applied to the solid *dof* of the top surface nodes. In order to simulate the one dimensional compression, all the degrees of freedom at the same level are connected in a masterslave fashion.

The nodes of the bottom surface (5,6,7,8) are connected to the ground (1,2,3,4) through contact/interface/joint elements. Under the hypothesis of laminar flow, no cavitation and one-dimensional type of problem, the water has to fill up all the voids generated into the media while the displacement field is acting on the top surface. This means that if the soil and the ground are separated because of the detachment of the contact/interface/joint element, the water has to fill the gap. Even the pore pressure at both sides of the gap has to assume the same value. Such boundary conditions can be introduced by adding masterslave between each node of the bottom surface (5,6,7,8) and the corresponding one belonging to the ground (1,2,3,4).

In this paragraph a parametric study is performed in order to examine the performance of this *u-p-U* contact/interface/joint element. The analyses consider several configuration of permeability and soil stiffness. In fact, three values of elastic modulus (*E*) are taken into consideration referring to a Stiff, Medium and Soft soil (called respectively StS, MS and SoS) and three values of the darcy permeability are similarly defined. All soil and contact/interface/joint parameters are listed respectively in Table 309.4 and Table 309.1.

This kind of excitation (a sine wave) applied at the top of the model is clearly composed of waves of all kinds of frequency, especially at the initial strong change in acceleration and velocity for $t = 0s$. Due to this fact, a fairly dense mesh of 100 *u-p-U* brick finite elements of dimensions $1m \cdot 1m \cdot 1cm$ was chosen. Therefore, the time step Δt needs to be limited to $\Delta t = \Delta h/v$, where *v* is the highest wave velocity. In our case, the temporal integration involves 4000 steps of , which allows a maximum wave velocity of . The propagation velocity can be calculated by the following equation given by de Boer et al. (1993) and is equal to

$$\nu = \sqrt{\frac{n^2(1-\nu)E}{(1+\nu)(1-2\nu)[n^2(1-n)\rho_s + (1-n)^2n\rho_f]}} \quad (309.1)$$

The artificial oscillation are diminished by introducing some numerical damping into the analysis through $\alpha = 0.6$ and $\beta = 0.3025$ for the Newmark integrator.

Figure 309.27: Four eight-node brick elements. The nodes of the bottom surface are connected to the ground floor through contact/interface/joint elements. Vertical time-history displacement applied to the nodes of the top surface.

The specific permeability, k and the time needed for completion of the 1D consolidation process, t , can be estimated using the darcy permeability K through (309.2) and (309.3) respectively, where ρ_w is the mass density of the fluid (water), g is the acceleration of gravity equal to $9.81m/s^2$, H is the thickness of the soil layer and E_{oed} is the one dimensional soil stiffness:

$$k = \frac{K}{\rho_w \cdot g} \quad (309.2)$$

$$t = \frac{H^2}{c_v} = \frac{H^2 \cdot \rho_w \cdot g}{K \cdot E_{oed}} \quad (309.3)$$

The time t is computed and listed in Table 309.4.2 for each soil type condition. As can be seen, for the stiff soil (StS), the consolidation time is much lower than the loading acting on the top surface, therefore no excess pore pressure is developed into the soil and drained response is occurred.

STIFF SOIL - (StS)				
Parameter	Symbol	Value		
Young's Modulus	E [kPa]	$1.0 \cdot 10^{10}$	$1.0 \cdot 10^{10}$	$1.0 \cdot 10^{10}$
Poisson ratio	ν [-]	0.0	0.0	0.0
Solid particle bulk modulus	K_s [kPa]	$3.6 \cdot 10^7$	$3.6 \cdot 10^7$	$3.6 \cdot 10^7$
Fluid bulk modulus	K_f [kPa]	$2.17 \cdot 10^6$	$2.17 \cdot 10^6$	$2.17 \cdot 10^6$
Solid density	ρ_s [Mg/m ³]	2.7	2.7	2.7
Fluid density	ρ_f [Mg/m ³]	1.0	1.0	1.0
Porosity	n [-]	0.46	0.46	0.46
Darcy permeability	K [m/s]	$1.0 \cdot 10^{-3}$	$1.0 \cdot 10^{-5}$	$1.0 \cdot 10^{-7}$
MEDIUM SOIL - (MS)				
Parameter	Symbol	$1.0 \cdot 10^7$	$1.0 \cdot 10^7$	$1.0 \cdot 10^7$
Young's Modulus	E [kPa]	$1.0 \cdot 10^7$	$1.0 \cdot 10^7$	$1.0 \cdot 10^7$
Poisson ratio	ν [-]	0.0	0.0	0.0
Solid particle bulk modulus	K_s [kPa]	$3.6 \cdot 10^7$	$3.6 \cdot 10^7$	$3.6 \cdot 10^7$
Fluid bulk modulus	K_f [kPa]	$2.17 \cdot 10^6$	$2.17 \cdot 10^6$	$2.17 \cdot 10^6$
Solid density	ρ_s [Mg/m ³]	2.7	2.7	2.7
Fluid density	ρ_f [Mg/m ³]	1.0	1.0	1.0
Porosity	n [-]	0.46	0.46	0.46
Darcy permeability	K [m/s]	$1.0 \cdot 10^{-3}$	$1.0 \cdot 10^{-5}$	$1.0 \cdot 10^{-7}$
SOFT SOIL - (SoS)				
Parameter	Symbol	$1.0 \cdot 10^4$	$1.0 \cdot 10^4$	$1.0 \cdot 10^4$
Young's Modulus	E [kPa]	$1.0 \cdot 10^4$	$1.0 \cdot 10^4$	$1.0 \cdot 10^4$
Poisson ratio	ν [-]	0.0	0.0	0.0
Solid particle bulk modulus	K_s [kPa]	$3.6 \cdot 10^7$	$3.6 \cdot 10^7$	$3.6 \cdot 10^7$
Fluid bulk modulus	K_f [kPa]	$2.17 \cdot 10^6$	$2.17 \cdot 10^6$	$2.17 \cdot 10^6$
Solid density	ρ_s [Mg/m ³]	2.7	2.7	2.7
Fluid density	ρ_f [Mg/m ³]	1.0	1.0	1.0
Porosity	n [-]	0.46	0.46	0.46
Darcy permeability	K [m/s]	$1.0 \cdot 10^{-3}$	$1.0 \cdot 10^{-5}$	$1.0 \cdot 10^{-7}$

Table 309.4: Stiff, Medium and Soft soil parameters (StS, MS and SoS).

Soil type	Symbol	Value		
		K [m/s]	$1.0 \cdot 10^{-3}$	$1.0 \cdot 10^{-5}$
Stiff soil (StS)	t [s]	$1.0 \cdot 10^{-6}$	$1.0 \cdot 10^{-4}$	$1.0 \cdot 10^{-2}$
Medium-Stiff soil (MS)	t [s]	$1.0 \cdot 10^{-3}$	$1.0 \cdot 10^{-1}$	$1.0 \cdot 10^1$
Soft soil (SoS)	t [s]	$1.0 \cdot 10^0$	$1.0 \cdot 10^2$	$1.0 \cdot 10^4$

Table 309.5: The time needed for completion of the 1D consolidation process, t , estimated through the Darcy permeability K for each soil type condition.

309.5 Verification of Static, Isolator Element Modeling and Simulation

Chapter 310

Verification and Validation for Coupled, Porous Solid – Pore Fluid Problems

(2000-2003-2007-2009-2010-2016-2017-2020-2021-)

(In collaboration with Prof. Zhao Cheng, Dr. Panagiota Tasiopoulou, Ms. Fatemah Behbehani, Prof. Han Yang and Mr. Yusheng Yang)

310.1 Chapter Summary and Highlights

310.2 Introduction

presented here are verification examples for u-p-U formulation. Examples include:

1. Drilling of a borehole
2. The case of a spherical cavity
3. Consolidation of a soil layer
4. Line injection of a fluid in a reservoir
5. Shock wave propagation
6. Vertical Consolidation of a soil layer by Coussy (2004)
7. One dimensional shock wave propagation with a step displacement boundary condition by [Gajo and Mongiovi \(1995\)](#)
8. One dimensional shock wave propagation with step loading at the surface by [de Boer et al. \(1993\)](#)
9. One dimensional shock wave propagation with a step velocity boundary condition by [Hiremath et al. \(1988\)](#)

310.3 Drilling of a well

310.3.1 The Problem

Let us consider an infinite half space domain composed of an isotropic, homogeneous and saturated thermoporoelastic material. At its reference state, it is assumed that the temperature, fluid pressure and stress fields are uniform and equal respectively, to T_0 , p_0 and $\sigma^0 = \sigma^0 \mathbf{1}$ (with $\sigma^0 < 0$). At time = 0, an infinite cylinder of radius r_0 is instantaneously drilled parallel to the vertical axis Oz . It is filled with a fluid of the same nature as that saturating the porous medium but at a different pressure and temperature at the values of p_1 and T_1 respectively. The interface $r = r_0$ between the well and the porous medium is assumed to be in thermodynamic equilibrium.

In cylindrical coordinates (r, θ, z) , the boundary conditions can be summarized as follows (see Fig.310.1):

$$t \leq 0 \rightarrow \sigma^0 = \sigma^0 \mathbf{1} \quad p(r) = p_0 \quad T(r) = T_0 \quad (310.1)$$

$$t > 0 \rightarrow \sigma_{rr}(r_0) = -p_1 \quad \sigma_{r\theta}(r_0) = \sigma_{rz}(r_0) = 0$$

$$\sigma_{rr}(r \rightarrow \infty) \rightarrow \sigma^0 \quad \sigma_{r\theta}(r \rightarrow \infty) = \sigma_{rz}(r \rightarrow \infty) \rightarrow 0$$

$$p(r_0, t) = p_1 \quad p(r \rightarrow \infty) \rightarrow p_0$$

$$T(r_0) = T_1 \quad T(r \rightarrow \infty) \rightarrow T_0 \quad (310.2)$$

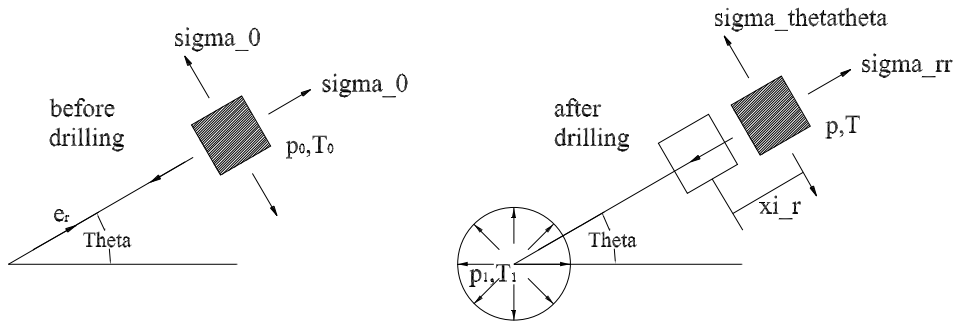


Figure 310.1: Boundary Conditions for Drilling of a Borehole

310.3.2 Analytical Solution

Since the well is assumed to be infinite long in its vertical axis Oz , the analysis is performed under plane strain hypothesis ($\epsilon_{zz} = 0$). Therefore,

$$\xi = \xi^r(r)e_r \quad p = p(r) \quad T = T(r) \quad (310.3)$$

in which ξ^r is the radial displacement. In cylindrical coordinates, Eqn. 310.48 yields

$$\epsilon_{rr} = \frac{\partial \xi^r}{\partial r} \quad \epsilon_{\theta\theta} = \frac{\xi^r}{r} \quad \text{other} \quad \epsilon_{ij} = 0 \quad (310.4)$$

Based on the constitutive equations from Coussy (1995), it follows that

$$\sigma_{rr} = \sigma^0 + \lambda_0 \left(\frac{\partial \xi^r}{\partial r} + \frac{\xi^r}{r} \right) + 2\mu \frac{\partial \xi^r}{\partial r} - b(p - p_0) - 3\alpha K_0(T - T_0) \quad (310.5)$$

$$\sigma_{\theta\theta} = \sigma^0 + \lambda_0 \left(\frac{\partial \xi^r}{\partial r} + \frac{\xi^r}{r} \right) + 2\mu \frac{\partial \xi^r}{\partial r} - b(p - p_0) - 3\alpha K_0(T - T_0) \quad (310.6)$$

$$\sigma_{zz} = \sigma^0 + \lambda_0 \left(\frac{\partial \xi^r}{\partial r} + \frac{\xi^r}{r} \right) - b(p - p_0) - 3\alpha K_0(T - T_0) \quad (310.7)$$

$$other \quad \sigma_{ij} = 0 \quad (310.8)$$

Finally combined with the Eqns. 310.5-310.8, it yields the near field or long-term solution (Coussy, 1995)

$$\xi^r = \frac{\sigma^0 + p_1}{2\mu} \frac{r_0^2}{r} + \frac{r_0[b(p_1 - p_0) + 3\alpha K_0(T_1 - T_0)]}{2(\lambda_0 + 2\mu)} \left(\frac{r}{r_0} - \frac{r_0}{r} \right) \quad (310.9)$$

$$\sigma_{rr} = -p_1 \frac{r_0^2}{r^2} - \left\{ \sigma_0 - \frac{\mu[b(p_1 - p_0) + 3\alpha K_0(T_1 - T_0)]}{\lambda_0 + 2\mu} \right\} \left(1 - \frac{r_0^2}{r^2} \right) \quad (310.10)$$

$$\sigma_{\theta\theta} = (2\sigma_0 + p_1) \frac{r_0^2}{r^2} - \frac{\mu[b(p_1 - p_0) + 3\alpha K_0(T_1 - T_0)]}{\lambda_0 + 2\mu} \left(1 + \frac{r_0^2}{r^2} \right) \quad (310.11)$$

$$\sigma_{zz} = \sigma^0 - \frac{2\mu}{\lambda_0 + 2\mu} [b(p_1 - p_0) + 3\alpha K_0(T_1 - T_0)] \quad (310.12)$$

And the diffusion process can be achieved if that the time are large enough with respect to the characteristics diffusion time relative to point r . When the boundary conditions for $r = r_0$ in fluid pressure and temperature which are $p = p_1$ and $T = T_1$ apply for the whole model, the following equations correspond to the undrained solution of the instantaneous drilling of a borehole in an infinite elastic medium.

$$\begin{aligned} \xi^r &= \frac{\sigma^0 + p_1}{2\mu} \frac{r_0^2}{r} & \sigma_{rr} &= \sigma^0 - (\sigma_0 + p_1) \frac{r_0^2}{r^2} \\ \sigma_{\theta\theta} &= \sigma^0 + (\sigma_0 + p_1) \frac{r_0^2}{r^2} & \sigma_{zz} &= \sigma_0 \end{aligned} \quad (310.13)$$

310.3.3 Discussion of the Results

As the problem is Axisymmetric, we construct the model as a quarter of a donut. The inside diameter of the donut is 10 cm and the outside diameter is 1 m. To accommodate both the plain strain hypothesis and the geometry of the element for finite element, the thickness of the model is chosen to be 5 cm. The final mesh is generated as Fig.310.2. And the boundary conditions is as follows: As a consequence of plain strain problem, all the movements for solid and fluid in vertical direction Oz are suppressed; the solid and fluid displacement for the nodes along the X axis and Y axis are fixed in Y and X direction respectively for the reason of axisymmetry; the nodes along the outside perimeter are fixed in the solid and fluid displacement with the assumption of infinite medium. the pressure is translated into nodal forces

Parameter	Symbol	Value	Units
Poisson Ratio	ν	0.2	-
Young's Modulus	E	1.2E+6	kN/m^2
Solid Bulk Modulus	K_s	3.6E+7	kN/m^2
Fluid Bulk Modulus	K_f	1.0E+17	kN/m^2
Solid Density	ρ_s	2.7	ton/m^3
Fluid Density	ρ_f	1.0	ton/m^3
Porosity	n	0.4	-

Table 310.1: Material Properties used to study borehole problem

and applied on the nodes along the inside perimeter. For simplicity, the hydrostatic stress σ_0 is equal to zero and with the assumption of thermodynamic equilibrium through the process, the temperature factor can be neglected. Also the initial fluid pressure p_0 is set to be 0 kPa. The analytical solution is studied below using the following set of parameters shown in Table 310.1.

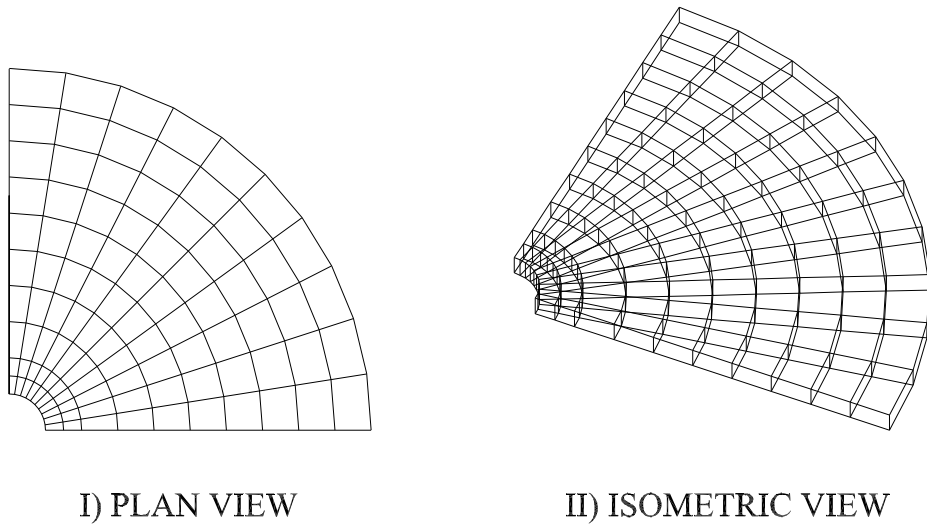


Figure 310.2: The mesh generation for the study of borehole problem

In the analysis, ten loading cases for final fluid pressure from 10 kPa to 100 kPa are studied. And by manipulating the permeability, it is possible to investigate both the drained behavior and undrained behavior. For the drained behavior, we choose the permeability as $k = 3.6 \times 10^{-4} m/s$, which is a typical value for sand, the comparison between the close solution and experimental result is shown in Fig.310.3. From the results, we can see that along the inside perimeter, the close solution and experimental result

provide very good agreement to each other. But as the increase of the radius, we can see the analytical solution is getting more and more distant from the experimental results. In another word, the analytical solution can be interpreted as that with the increase from the loading surface, the radial displacement is larger. This is unreasonable in the point of view in soil mechanics. While the experimental result show the effect that with the increase of the radial distance, the radial displacement is decreasing.

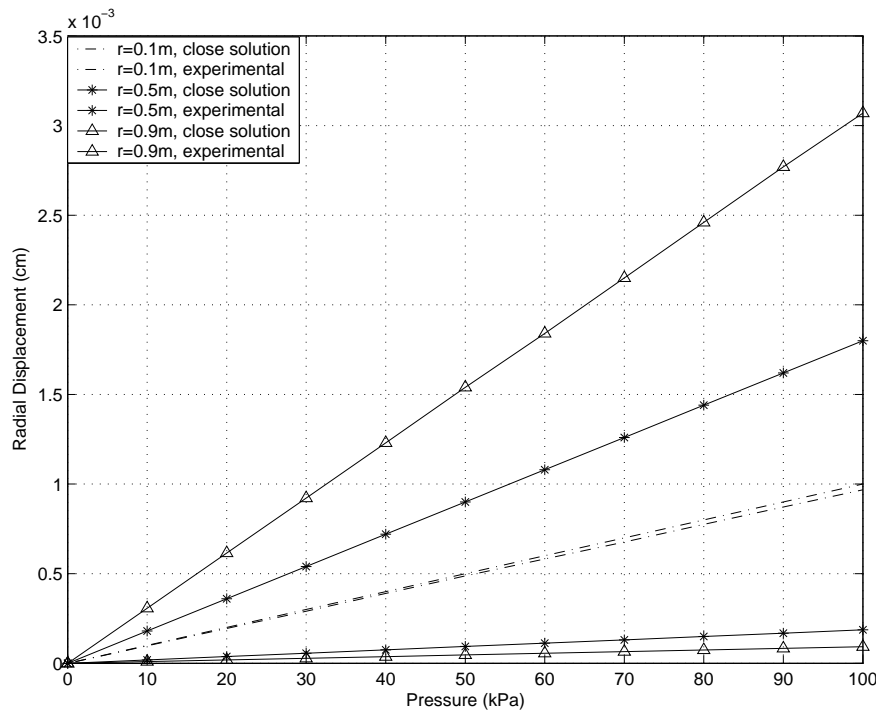


Figure 310.3: The comparison of radial solid displacement between analytical solution and experimental result for drained behavior

For the undrained behavior, the permeability of $k = 3.6 \times 10^{-8} m/s$ is selected as a representative value for typical clayey soil. The comparison between the close solution and experimental result is provided as well. From the Fig.310.4 we can see that, the analytical solution is linearly away from the experimental result by a ratio of approximately 1.6. It should also be noticed that the close solution of the drained and undrained behavior for the nodes along the inside perimeter are exactly the same, which is contradictory to the definition of drained and undrained behavior. For the drained behavior, as the water easily dissipate from the soil body, the problem can be treated with the knowledge of continuum mechanics using the parameters of the solid skeleton. While for the undrained behavior, with the involvement of the pore water, the elastic parameters for the mixture should be different, so the response will not be the same as well. As a result of this, the experimental results give a more reasonable conclusion.

As for the drained behavior, the fluid totally flows out of the soil body and all excessive pore pressure

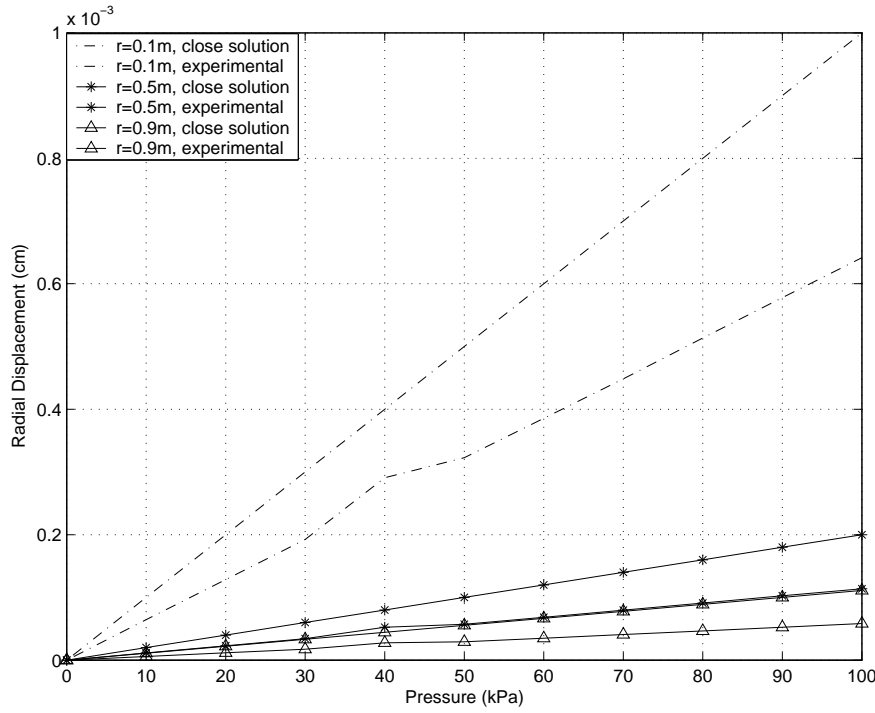


Figure 310.4: The comparison of radial solid displacement between analytical solution and experimental result for undrained behavior

dissipates, there is small coupling between the solid and fluid phase. We can use the continuum mechanics to treat this problem. Here introduces a problem of an infinite cylindrical tube, with the inner radius R_1 and outer radius R_0 , subjected to an internal pressure P_1 and an external pressure P_2 . The displacement field as follows ([S.Timoshenko and D.H.Young, 1940](#)):

$$\xi^r = \frac{R_1^2 P_1}{2(R_0^2 - R_1^2)} \left(\frac{r}{\lambda + \mu} + \frac{R_0^2}{\mu r} \right) \quad (310.14)$$

With $P_0 = 0$ and take the limit of $R_0 \rightarrow \infty$, we can obtain the following equation:

$$\xi^r = \frac{P_1 R_1^2}{2\mu} \frac{1}{r} \quad (310.15)$$

which is identical to Eq.[310.10](#). Also to minimize the effect of infinite boundary, we introduce the result from another model which is exactly the same as the previous one besides the expansion of the outer radius to 30m. At the final fluid pressure of 50 kPa, the results are shown in Fig.[310.5](#). From the plot we can make a conclusion that the undrained analytical solution from [Coussy \(1995\)](#) is actually the drained solution and the undrained solution still needs to be investigated.

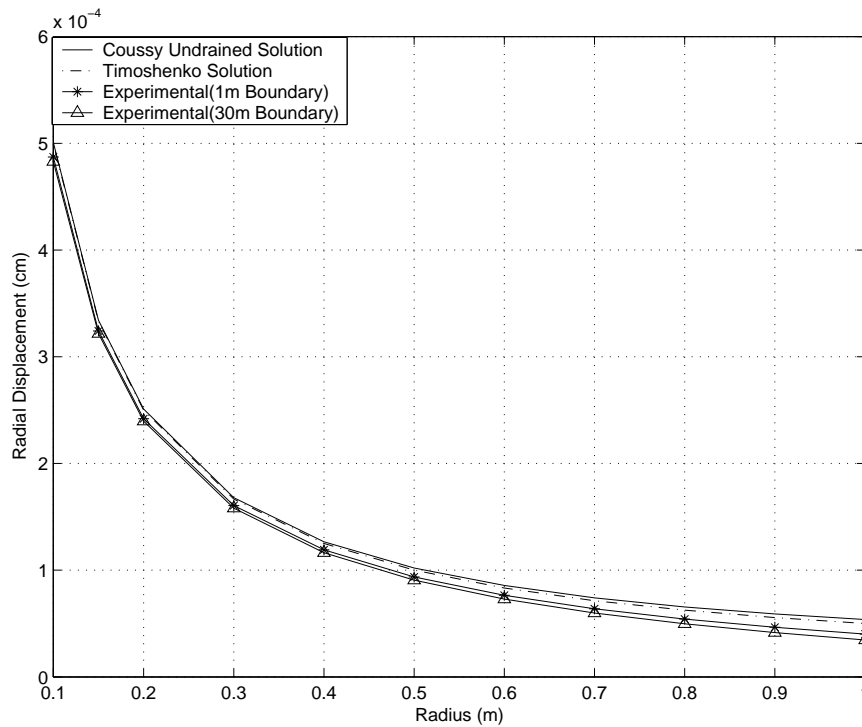


Figure 310.5: The comparison of radial solid displacement between two analytical solutions and expanded boundary

310.4 The Case of a Spherical Cavity

310.4.1 The Problem

Considering a medium composed of an isotropic, homogeneous, saturated thermoporoelastic material. In its initial state, it is assumed that the temperature, fluid pressure and stress fields are uniform and equal respectively, to T_0 , p_0 and $\sigma^0 = \sigma^0 \mathbf{1}$ (with $\sigma^0 < 0$). At time $t=0$, a spherical cavity of radius r_0 is immediately drilled and filled with the same saturating fluid in the medium. For $t > 0$, the temperature and the pressure of the fluid are kept constant with the value of T_1 and p_1 respectively. The interface $r = r_0$ between the well and the porous medium is assumed to be in the thermodynamic equilibrium.

In spherical coordinates (r, θ, φ) , the boundary conditions can be summarized as follows:

$$t \leq 0 \rightarrow \sigma^0 = \sigma^0 \mathbf{1} \quad p(r) = p_0 \quad T(r) = T_0 \quad (310.16)$$

$$t > 0 \rightarrow \sigma_{rr}(r_0) = -p_1 \quad \sigma_{r\theta}(r_0) = \sigma_{r\varphi}(r_0) = 0$$

$$\sigma_{rr}(r \rightarrow \infty) \rightarrow \sigma^0 \quad \sigma_{r\theta}(r \rightarrow \infty) = \sigma_{r\varphi}(r \rightarrow \infty) \rightarrow 0$$

$$p(r_0, t) = p_1 \quad p(r \rightarrow \infty) \rightarrow p_0$$

$$T(r_0) = T_1 \quad T(r \rightarrow \infty) \rightarrow T_0 \quad (310.17)$$

Strictly speaking, the expressions for $r \rightarrow \infty$ are not boundary conditions. They are complementary conditions to be satisfied by the solution. It is used to model that at the point far from the disturbed area, the state of the medium are held as its initial state.

310.4.2 Analytical Solution

This is a problem of spherical symmetry. The radial displacement is the only non-zero displacement and all the fields are r and t dependent. Therefore,

$$\xi = \xi^r(r)e_r \quad p = p(r) \quad T = T(r) \quad (310.18)$$

in which ξ^r is the radial displacement. In spherical coordinates, Eqn.310.18 yields

$$\epsilon_{rr} = \frac{\partial \xi^r}{\partial r} \quad \epsilon_{\theta\theta} = \frac{\xi^r}{r} \quad \text{other} \quad \epsilon_{ij} = 0 \quad (310.19)$$

Based on the constitutive equations from Coussy (1995), it follows that

$$\sigma_{rr} = \sigma^0 + \lambda_0 \left(\frac{\partial \xi^r}{\partial r} + \frac{\xi^r}{r} \right) + 2\mu \frac{\partial \xi^r}{\partial r} - b(p - p_0) - 3\alpha K_0(T - T_0) \quad (310.20)$$

$$\sigma_{\theta\theta} = \sigma_{\varphi\varphi} = \sigma^0 + \lambda_0 \left(\frac{\partial \xi^r}{\partial r} + \frac{\xi^r}{r} \right) + 2\mu \frac{\xi^r}{r} - b(p - p_0) - 3\alpha K_0(T - T_0) \quad (310.21)$$

$$\text{other} \quad \sigma_{ij} = 0 \quad (310.22)$$

Finally combined with the Eqns. 310.19-310.22, it yields the near field or long-term solution (Coussy, 1995)

$$\xi^r = \frac{\sigma^0 + p_1}{4\mu} \frac{r_0^3}{r^2} + \frac{r_0 [b(p_1 - p_0) + 3\alpha K_0(T_1 - T_0)]}{2(\lambda_0 + 2\mu)} \left(1 - \frac{r_0^2}{r^2} \right) \quad (310.23)$$

$$\sigma_{rr} = -p_1 \frac{r_0^3}{r^3} + \sigma_0 \left(1 - \frac{r_0^3}{r^3} \right) - \frac{2\mu [b(p_1 - p_0) + 3\alpha K_0(T_1 - T_0)]}{\lambda_0 + 2\mu} \left(\frac{r_0}{r} - \frac{r_0^3}{r^3} \right) \quad (310.24)$$

$$\sigma_{\theta\theta} = \sigma_{\varphi\varphi} = p_1 \frac{r_0^3}{2r^3} - \sigma_0(1 + \frac{r_0^3}{2r^3}) - \frac{\mu[b(p_1 - p_0) + 3\alpha K_0(T_1 - T_0)]}{\lambda_0 + 2\mu} [\frac{r_0}{r}(1 + \frac{r_0^2}{r^2})] \quad (310.25)$$

And the diffusion process can be achieved if that the time are large enough with respect to the characteristics diffusion time relative to point r . When the boundary conditions for $r = r_0$ in fluid pressure and temperature which are $p = p_1$ and $T = T_1$ apply for the whole model, the following equations correspond to the undrained solution of the instantaneous drilling of a borehole in an infinite elastic medium.

$$\begin{aligned} \xi^r &= \frac{\sigma_0 + p_1}{4\mu} \frac{r_0^3}{r^2} & \sigma_{rr} &= -p_1 \frac{r_0^3}{r^3} + \sigma_0(1 + \frac{r_0^3}{2r^3}) \\ \sigma_{\theta\theta} = \sigma_{\varphi\varphi} &= p_1 \frac{r_0^3}{2r^3} + \sigma_0(1 + \frac{r_0^3}{2r^3}) \end{aligned} \quad (310.26)$$

310.4.3 Discussion of the Results

The model is constructed as a quarter of a half ball. The cavity radius is 10cm. As the outside boundary is fixed, to minimize the possibility of the sudden increase of the fluid bulk modulus, the outside radius of the sphere is set to be 2 m. The final mesh is generated as Fig.310.6. And the following boundary conditions apply: The nodes on XZ and YZ plane are fixed for solid and fluid displacement in Y and X direction respectively; the vertical solid and fluid displacement for the nodes on the XY plane are suppressed; for the nodes along the outside surface, to satisfy the complementary conditions, all the solid and fluid displacements are set to be zero as well. The pressure is translated in to nodal forces and applied in the radial direction. For simplicity, the hydrostatic stress σ_0 is equal to zero and with the assumption of thermodynamic equilibrium through the process, the temperature factor can be neglected. Also the initial fluid pressure p_0 is set to be 0 kPa. The analytical solution is studied below using the following set of parameters shown in Table 310.2.

As the same procedure in the previous drilling of borehole problem, we compared both the drained and undrained behavior. The drained and undrained behavior are tested by the permeability of $k = 3.6 \times 10^{-4} m/s$ and $k = 3.6 \times 10^{-8} m/s$ respectively. In drained behavior, we can see along the cavity surface, the experimental result of the radial displacement match the analytical solution very well. While with the increase of the radius, the decrease of the radial displacement for close solution is much smaller than that of the experimental results. For the undrained behavior, we can see the radial displacement of the experimental results are always smaller than the close solution. Again it should be noted that the close solutions for the drained and undrained behavior along the cavity surface are exactly the same. This can be explained in the same way as the previous drilling of the borehole problem. When the experimental results from drained behavior are compared with the analytical undrained solution, it is observed they provide good agreement to each other as well.

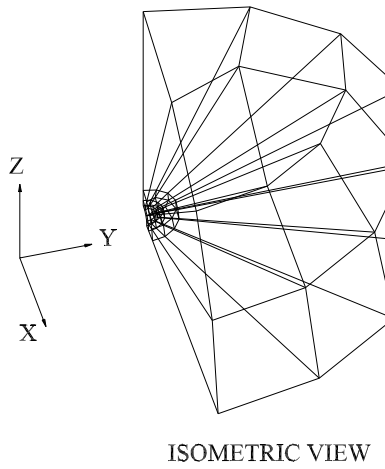


Figure 310.6: The mesh generation for the study of spherical cavity

Parameter	Symbol	Value	Units
Poisson Ratio	ν	0.2	-
Young's Modulus	E	1.2E+6	kN/m^2
Solid Bulk Modulus	K_s	3.6E+7	kN/m^2
Fluid Bulk Modulus	K_f	1.0E+17	kN/m^2
Solid Density	ρ_s	2.7	ton/m^3
Fluid Density	ρ_f	1.0	ton/m^3
Porosity	n	0.4	-

Table 310.2: Material Properties used to study spherical cavity problem

310.5 Line Injection of a fluid in a Reservoir

310.5.1 The Problem

Liquid water is usually injected into a reservoir from a primary well in order to recover the oil from a secondary well in petroleum engineering. This induces a problem of injecting a fluid into a cylindrical well of negligible dimensions.

Consider a reservoir of infinite extent composed of an isotropic, homogeneous and saturated poroelastic material. Through a cylindrical well of negligible dimensions, the injection of the same fluid is performed in all directions orthogonal to the well axis forming the Oz axis of coordinates. As a result of the axisymmetry and cylindrically infinite, all quantities spatially depends on r only. The injection starts at time $t = \Gamma$ and stops at time $t = \Gamma$. The flow rate of fluid mass injection is constant and equal to

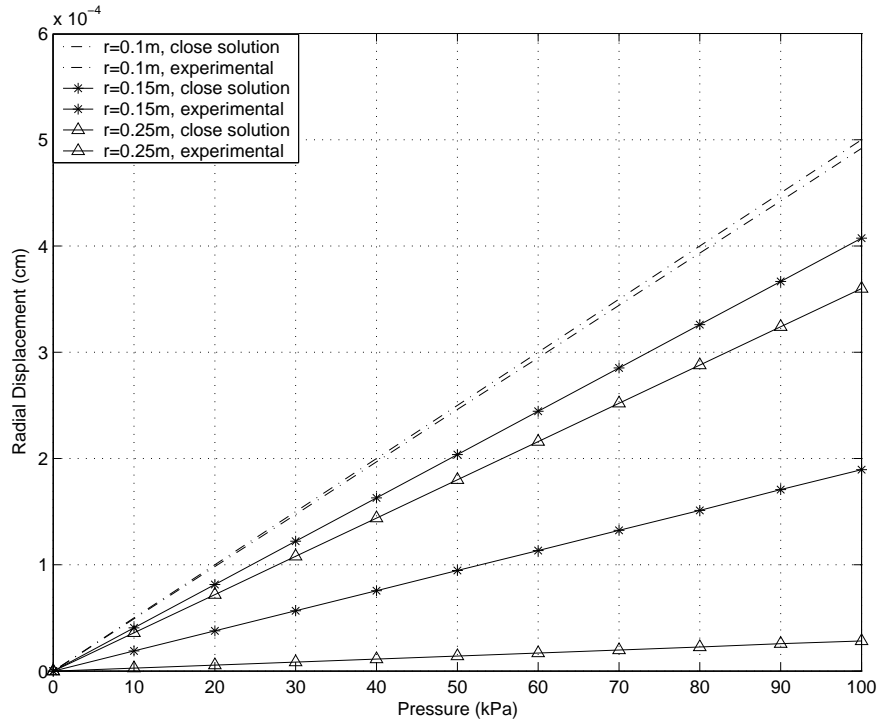


Figure 310.7: The comparison of radial solid displacement between analytical solution and experimental result for drained behavior

q. As a finite amount of Ω of fluid mass is injected instantaneously(i.e. $\Gamma q \rightarrow \Omega$ as $\Gamma \rightarrow 0$).

310.5.2 Analytical Solution

This is a problem of cylindrically symmetry. Consequently the cylindrical coordinates(r, θ, z) is adopted. The vector of relative flow of fluid mass w reads

$$\mathbf{w} = w(r, t) \mathbf{e}_r \quad (310.27)$$

where \mathbf{e}_r is the unit vector along the radius. Using the fluid mass balance relationship, it yields

$$\int_0^r \frac{\partial m}{\partial t}(r, t) 2\pi r dr = q - 2\pi r w(r, t) \quad \forall r, t \quad (310.28)$$

In addition, we require the fluid flow to reduce to zero infinitely far from the well

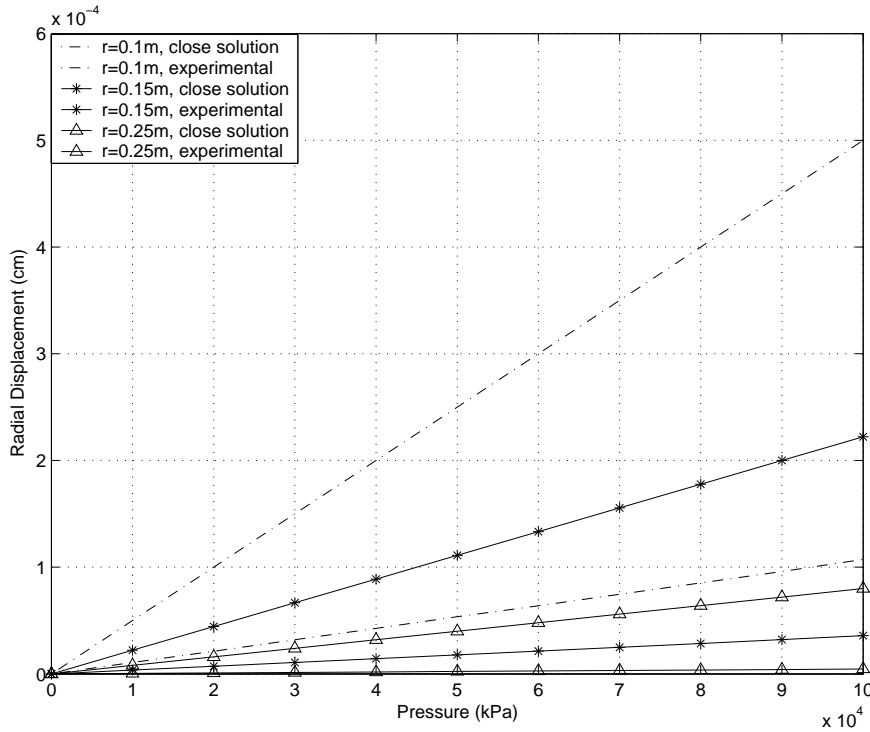


Figure 310.8: The comparison of radial solid displacement between analytical solution and experimental result for undrained behavior

$$rw \rightarrow 0 \quad r \rightarrow \infty \quad t < \infty$$

$$\int_0^\infty \frac{\partial m}{\partial t}(r, t) r dr = \frac{q}{2r} \quad \forall 0 < t < \infty \quad (310.29)$$

Based on above Eqs.310.28-310.29, the radial displacement is derived in the form

$$p = \frac{\Omega}{4\pi\rho_0^f kt} \exp\left(-\frac{r^2}{4c_{mt}}\right)$$

$$\xi_r = \frac{bM\Omega}{2\pi\rho_0^f(\lambda + 2\mu)r} \left[1 - \exp\left(-\frac{r^2}{4c_{mt}}\right)\right] \quad (310.30)$$

Using the constitutive equation, the stress field can be derived as follows:

$$\sigma_{rr} = -2\mu \frac{\xi_r}{r} \quad \sigma_{\theta\theta} = 2\mu \frac{\xi_r}{r} - \frac{2\mu b}{\lambda_0 + 2\mu} p$$

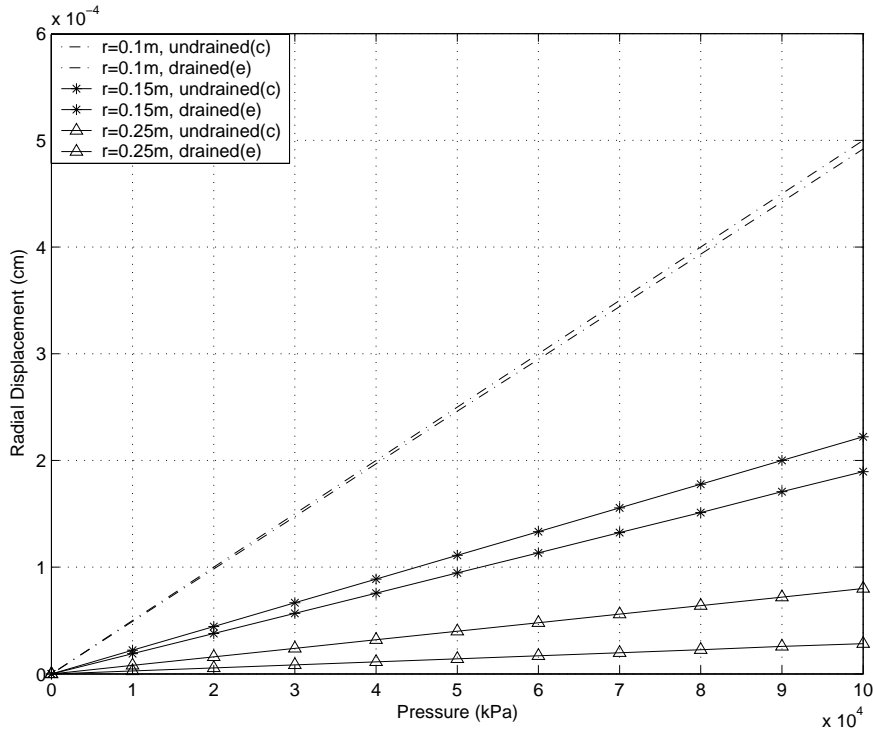


Figure 310.9: The comparison of radial solid displacement between analytical solution for undrained behavior and experimental result for drained behavior

$$\sigma_{zz} = -\frac{2\mu b}{\lambda_0 + 2\mu u} p \quad (310.31)$$

310.5.3 Discussion of the Results

As a result of axisymmetry, the model can be constructed as a quarter of a pie. The radius of the pie is 1 m and the thickness of the pie is 5 cm. A cylindrical well is drilled at the center of the pie, and its radius is 1 cm, which can be neglected in dimension when compared with the whole pie. The final mesh is shown as Fig.310.10. And the boundary conditions is as follows: As a consequence of plain strain problem, all the movements for solid and fluid in vertical direction Oz are suppressed; the solid and fluid displacement for the nodes along the X axis and Y axis are fixed in Y and X direction respectively for the reason of axisymmetry; the nodes along the outside perimeter are fixed in the solid and fluid displacement with the assumption of infinite medium. To the difference with the previous problems, the traction boundary conditions are applied on the fluid displacement. It should be noted that the Ω mention in the above equations is the volume of the fluid injected per unit of vertical well length and has a unit of m^3/m . In order to generate the volume of $1 \text{ cm}^3/m$, the corresponding fluid displacement of the nodes along the well has been calculated and applied as a step function at the time of 0 sec. For

simplicity, the initial fluid pressure p_0 is set to be 0 kPa. The analytical solution is studied below using the following set of parameters shown in Table 310.3.

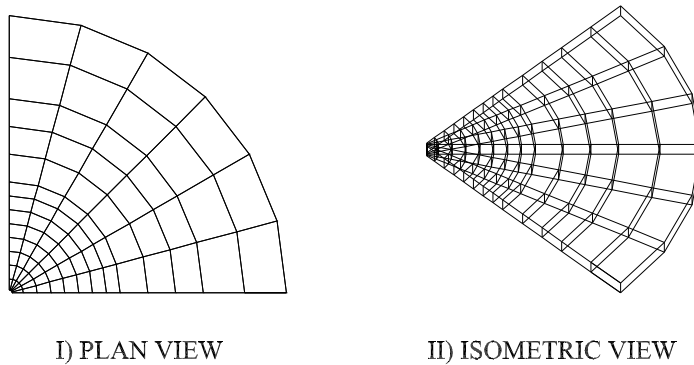


Figure 310.10: The mesh generation for the study of line injection problem

In the analysis, the pore pressure and the radial displacement are studied. The results are recorded from three points at the radius of 10 cm, 50 cm and 85 cm. The close solution and experimental results are shown in Fig.?? and Fig.???. As the time step is set to be 1 sec, the first data point starts at the time of 1 sec. From the pore pressure plot we can see that the build-up of the pore pressure reach the peak value of 34 kPa at the radius of 85 cm. With the decrease of the radius, the pore pressure decreases as well. This can be explained by the fact that the closer the point to the injection location, the earlier and the larger load is applied, so the pore pressure dissipates faster. And as time passes by, we can see the pore pressure progressively dissipates and finally almost reaches the same value within the model. The same phenomena can be observed from the radial solid displacement. The maximum solid displacement occurs at the radius of 85 cm, which means more coupling between the solid and fluid phase, as consequence, the pore pressure should have the largest value. This corresponds to the previous result. With the increase of the time, the radial solid displacement get closer to zero, which means the fluid moves out the solid skeleton.

Parameter	Symbol	Value	Units
Poisson Ratio	ν	0.2	-
Young's Modulus	E	1.2E+6	kN/m^2
Solid Bulk Modulus	K_s	3.6E+7	kN/m^2
Fluid Bulk Modulus	K_f	1.0E+17	kN/m^2
Undrained Bulk Modulus	K_u	6.0E+7	kN/m^2
Bulk Modulus	K	6.7E+5	kN/m^2
Solid Density	ρ_s	2.7	ton/m^3
Fluid Density	ρ_f	1.0	ton/m^3
Fluid Diffusivity coefficient	c_f	0.4973	m^2/s
Porosity	n	0.4	-
Permeability	k	3.6E-6	m/s

Table 310.3: Material Properties used to study the line injection problem

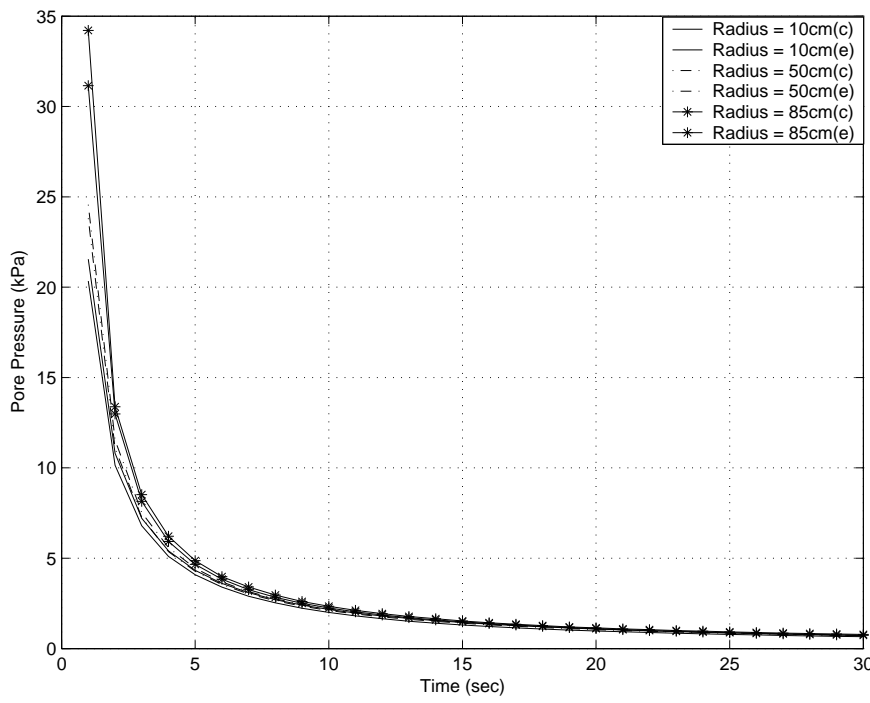


Figure 310.11: The comparison between analytical solution and experimental result for pore pressure

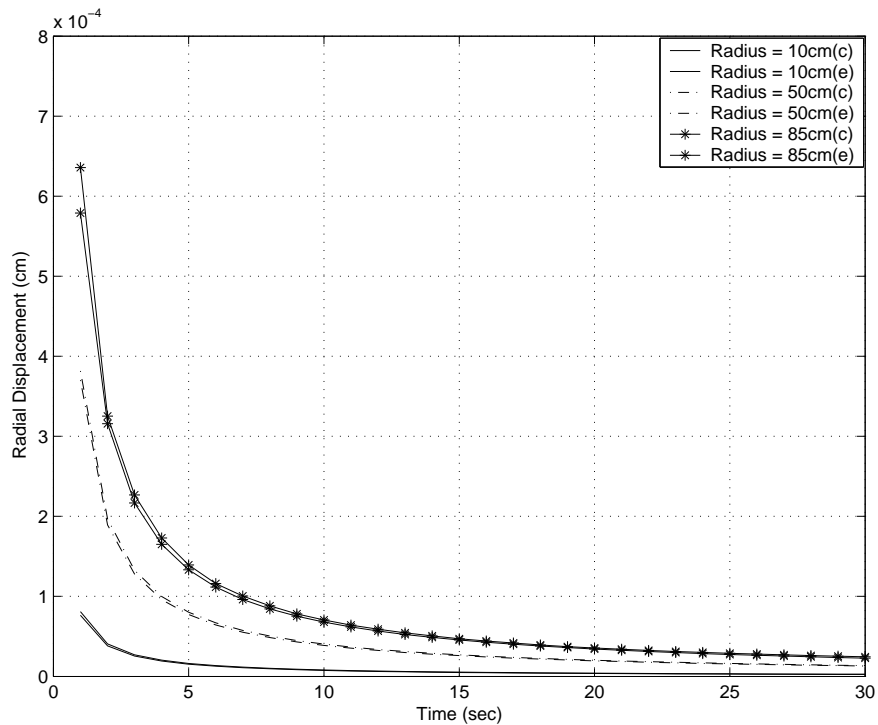


Figure 310.12: The comparison between analytical solution and experimental result for radial displacement

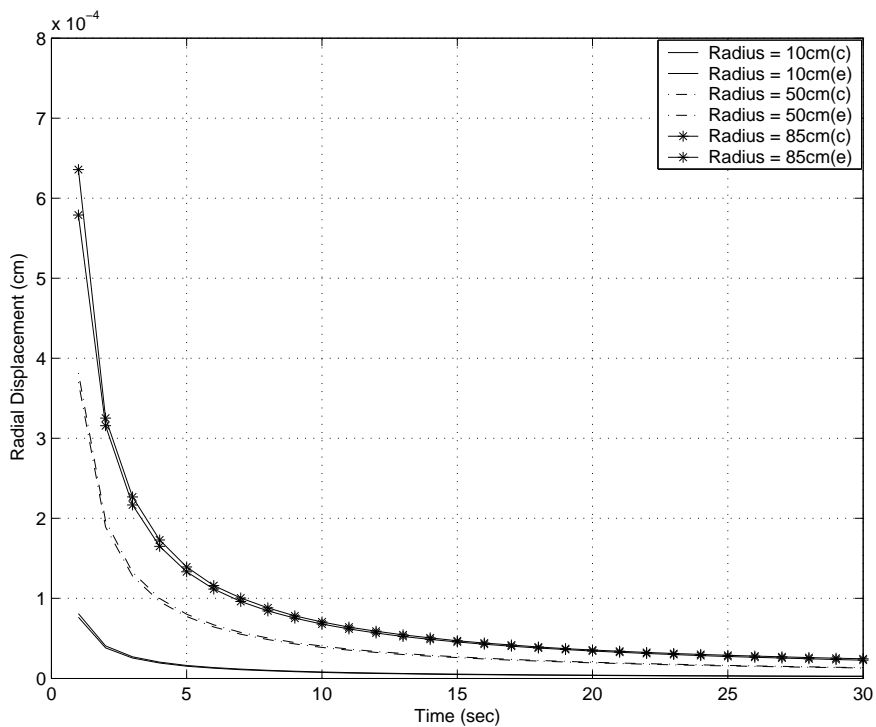


Figure 310.13: The comparison between analytical solution and experimental result for radial displacement

Table 310.4: Simulation parameters used for the shock wave propagation verification problem.

Parameter	Symbol	Value
Poisson ratio	ν	0.3
Young's modulus	E	$1.2 \times 10^6 \text{ kN/m}^2$
Solid particle bulk modulus	K_s	$3.6 \times 10^7 \text{ kN/m}^2$
Fluid bulk modulus	K_f	$2.17 \times 10^6 \text{ kN/m}^2$
Solid density	ρ_s	2700 kg/m^3
Fluid density	ρ_f	1000 kg/m^3
Porosity	n	0.4
Newmark parameter	γ	0.6

310.6 Shock Wave Propagation in Saturated Porous Medium

In order to verify the dynamic behavior of the system, an analytic solution developed by Gajo (1995) and Gajo and Mongiovi (1995) for 1C shock wave propagation in elastic porous medium was used. A model was developed consisting of 1000 eight node brick elements, with boundary conditions that mimic 1D behavior. In particular, no displacement of solid ($u_x = 0, u_y = 0$) and fluid ($U_x = 0, U_y = 0$) in x and y directions is allowed along the height of the model. Bottom nodes have full fixity for solid ($u_i = 0$) and fluid ($U_i = 0$) displacements while all the nodes above base are free to move in z direction for both solid and fluid. Pore fluid pressures are free to develop along the model. Loads to the model consist of a unit step function (Heaviside) applied as (compressive) displacements to both solid and fluid phases of the model, with an amplitude of 0.001 cm. The u–p–U model dynamic system of equations was integrated using Newmark algorithm (see section 108.3). Table 310.4 gives relevant parameters for this verification.

Two set of permeability of material were used in our verification. The first model had permeability set $k = 10^{-6} \text{ cm/s}$ which creates very high coupling between porous solid and pore fluid. The second model had permeability set to $k = 10^{-2} \text{ cm/s}$ which, on the other hand creates a low coupling between porous solid and pore fluid. Comparison of simulations and the analytical solution are presented in Figure 310.14.

Before proceeding to the analysis, the following assumptions are made: For high-frequency components, the permeability remains constant; thus, the dependency of the permeability on the frequency is neglected. Unless specified, all the models in this report are elastic isotropic.

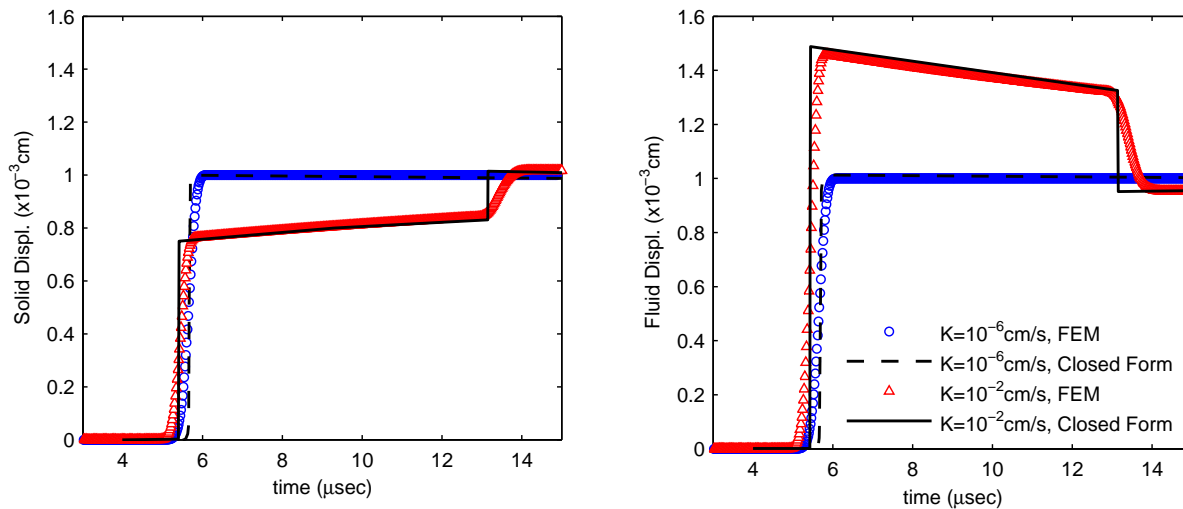


Figure 310.14: Compressional wave in both solid and fluid, comparison with closed form solution.

310.7 Vertical Consolidation of a soil layer by Coussy (2004)

310.7.1 Brief review of Analytical Solution for Consolidation by Coussy (2004)

The consolidation process can be defined as follows: When an elastic soil layer is subjected to an external change in mean normal stress, immediately the water will alone sustain this increment of mean normal stress and cause the build-up the excessive pore water pressure. In the progress of the flow of the water to the surface, the load is gradually transferred to the soil skeleton and the excessive pore water pressure will dissipate. At the same time, the settlement of the soil layer occurs. As settlement is usually a major concern in geotechnical engineering, this is a key problem in soil mechanics.

Consider a soil layer composed of an isotropic, homogeneous and saturated thermoporoelastic material. The layer has a thickness of h in the Oy direction and of infinite extent in the two other directions Ox and Oz . The layer is underlain by a rigid and impervious base at $y = 0$. And the top surface at $y = h$ is so perfectly drained that the pore pressure is held constant as zero.

At the initial state of the soil layer, the thermal effects are neglected so that the boundary conditions follow that:

$$t \leq 0 \rightarrow \quad y = h \quad p = 0 \quad (310.32)$$

$$y = 0 \quad \frac{\partial p}{\partial z} = 0 \quad (310.33)$$

At time $t = 0$, an instantaneous vertical load $-\varpi e_y$ is suddenly applied on the top surface $y = h$, the

induced boundary conditions require that

$$t > 0 \rightarrow \quad y = h \quad \sigma e_y = -\varpi e_y \quad (310.34)$$

The undeforability of the substratum reads

$$y = 0 \quad \xi = 0 \quad (310.35)$$

The impermeability implies

$$y = 0 \quad -w \cdot e_y = -w_y = 0 \quad (310.36)$$

The problem is then to determine the new fields of fluid pressure, stress and displacement induced by the external loading.

Since this is a one-dimensional problem, the only non-zero displacement is the vertical displacement ξ^y . But in particular the fluid pressure depends only on y and t .

$$\xi = \xi^y(y, t) e_y \quad p = p(y, t) \quad (310.37)$$

Based on the constitutive equations from [Coussy \(2004\)](#), it follows that

$$\sigma_{yy} = (\lambda_0 + 2\mu) \frac{\partial \xi^y}{\partial y} + bp \quad (310.38)$$

$$\sigma_{xx} = \sigma_{zz} = \frac{\lambda_0}{(\lambda + 2\mu)} \sigma_{yy} - \frac{2\mu b}{\lambda_0 + 2\mu} p \quad (310.39)$$

And because the fluid pressure p must be an ordinary function of time t , although the derivative of p is infinite at time $t = 0$ according to the consolidation equation ([Coussy, 2004](#)), the discontinuity of the fluid pressure p at time $t = 0$ must satisfy

$$p(y, t = 0^+) = \eta\varpi \quad \varpi = \frac{\nu - \nu_0}{(1 - \nu)(1 - 2\nu_0)b} \quad (310.40)$$

where ν and ν_0 are the drained and undrained Poisson ratio, respectively. For time $t > 0$, the vertical stress $\sigma_{yy} = -\varpi$ is constant in time and space, therefore the diffusion equation reads

$$t > 0 \quad c_m \frac{\partial^2}{\partial y^2} p = \frac{\partial}{\partial t} p \quad (310.41)$$

Collecting the above results, finally the fluid pressure reads

$$p(y, t) = \eta\varpi \sum_{n=0}^{\infty} \frac{4(-1)^n}{\pi(2n+1)} \cos\left[\frac{(2n+1)\pi}{2}\frac{y}{h}\right] \exp\left[-\frac{(2n+1)^2\pi^2}{4}\frac{t}{\tau}\right] \quad (310.42)$$

Each term of the series decreases exponentially with respect to the ratio $\frac{t}{\tau}$, in which τ is a characteristics consolidation time

$$\tau = \frac{h^2}{c_m} \quad c_m = kM \frac{\lambda_0 + 2\mu}{\lambda + 2\mu} \quad (310.43)$$

where λ and λ_0 are the drained and undrained Lame coefficient, respectively. Given by the Eqn.310.39, the only non-zero displacement ξ^y satisfies

$$\frac{\partial \xi^y}{\partial y} = \frac{1}{\lambda_0 + 2\mu} (\sigma_{yy} + bp) \quad (310.44)$$

By substituting the value of $-\varpi$ of the vertical stress and expression of (310.44), the series converges and it can integrated term by term yielding

$$\xi^y(y, t) = \frac{\varpi}{\lambda_0 + 2\mu} \left(\frac{y}{h} + \frac{8\eta b}{\pi^2}\right) \sum_{n=0}^{\infty} \frac{(-1)^n}{(2n+1)^2} \sin\left[\frac{(2n+1)\pi}{2}\frac{y}{h}\right] \exp\left(-\frac{(2n+1)^2\pi^2}{4}\frac{t}{\tau}\right) \quad (310.45)$$

$$(310.46)$$

Using Eqn.310.46 and substitute $y = h$, the settlement can be expressed as

$$s(t) = s_\infty + (s_{0^+} - s_\infty) \sum_{n=0}^{\infty} \frac{8}{\pi^2(2n+1)^2} \exp\left\{-\frac{(2n+1)^2\pi^2}{4}\frac{t}{\tau}\right\} \quad (310.47)$$

$$s_{0^+} = \frac{h\varpi}{\lambda + 2\mu} \quad s_\infty = \frac{h\varpi}{\lambda_0 + 2\mu} \quad (310.48)$$

310.7.2 Numerical Analysis

A soil column of ten brick $u-p-U$ finite elements is used to model the horizontal layer. The height of the soil column is 10 m and the height of each element has dimensions $1m \times 1m \times 1m$, illustrated in Fig. 310.15. The material properties, shown in Table 310.5, are chosen as representative values for the natural soil deposit. Developed $u-p-U$ finite element model, can simulate realistic compressibility of the pore fluid. However, it is important to note that the analytical solution for the vertical consolidation is based on the assumption that both the soil particles and the pore fluid (water) are completely incompressible. A uniform vertical pressure of 400 kPa is applied on the top surface of the soil column. The numerical analysis was performed in two stages:

- (I) Self-Weight application (see Figures 310.15 to 310.19).
- (II) Consolidation with drainage at top due to uniform vertical pressure of 400 kPa at the surface (see Figures 310.20 to 310.26).

Table 310.5: Material Properties used to study consolidation of a soil layer.

Parameter	Symbol	Value
gravity acceleration	g	9.81 m/s^2
soil matrix Young's Modulus	E	$10 \times 10^3 \text{ kN/m}^2$
soil matrix Poisson's ratio	ν	0.25
solid particle density	ρ_s	$2.65 \times 10^3 \text{ kg/m}^3$
water density	ρ_f	$1.0 \times 10^3 \text{ kg/m}^3$
solid particle bulk modulus	K_s	$37.0 \times 10^6 \text{ kN/m}^2$
fluid bulk modulus	K_f	$2.2 \times 10^6 \text{ kN/m}^2$
porosity	n	0.46
Biot coefficient	α	1.0

The following boundary conditions are applied to the model (Fig 310.27): As the bottom of the soil column is modeled as an undeformable and impermeable layer, both the solid and fluid displacements are fixed. The pore pressure is kept constant as zero at the top surface of the soil column because of the perfectly drained condition. In order to simulate the 1D consolidation problem, all the lateral movement of the solid and fluid phase are suppressed so that the vertical displacement is the only non-zero displacement for the intermediate nodes. To capture both the long term ($t > 0.1 \text{ sec}$) and short term ($t < 0.1 \text{ sec}$) response of the soil column, two different time steps are adopted: 0.1 sec and 0.005 sec, respectively. In order to observe the dissipation of the excessive pore water pressure in a reasonable

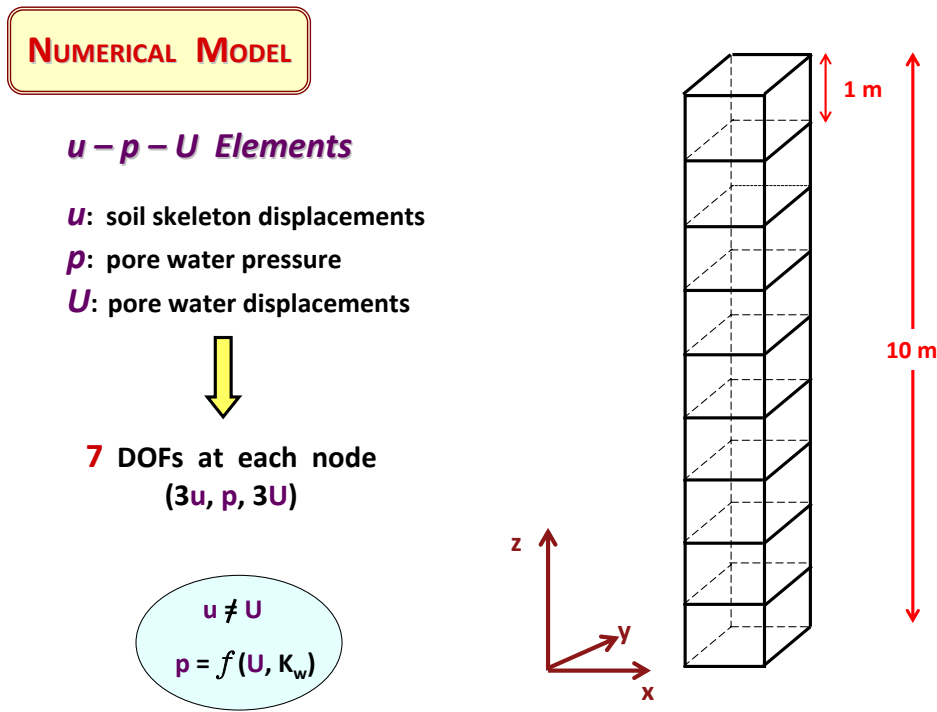


Figure 310.15: Numerical Simulation of self weight application and consolidation of a soil layer using u-p-U brick elements.

and convenient period, we select $k = 1.0 \times 10^{-4} m/s$ as the value for the permeability. To cure the artificial oscillation, some numerical damping is introduced into the analysis by using $\gamma = 0.6$ and $\beta = 0.3025$ for the Newmark integrator. Fig. 310.20 illustrates the physical geometry of the problem whereas Fig. 310.21 shows the numerical modeling.

Based on the above parameters, the other relative parameters can be calculated as follows:

The bulk modulus of the mixture:

$$K = \frac{E}{3(1-2\nu)} = 6.67 \times 10^3 kPa \quad (310.49)$$

$$\lambda = \frac{E\nu}{(1+\nu)(1-2\nu)} = 6.67 \times 10^3 kPa \quad \mu = \frac{E}{2(1+\nu)} = 4 \times 10^3 kPa \quad (310.50)$$

The Biot coefficient:

$$b = 1 - \frac{K}{K_s} = 0.9998 \quad (310.51)$$

The undrained bulk modulus of the mixture:

$$N = \frac{K_s}{b-n} = 6.85 \times 10^7 kPa \quad M = \frac{K_f N}{K_f + Nn} = 4.47 \times 10^6 kPa \quad (310.52)$$

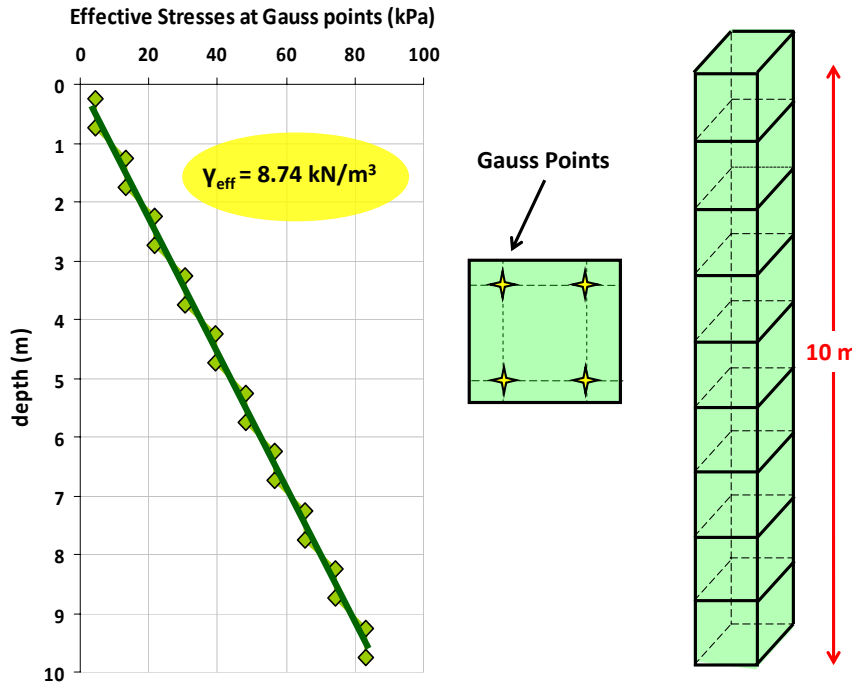


Figure 310.16: The distribution of the vertical effective stresses with depth due to self-weight. The stresses are calculated at the Gauss points within each brick element. The stresses obtained from the numerical analysis are equal for all the Gauss points within the element, due to the compatibility of deformations at the element interfaces.

$$K_u = K + b^2 M = 4.4 \times 10^6 \text{ kPa} \quad (310.53)$$

The diffusion coefficient and characteristic time of consolidation:

$$c_f = \frac{kM}{\gamma_w} \frac{K + \frac{4\mu}{3}}{K_u + \frac{4\mu}{3}} = 1.2 \text{ m}^2/\text{s} \quad t = \frac{h^2}{c_f} = 83.33 \text{ s} \quad (310.54)$$

310.7.3 Discussion of Numerical Results - Conclusions

The stage of self weight application shows in Fig. 310.19 that the expected estimated settlement is quite close to the one obtained from the analysis. The difference in the two values is due to the stress distribution coming out of the analysis which is slightly different than the one considered in theory (see Fig. 310.16) and possibly due to the compressibility of soil particles in the numerical analysis.

In Fig. 310.24, the normalized fluid pressure is plotted against the location for various normalized times. For normalized time $T_v = 0.1$, only the nodes close to the top free flow surface display the dissipation of the pore pressure. The experimental result provide good agreement with the analytical

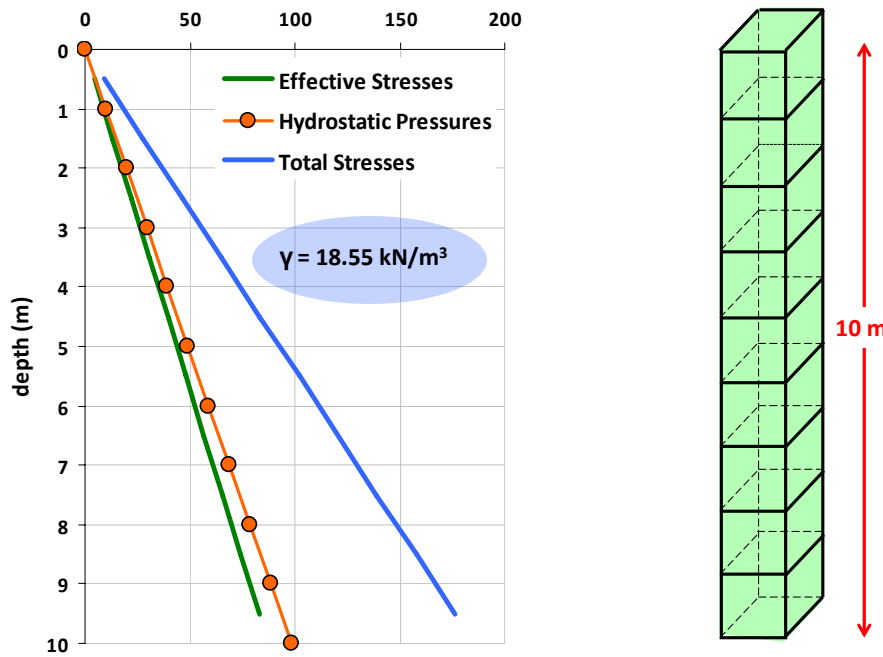


Figure 310.17: The distribution of the hydrostatic pore pressures, the effective and total stresses with depth, obtained from the numerical analysis after self-weight application.

solution. With the increase of the normalized time, we can clearly see the tendency of the dissipation of the water. At normalized time $T_v = 1.0$ (natural time $t = 83$ sec), the maximum normalized pore pressure is only about 0.11. It can be concluded that the numerical analysis can effectively demonstrate the process of the dissipation of the pore pressure.

In Fig. 310.26, the change of the porosity is predicted due to the consolidation of the soil layer. Both the change of volume of the soil ($0.1782 m^3$) and the fluid ($0.1794 m^3$) have been calculated. Theoretically, these two values should be the same, according to the fact that the settlement of the soil layer is due the fluid which is squeezed out, assuming that the soil grains are incompressible. However, this difference in the values is due to the compressibility of the soil grains, which was not considered infinite in the numerical analysis.

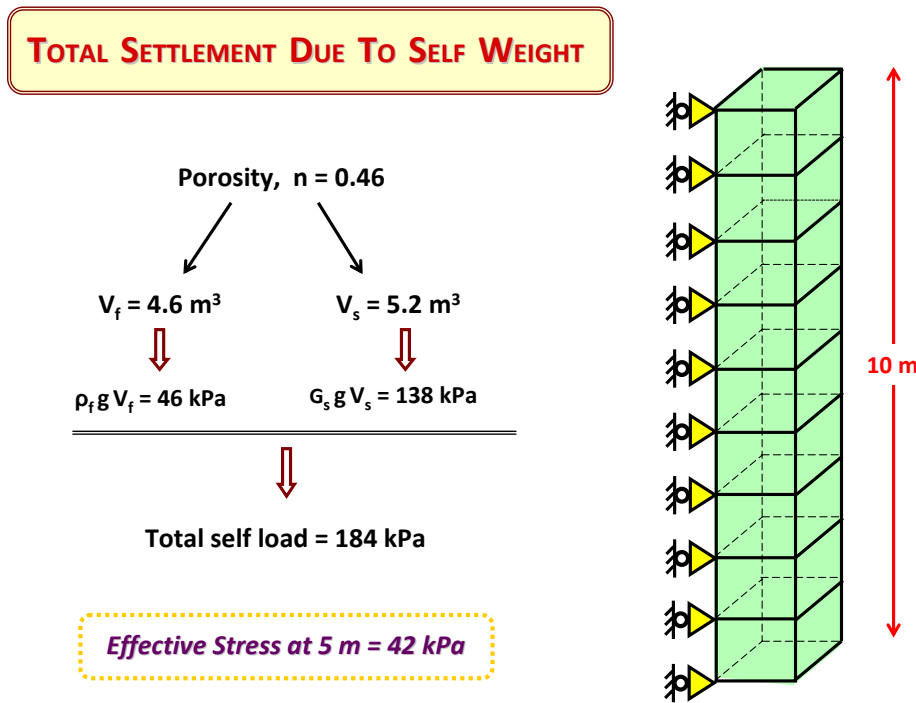


Figure 310.18: Estimation of the total self load, as it is obtained from the numerical analysis, given the porosity and the densities of the fluid (ρ_f) and the grains (ρ_s or G_s).

310.8 One dimensional wave propagation in elastic porous media subjected to step displacement boundary condition

310.8.1 Brief review of Analytical Solution by Gajo and Mongiovi (1995)

An one-dimensional exact analytical solution of the Biot's equations is provided by [Gajo and Mongiovi \(1995\)](#) for the completely general solution of the transient problem in saturated, linear, elastic, porous media. The analytical solution was obtained was obtained by Fourier series. This solution is considered to be completely general because it is not based on any assumptions with respect to the inertial, viscous or mechanical coupling. Furthermore, it can be applied to any type of boundary-initial value problem.

The advantage of this analytical solution consists of showing the mechanics of dispersive wave propagation in saturated elastic solids. This is achieved by allowing the detailed analysis of wave fronts of the first and second kind of longitudinal waves and by analyzing accurately the effects of each term of coupling on the transient behavior of saturated porous media. In particular, since each term of the Fourier series represents a frequency component of the excitation signal, the analytical solution can

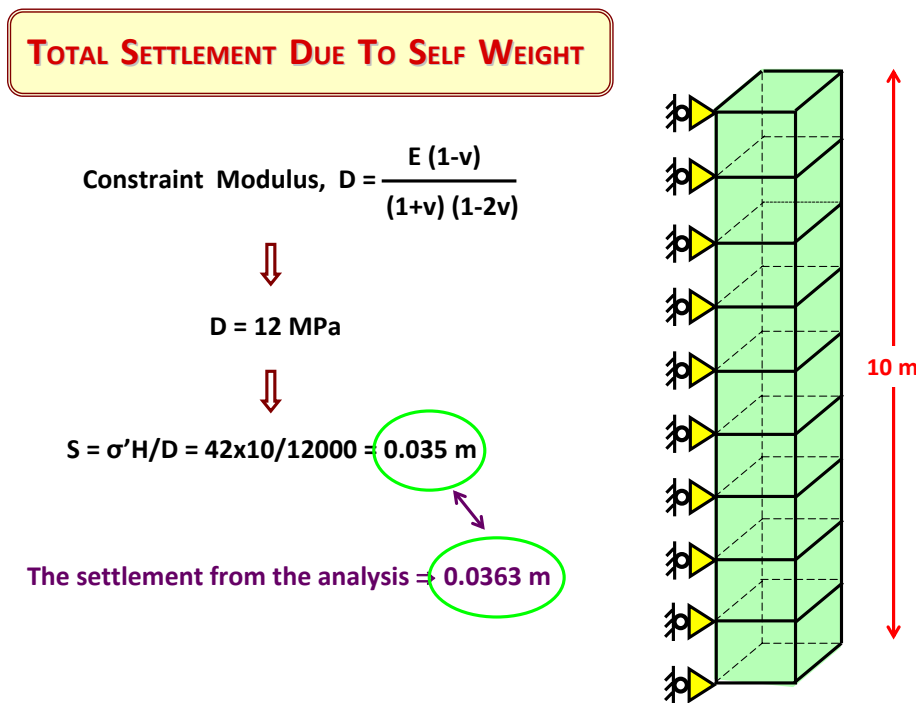


Figure 310.19: Prediction of the total settlement due to self-weight and comparison with the numerical result.

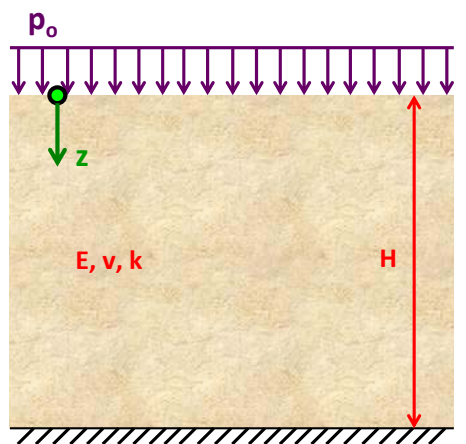
describe the behavior of each frequency component. Thus, it can illustrate the mechanics of dispersive wave propagation in which higher frequencies propagate with two waves and lower frequencies with only one wave, as a function of permeability and travel length.

Considering the above mentioned arguments, the analytical solution can provide a useful comparative term towards the verification and the validation of the existing numerical solutions based on the finite element method. Such a study was conducted by Gajo et al. (1994), by comparing analytical results with numerical ones obtained by a $u - p - U$ numerical formulation.

In the paper by Gajo and Mongiovi (1995), the transient response of porous media is shown for typical material properties of a natural granular deposit and for different degrees of viscous coupling. Specifically, analytical results are given from the solution of the following one-dimensional boundary value problem: at the top and bottom surfaces of a soil layer of finite thickness L , the excitation consisting of a step displacement boundary condition (Heaviside function) is applied to both solid and fluid phases. This problem can demonstrate better the mechanics of dispersive wave propagation, since the step excitation contains waves of all kind of frequencies. The analytical solution is relative only to the first arrival of the waves of the first and second kind.

CONSOLIDATION WITH SINGLE DRAINAGE AT TOP

$$p_e = \sum_{m=1}^{\infty} \left[\left(\frac{2P_0}{m\pi} \right) (1 - \cos m\pi) \sin \left(\frac{m\pi z}{2H_0} \right) \exp \left(\frac{-m^2\pi^2 T}{4} \right) \right]$$



Time Factor: $T_v = C_v t / H^2$

Coefficient of Consolidation:

$$C_v = k D / \gamma_w$$

In our case:

$$C_v = 10^{-3} \cdot 12000 / 10 = 1.2$$

$$t_{\text{total}} = H^2 / C_v = 100 / 1.2 = 83.33 \text{ sec}$$

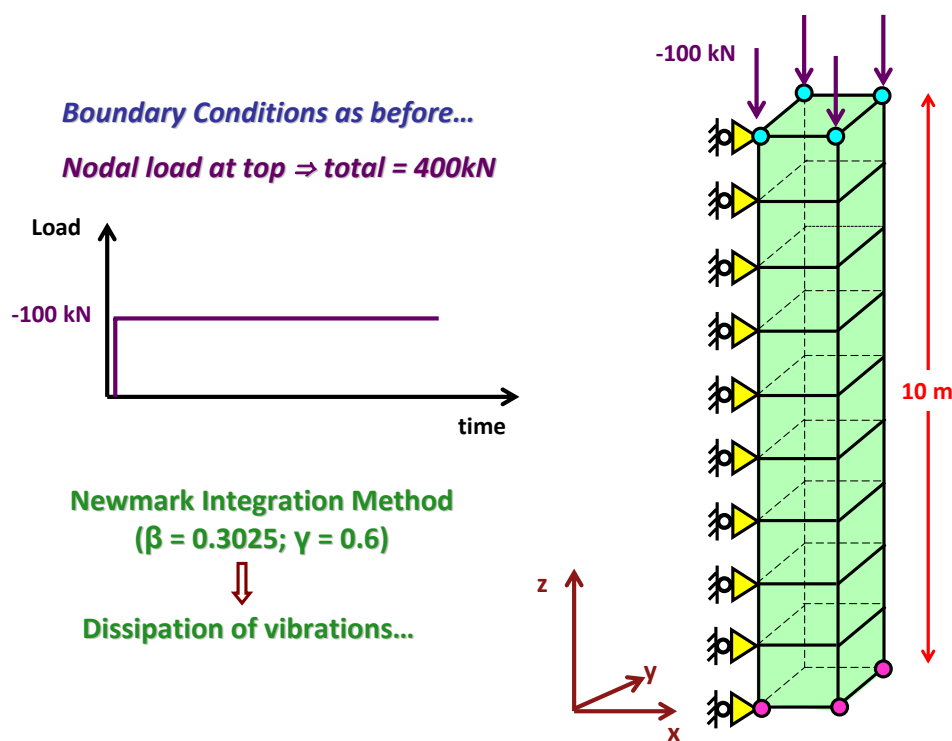


Figure 310.21: Numerical simulation of 1D consolidation of a soil layer.

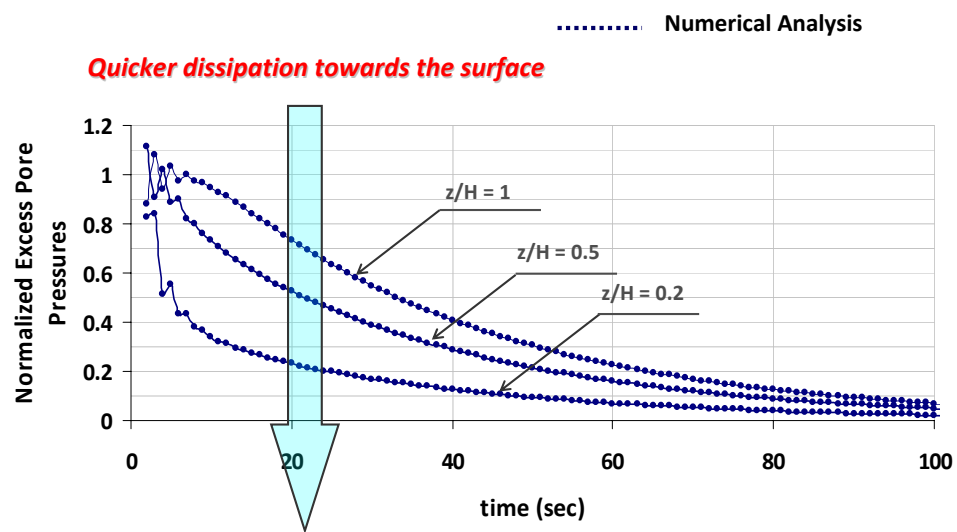


Figure 310.22: Time history of the normalized excess pore pressure for three different normalized depths indicating faster dissipation close to the surface. The dissipation has practically been completed at $t = 83.33\text{sec}$, as predicted.

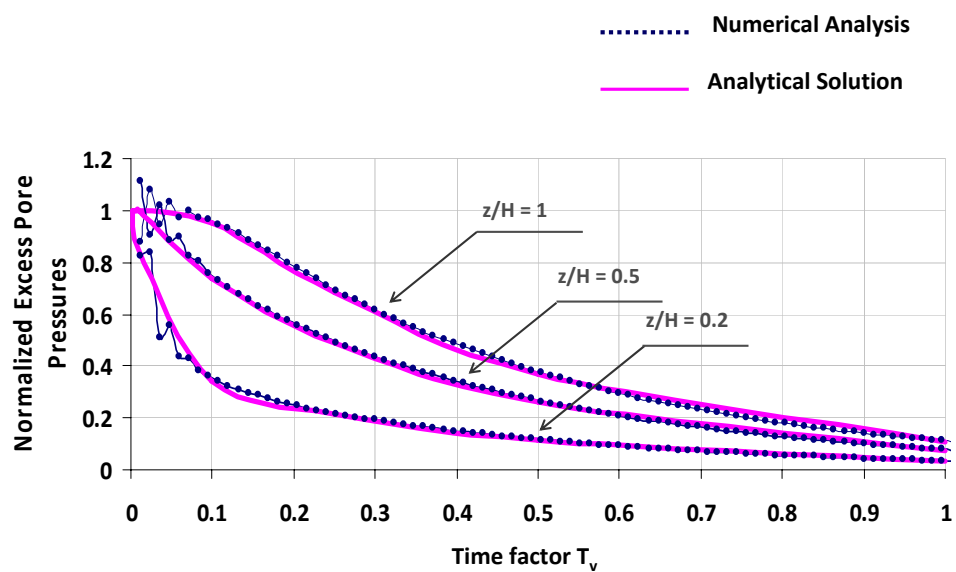


Figure 310.23: Normalized excess pore pressures versus normalized time for three different normalized depths. Comparison of numerical results with the analytical ones.

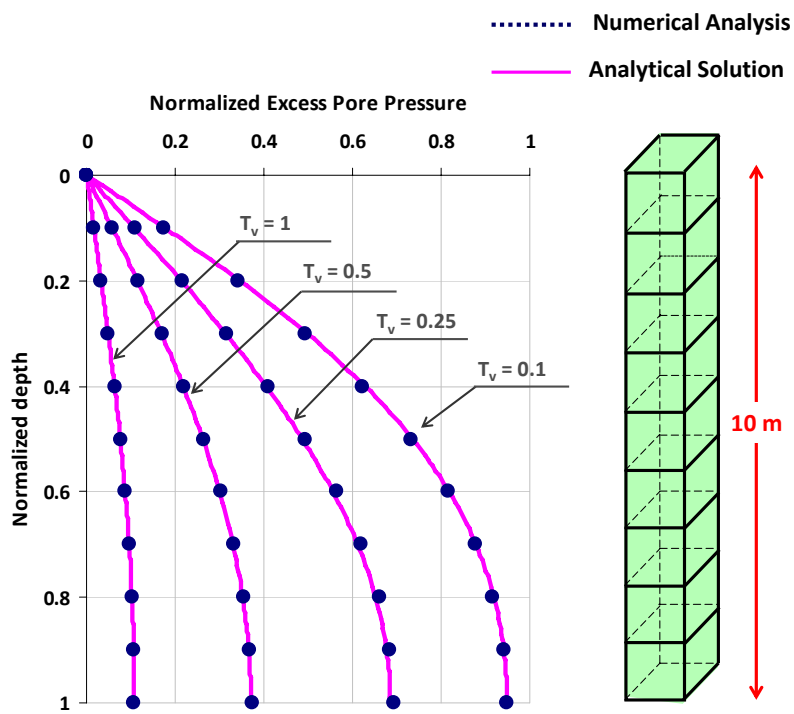


Figure 310.24: Distribution of normalized excess pore pressures with normalized depth for four different time factors. Comparison of numerical results with the analytical ones.

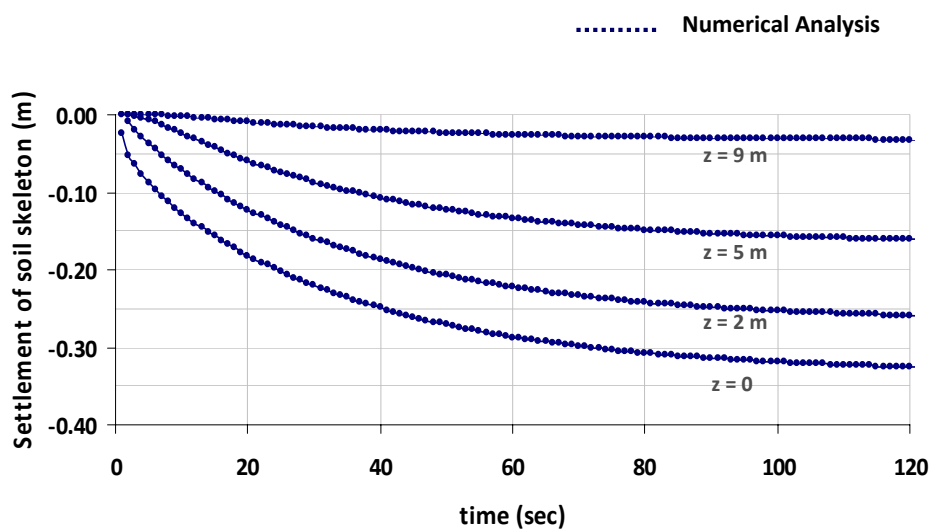


Figure 310.25: Time history of the settlements for four different depths.

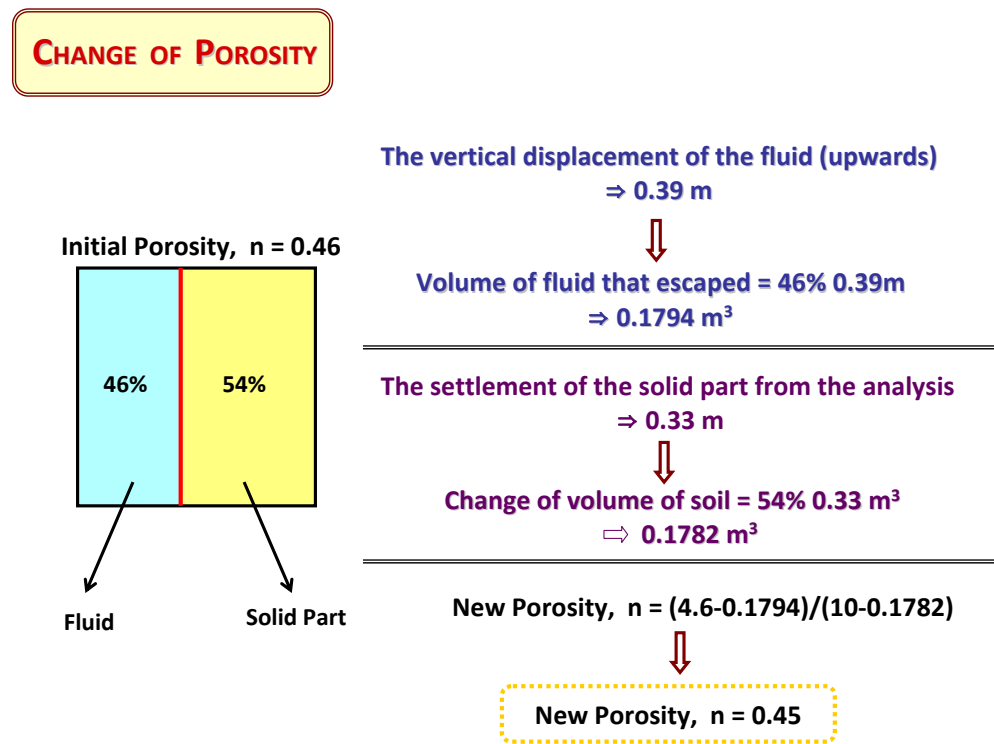


Figure 310.26: Prediction of the change in porosity of the soil layer due to consolidation.

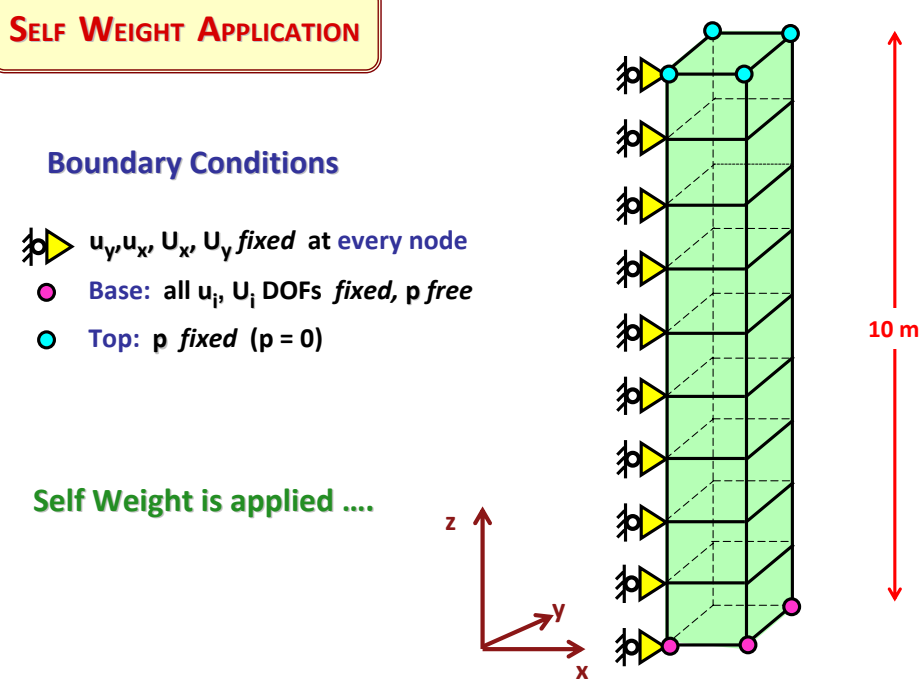


Figure 310.27: Boundary Conditions applied to the numerical model throughout the self-weight application and the process of consolidation due to extra load applied to the surface of the soil column.

310.8.2 Numerical Analysis

Numerical examples for three different values of viscous coupling ($k = 10^{-8} \text{ cm}^3 \text{s/g}$, $k = 10^{-6} \text{ cm}^3 \text{s/g}$, $k = 10^{-5} \text{ cm}^3 \text{s/g}$) were solved in order to verify the previously mentioned $u - p - U$ formulation in a wide range of drag. The numerical model used for the simulation of the 1C shock wave propagation consists of 400 u-p-U brick finite elements of dimensions $0.01\text{cm} \times 0.01\text{cm} \times 0.01\text{cm}$ creating a soil column 4cm thick. Figure 310.28 illustrates the transition from the physical configuration of the problem to its numerical simulation. Table 310.6 shows the soil properties of the numerical model.

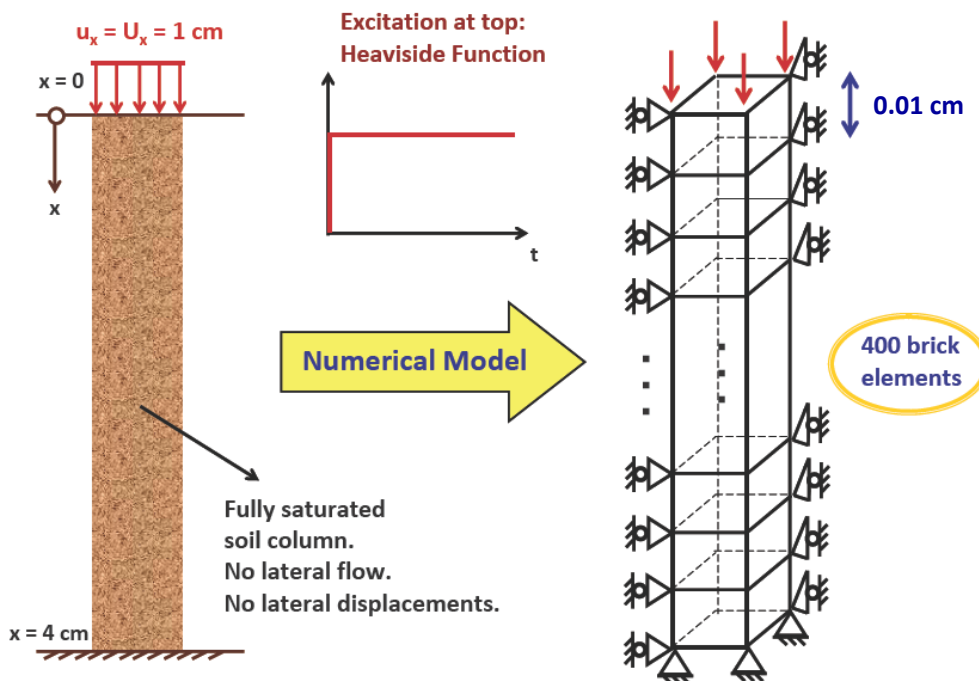


Figure 310.28: The numerical model used for the verification of the finite element implementation through comparison with the analytical results provided by Gajo and Mongiovi (1995).

At the top surface of the soil column, a step displacement of $1.0 \times 10^{-3} \text{ cm}$ is applied both to the solid and the fluid phase. Only the vertical displacement is free. There is no lateral flow or displacement. The degree of freedom related to the pore pressures is constrained at the top surface to be equal to the atmospheric pressure and is free at the rest of the nodes. The base of the model is rigid and impervious.

This kind of excitation (Heaviside function) applied at the top of the model, results clearly in waves of all kinds of frequency, first due to its nature and secondarily due to the way of its application. This fact together with the great stiffness of the solid skeleton (see Table 310.6 require a very dense spatial

Table 310.6: Soil Properties for 1C shock wave propagation for the problem by Gajo and Mongiovi (1995).

Parameter	Symbol	Value
gravity acceleration	g	9.81 m/s^2
soil matrix Young's Modulus	E	$1.2 \times 10^6 \text{ kN/m}^2$
soil matrix Poisson's ratio	ν	0.3
solid particle density	ρ_s	$2.7 \times 10^3 \text{ kg/m}^3$
water density	ρ_f	$1.0 \times 10^3 \text{ kg/m}^3$
solid particle bulk modulus	K_s	$36.0 \times 10^6 \text{ kN/m}^2$
fluid bulk modulus	K_f	$2.177 \times 10^6 \text{ kN/m}^2$
porosity	n	0.4
Biot coefficient	α	1.0

discretization. Here, 400 u-p-U brick finite elements of dimensions $0.01\text{cm} \times 0.01\text{cm} \times 0.01\text{cm}$, following similar discretization with [Gajo et al. \(1994\)](#). The time step, δt required needs to be limited to

$$\delta t < \frac{\delta h}{v} \quad (310.55)$$

$$(310.56)$$

where v is the highest wave velocity. In our case, the temporal integration involves 800 steps of $2.0 \times 10^{-8}\text{sec}$, which allows a maximum wave velocity of $5.0 \times 10^5\text{m/s}$.

Two different time integration methods where used: i) The Newmark integrator and ii) The Hilber-Hughes-Taylor (HHT) Integrator. Sets of parameters, assuring unconditionally numerical stability, were chosen for both integrators. For the case of Newmark integrator (see Figures 310.29 - 310.44), the following sets of parameters were used:

- a) $\gamma = 0.5$ and $\beta = 0.25$,
- b) $\gamma = 0.6$ and $\beta = 0.3025$,
- c) $\gamma = 0.7$ and $\beta = 0.4$.

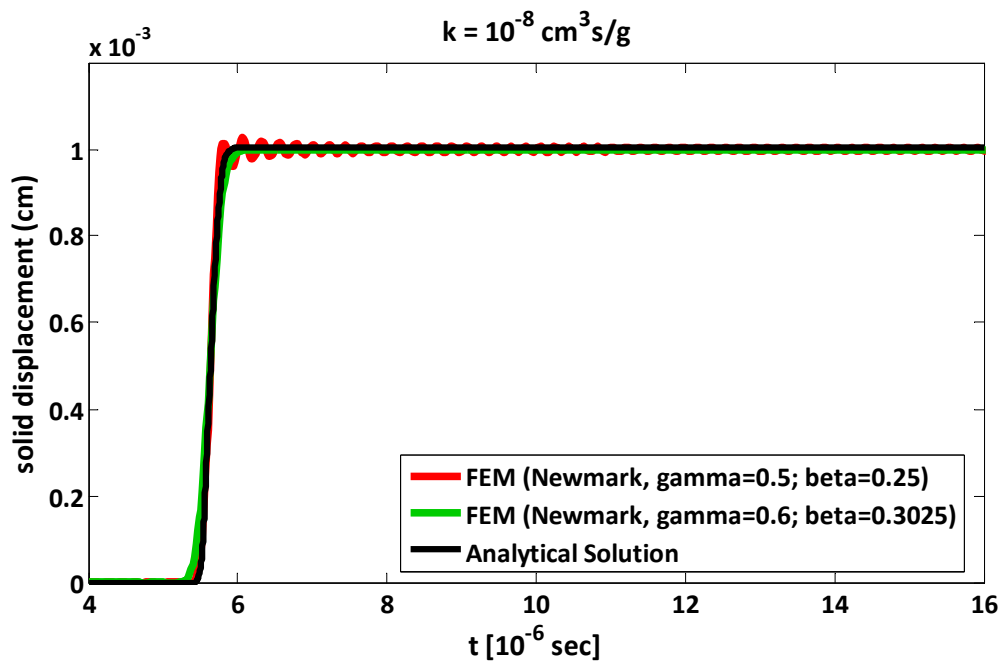


Figure 310.29: Time history of solid displacements of longitudinal waves at 1 cm below the surface. Comparison of numerical results (FEM) with the analytical solution by Gajo and Mongiovi (1995) for the case of viscous coupling ($k = 10^{-8} \text{ cm}^3 \text{s/g}$). Two different sets of Newmark parameters were used for the numerical analysis.

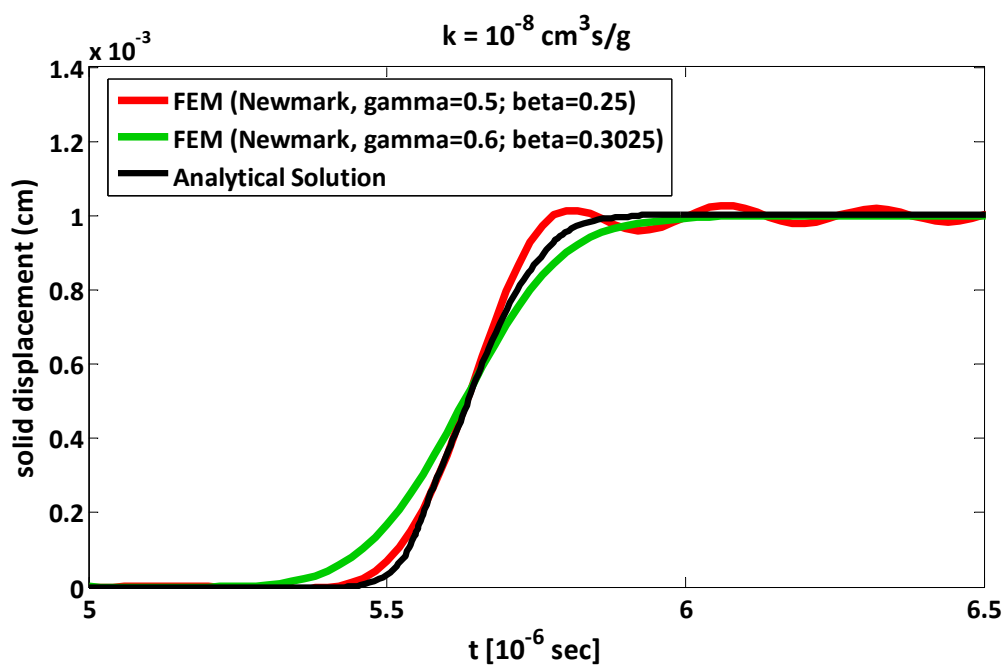


Figure 310.30: A magnified view of Figure 310.29 illustrating the details of wave front of the longitudinal wave of first kind.

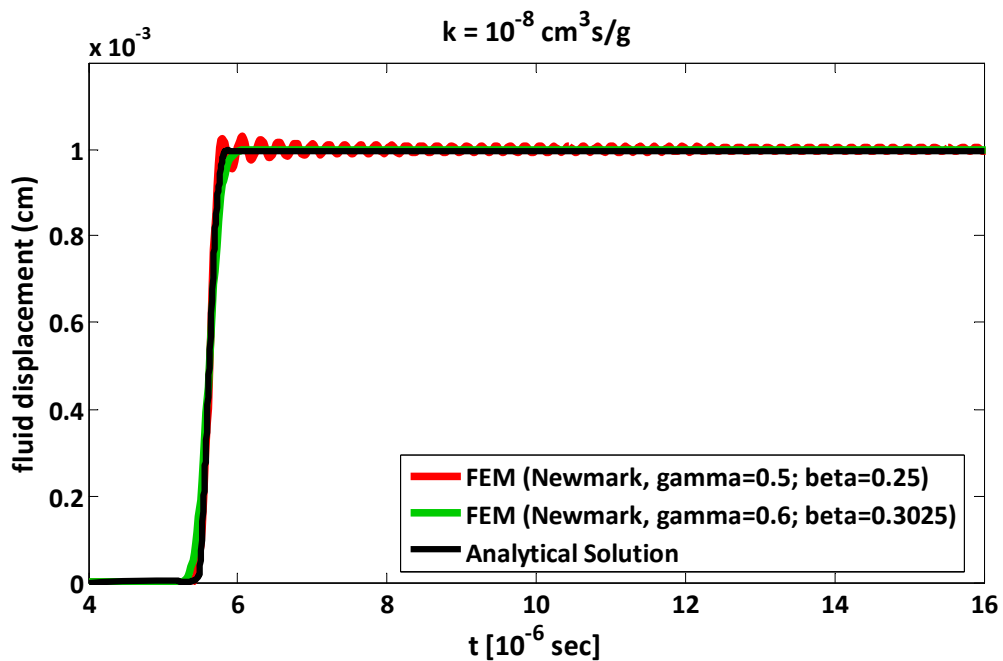


Figure 310.31: Time history of fluid displacements of longitudinal waves at 1 cm below the surface. Comparison of numerical results (FEM) with the analytical solution by Gajo and Mongiovi (1995) for the case of viscous coupling ($k = 10^{-8} \text{ cm}^3 \text{s/g}$). Two different sets of Newmark parameters were used for the numerical analysis.

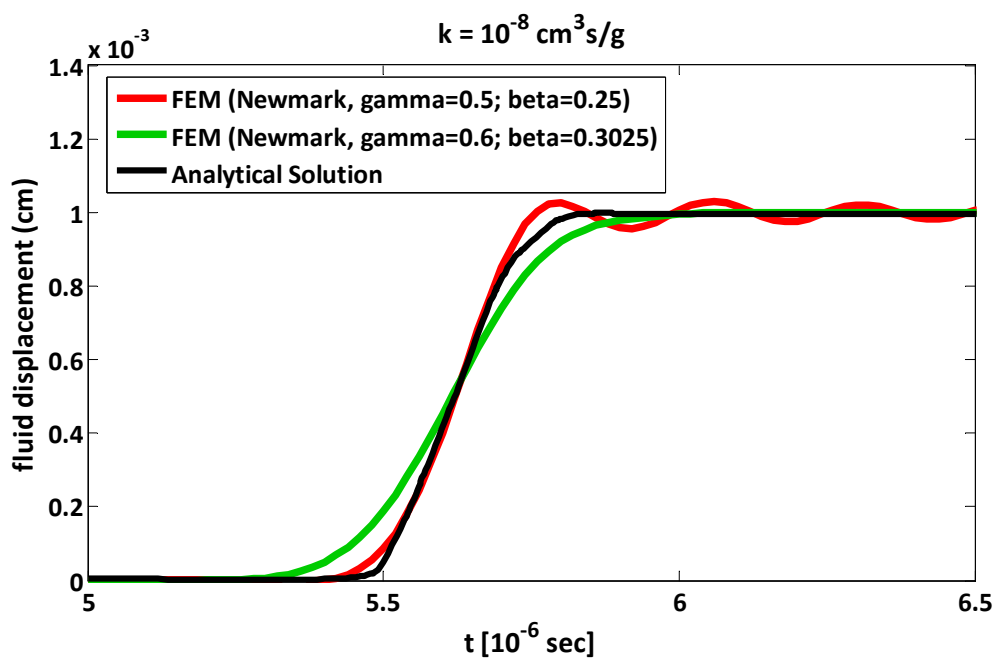


Figure 310.32: A magnified view of Figure 310.31 illustrating the details of wave front of the longitudinal wave of first kind.

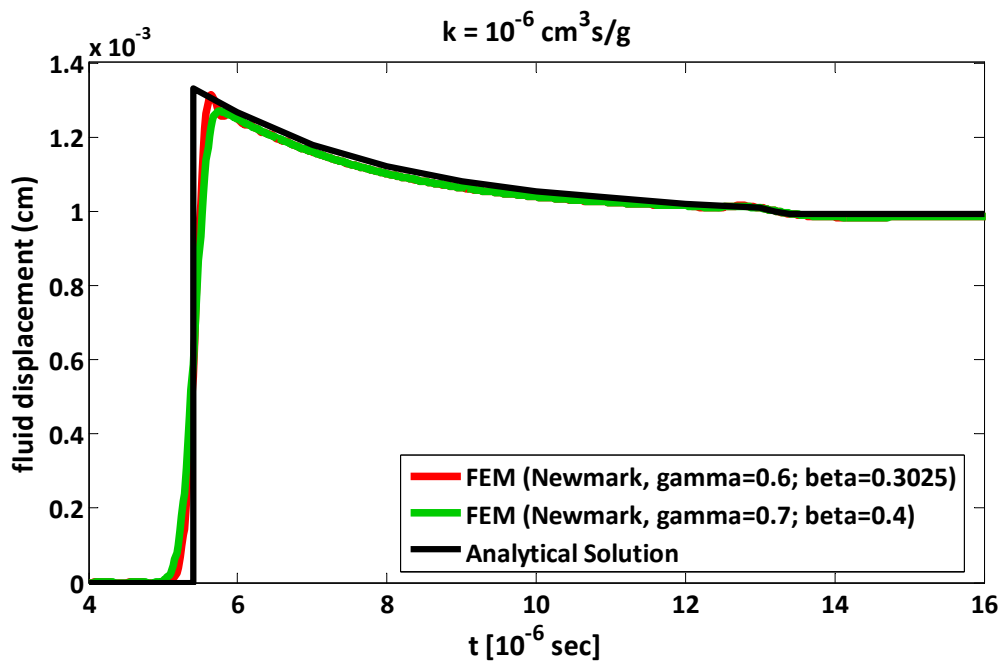


Figure 310.33: Time history of solid displacements of longitudinal waves at 1 cm below the surface. Comparison of numerical results (FEM) with the analytical solution by Gajo and Mongiovi (1995) for the case of viscous coupling ($k = 10^{-6} \text{ cm}^3 \text{s/g}$). Two different sets of Newmark parameters were used for the numerical analysis.

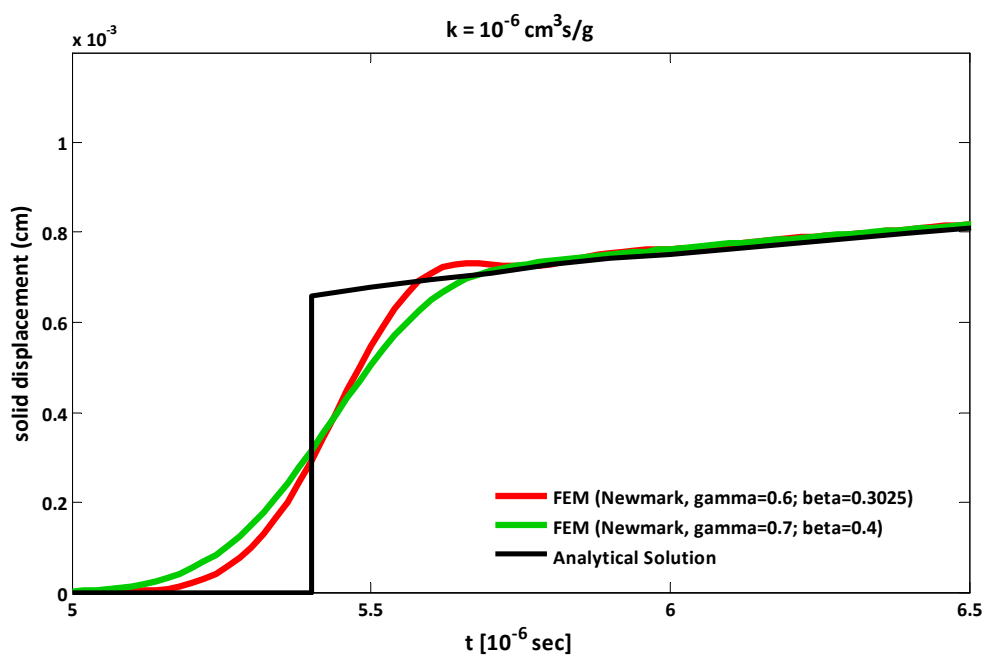


Figure 310.34: A magnified view of Figure 310.33 illustrating the details of wave front of the longitudinal wave of first kind.

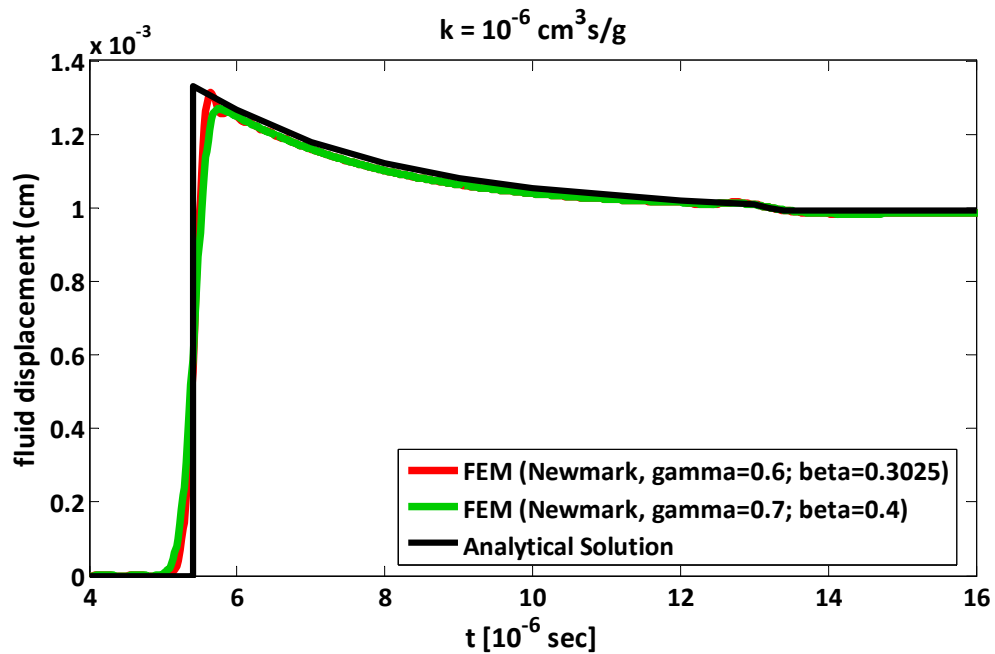


Figure 310.35: Time history of fluid displacements of longitudinal waves at 1 cm below the surface. Comparison of numerical results (FEM) with the analytical solution by Gajo and Mongiovi (1995) for the case of viscous coupling ($k = 10^{-6} \text{ cm}^3 \text{s/g}$). Two different sets of Newmark parameters were used for the numerical analysis.

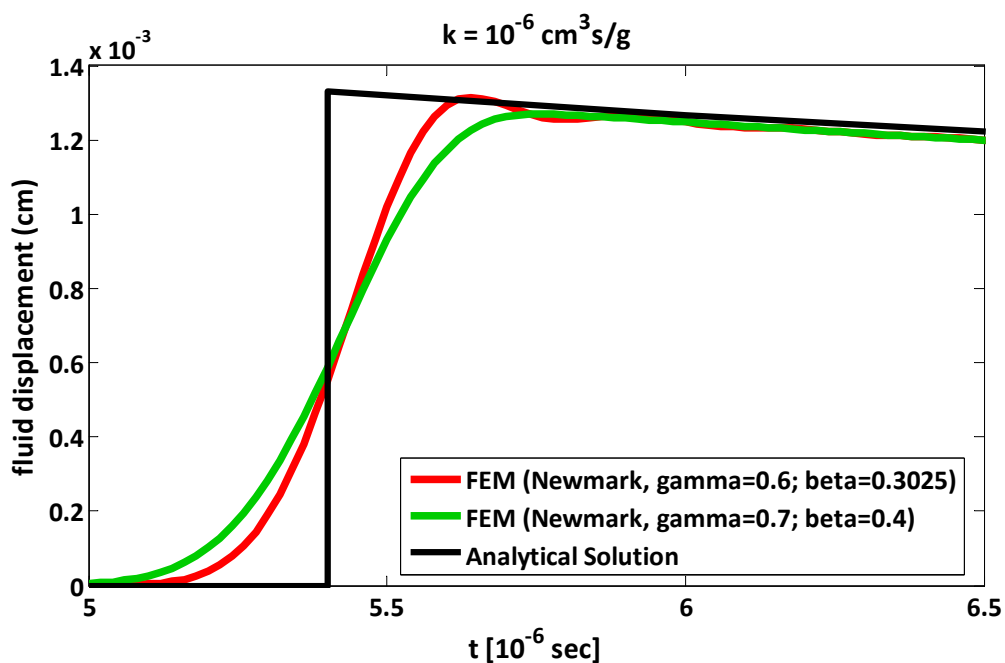


Figure 310.36: A magnified view of Figure 310.35 illustrating the details of wave front of the longitudinal wave of first kind.

For the HHT integrator (see Figures 310.45 - 310.56), the following sets of parameters were used:

- $\alpha = -0.1$, $\gamma = 0.6$ and $\beta = 0.3025$,
- $\alpha = -0.3$, $\gamma = 0.8$ and $\beta = 0.4225$.

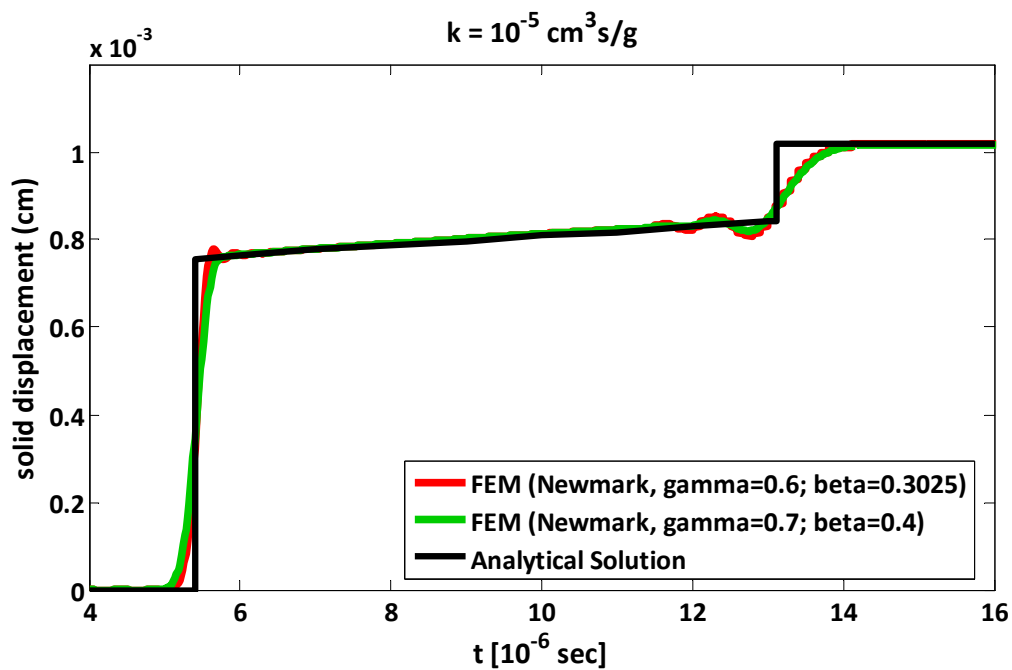


Figure 310.37: Time history of solid displacements of longitudinal waves at 1 cm below the surface. Comparison of numerical results (FEM) with the analytical solution by Gajo and Mongiovi (1995) for the case of viscous coupling ($k = 10^{-5} \text{ cm}^3 \text{s/g}$). Two different sets of Newmark parameters were used for the numerical analysis.

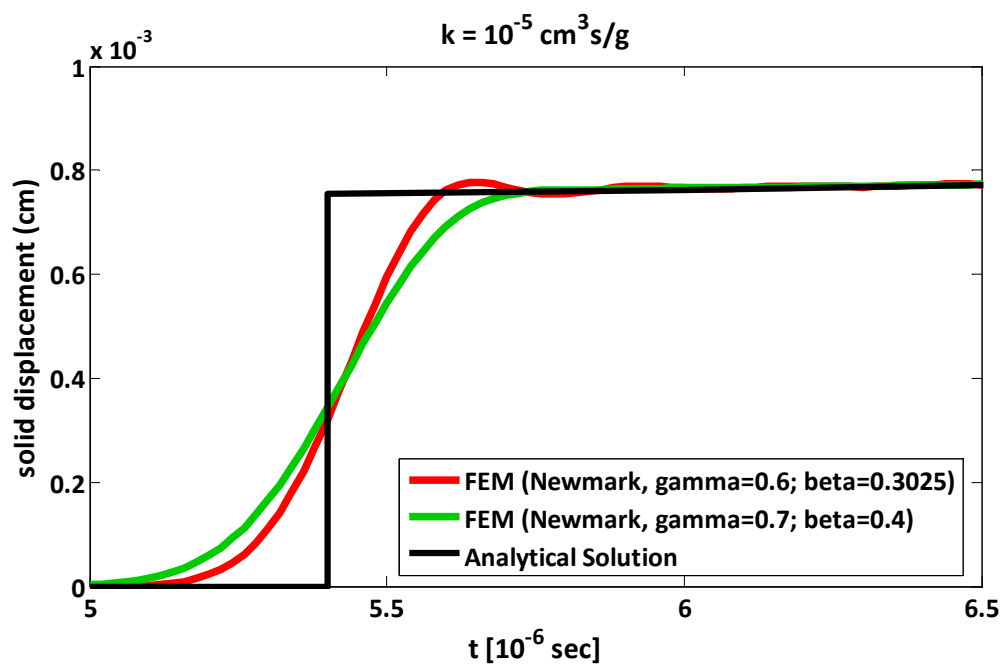


Figure 310.38: A magnified view of Figure 310.37 illustrating the details of wave front of the longitudinal wave of first kind.

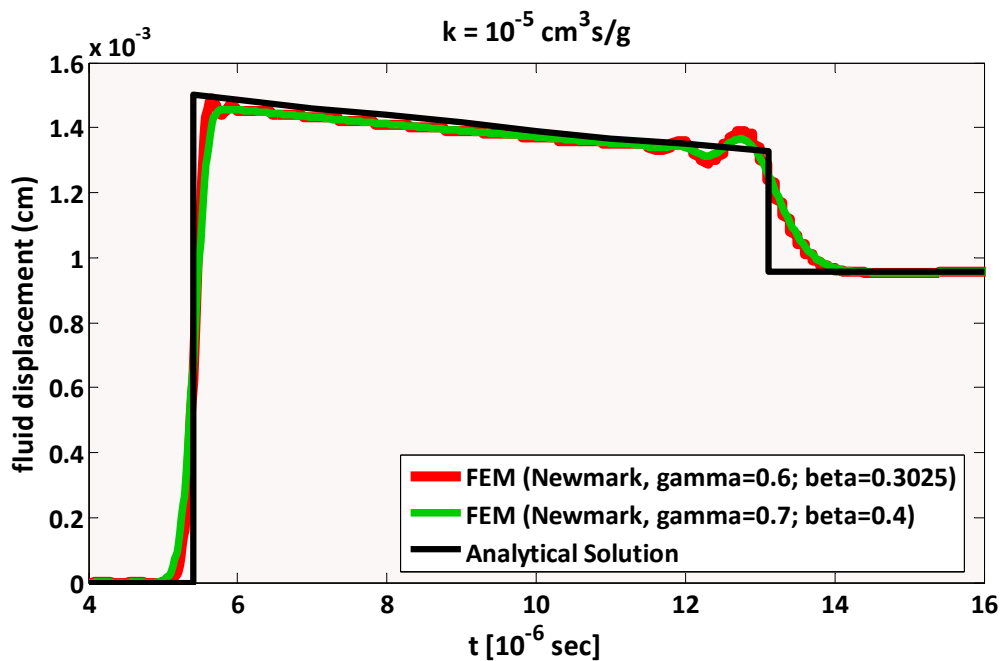


Figure 310.39: Time history of fluid displacements of longitudinal waves at 1 cm below the surface. Comparison of numerical results (FEM) with the analytical solution by Gajo and Mongiovi (1995) for the case of viscous coupling ($k = 10^{-5} \text{ cm}^3 \text{s/g}$). Two different sets of Newmark parameters were used for the numerical analysis.

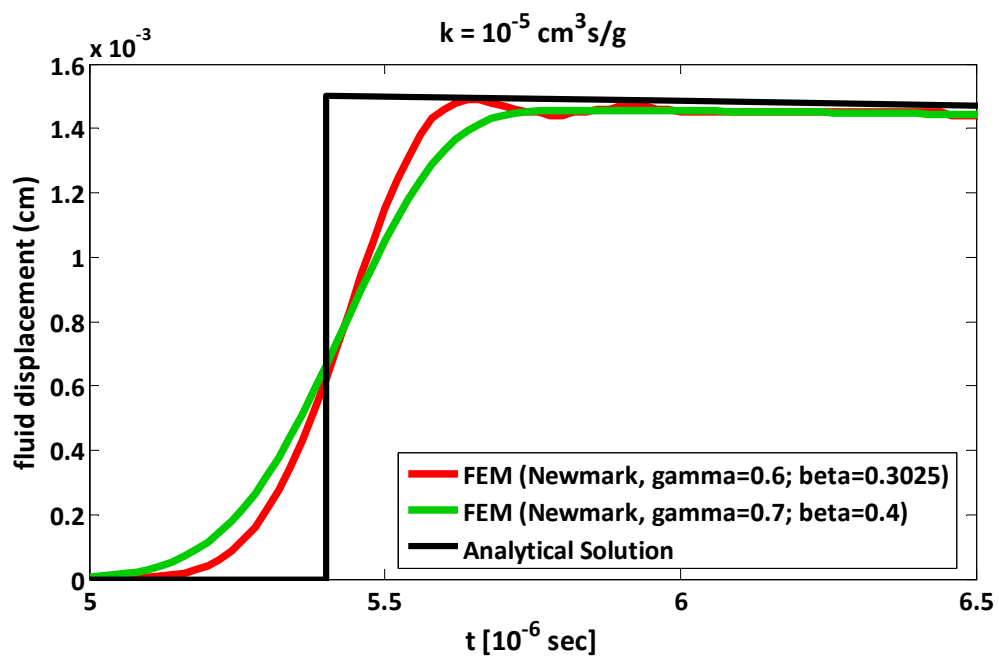


Figure 310.40: A magnified view of Figure 310.39 illustrating the details of wave front of the longitudinal wave of first kind.

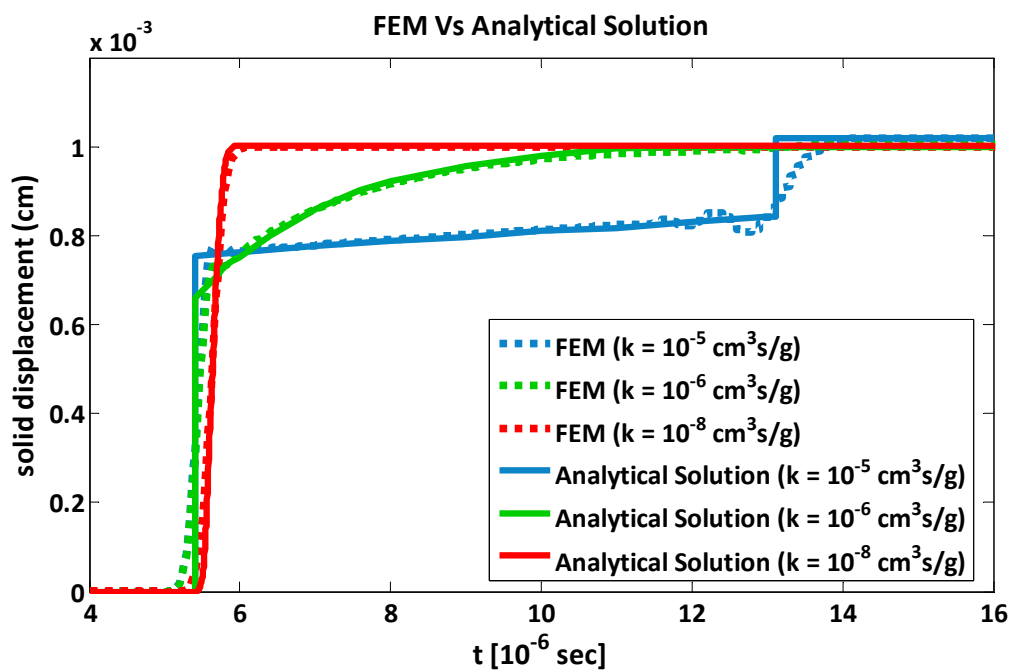


Figure 310.41: Time history of solid displacements of longitudinal waves at 1 cm below the surface. Comparison of numerical results (FEM) with the analytical solution by Gajo and Mongiovi (1995) for three different values of viscous coupling. The Newmark set of parameters used for the numerical solution was: $\gamma = 0.6$ and $\beta = 0.3025$.

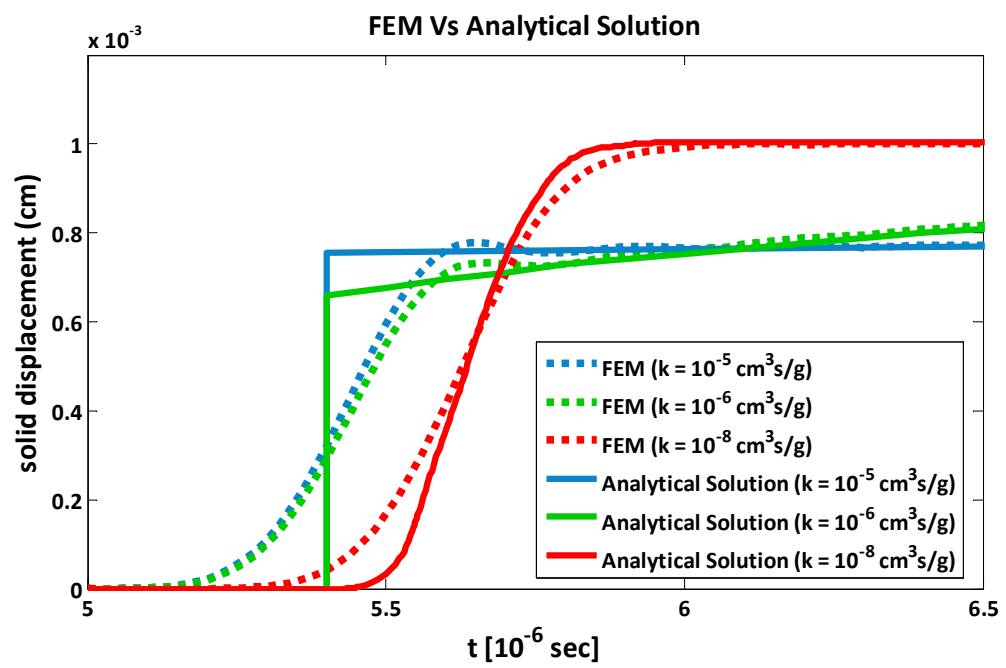


Figure 310.42: A magnified view of Figure 310.41 illustrating the details of wave front of the longitudinal wave of first kind.

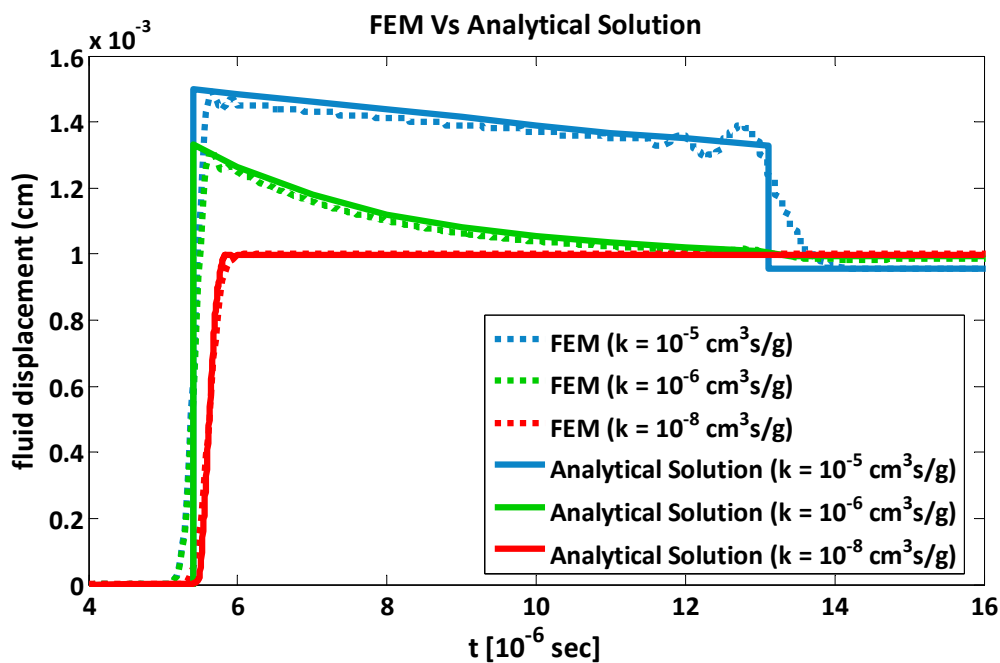


Figure 310.43: Time history of fluid displacements of longitudinal waves at 1 cm below the surface. Comparison of numerical results (FEM) with the analytical solution by Gajo and Mongiovi (1995) for three different values of viscous coupling. The Newmark set of parameters used for the numerical solution was: $\gamma = 0.6$ and $\beta = 0.3025$.

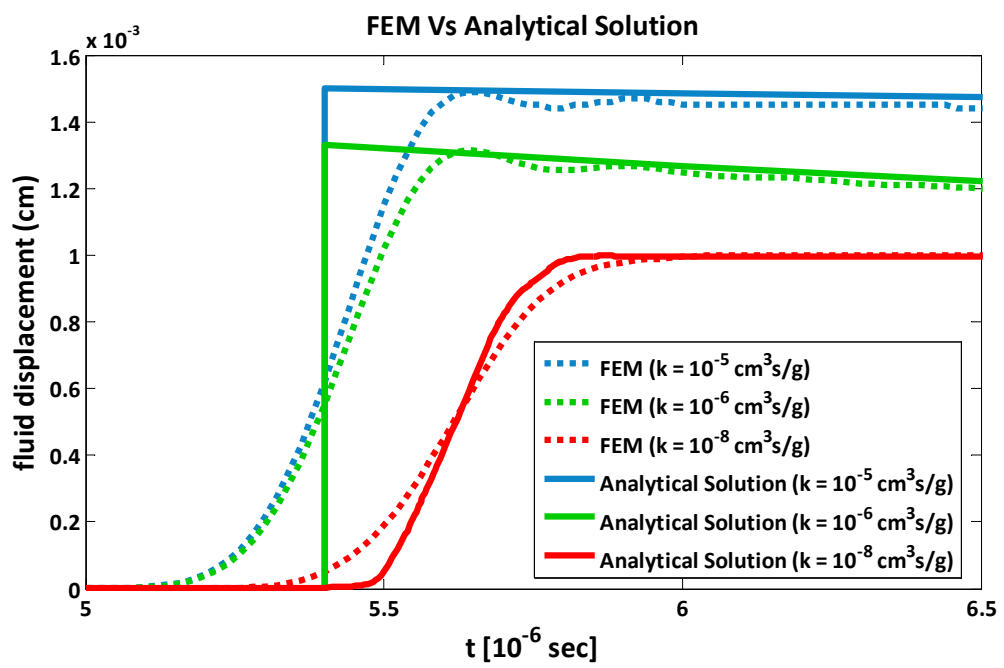


Figure 310.44: A magnified view of Figure 310.43 illustrating the details of wave front of the longitudinal wave of first kind.

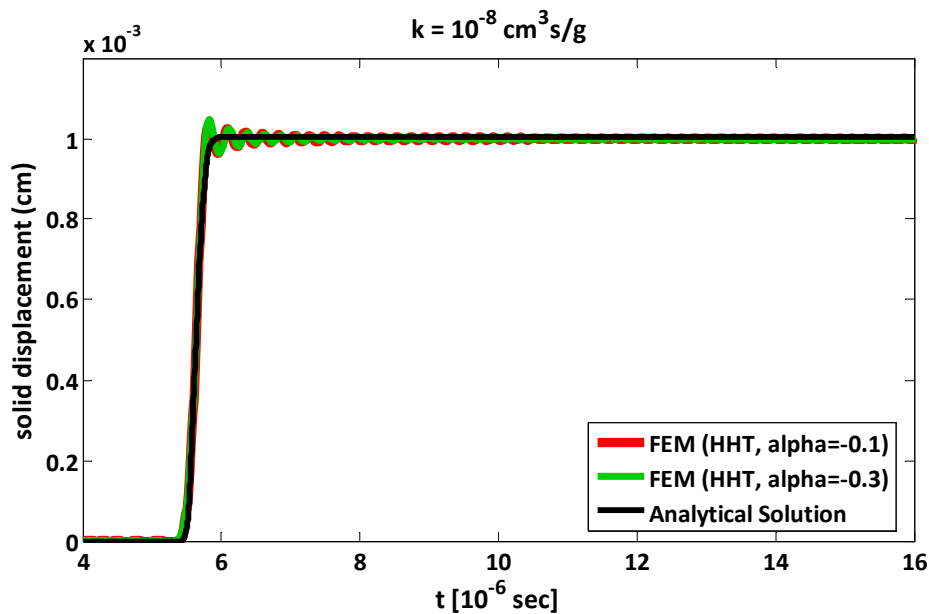


Figure 310.45: Time history of solid displacements of longitudinal waves at 1 cm below the surface. Comparison of numerical results (FEM) with the analytical solution by [Gajo and Mongiovi \(1995\)](#) for the case of viscous coupling($k = 10^{-8} \text{ cm}^3 \text{s/g}$). Two different sets of unconditional stable HHT parameters were used for the numerical analysis.

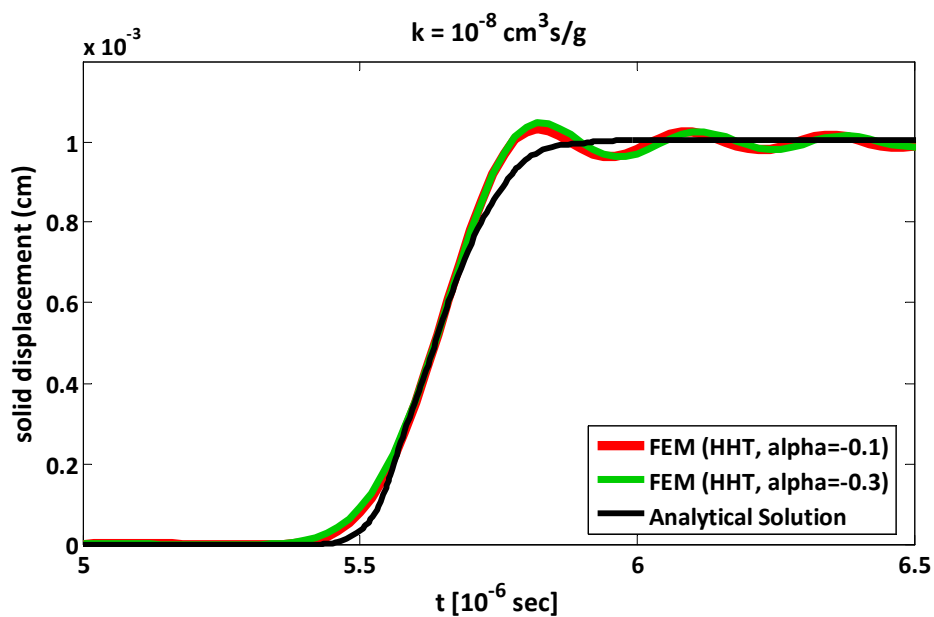


Figure 310.46: A magnified view of Figure 310.45 illustrating the details of wave front of the longitudinal wave of first kind.

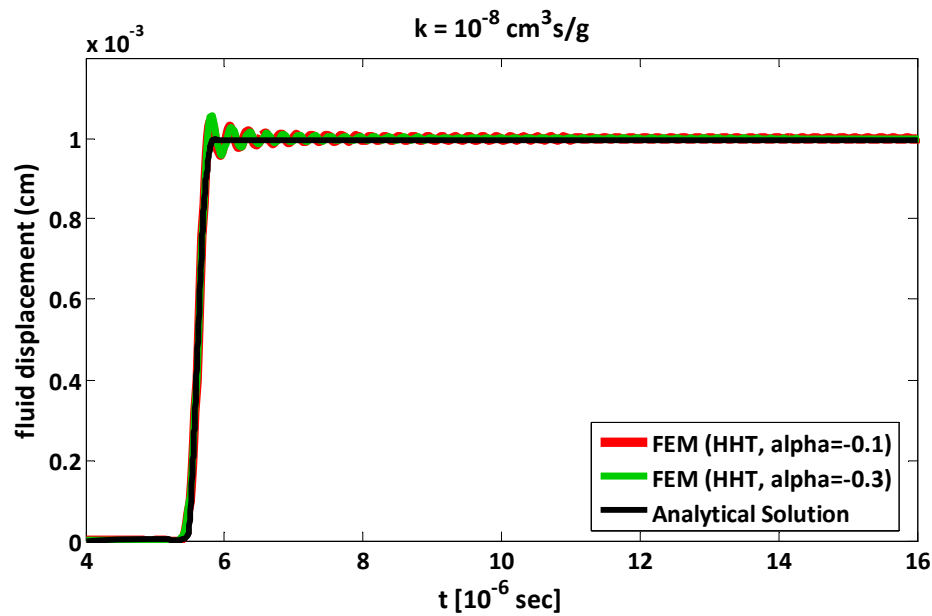


Figure 310.47: Time history of fluid displacements of longitudinal waves at 1 cm below the surface. Comparison of numerical results (FEM) with the analytical solution by Gajo and Mongiovì (1995) for the case of viscous coupling ($k = 10^{-8} \text{ cm}^3 \text{s/g}$). Two different sets of unconditional stable HHT parameters were used for the numerical analysis.

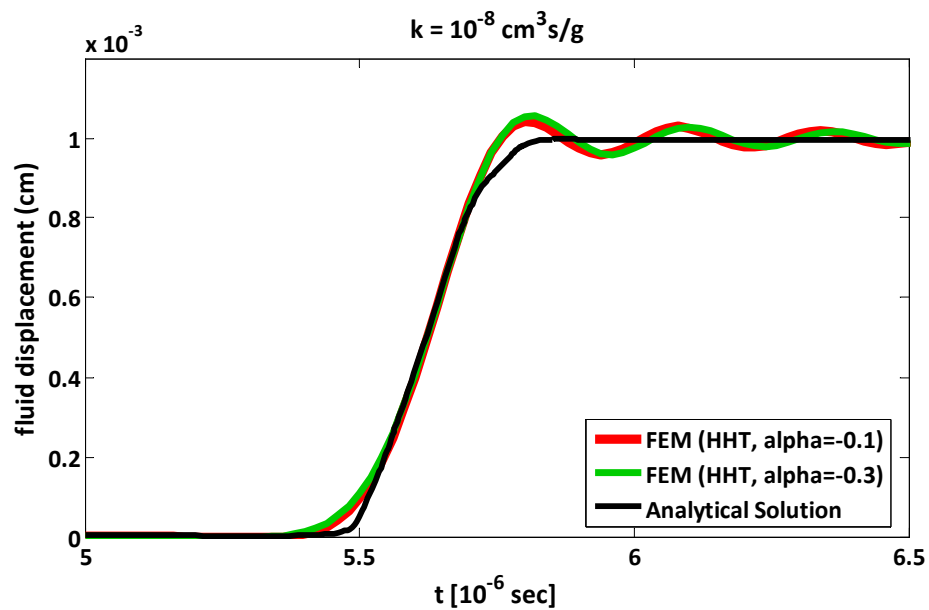


Figure 310.48: A magnified view of Figure 310.47 illustrating the details of wave front of the longitudinal wave of first kind.

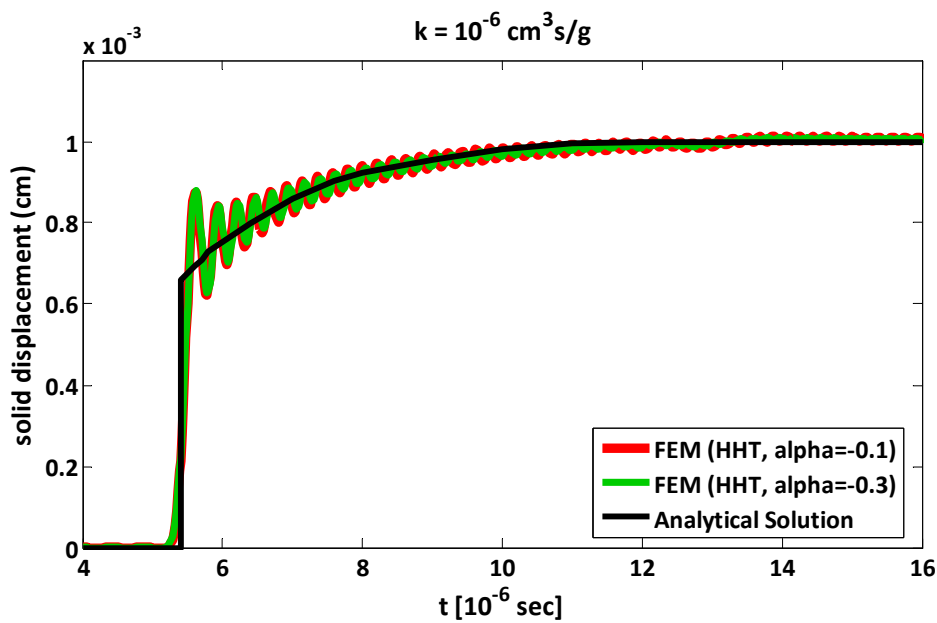


Figure 310.49: Time history of solid displacements of longitudinal waves at 1 cm below the surface. Comparison of numerical results (FEM) with the analytical solution by Gajo and Mongiovì (1995) for the case of viscous coupling ($k = 10^{-6} \text{ cm}^3 \text{s/g}$). Two different sets of unconditional stable HHT parameters were used for the numerical analysis.

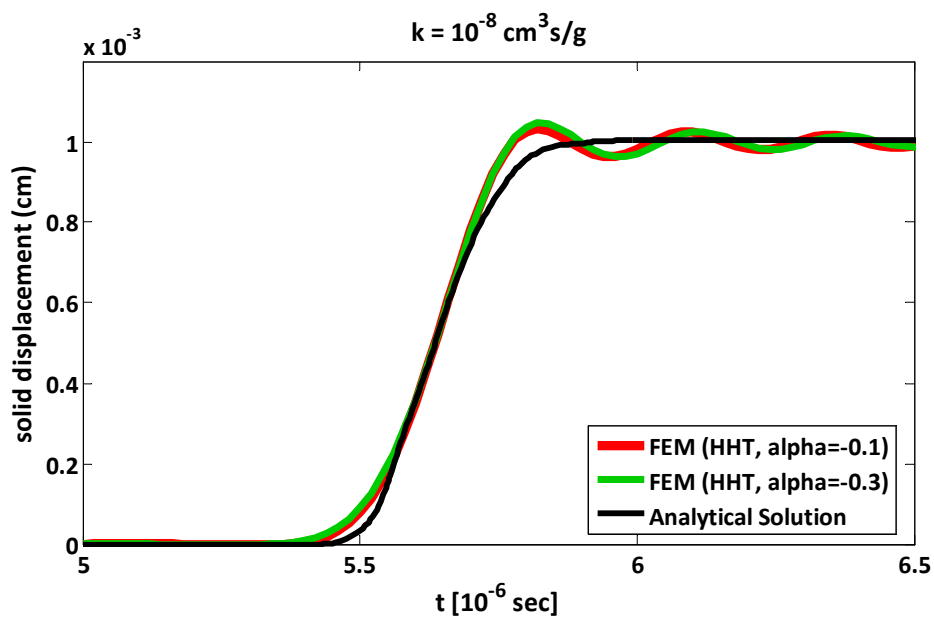


Figure 310.50: A magnified view of Figure 310.49 illustrating the details of wave front of the longitudinal wave of first kind.

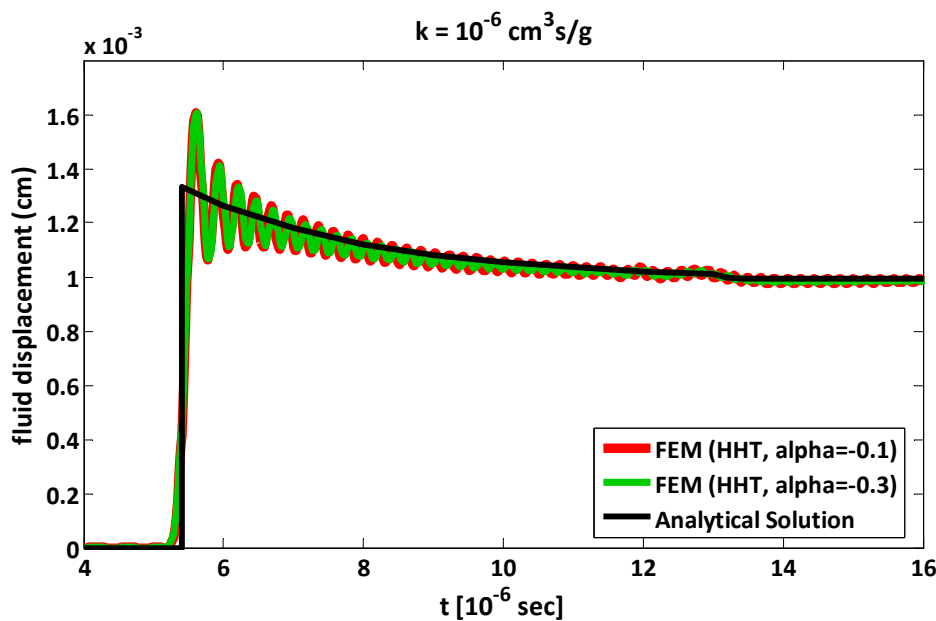


Figure 310.51: Time history of fluid displacements of longitudinal waves at 1 cm below the surface. Comparison of numerical results (FEM) with the analytical solution by Gajo and Mongiovì (1995) for the case of viscous coupling($k = 10^{-6} \text{ cm}^3 \text{s/g}$). Two different sets of unconditional stable HHT parameters were used for the numerical analysis.

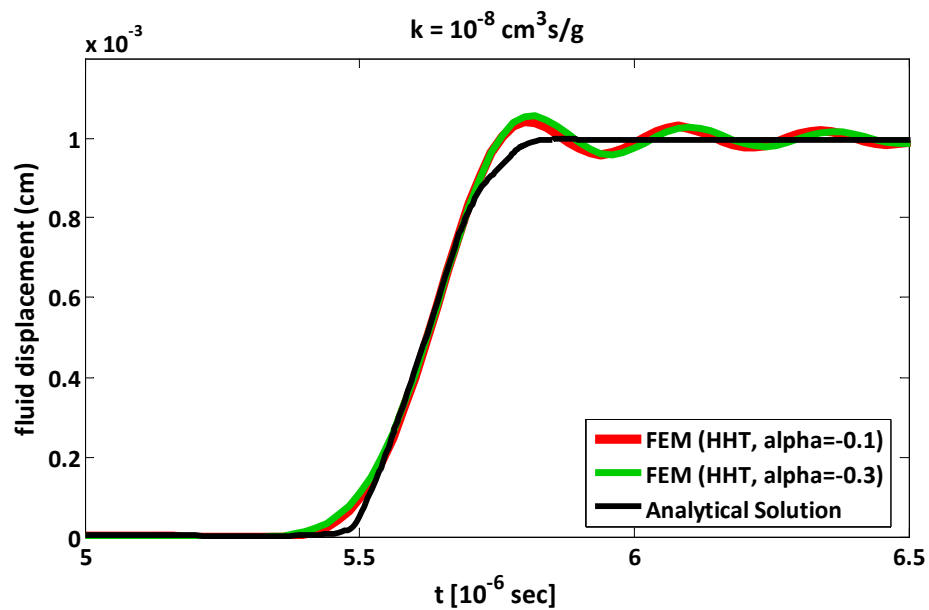


Figure 310.52: A magnified view of Figure 310.51 illustrating the details of wave front of the longitudinal wave of first kind.

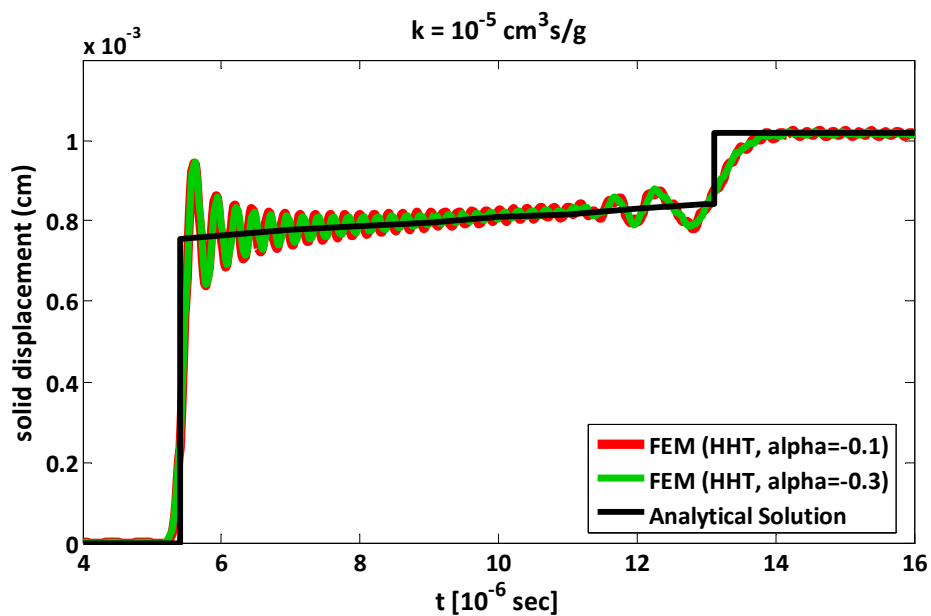


Figure 310.53: Time history of solid displacements of longitudinal waves at 1 cm below the surface. Comparison of numerical results (FEM) with the analytical solution by Gajo and Mongiovi (1995) for the case of viscous coupling($k = 10^{-5} \text{ cm}^3 \text{s/g}$). Two different sets of unconditional stable HHT parameters were used for the numerical analysis.

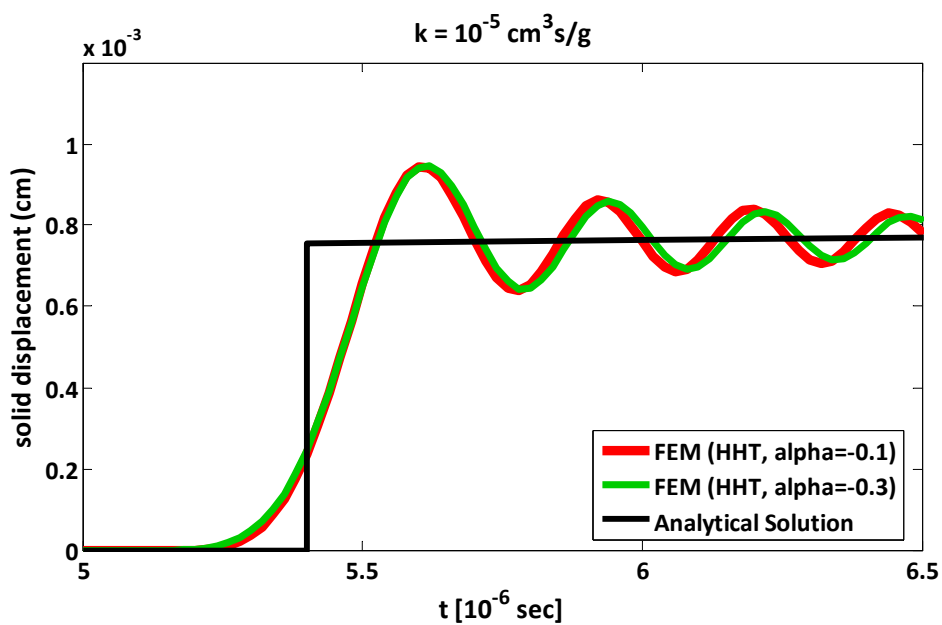


Figure 310.54: A magnified view of Figure 310.53 illustrating the details of wave front of the longitudinal wave of first kind.

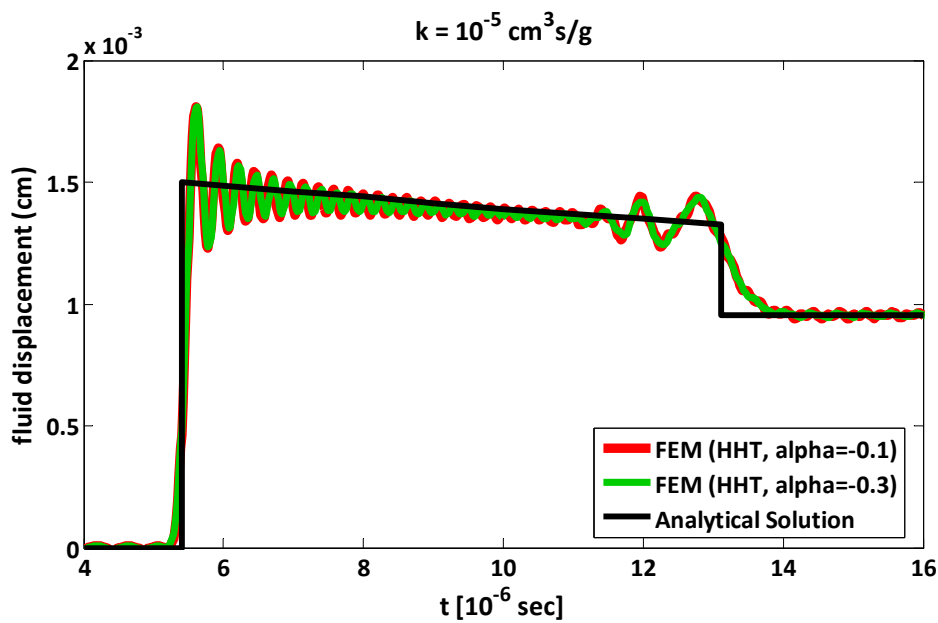


Figure 310.55: Time history of fluid displacements of longitudinal waves at 1 cm below the surface. Comparison of numerical results (FEM) with the analytical solution by Gajo and Mongiovì (1995) for the case of viscous coupling($k = 10^{-5} \text{ cm}^3 \text{s/g}$). Two different sets of unconditional stable HHT parameters were used for the numerical analysis.

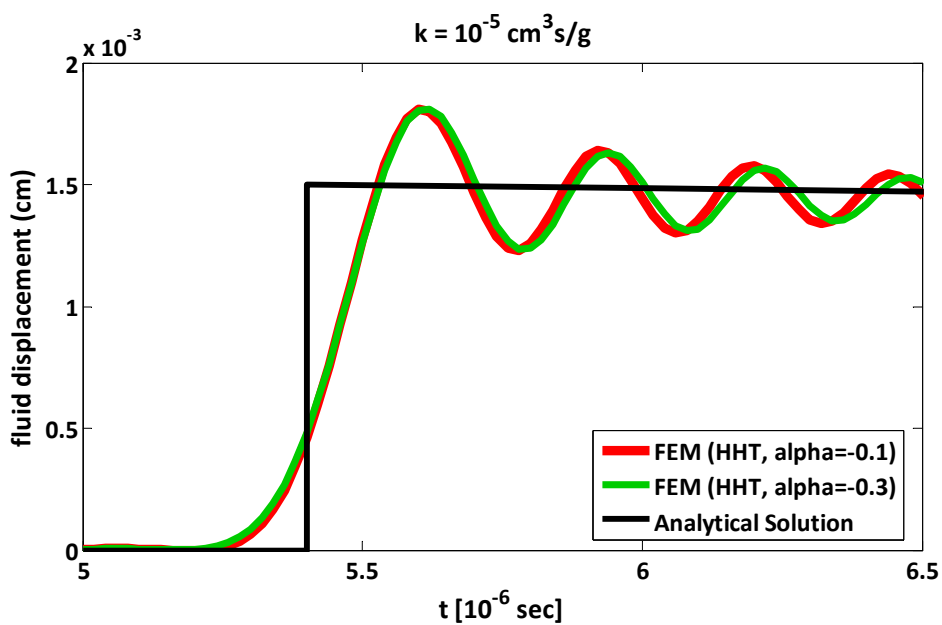


Figure 310.56: A magnified view of Figure 310.55 illustrating the details of wave front of the longitudinal wave of first kind.

310.8.3 Discussion of Numerical Results - Conclusions

Biot has shown than when dissipation is present, each frequency component propagated with its own velocity. Thus, especially in the case of numerical solutions using a finite element procedure, the response is very sensitive to the numerical damping introduced to the system. Generally, a drawback of all types of numerical solutions is the distortion and the smearing of the wave fronts, which are linked to the highest frequency that is allowed by the computational grid and the numerical damping due to the time integration method. The numerical results presented here, show a larger rise time than the analytical solution, that it could potentially be improved by using a finer spatial and temporal discretization.

In particular, the dissipation of high frequency oscillations is achieved more efficiently by the Newmark integrator than the HHT one. Due to the fact that the filtering of high frequencies is less in case of HHT integrator, the smearing of the wave front of the first kind of longitudinal waves is not so extensive as in the Newmark case. Obviously, for both cases, as the numerical damping increases by changing the sets of parameters, the rise time of the water fronts increases too. It is also worth mentioning that the rise time of the wave front of the second kind low-frequency longitudinal wave is even longer than that of the first kind.

Figures 310.41 and 310.44 illustrate the comparative results for all the three different values of viscous coupling using the Newmark integration method. In general, it is worth noting that the numerical results are in good agreement with the main characteristics of the mechanics of dispersive wave propagation in fully saturated, porous media, as indicated by the analytical results. For example, numerical results well demonstrate that during the propagation of the first wave, the solid and fluid displacement are in phase with each other, whereas during the propagation of second wave, the displacements of the two phases are in opposition. Overall, the finite element solutions reproduce correctly the forms of wave propagation for a wide range of permeability.

310.9 One dimensional wave propagation in elastic porous media subjected to step loading at the surface

310.9.1 Brief review of Analytical Solution by de Boer et al. (1993)

An analytical solution for the one-dimensional transient wave propagation fluid-saturated elastic porous media is provided by [de Boer et al. 1993](#). The fluid-saturated porous material is modeled as a two phase system composed of an incompressible solid phase and an incompressible fluid phase. An exact analytical solution is obtained via Laplace transform technique considering initial and boundary conditions, which exhibits only one independent compressive wave in both the solid and fluid phases, as a result of the

incompressibility constraint.

The problem configuration, which the analytical solution is addressed to, consists of an one-dimensional infinitely long column, separated from the half-space of a fluid-saturated porous elastic skeleton material. The motion of both the solid and the fluid materials is constrained to occur in the vertical direction. Loading as a function of time, $\sigma(z = 0, t) = f(t)$, is applied to the half space surface boundary by a permeable punch with ideal permeability. Homogeneous pore distribution and free pore fluid surface are assumed. The wave motion in the porous medium is expressed by the solid and fluid displacements or the solid extra stresses, respectively, but it cannot be expressed by the pore pressure which is just the Lagrangian multiplier corresponding to the incompressibility constraint of the medium.

In particular, in the paper by de Boer et al. (1993), the solid and the fluid displacements, the solid skeleton extra stresses and the pore pressure are given with respect to time and with respect to different depths in the soil column within the framework of three loading forms: i) sinusoidal, ii) step loading and iii) impulsive loading. These results can be taken for a quantitative comparison to various numerical solutions.

310.9.2 Numerical Analysis

Numerical example for the step loading case was solved in order to verify the previously mentioned $u - p - U$ formulation. The numerical model used for the simulation of the 1C shock wave propagation consists of 1000 u-p-U brick finite elements of dimensions $1\text{cm} \times 1\text{cm} \times 1\text{cm}$ creating a soil column 10m thick. Obviously, the numerical simulation of a semi infinite soil column is not possible; thus, a soil column of thickness of 10 cm was considered adequate for the current problem configuration. Figure 310.57 illustrates the transition from the physical configuration of the problem to its numerical simulation. Table 310.7 shows the soil properties of the numerical model, which are the same with those used for the analytical results presented in the paper by de Boer et al. (1993).

The only difference is noted on the elastic modulus, which was selected to be 20MN/m^2 for the numerical solution (FEM) instead of 30MN/m^2 , as it is mentioned in the previously mentioned paper. This is due to the fact that the numerical results indicated that the results given in the paper correspond to a soil column with elastic modulus equal to 20MN/m^2 instead of 30MN/m^2 . Moreover, it should be mentioned that the solid and fluid compressibility were given realistic values (see Table 310.7), which practically means that the two constituents are incompressible.

At the top surface of the soil column, a step loading of $\sigma(z = 0, t) = 3\text{kN/m}^2$ is applied to the solid part, as a nodal load equally distributed to the four top nodes. The nodal load is expressed as:

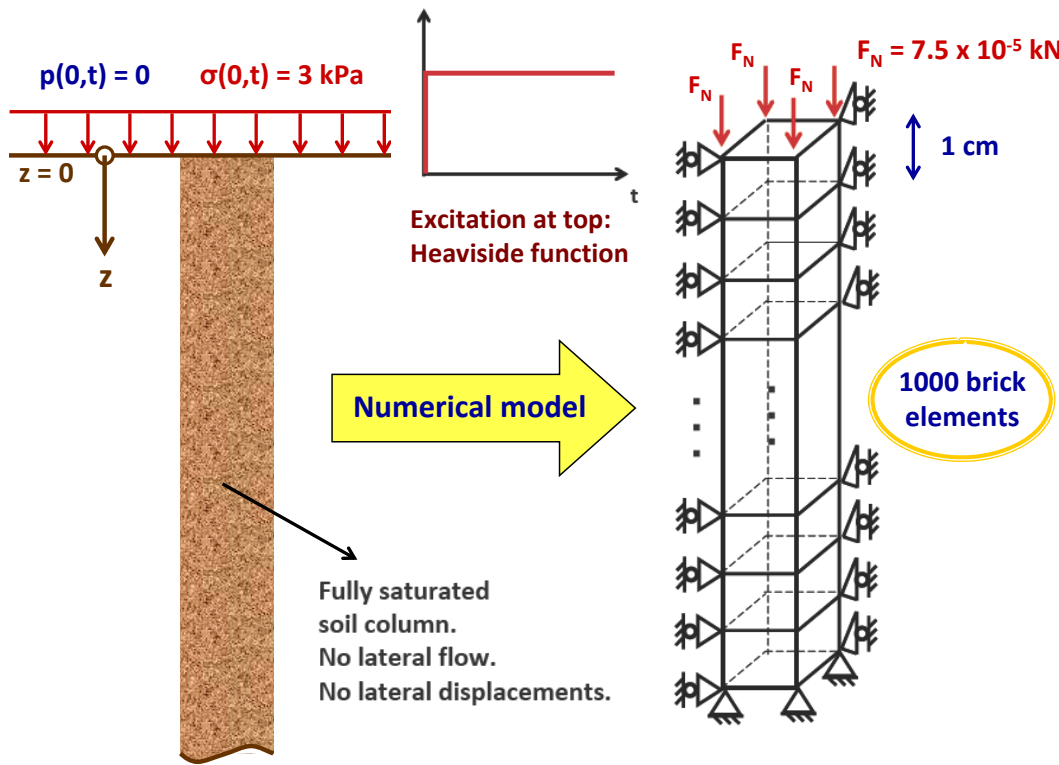


Figure 310.57: The numerical model used for the verification of the finite element implementation through comparison with the analytical solution provided by [de Boer et al. \(1993\)](#).

$$F_N(z = 0, t) = \frac{\sigma(z = 0, t) \times A}{4} = \frac{3 \text{ kN/m}^2 \times 0.01 \text{ m} \times 0.01 \text{ m}}{4} = 7.5 \times 10^{-5} \text{ kN} \quad (310.57)$$

Only the vertical displacement is free. There is no lateral flow or displacement. The degree of freedom related to the pore pressure is constrained at the top surface to be equal to the atmospheric pressure, while it is free at the rest of the nodes. The base of the model is rigid and impervious.

This kind of excitation (Heaviside function) applied at the top of the model, results clearly in waves of all kinds of frequency, first due to its nature and secondarily due to the way of its application. Due to this fact, a fairly dense mesh of 1000 u-p-U brick finite elements of dimensions $1\text{cm} \times 1\text{cm} \times 1\text{cm}$ was chosen. The time step, δt required needs to be limited to

$$\delta t < \frac{\delta h}{v} \quad (310.58)$$

$$(310.59)$$

Table 310.7: Soil Properties for 1C shock wave propagation for the problem by de Boer et al. (1993)

Parameter	Symbol	Value
gravity acceleration	g	9.81 m/s^2
soil matrix Young's Modulus	E	$20 \times 10^3 \text{ kN/m}^2$
soil matrix Poisson's ratio	ν	0.2
soil matrix Lame's constant	λ	$5.55 \times 10^3 \text{ kN/m}^2$
soil matrix shear modulus	μ	$8.33 \times 10^3 \text{ kN/m}^2$
solid particle density	ρ_s	$2.0 \times 10^3 \text{ kg/m}^3$
water density	ρ_f	$1.0 \times 10^3 \text{ kg/m}^3$
solid particle bulk modulus	K_s	$36.0 \times 10^6 \text{ kN/m}^2$
fluid bulk modulus	K_f	$2.177 \times 10^6 \text{ kN/m}^2$
porosity	n	0.33
Darcy's permeability	k_D	0.01 m/s

where v is the highest wave velocity. In our case, the temporal integration involves 4000 steps of $1.0 \times 10^{-4} \text{ sec}$, which allows a maximum wave velocity of 100 m/s . The propagation velocity can be calculated by the following equation given by de Boer et al. (1993) and is equal to 90.7 m/s .

$$v = \sqrt{\frac{n^2(\lambda + 2\mu)}{n^2(1-n)\rho_s + (1-n)^2(n\rho_f)}} = 90.7 \text{ m/s} \quad (310.60)$$

The Newmark time integration method was used, which dissipates more efficiently the high frequencies introduced in the system due to numerics than HHT integrator, as shown in section 4.3. The following set of parameters was chosen, assuring unconditionally numerical stability: $\gamma = 0.7$ and $\beta = 0.4$.

310.9.3 Discussion of Numerical Results - Conclusions

Figures 310.58 to 310.67 illustrate the comparative results between analytical and numerical solution. In general, it is worth noting that the numerical results are in good agreement, with respect to time and with respect to depth, with those obtained by the analytical solution. The responses of the medium due to step loading are indicative of the consolidation process in case of a free pore water surface. The solid moves downwards, indicating that settlement occurs and the fluid is squeezed out from the pore volume creating an upward flow. During the consolidation process, the extra solid skeleton stresses increase with time at a certain depth. However, they decrease with the distance from the loading surface at a certain

time. In opposition to the extra solid skeleton stresses, the pore pressure decreases with time tending to zero, while it increases with depth.

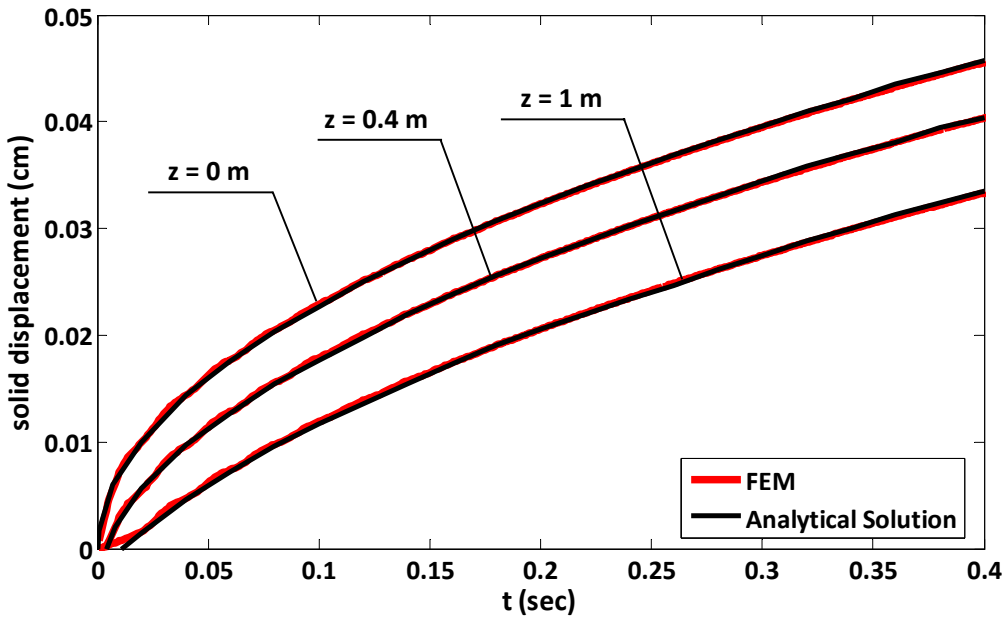


Figure 310.58: Time history of solid displacements at different depths due to step loading. Comparison of numerical results (FEM) with the analytical solution by de Boer et al. (1993).

Overall, it is worth mentioning that the results obtained from the finite element procedure practically coincide with the ones given by the analytical solution. The only difference is located to the pore pressure (see Figures 310.64 to 310.67), where numerical response is oscillatory in contrast to the analytical solution. This may be due to the high frequencies introduced to the system by the temporal and spatial discretization and/or the compressibility of the solid and fluid phases. It should be mentioned again, that in the analytical solution, the two constituents are assumed incompressible whereas in the numerical model, the solid and fluid bulk moduli have realistic values (see Table 310.7). That is why in Figure 310.68, numerical examples with different values of fluid compressibility were solved. It is obvious that the oscillations decrease as the the fluid becomes more and more compressible because the stiffness of the system decreases and the high frequencies are dissipated faster. Moreover, Figure 310.68 indicated that better quantitative agreement between the numerical and analytical solution is achieved when the bulk modulus of the fluid is 2.2×10^6 kPa - realistic value - instead of 2.2×10^9 kPa, which would be expected since the pore fluid is assumed to be incompressible in the framework of the analytical solution. Comparing the pore pressures obtained from these two cases, it can be observed that the pore pressure

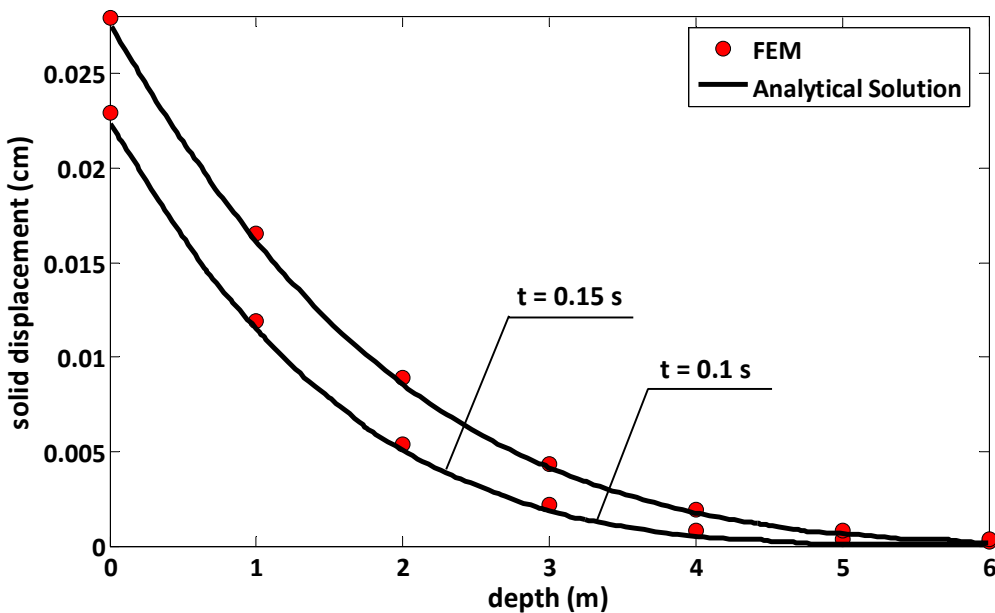


Figure 310.59: Response of solid displacements versus depth at different time moments due to step loading. Comparison of numerical results (FEM) with the analytical solution by [de Boer et al. \(1993\)](#).

generation in the more compressible fluid is slightly higher than that of the almost incompressible fluid because of the existence of the oscillatory waves, as mentioned by [\(Zienkiewicz and Shiomi, 1984\)](#).

310.10 One dimensional wave propagation in elastic porous media subjected to step velocity boundary condition

310.10.1 Brief review of Analytical Solution by [Hiremath et al. \(1988\)](#)

[Hiremath et al. \(1988\)](#) present a solution of Biot's dynamic equation of motion for one-dimensional wave propagation in a fluid-saturated linear elastic isotropic soil using Laplace transformation followed by numerical inversion. This study is considered to be an extension of the exact transient solution presented by [Garg et al. \(1974\)](#) for two limiting cases of infinitely small and infinitely large viscous coupling. In both cases, a soil column of finite dimension subjected to velocity boundary conditions was analyzed, allowing for reflection of waves at the boundaries.

In particular, [Hiremath et al. \(1988\)](#) examines two cases allowing for weak and strong viscous coupling, or else, as it is referred in the related paper, low and high drag, respectively. Moreover, two different

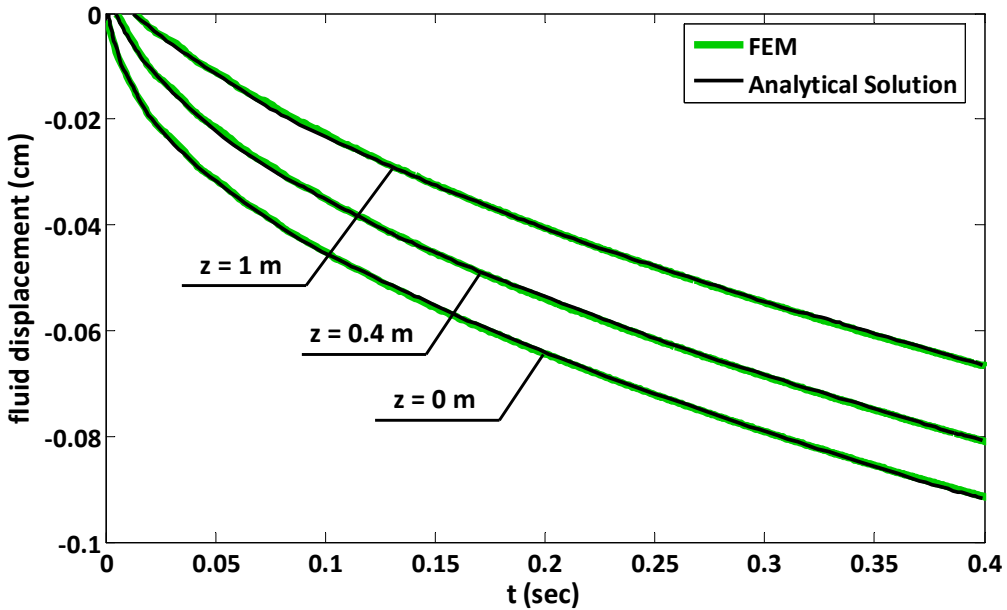


Figure 310.60: Time history of fluid displacements at different depths due to step loading. Comparison of numerical results (FEM) with the analytical solution by [de Boer et al. \(1993\)](#).

types of excitations were applied at the boundary surface in terms of solid and fluid velocity. In the first case, a unit step boundary condition boundary condition was applied at the top surface for both solid and fluid phases. In the second case, the fluid velocity specified at the boundary is different from the specified solid velocity increasing gradually to unity over the time scale. The results obtained from the numerical inversion allowed for six reflections of the fast compressional wave of first kind and two reflections of the secondary slow longitudinal wave.

One of the most important observations which both [Garg et al. \(1974\)](#) and [Hiremath et al. \(1988\)](#) concluded to, is that in case of strong viscous coupling (high drag), the material behaves as a single continuum with internal dissipation and the two wave fronts tend to become a single one.

[Hiremath et al. \(1988\)](#) presented a comparison of finite element solution of Biot's equations of motion with one based on numerical inversion of the Laplace transform solution. It is explained in the paper that a proper choice of element type and time domain integration is essential for capturing the results coming from the semi-analytical solution. Moreover, the spatial discretization needs to be combined with an appropriate temporal one, so that the wave does not traverse more than one element length during a single time step. In detail, [Hiremath et al. \(1988\)](#) suggests 100 linear elements of 0.005 m length and 986 time steps of size 10^{-6} sec.

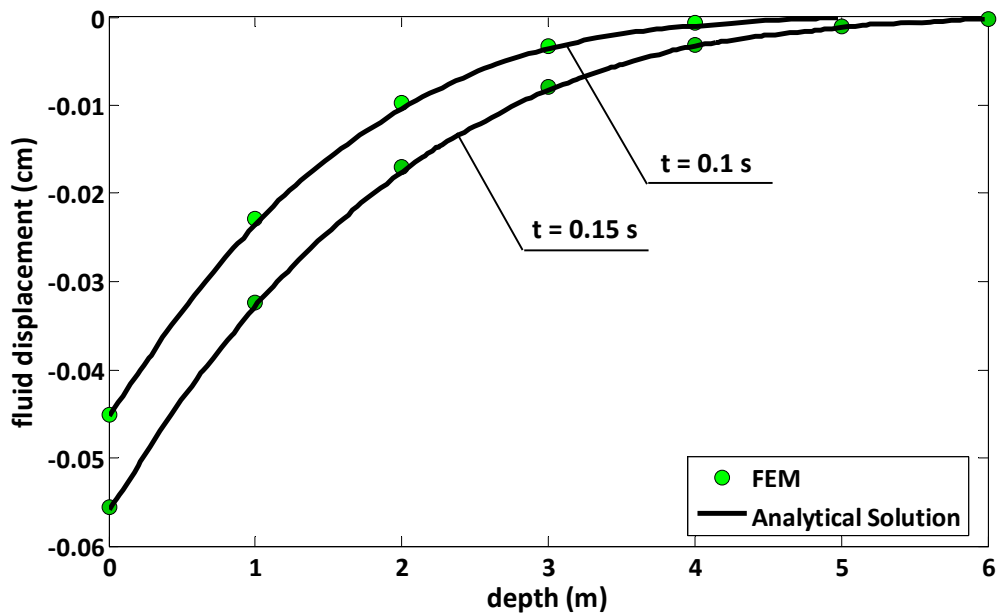


Figure 310.61: Response of fluid displacements versus depth at different time moments due to step loading. Comparison of numerical results (FEM) with the analytical solution by [de Boer et al. \(1993\)](#).

310.10.2 Numerical Analysis

Numerical examples for two extreme values of viscous coupling: a) high drag ($k = 0.148 \times 10^{-8} \text{ cm}^3 \text{s/g}$) and b) low drag ($k = 0.148 \times 10^{-2} \text{ cm}^3 \text{s/g}$), were solved in order to verify the previously mentioned $u - p - U$ formulation by comparing the results with the semi-analytical solution provided by [Hiremath et al. \(1988\)](#). The numerical model used for the simulation of the 1C shock wave propagation consists of 100 u-p-U brick finite elements of dimensions $0.005\text{m} \times 0.005\text{m} \times 0.005\text{m}$ creating a soil column 50cm thick. Figure 310.69 illustrates the transition from the physical configuration of the problem to its numerical simulation. Table 310.8 shows the soil properties of the numerical model.

At the top surface of the soil column, a step velocity of $1.0 \times 10^{-2} \text{ m/sec}$ is applied both to the solid and the fluid phase. Only the vertical translational degrees of freedom are free. The horizontal translational degrees of freedom are constrained so that there is no lateral flow or displacement. The base of the model is rigid and impervious.

This kind of excitation (Heaviside function) applied at the top of the model, results clearly in waves of all kinds of frequency, first due to its nature and secondarily due to the way of its application. This fact together with the great stiffness of the solid skeleton (see Table 310.8 require a very dense spatial

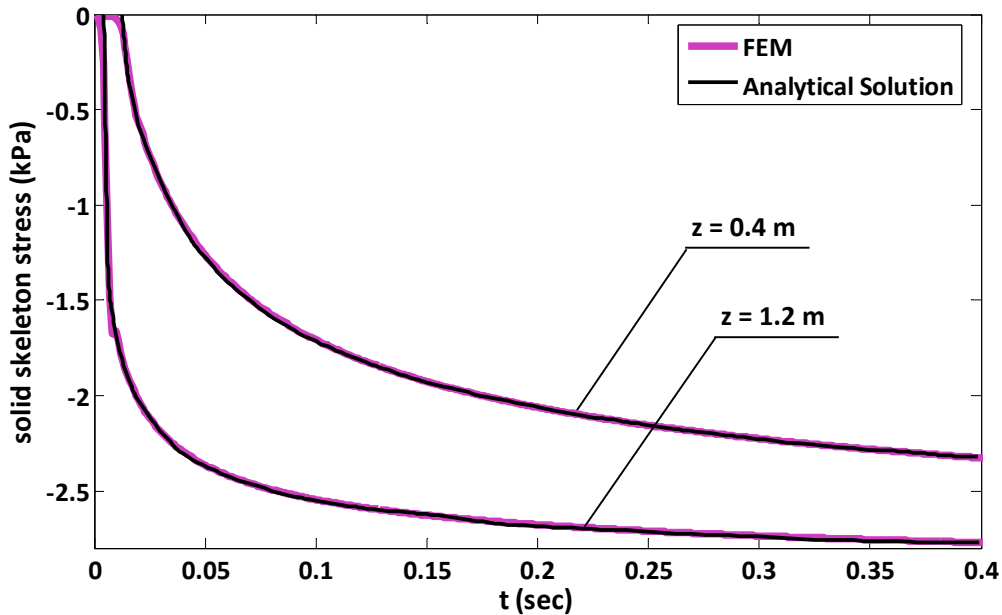


Figure 310.62: Time history of solid skeleton stresses at different depths due to step loading. Comparison of numerical results (FEM) with the analytical solution by de Boer et al. (1993).

Table 310.8: Soil Properties for 1C shock wave propagation for example by Hiremath et al. (1988).

Parameter	Symbol	Value
gravity acceleration	g	9.81 m/s^2
soil matrix Young's Modulus	E	$23.21 \times 10^6 \text{ kN/m}^2$
soil matrix Poisson's ratio	ν	0.171
solid particle density	ρ_s	$2.66 \times 10^3 \text{ kg/m}^3$
water density	ρ_f	$1.0 \times 10^3 \text{ kg/m}^3$
solid particle bulk modulus	K_s	$36.0 \times 10^6 \text{ kN/m}^2$
fluid bulk modulus	K_f	$2.2 \times 10^6 \text{ kN/m}^2$
porosity	n	0.18
Biot coefficient	α	0.6772

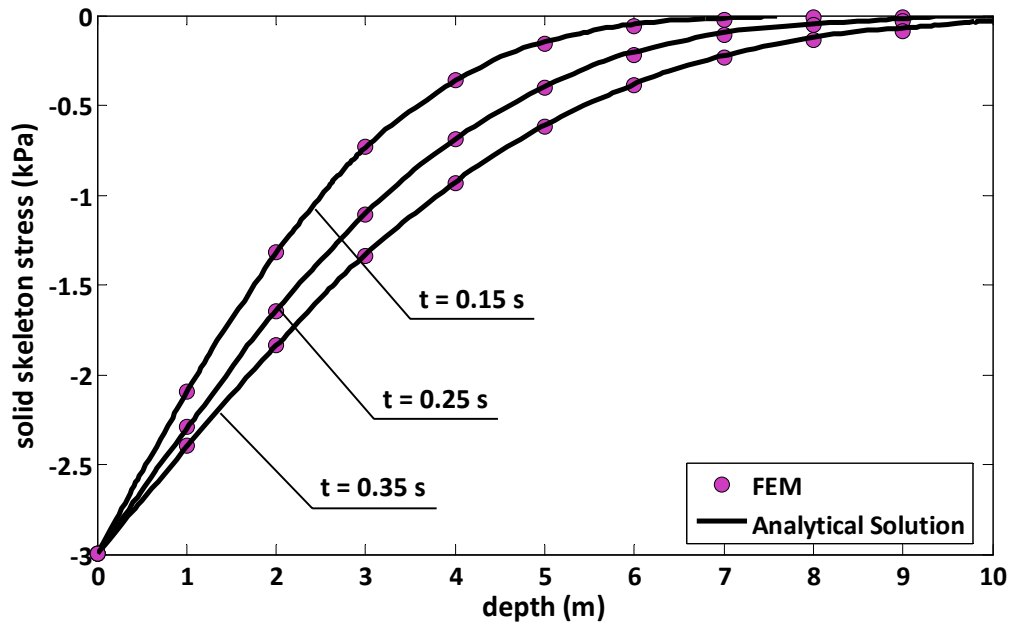


Figure 310.63: Response of solid skeleton stresses versus depth at different time moments due to step loading. Comparison of numerical results (FEM) with the analytical solution by [de Boer et al. \(1993\)](#).

discretization. Here, 100 u-p-U brick finite elements of dimensions $0.005m \times 0.005m \times 0.005m$ were chosen, following similar discretization with [Hiremath et al. \(1988\)](#). The time step, δt required needs to be limited to

$$\delta t < \frac{\delta h}{v} \quad (310.61)$$

$$(310.62)$$

where v is the highest wave velocity. In our case, the temporal integration involves 1972 steps of $5.0 \times 10^{-7} sec$, in comparison with 986 time steps of size $10^{-6} sec$, used by [Hiremath et al. \(1988\)](#). The time integration method used was the Newmark integrator with parameters: $\gamma = 0.6$ and $\beta = 0.3025$.

310.10.3 Discussion of Numerical Results - Conclusions

Biot has shown than when dissipation is present, each frequency component propagates with its own velocity. Thus, especially in the case of numerical solutions using a finite element procedure, the response is very sensitive to the numerical damping introduced to the system. Generally, a drawback of all types

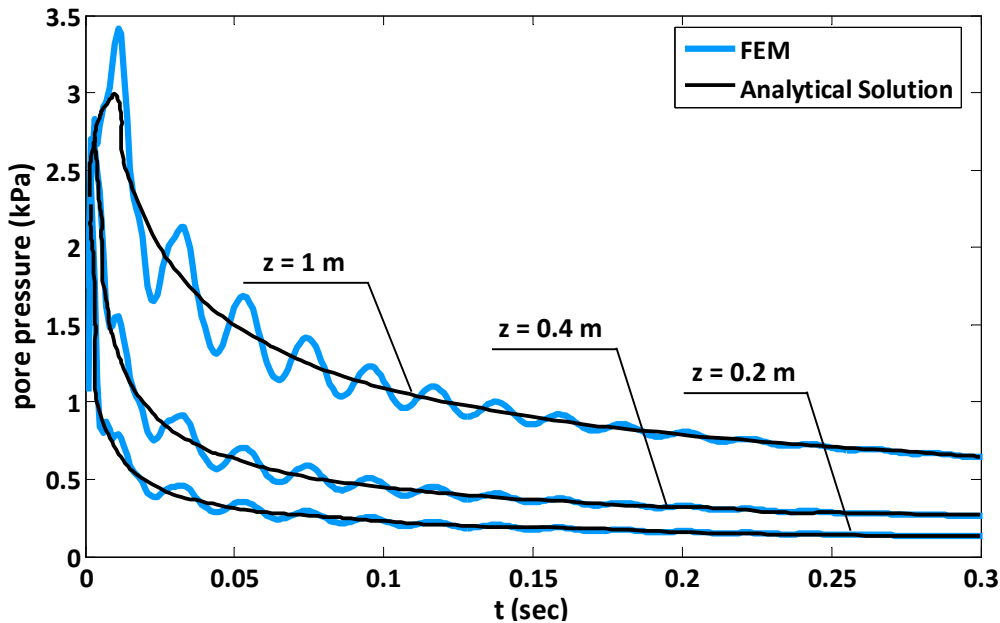


Figure 310.64: Time history of pore pressure at different depths due to step loading. Comparison of numerical results (FEM) with the analytical solution by [de Boer et al. \(1993\)](#).

types of numerical solutions is the distortion and the smearing of the wave fronts, which are linked to the highest frequency that is allowed by the computational grid and the numerical damping due to the time integration method. The numerical results presented here, show some oscillations at the rough changes in velocity due to reflection of wave fronts that could be possibly diminished by using a finer spatial and temporal discretization.

Figures 310.70 to 310.77 illustrate the comparative results for both extreme cases of viscous coupling. In general, it is worth noting that the numerical results are in good agreement with the main characteristics of the mechanics of dispersive wave propagation in fully saturated, porous media, as indicated by the semi-analytical results. For example, numerical results well demonstrate that for the case of strong viscous coupling (high drag), the solid and fluid are in phase with each other, implying that the two-phase material behaves as a single continuum. Overall, the finite element solutions reproduce correctly the trends of wave propagation in both limiting cases of viscous coupling.

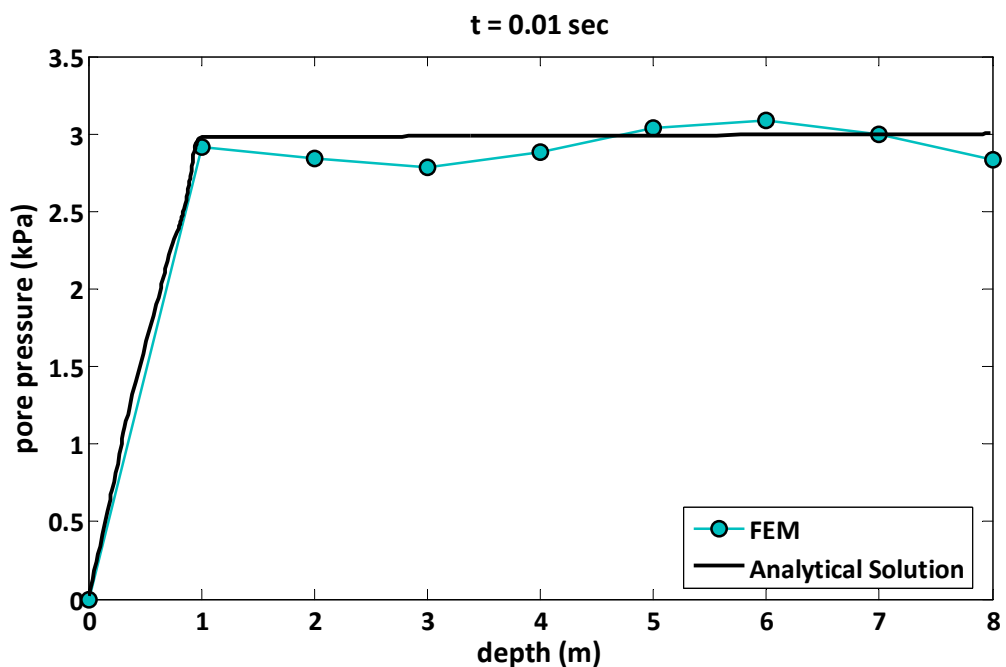


Figure 310.65: Response of pore pressure versus depth at $t = 0.01\text{sec}$ due to step loading. Comparison of numerical results (FEM) with the analytical solution by de Boer et al. (1993).

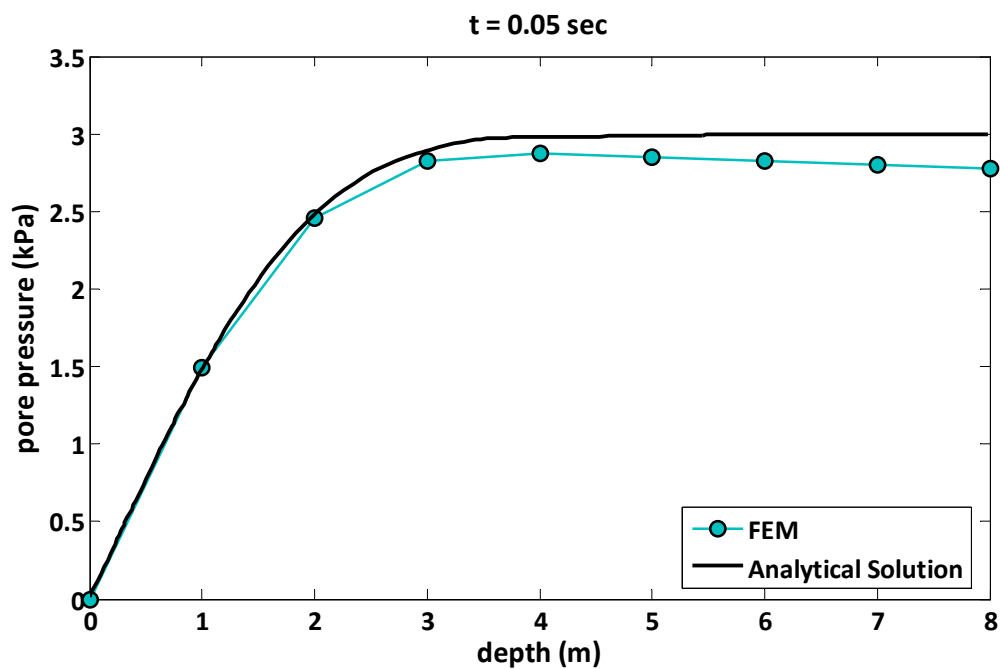


Figure 310.66: Response of pore pressure versus depth at $t = 0.05\text{sec}$ due to step loading. Comparison of numerical results (FEM) with the analytical solution by de Boer et al. (1993).

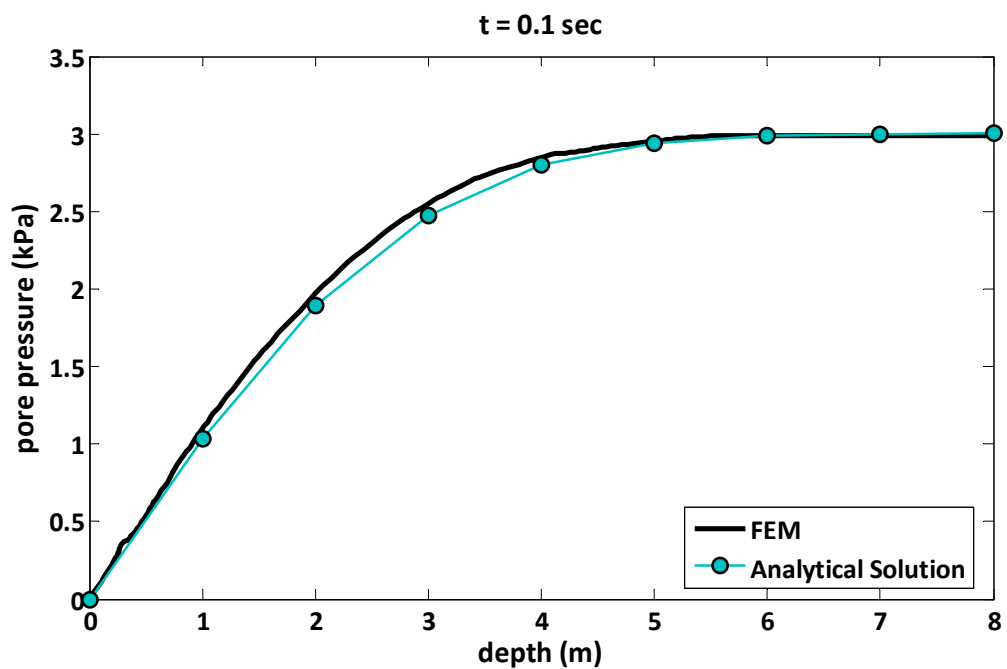


Figure 310.67: Response of pore pressure versus depth at $t = 0.1\text{sec}$ due to step loading. Comparison of numerical results (FEM) with the analytical solution by [de Boer et al. \(1993\)](#).

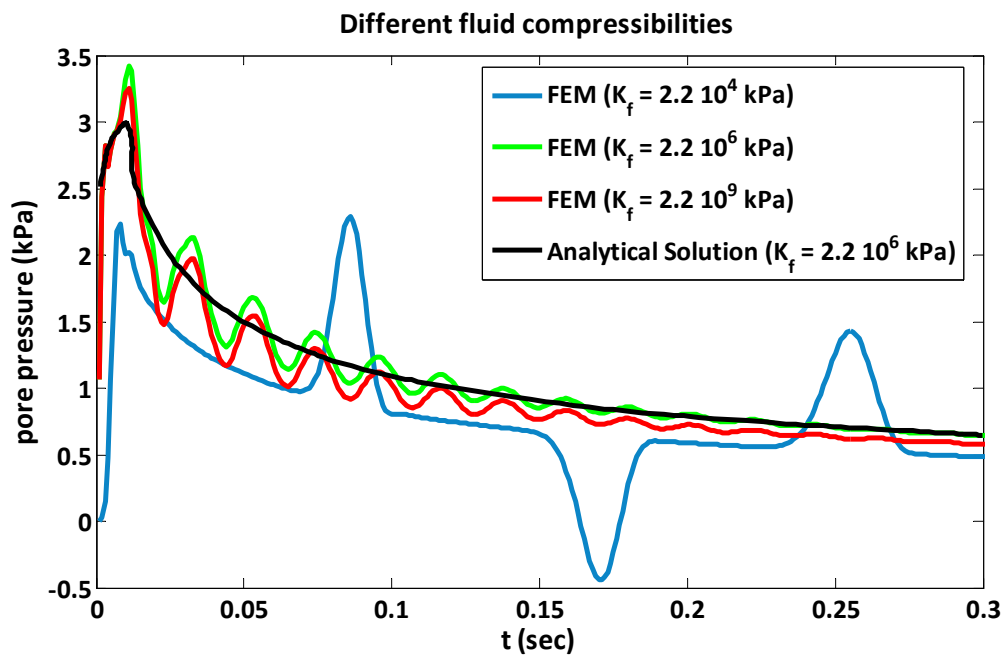


Figure 310.68: Time history of pore pressure at 1 m below the ground surface due to step loading for different fluid compressibility. Comparison of numerical results (FEM) with the analytical solution by de Boer et al. (1993).

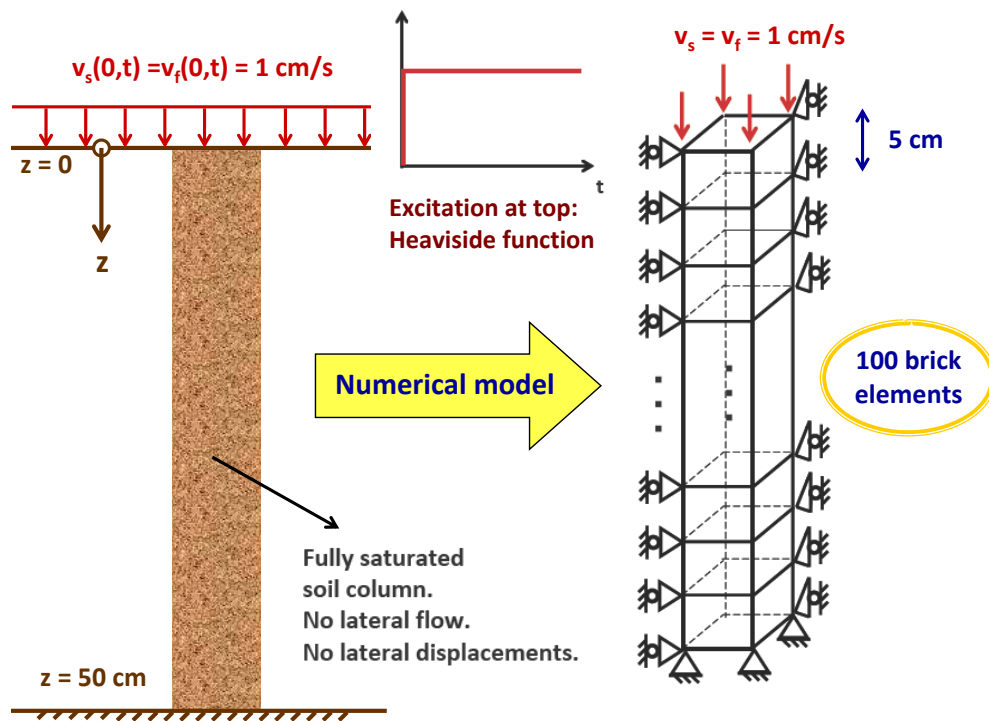


Figure 310.69: The numerical model used for the verification of the finite element implementation through comparison with the semi-analytical results provided by [Hiremath et al. \(1988\)](#).

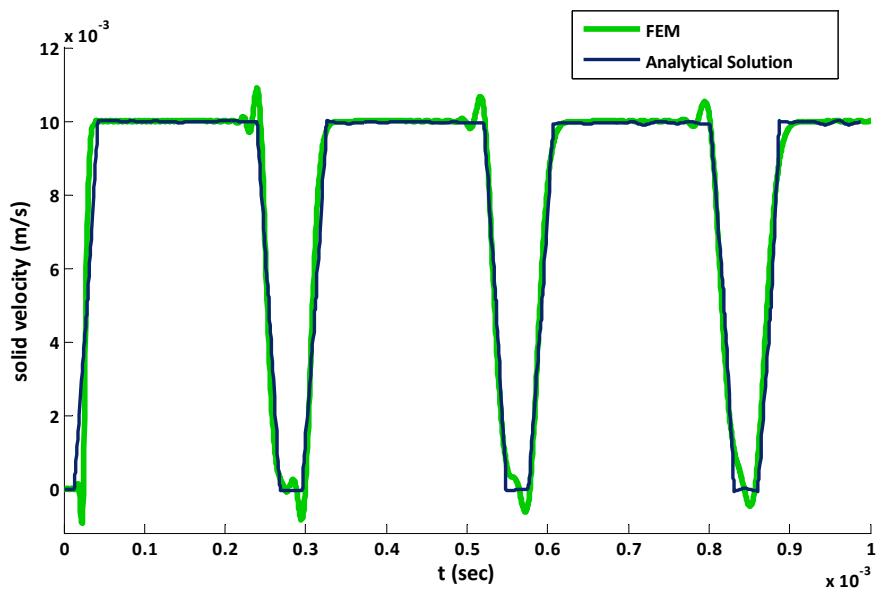


Figure 310.70: Time history of solid velocity at 10 cm below the surface. Comparison of numerical results (FEM) with the semi-analytical solution by [Hiremath et al. \(1988\)](#) for the case of high drag ($k = 0.148 \times 10^{-8} \text{cm}^3 \text{s/g}$).

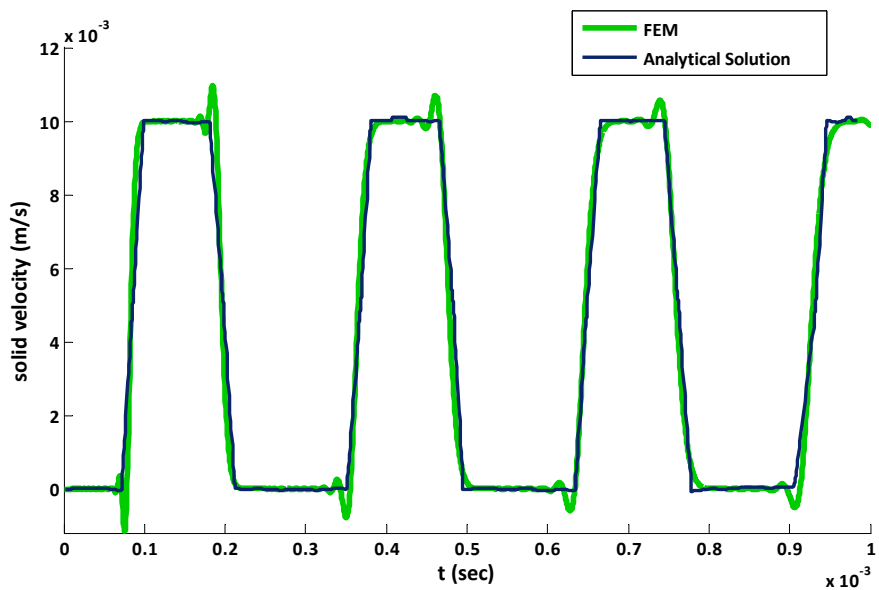


Figure 310.71: Time history of solid velocity at 30 cm below the surface. Comparison of numerical results (FEM) with the semi-analytical solution by [Hiremath et al. \(1988\)](#) for the case of high drag ($k = 0.148 \times 10^{-8} \text{ cm}^3 \text{s/g}$).

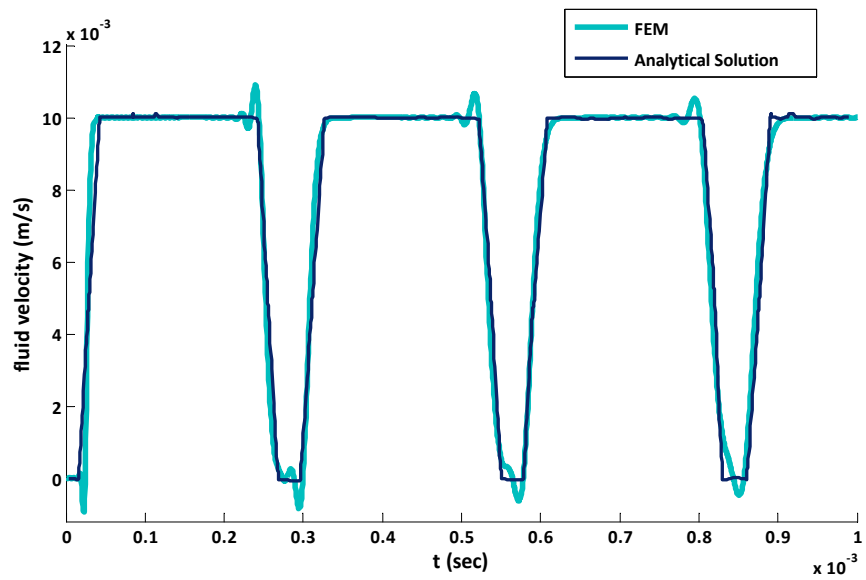


Figure 310.72: Time history of fluid velocity at 10 cm below the surface. Comparison of numerical results (FEM) with the semi-analytical solution by [Hiremath et al. \(1988\)](#) for the case of high drag ($k = 0.148 \times 10^{-8} \text{cm}^3 \text{s/g}$).

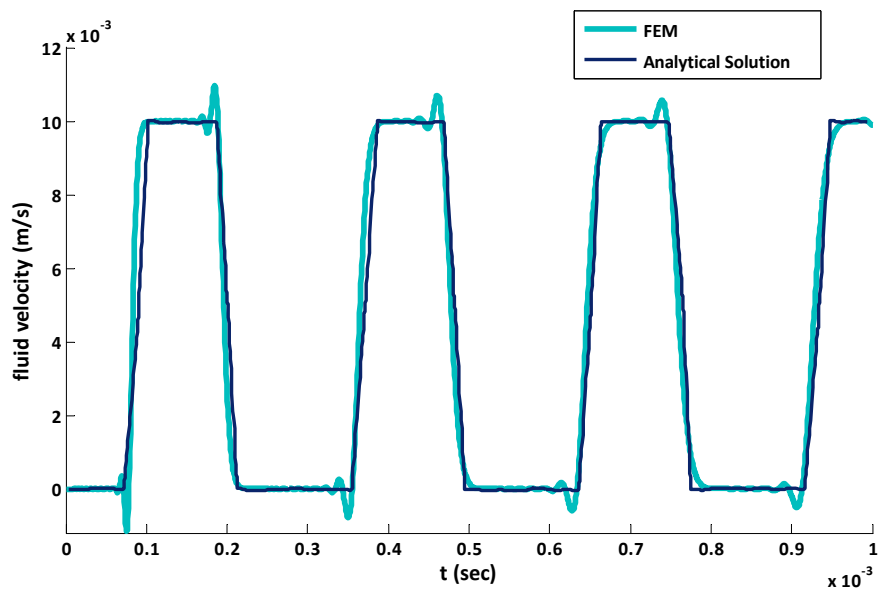


Figure 310.73: Time history of fluid velocity at 30 cm below the surface. Comparison of numerical results (FEM) with the semi-analytical solution by [Hiremath et al. \(1988\)](#) for the case of high drag ($k = 0.148 \times 10^{-8} \text{ cm}^3 \text{s/g}$).

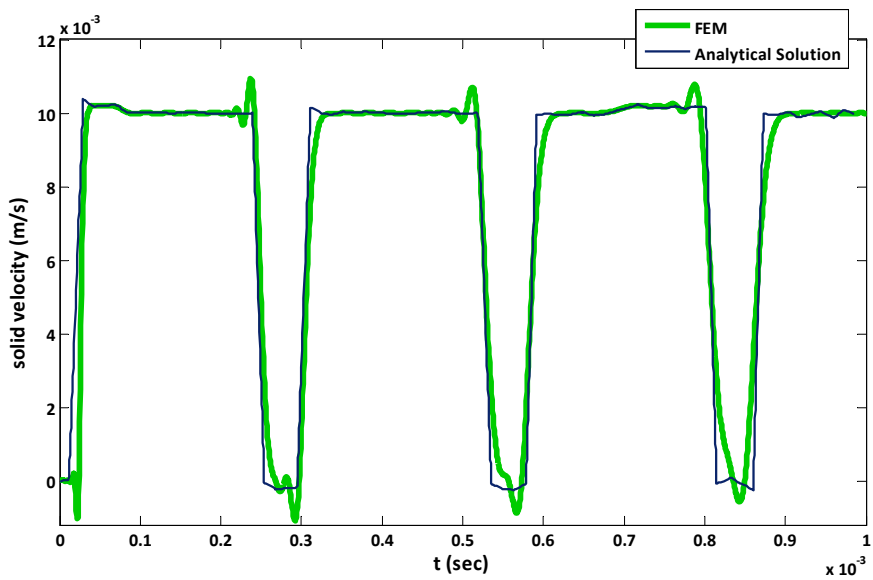


Figure 310.74: Time history of solid velocity at 10 cm below the surface. Comparison of numerical results (FEM) with the semi-analytical solution by [Hiremath et al. \(1988\)](#) for the case of high drag ($k = 0.148 \times 10^{-2} \text{cm}^3 \text{s/g}$).

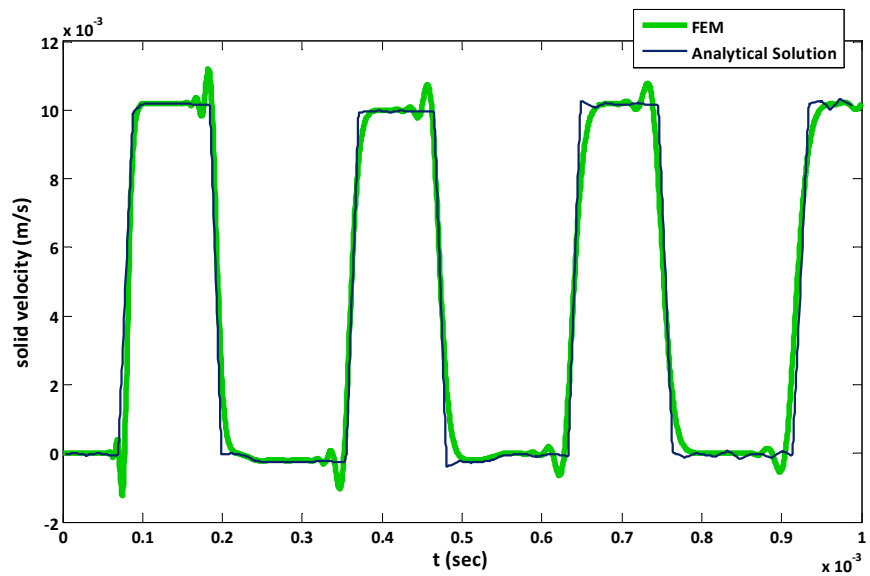


Figure 310.75: Time history of solid velocity at 30 cm below the surface. Comparison of numerical results (FEM) with the semi-analytical solution by [Hiremath et al. \(1988\)](#) for the case of high drag ($k = 0.148 \times 10^{-2} \text{cm}^3 \text{s/g}$).

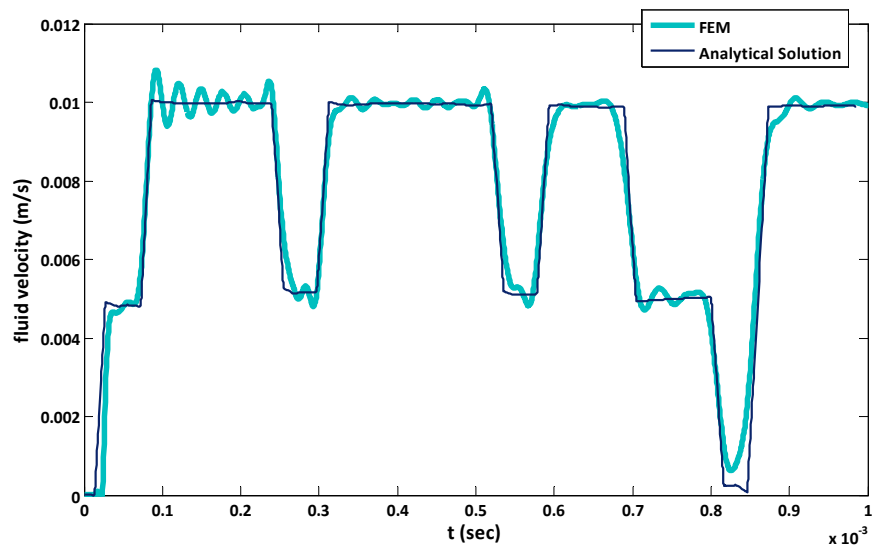


Figure 310.76: Time history of fluid velocity at 10 cm below the surface. Comparison of numerical results (FEM) with the semi-analytical solution by [Hiremath et al. \(1988\)](#) for the case of high drag ($k = 0.148 \times 10^{-2} \text{cm}^3 \text{s/g}$).

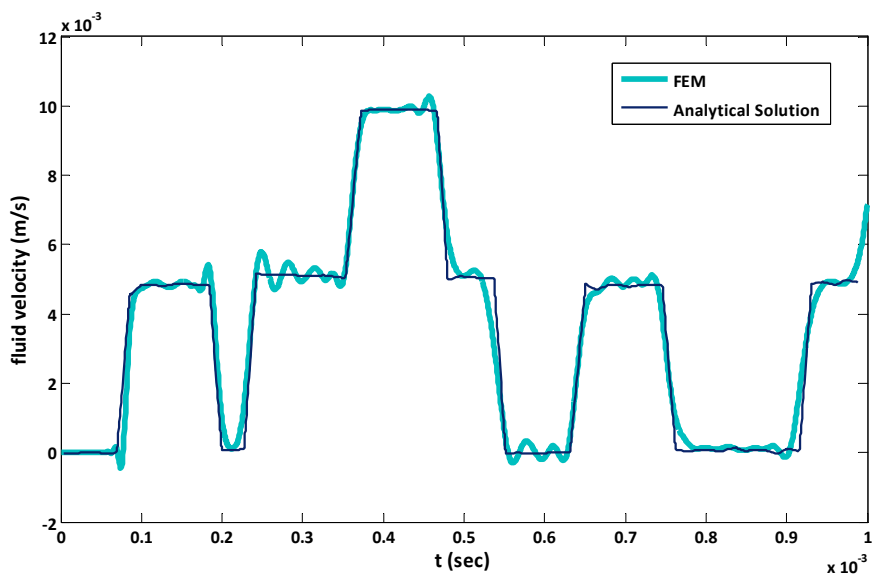


Figure 310.77: Time history of fluid velocity at 30 cm below the surface. Comparison of numerical results (FEM) with the semi-analytical solution by [Hiremath et al. \(1988\)](#) for the case of high drag ($k = 0.148 \times 10^{-2} \text{cm}^3 \text{s/g}$).

Chapter 311

Verification and Validation for Seismic Wave Propagation Problems

(1989-2000-2004-2005-2008-2009-2010-2011-2017-2018-2019-2021-)

(In collaboration with Dr. Nima Tafazzoli, Dr. Matthias Preisig, Dr. Federico Pisanò, Mr. Kohei Watanabe, Mr. Chao Luo, and Dr. Hexiang Wang)

311.1 Chapter Summary and Highlights

311.2 Wavelet Seismic Signals

A wavelet is a wave with specific definitions and parameters. The amplitude of a wavelet usually starts at zero, increases by time and ended up at zero again. Typically a wavelet can be plotted as a brief oscillation such as a the small oscillation recorded by seismogram. There are different types of wavelets each with their own properties used for specific purpose in signal processing. For specific purposes different wavelets might be summed up to come up with new type of wave. A recently developed wavelet analysis has become a powerful tool to analyze the soil-structure systems for transient loads providing information both in time and frequency domains. In wavelet representation the basis functions are localized and contained in finite time domains ([Sarica and Rahman \(2003\)](#)).

311.2.1 Ricker Wavelet

One type of wavelet motions is the Ricker wave ([Ryan \(1994\)](#), [Mavroeidis and Papageorgiou \(2003\)](#)). The formulation of Ricker wavelet is shown in Equations (311.1):

$$R(t) = A \ (1 - 2\pi^2 f^2 t^2) \ \exp(-\pi^2 f^2 t^2) \quad (311.1)$$

where $R(t)$ is the amplitude of the function in time, A if the maximum amplitude, and f is the peak frequency on the wavelet's frequency spectrum. Figure (311.1) shows the actual time history and fast Fourier transform of Ricker wavelet, where A is taken as 1 and f is taken as 5Hz. As it is shown, the frequency range of the motion is narrower compared to the real earthquake motion.

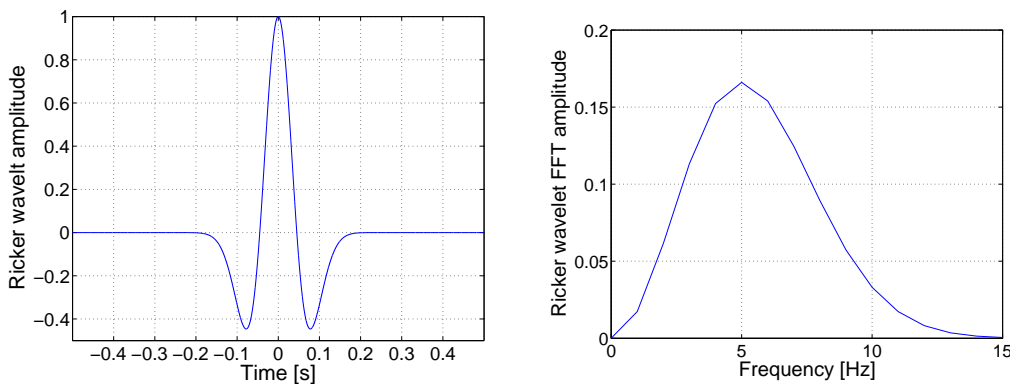


Figure 311.1: Frequency content and a time domain representation of Ricker wavelet

311.2.2 Ormsby Wavelet

Another example of interesting wavelet is called Ormsby wavelet ([Ryan \(1994\)](#)) which features a controllable flat frequency content with formulation shown in Equation (311.2).

$$\begin{aligned} f(t) = & A \left(\left(\frac{\pi f_4^2}{f_4 - f_3} \text{sinc}(\pi f_4(t - t_s))^2 - \frac{\pi f_3^2}{f_4 - f_3} \text{sinc}(\pi f_3(t - t_s))^2 \right) \right. \\ & \left. - \left(\frac{\pi f_2^2}{f_2 - f_1} \text{sinc}(\pi f_2(t - t_s))^2 - \frac{\pi f_1^2}{f_2 - f_1} \text{sinc}(\pi f_1(t - t_s))^2 \right) \right) \end{aligned} \quad (311.2)$$

where f_1 and f_2 define the lower range frequency band, f_3 and f_4 define the higher range frequency band, A is the amplitude of the function, and t_s is the time that maximum amplitude is happening, and $\text{sinc}(x) = \sin(x)/x$.

[Figure \(311.2\)](#) shows an example of Ormsby wavelet in time domain and frequency domain. In this case, wave has a flat frequency range of 5Hz to 20Hz. Shown in [Figure \(311.3\)](#) is half of the Ormsby wavelet in frequency domain which the frequency range starts from 0 and remains constant up to 20Hz. This type of motion could be useful when low frequency range of motions are required for dynamic analysis of the systems.

Such broad band signals could be used to assess different aspects of soil-structure systems and with different incoming wave inclinations. While wavelet time domain motions are not the same as actual earthquakes, the idea is to use them for dynamic analysis of soil-structure systems for possible problems coming out of dynamic behavior, at different frequencies and for different energy input levels.

When used with the DRM, motions developed from different directions, different incident angles and different energies, will create a full envelope of these motions, which then can be used to evaluate performance based response of the soil-structure systems.

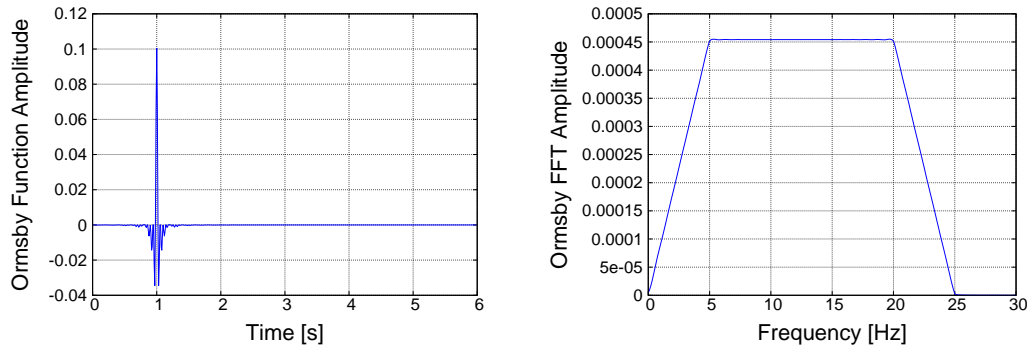


Figure 311.2: Frequency content and a time domain representation of an Ormsby wavelet, with constant frequency content between 5Hz and 20Hz

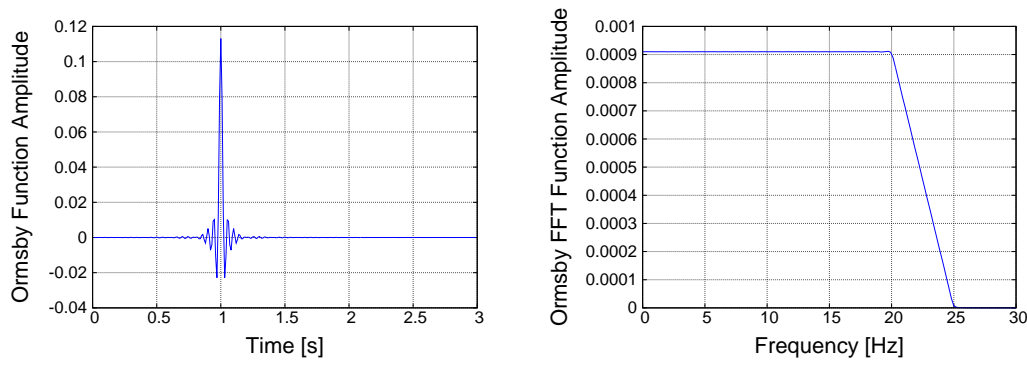


Figure 311.3: Frequency content and a time domain representation of half of Ormsby wavelet formulation, with minimum frequency of zero and maximum of 20Hz

311.3 Finite Element Mesh Size Effects on Seismic Wave Propagation Modeling and Simulation

311.3.1 Analysis Cases

Summary of the cases is shown in Table below. the input motion used is Ormsby wavelet which the corner cutoff frequency is shown in the table.

Case Number	Model Height (m)	Shear Wave Velocity (m/s)	Element Size (m)	Frequency Cutoff (Hz)	Maximum Propagation Frequency (Hz)
1	1000	1000	10	3	10
2	1000	1000	20	3	5
3	1000	1000	10	8	10
4	1000	1000	20	8	5
5	1000	1000	50	3	2
6	1000	1000	50	8	2
7	100	100	1	3	10
8	100	100	2	3	5
9	100	100	1	8	10
10	100	100	2	8	5
11	100	100	10	8	1
12	1000	100	10	8	1
13	1000	100	20	8	0.5
14	1000	100	50	8	0.2

311.3.2 Comparison of Case 1 and 2

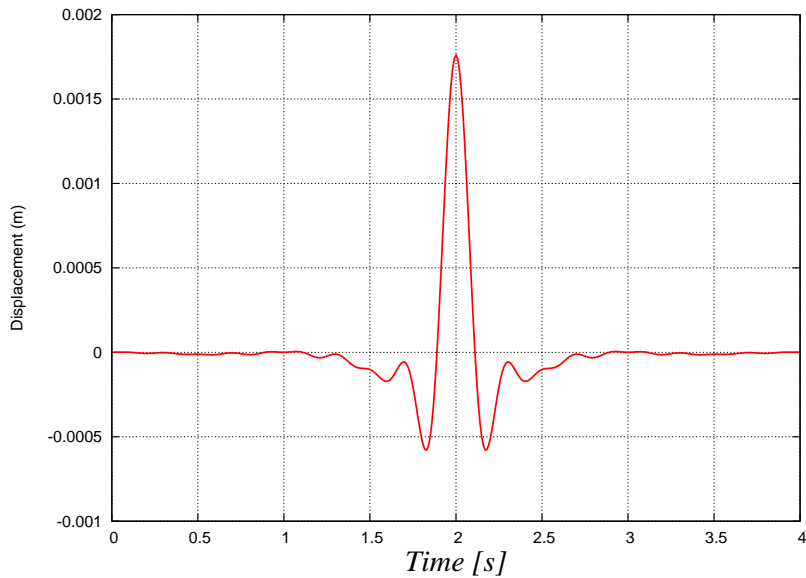


Figure 311.4: Displacement time history of input motion (Ormsby Wavelet)

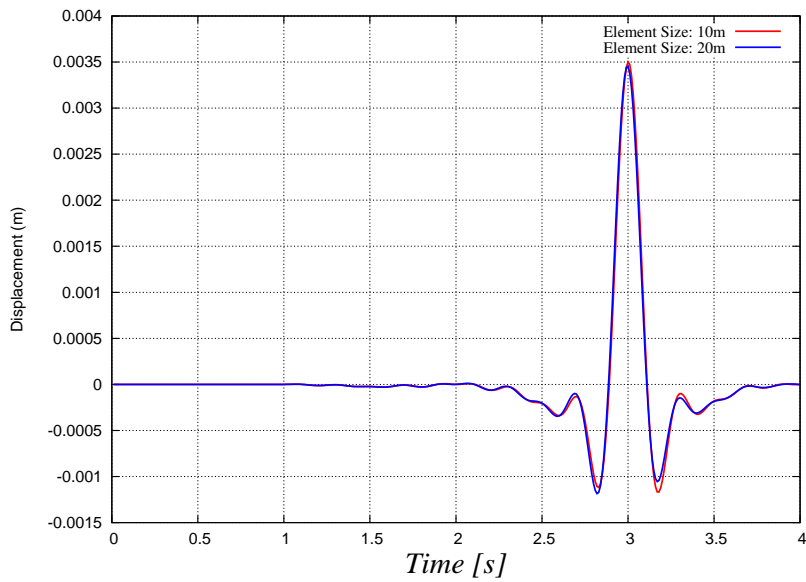


Figure 311.5: Comparison of displacement time histories of case 1 and 2 at top of the model

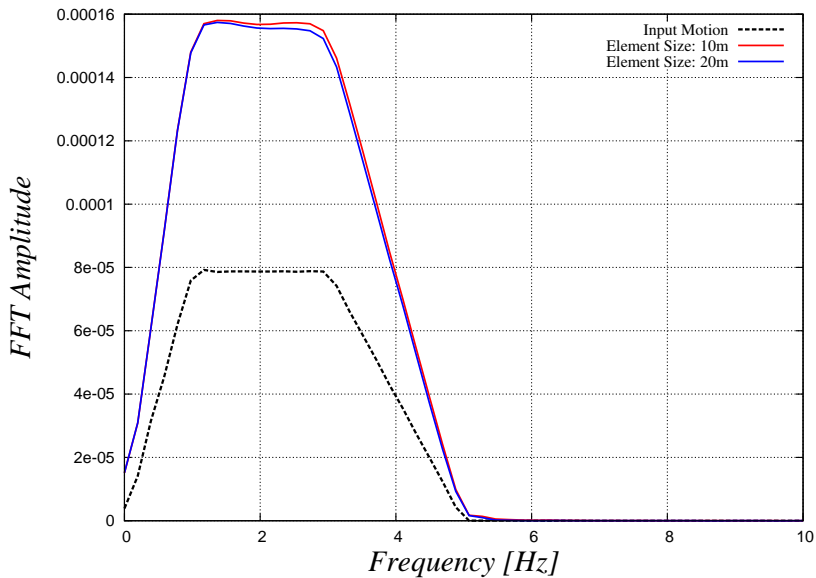


Figure 311.6: Comparison of FFT of case 1 and 2 at top of the model and input motion at the bottom of model

311.3.3 Comparison of Case 3 and 4

311.3.4 Comparison of Cases 3, 4, and 6

311.3.5 Comparison of Case 7 and 8

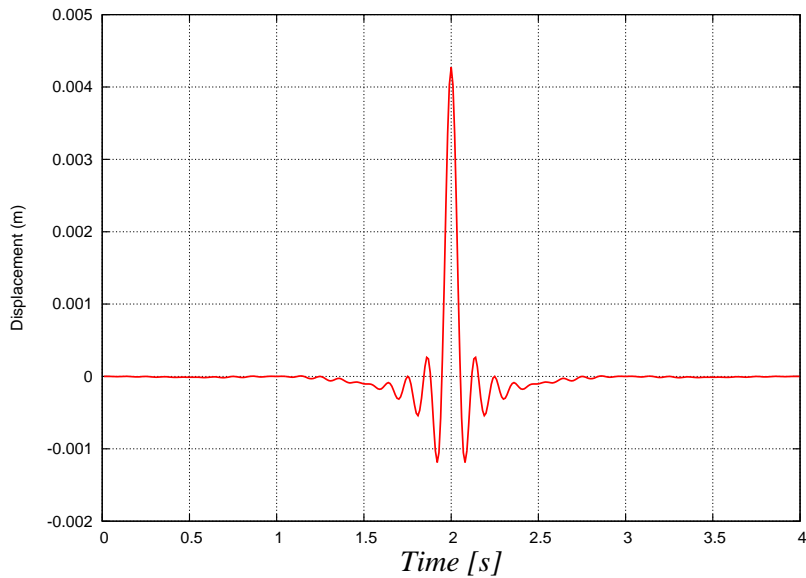


Figure 311.7: Displacement time history of input motion (Ormsby Wavelet)

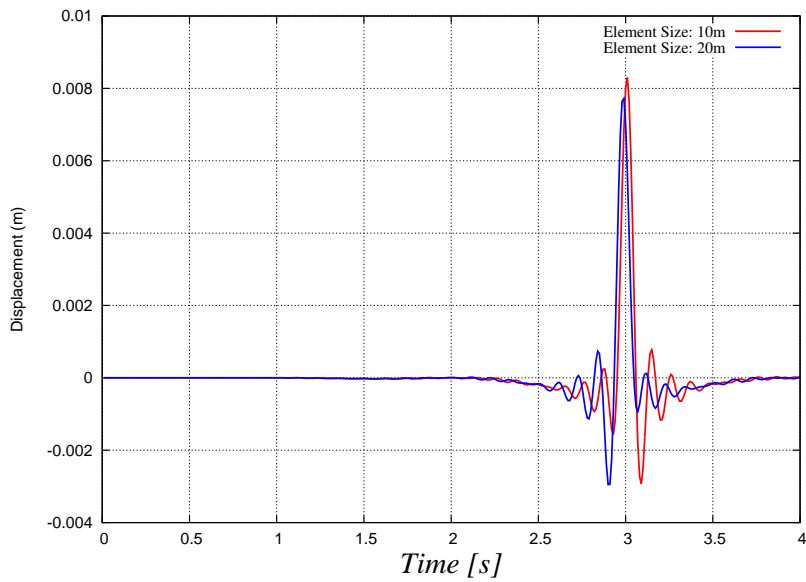


Figure 311.8: Comparison of displacement time histories of case 3 and 4 at top of the model

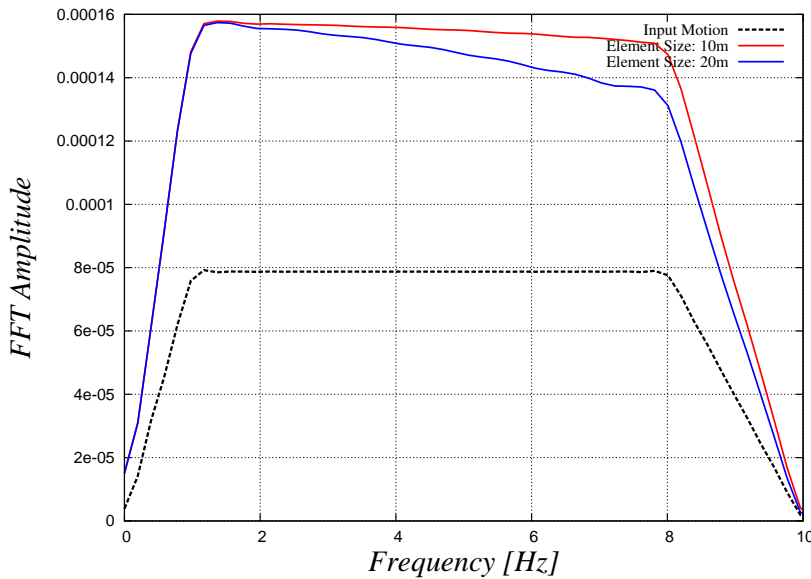


Figure 311.9: Comparison of FFT of case 3 and 4 at top of the model and input motion at the bottom of model

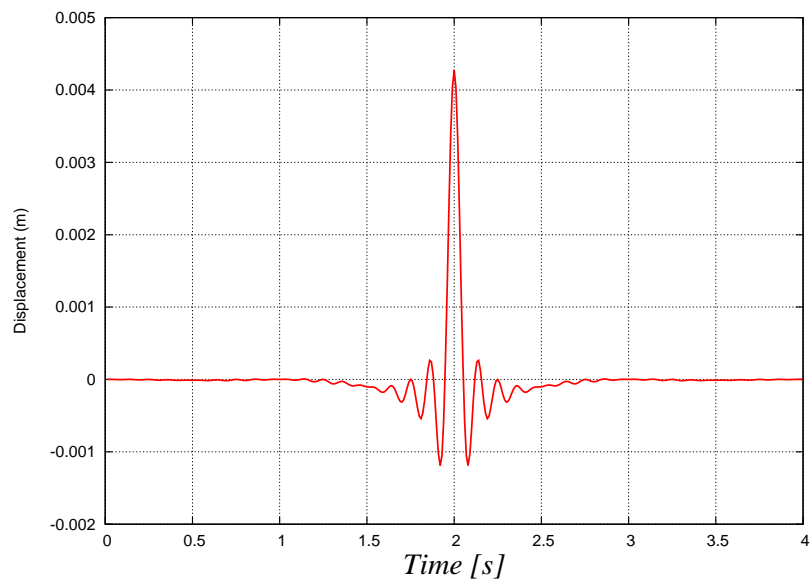


Figure 311.10: Displacement time history of input motion (Ormsby Wavelet)

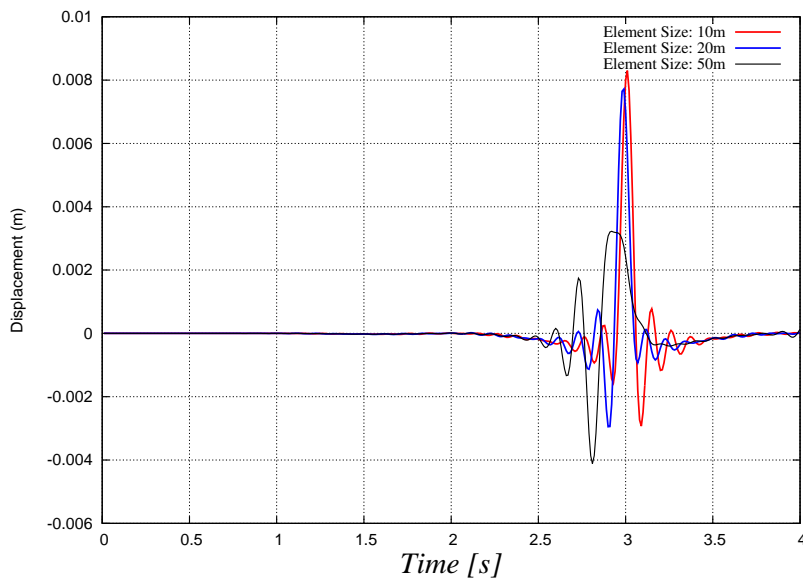


Figure 311.11: Comparison of displacement time histories of case 3, 4, and 6 at top of the model

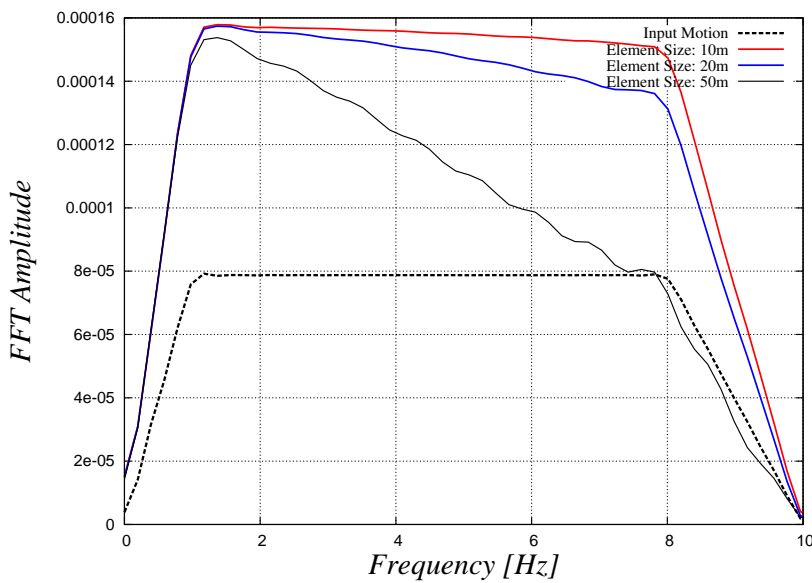


Figure 311.12: Comparison of FFT of case 3, 4, and 6 at top of the model and input motion at the bottom of model

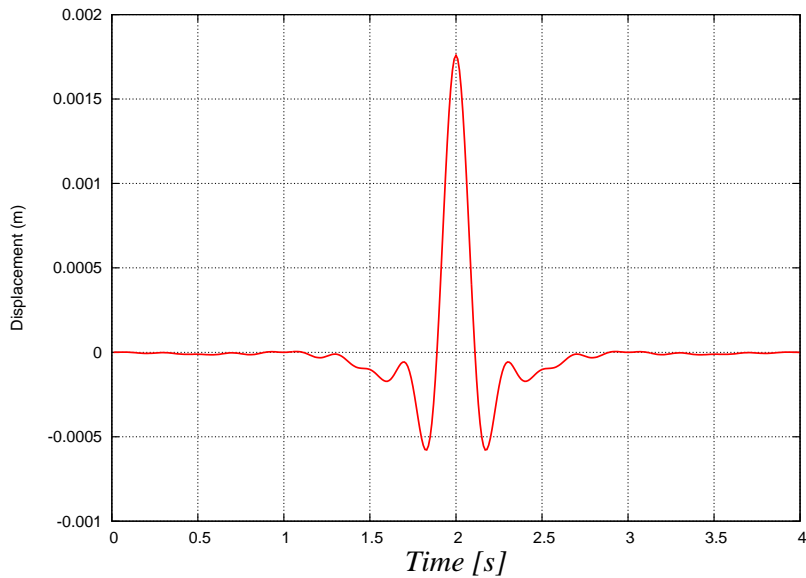


Figure 311.13: Displacement time history of input motion (Ormsby Wavelet)

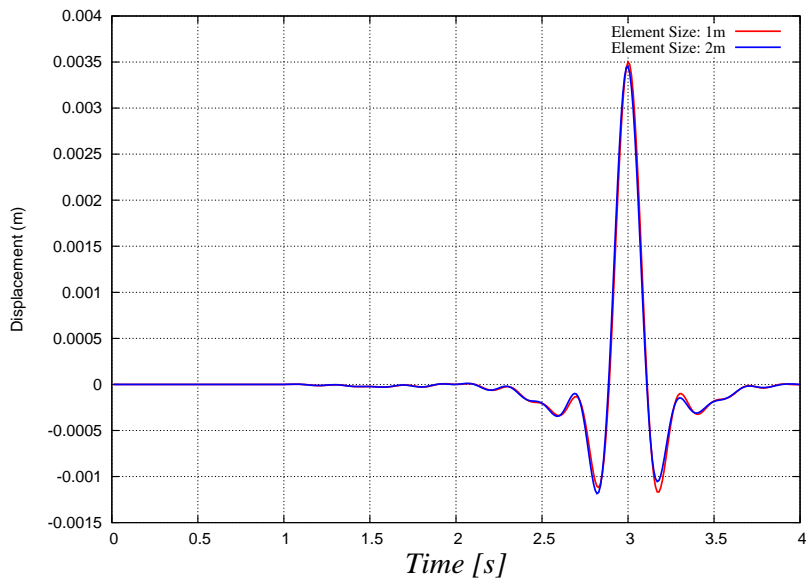


Figure 311.14: Comparison of displacement time histories of case 7 and 8 at top of the model

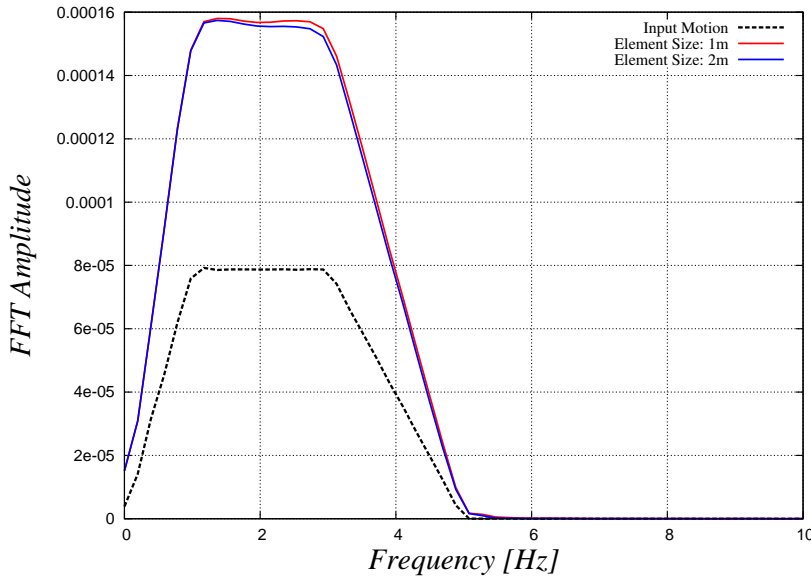


Figure 311.15: Comparison of FFT of case 7 and 8 at top of the model and input motion at the bottom of model

311.3.6 Comparison of Case 9, 10, and 11

311.3.7 Comparison of Case 12, 13, and 14

311.4 Damping of the Outgoing Waves

311.4.1 Comparison of Rayleigh Damping and Caughey 4th Order Damping

As mentioned before, Caughey damping in general will damp out the motions at specified modes (frequencies) to be specified which could also be the natural frequencies of the system. Depending on the type of damping to be used, the response of those modes would be affected. In order to observe the damping effect on certain modes, a soil profile is made with thickness of 50m and shear wave velocity of 100m/s. For input motion, an Ormsby wavelet with frequency range of 0 to 7 Hz is considered at the base of model. The wave is propagated through the soil layer using the elastic transfer functions and comparison is made between the case which Rayleigh damping is used versus the case which the frequency independent damping is used in the model. The same procedure is done by using Caughey damping.

Figures (311.22) and (311.23) show the base motion (Ormsby wavelet), motion at the surface

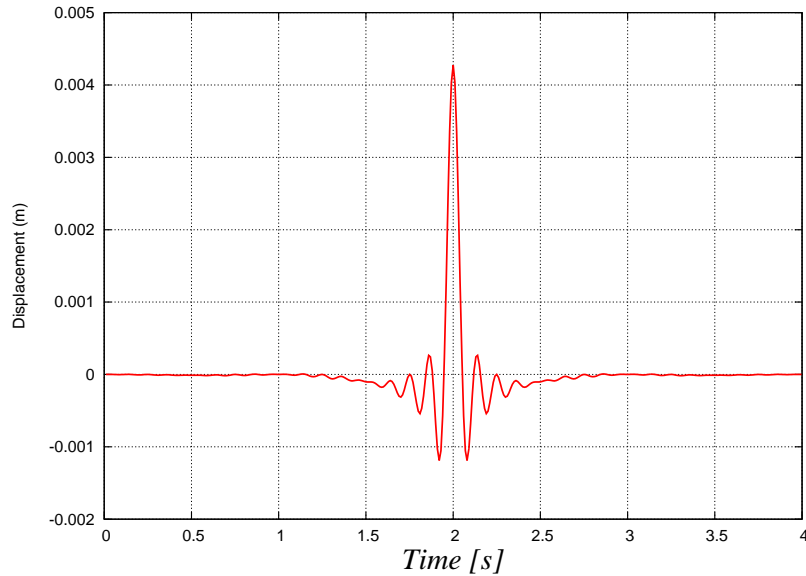


Figure 311.16: Displacement time history of input motion (Ormsby Wavelet)

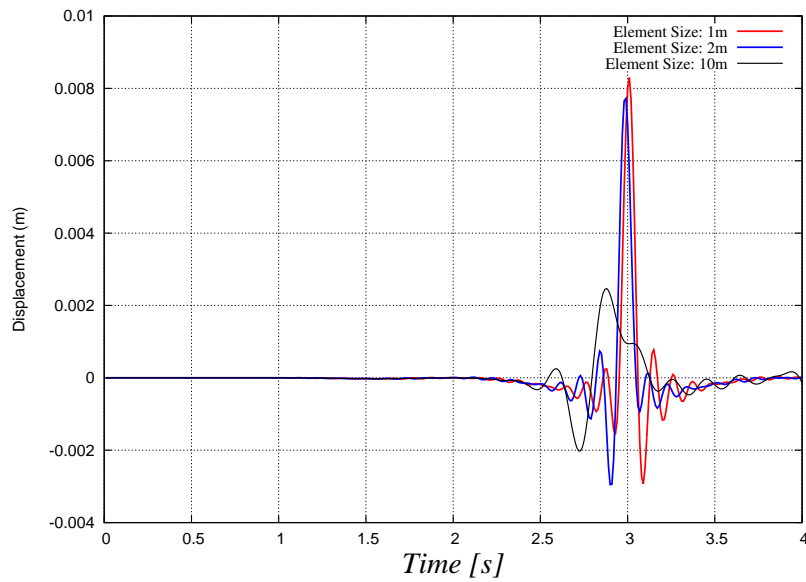


Figure 311.17: Comparison of displacement time histories of case 9, 10, and 11 at top of the model

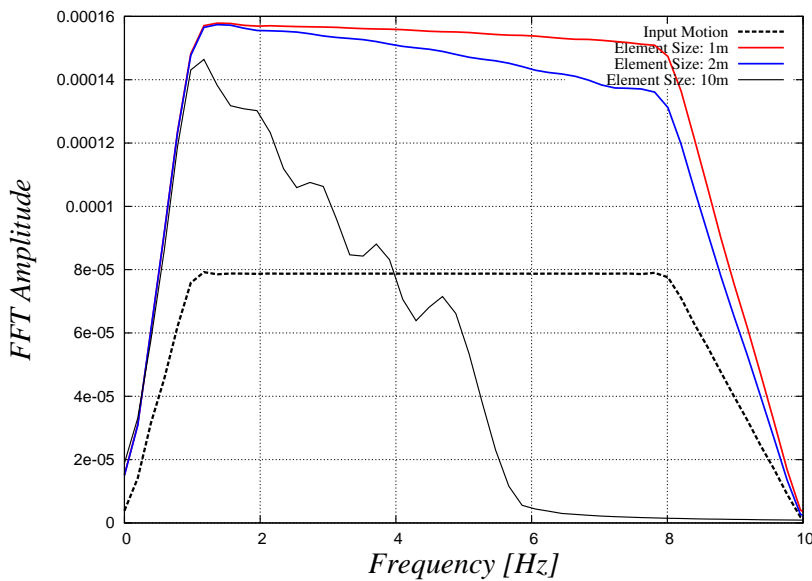


Figure 311.18: Comparison of FFT of case 9, 10, and 11 at top of the model and input motion at the bottom of model

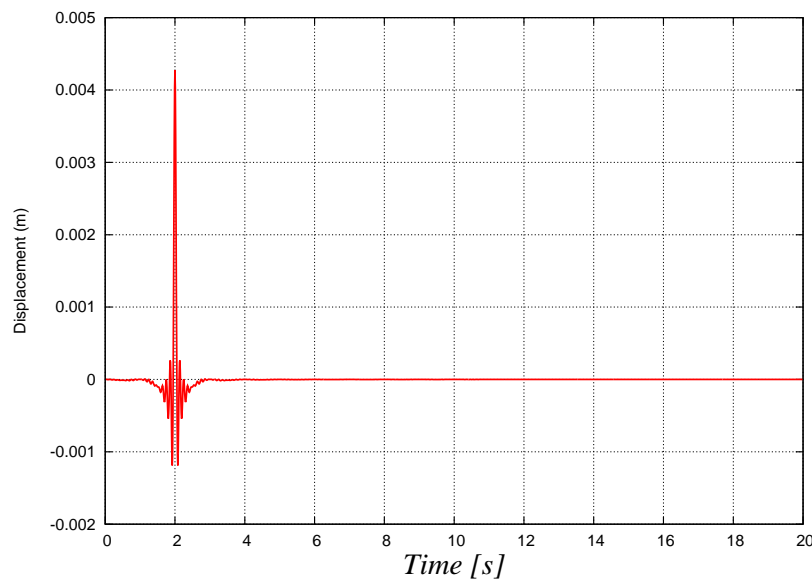


Figure 311.19: Displacement time history of input motion (Ormsby Wavelet)

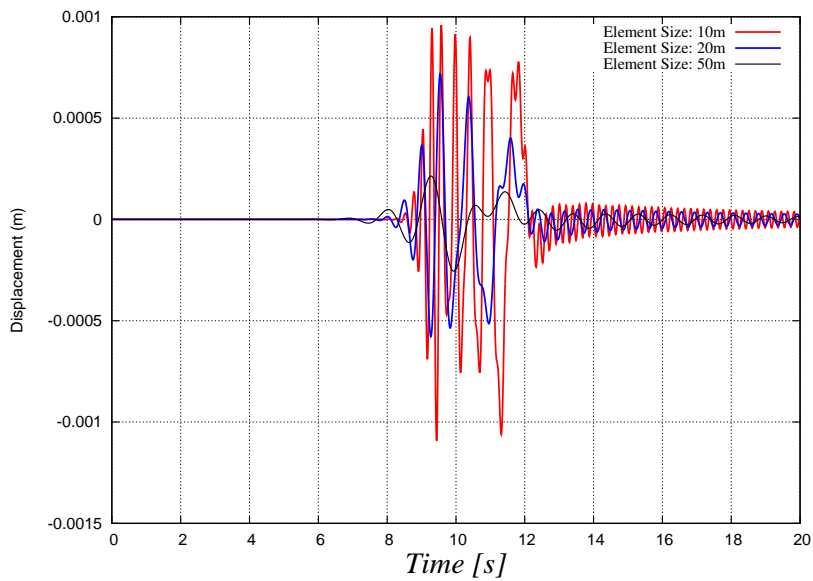


Figure 311.20: Comparison of displacement time histories of case 12, 13, and 14 at top of the model

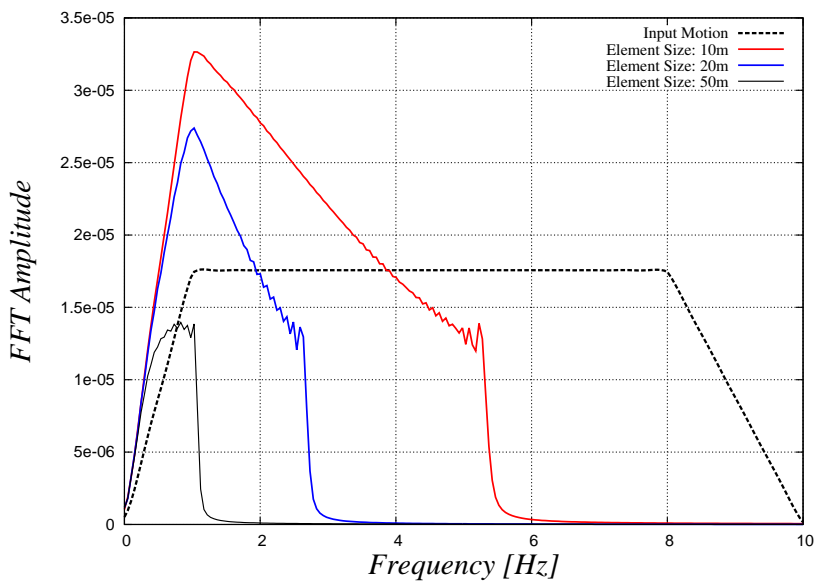


Figure 311.21: Comparison of FFT of case 12, 13, and 14 at top of the model and input motion at the bottom of model

considering the frequency independent damping, motion at the surface using Rayleigh wave (frequency dependent), motion at the surface using Caughey damping of 4th order (frequency dependent) as well as how Rayleigh and Caughey damping ratio change with frequency. It can be observed how the response is affected at different modes using Rayleigh damping versus using Caughey damping.

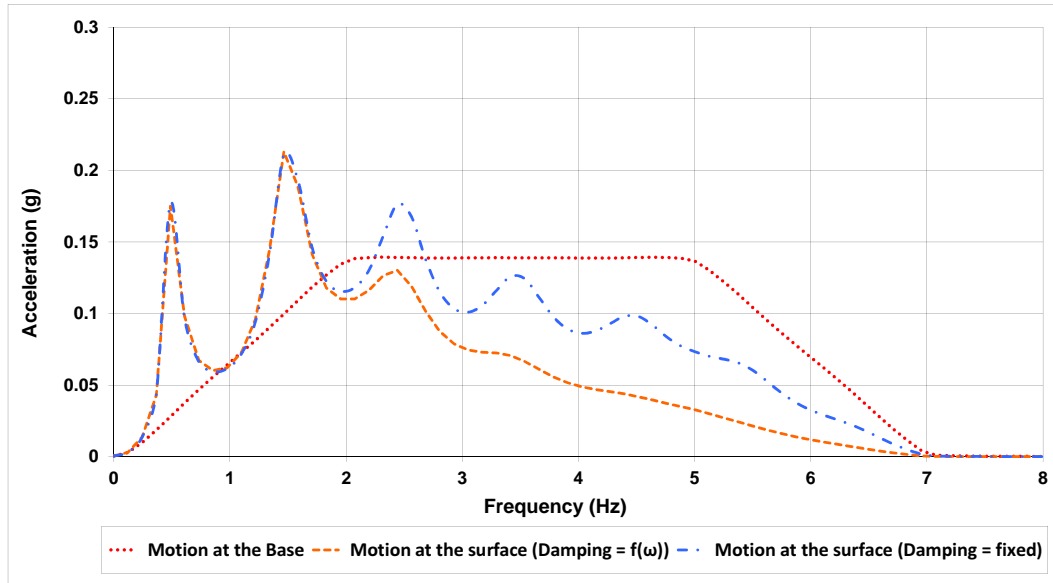


Figure 311.22: Comparison of obtained motion at the surface using frequency independent damping and frequency dependent Rayleigh damping.

311.4.2 Parametric Study on Effect of Rayleigh Damping on Reflected Waves

As mentioned in previous chapter, one of the issues of the modeling in dynamic analysis is reflecting of the motions from the boundaries since there are limitations regarding the size of the problems we can model. In order to reduce the computational cost of the problems, the size of the mesh has to be reduced. By reducing the size of the model the chance of reflecting the motions from the boundaries gets higher since there is less volume for the waves to get dissipated.

There are different ways to reduce reflection of the waves from the numerical boundaries such as PML, viscous dampers, infinite elements, or considering Rayleigh damping for specific elements. Presented here show the results of wave propagation models considering Rayleigh damping. There are different damping patterns used here such as constant damping ratio for all the elements in the damping zone or linear pattern of increasing the damping ratio.

In order to find the Rayleigh damping coefficients, two frequencies have to be considered. In these examples both cases of using the natural frequencies of the soil column and also using the dominant